Dirac fermions, i.e. electrons with a linear relation between momentum and energy, are highly suitable for electronic devices due to the reduced backscattering of these particles. Possible platforms for their emergence are topological insulators and graphene, which have attracted considerable scientific interest in the last two decades. In this work, quantum transport of charge and spin of Dirac electrons is studied numerically in a variety of different setups built from these materials. By applying a broad range of theoretical approaches not only the normal state is considered, but also effects arising in the superconducting state are discussed. The obtained transport features are related to the spectral properties of the charge or spin carriers and cantherefore be used in actual experiments to identify these special states.

Universität Regensburg
UNIVERSITÄTSBIBLIOTHEK

ISBN 978-3-88246-492-4
9 783882 464924

Spectral properties and quantum transport in hybrid Dirac systems

Michael Barth

Michael Barth

Spectral properties and quantum transport in hybrid Dirac systems

Eine Publikation der
Universitätsbibliothek Regensburg

Spectral properties and quantum transport in hybrid Dirac systems

DISSERTATION ZUR ERLANGUNG DES DOKTORGRADES DER NATURWISSEN-
SCHAFTEN (DR. RER. NAT.) DER FAKULTÄT FÜR PHYSIK

DER UNIVERSITÄT REGENSBURG

vorgelegt von

Michael Barth aus

Neumarkt i.d.OPf.

im Jahr 2023

Promotionsgesuch eingereicht am: 17.01.2023

Das Promotionskolloquium fand statt am: 17.07.2023

Die Arbeit wurde angeleitet von: Prof. Dr. Klaus Richter

Prüfungsausschuss

Vorsitzender: Prof. Dr. Dieter Weiss
1. Gutachter: Prof. Dr. Klaus Richter
2. Gutachterin: Prof. Dr. Milena Grifoni
Weiterer Prüfer: Prof. Dr. Christoph Lehner

Bibliografische Information der Deutschen Nationalbibliothek

Die Deutsche Nationalbibliothek verzeichnet diese Publikation in der Deutschen Nationalbibliografie. Detaillierte bibliografische Daten sind im Internet unter http://dnb.dnb.de abrufbar.

ISBN (Print): 978-3-88246-492-4

ISBN (PDF): 978-3-88246-493-1

DOI: 10.5283/epub. 54940

Link zur Online-Version: https://epub.uni-regensburg.de/54940

Satz und Layout: Michael Barth

Titelbild: Michael Barth

Umschlaggestaltung: Peter Brünsteiner

Herstellung: Universitätsbibliothek Regensburg

Erscheinungsort: Regensburg, 2023

Druck und Bindung: Digital Print Group o. Schimek GmbH, Nürnberg

Abstract

Topological insulators and graphene host peculiar states, which have a linear dispersion and can be described by an effective Dirac Hamiltonian. In this thesis, we numerically study quantum transport phenomena and spectral properties of such materials. We consider three dimensional systems and nanowires, which exhibit quantization effects, and also examine the physical properties of superconducting hybrid platforms. The influence of external magnetic fields and geometrical properties are taken into account. Additionally, we device methods to treat such systems in a computationally efficient way and discuss a variety of numerical approaches to calculate the desired quantities.
The achievements of this thesis are threefold. First, we managed to make theoretical predictions for physical effects which might be observable in actual experiments. Transport simulations show flux-periodic conductance oscillations for topological insulator core-shell nanowires, where the periodicity is determined by the cross-sectional geometry. Moreover, by exploiting constrictions in topological insulator nanowires, it could be possible to generate resonant Dirac states, which can be probed in terms of gate and magnetic flux dependence by a simple two terminal measurement. Additionally, due to the Dirac nature of topological nanowire surface states, perfect crossed Andreev reflection can occur in T-junctions [1], which is tunable by an external magnetic field. The capability to switch it on and off in combination with its robustness could serve as a clear experimental signature. Also for graphene platforms predictions could be made. Spin relaxation in single and bilayer graphene originating from scattering at magnetic impurities should show either an increasing or decreasing behavior as a function of temperature [2, 3] when the chemical potential in the system is tuned. This finding is in contrast to known theory and related to the spectral properties of localized Yu-Shiba-Rusinov states. In combination with conceptually simpler experiments on Josephson junctions, these features could be studied in detail.
Second, we were able to give theoretical explanations for experimental measurements. HgTe nanowire Josephson junctions exhibit $h/(4e)$-flux periodic supercurrent oscillations in low transparency samples [4]. The origin of such oscillations lies in a partial proximitization of the nanowire surface and local barriers between normal and superconducting regions. Andreev bound states pick up certain phases due to the special geometry and the applied axial magnetic flux, which then leads to the observed critical current signatures. The effect should not be limited to topological surface states, but could instead be also observable in semiconductor nanowire Josephson junctions with trivial surface states in a surface accumulation layer.
Third, we managed to develop schemes and methods to advance the possibilities of studying normal and superconducting systems. In order to get access to the spin-relaxation rate in superconducting systems a detailed implementation procedure was

given and the quantity was related to the scattering matrix S [2, 3]. Thereby, we could show the above mentioned discrepancy with the known theory. Lastly, a non-uniform tight-binding approach to treat two dimensional topological insulators and hybrid systems was devised. It greatly reduces the numerical cost, while increasing the computational accuracy of the calculated results and might enable to treat system sizes which are experimentally more realistic.

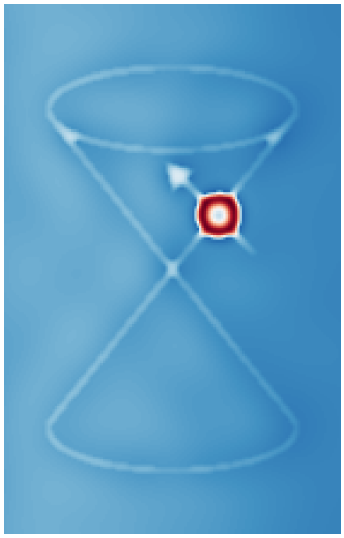

Local density of surface scattering states calculated with Kwant.

List of used acronyms:

1D	– one-dimensional/one dimension
2D	– two-dimensional/two dimensions
3D	– three-dimensional/three dimensions
2DEG	– two-dimensional electron gas
ABS	– Andreev bound state
BCS	– Bardeen-Cooper-Schrieffer
BdG	– Bogoliubov-de Gennes
BHZ	– Bernevig-Hughes-Zhang
CAR	– crossed Andreev reflection
CF	– correlation function
CPR	– current-phase relation
DOS	– density of states
FFT	– fast Fourier transformation
FM	– ferromagnetic metal
LDOS	– local density of states
N	– normal-conducting material
PBC	– periodic boundary conditions
PSD	– power spectral density
S	– superconductor
SOC	– spin-orbit coupling
TI	– topological insulator
YSR	– Yu-Shiba-Rusinov

Contents

1. Introduction

In the last two decades research on topological materials has risen to one of the most important disciplines of condensed matter physics. The topic has rapidly attracted an enormous amount of scientific interest after the discovery of the quantum spin Hall effect by Kane and Mele [5, 6] in 2005. The novel feature of the considered system was the emergence of states that are energetically located inside of the bulk band gap separating the conduction and valence bands. These conducting states can carry a current and are strongly localized at the edges of the system, where the edges are given by the boundaries of the bulk material with vacuum or other topologically trivial system materials. In contrast, the bulk of the material is in an insulating state. Even more remarkably, these states are spin polarized and counterpropagating modes have oppositely aligned spins. These features are responsible for the finding that backscattering of electrons in these states should be strongly suppressed. Less inelastic scattering means less loss of energy, which might be transformed into heat and therefore vanishes into the environment. This reasoning makes such states perfect candidates for efficient electronic devices.

Microscopically, the origin of these so-called topological states lies in spin-orbit coupling (SOC), which acts as an intrinsic magnetic field [7]. This connects these topological states with the well-known quantum Hall effect, which was first measured in 1980 [8], where chiral edge states form due to an externally applied magnetic field. It turns out that many materials can be classified by so-called topological invariants, where the most prominent one is the Chern number n [9]. By taking into account the actual bandstructure of the studied system, the topological invariants can be determined and used to distinguish between topologically trivial and non-trivial materials. As long as the bulk band gap is not being closed, external perturbations cannot change the topological invariants, making topological states extremely robust against such perturbations. This property is, for example, reflected in the reduced backscattering of quantum (spin) Hall states.

Soon after the proposal by Kane and Mele [5, 6], other material compounds were predicted to likewise host these topological electronic states. Not only two-dimensional (2D) materials can host them on their edges, but also three-dimensional (3D) bulk systems [10] are able to form analogous states on their 2D surfaces. Due to their insulating bulk behavior and the presence of topologically protected conducting surface or edge sates, these systems are denoted as topological insulators (TIs). Famous examples are bismuth-based materials [11] and mercury-telluride (HgTe) quantum wells [12]. By now, thousands of material compounds are predicted to host topological states [13].

Large experimental efforts are being made to improve the system properties in order to keep their special features also at room temperature. The already performed experiments and the vast amount of possible theoretically predicted effects lead to a fundamental research interest regarding these materials.

Shortly before topological insulators became a topic of interest, Geim and Novoselov managed to produce a single layer of graphite, namely graphene, by the process of micromechanical cleavage in 2004 [14]. In 2010, they were awarded the Physics Nobel prize for their discovery, which can be considered the starting point of extensive studies on purely 2D materials.
Graphene, with its 2D hexagonal lattice structure of carbon atoms, is analogously to topological insulators a promising candidate for electronic devices and applications. It has charge carriers with high mobilities [15] and its predicted long spin coherence length [16] makes it particularly relevant to spintronic applications. The properties of first samples suffered from strong lattice deformations, defects, and external impurities. But experimental improvements increased material qualities considerably, for example, by encapsulating the graphene layer in boron-nitride monolayers [17]. This protects the carbon sheet from external influences and stabilizes the hexagonal lattice structure. Furthermore, the electronic and optical properties can be tuned [18, 19] by stacking graphene with other 2D materials, for instance, with transition-metal dichalcogenides. This procedure allows to enhance, e.g., the SOC inside graphene [20], further enhancing its suitability for spintronics. This procedure is necessary, as the intrinsic SOC of bare graphene has only a tiny magnitude of a few μeV [21]. Research in this field is also developing fast and technological advances would certainly give benefits to many areas of everyday life.

Both material classes, i.e., topological insulators and graphene, exhibit special states, which can be described by a Dirac Hamiltonian that is well known from high-energy physics. This connection obviously raises the question if relativistic effects are observable and measurable in condensed matter physics, and further enhances the importance of research on them. In the low-energy range, the topological surface or edge states of TIs, as well as the states at the touching points of conduction and valence bands in graphene, exhibit a linear dispersion in their energy spectrum. One of the most famous predictions to occur due to the linear dispersion is, for example, Klein tunneling [22] in graphene, where incoming modes cannot be backscattered from a potential-step barrier. However, in actual experiments, it is often hard to tune the Fermi energy of the system close to the Dirac point, such that the interesting properties of the linear bands are either strongly affected by band deformations or hidden beneath large bulk contributions. For example, in HgTe systems, the Dirac point is hidden inside the bulk valence band [12]. To some extent, this problem can be circumvented by adjusting the HgTe thickness and by inducing the right amount of strain in the crystal. Therefore, it is important to check for these bulk contributions and to perform a detailed analysis of actual experiments.

Note that not only larger samples of micron size are of interest for measurements and devices. Instead, also ribbons and wires, as well as quantum dots, constructed from TIs and graphene offer the possibility to discover new physics. On the one hand, TI nanowires host a single Dirac cone on their surface, where initially no linear dispersion is present due to the opening of a bandgap originating from a Berry phase of π [23]. The coherently wrapped states around the wire circumference are spin-momentum locked, such that the spin of a particle that circles once around the perimeter will pick up the additional Berry phase. This allows to tune the conductance by applying an axial magnetic field, such that the surface states will additionally be influenced by an Aharonov-Bohm phase [23, 24]. Signatures of this nanowire property have already been experimentally observed [24, 25]. On the other hand, graphene nanoribbons are known to show either semiconducting or metallic behavior depending on the wire-edge properties, which can be either in the zigzag or armchair configuration. Therefore, also the sample geometry can be used to modify the electronic properties.

TIs and graphene by themselves offer already a variety of interesting properties, but even more fascinating phenomena arise by combining them with superconducting components. Superconductivity was discovered more than one hundred years ago, but still many new aspects regarding this topic are being discovered. A lot of materials are not superconducting by themselves, at least when simply lowering the temperature. Instead, one can exploit the superconducting proximity effect, which arises if a normal-conducting material (N) like a specific TI is brought into close proximity to an s-wave superconductor (S) like aluminum or niobium. By constructing such a hybrid structure, superconducting pairing can also be induced in the otherwise normally conducting part of the system. For TIs, this has also been verified experimentally [26, 27]. Note that the surface states have now the novel properties of both components, and the setup is therefore denoted as a topological superconductor. Furthermore, in case of graphene, it has been recently shown that a bilayer structure can become superconducting [28] without the need of the proximity effect. The trick is to slightly rotate the two graphene sheets by the so-called magic-angle of around 1.1°. This structure is then denoted as twisted bilayer graphene. The emerging pairing mechanism corresponds to an unconventional superconducting state and is attributed to interactions which arise due to a high density of states introduced by flat bands [28] which originate from the twisting angle between the two carbon sheets. Nevertheless, despite being a very interesting research topic, we will focus on proximity-induced superconductivity in single-layer and bilayer graphene in this work.

In the center of research on topological superconductivity stands the search for Majorana fermions [29], which own the special property that they are their own antiparticles. These exceptional particles are promising candidates for the efficient and robust information storage in quantum computers [30]. In the last years, many setups were proposed for their generation and a review of possible platforms can be found, e.g., in Ref. [31]. These are ranging from semiconductor nanowires, over 2D Josephson-junction setups and chains of magnetic impurities, to vortices in topological

superconductor surfaces. Usual experiments rely on transport measurements in hybrid setups of normal and superconducting system parts. As Majorana fermions are predicted to be robust against external perturbations, the observed conductance should exhibit a zero-bias peak which is quantized exactly in quanta of $2e^2/h$. In topological insulator nanowires, a possible fingerprint of Majorana fermions is the 4π-periodic Josephson current-phase relation (CPR), for which a recent experimental work [32] already revealed promising signatures. However, up to now, no clear experimental evidence has been found as a bulletproof signature of the existence of Majorana fermions. The present work partially focuses on general transport effects in TI nanowire systems, where such states could, in principle, also emerge.

Below, an outline of this thesis is given by providing a brief summary of all the discussed topics of each chapter. In Chapter 2, the basic theoretical framework regarding the studied Dirac systems will be introduced. Initially, model Hamiltonians for the description of topological insulators are discussed. While a 2D effective Dirac Hamiltonian can be used to efficiently describe the surface states of TI nanowires [23, 24], the 3D Bernevig-Hughes-Zhang (BHZ) Hamiltonian [11, 33] will be employed for more complex geometries and to check the results of pure effective 2D models. Next, tight-binding descriptions of single-layer and bilayer graphene, as well as related impurity models, are given. Afterwards follows a short introduction to superconductivity, with all its related effects that are studied in this thesis, and lastly spin relaxation is introduced.

Chapter 3 covers all the relevant numerical techniques that are applied to the different systems of interest in this thesis. Tight-binding is a standard approach for transport simulations in physics and, by now, a variety of open-source software is available to simplify computations. In this work the Python package Kwant [34] will be employed. Therefore, the discretization of a continuous Hamiltonian and the incorporation of a magnetic field are initially explained. Then, the simulation procedure of effectively infinite 2D systems is discussed in detail, which will also be of big importance for the calculation of spin-relaxation rates. Additionally, the efficient generation of correlated disorder for transport simulations and the fermion doubling problem [35–37] for a Dirac Hamiltonian on a lattice are explained. Finally, the methods for treating superconducting systems are introduced. These concern the calculation of Andreev bound states with the corresponding supercurrents in Josephson junctions, as well as the numerical computation of spin-relaxation rates from the scattering matrix.

After the detailed discussion of the necessary fundamentals and methodologies in the first two chapters, these will be applied to topological insulator systems in Chapter 4. Realistic TI samples of bismuth compounds often have surface structures that resemble "islands" of different quintuple layer step heights. In order to make reliable theoretical predictions for experimental measurements, such structures are generated exploiting the aforementioned code for correlated disorder and the local density of states (LDOS) is studied for scattering of surface states off such steps. We find that the LDOS is

highest at the edges of surface steps, while it clearly decreases right before such structures on the lower surface plain. Moreover, contrary to the usual and well-known TI nanowires with a single Dirac cone on the surface, also core-shell nanowires can be grown. The latter have a second interface with the insulating core material. Therefore, the influence of an axial magnetic field on the bandstructure of such wires is studied in detail and transport signatures are examined by means of an effective surface model. Conductance calculations show clear signatures of flux-periodic modulations due to the interplay of modes on the inner and outer surfaces. Next, the bandstructure of Bi_2Se_3 nanowires in magnetic fields perpendicular to the wire axis, but with an arbitrary angle in the cross-section, is discussed and the generation of 1D hinge states in the context of higher-order TIs [38] is studied. Furthermore, advancing the research on TI nanowires with a non-constant cross-section on the basis of the PhD thesis of Dr. Kozlovsky, transport simulations are performed on constriction setups. Such systems are important to understand, as they are closer to realistic samples, particularly in regards of etched HgTe nanowires. Our results show that resonant Dirac states can be generated by a magnetic confinement that originates from the special geometry. These states obey the properties of the Dirac spectrum and therefore its features can be probed spectroscopically with conductance measurements. Making then the transition to superconducting systems, the process of crossed Andreev reflection (CAR) [39–42] is studied in a TI nanowire T-junction. We find that robust CAR can be switched on and off in the single mode regime by tuning an external magnetic field [1], which can serve as a smoking gun signature in actual experiments. Additionally, in favor of experimental realizations, CAR is also observable in a broad parameter range. Finally, by taking into account again a single TI nanowire, which is used as a normal region between two superconducting leads to form a Josephson junction, the Andreev bound state (ABS) spectrum and the supercurrent are computed with respect to an axially applied magnetic field. The junction is initially considered to be placed in weak magnetic fields with a uniformly induced superconducting gap, while afterwards an experimentally more relevant and more realistic system configuration is examined. For the latter, peculiar $h/(4e)$-flux periodic supercurrent oscillations can be measured in HgTe Josephson junctions, where we introduce a model that captures and explains such oscillations as a result of the special geometry and surface state transport [4].

As alternative Dirac systems, also single-layer and bilayer graphene are studied in Chapter 5. There, we concentrate on the superconducting phase and only consider the normal-conducting state for comparison. Initially, the emergence of Yu-Shiba-Rusinov (YSR) states is investigated in superconducting bilayer graphene, which is chemisorbed by a single magnetic hydrogen impurity. More precisely, the spectrum in dependence on the chemical potential is calculated and the LDOS of the YSR states is shown for different impurity positions. The results show that YSR energies separate from the superconducting continuum spectrum, whenever the chemical potential is close to resonances in the perturbed normal state DOS [3]. Next, the spin-relaxation rates for scattering off local impurities by the Elliot-Yafet spin scattering mechanism [43, 44] in superconducting single-layer and bilayer graphene is studied. The impurities are

considered to induce either local spin-orbit coupling or a local exchange coupling. For the latter, the influence of the emerging YSR states on the relaxation rate is further explained. We see that the separation of YSR states from the continuum spectrum for resonant doping levels can lead, contrary to expectations from the known theory, to a strong reduction of the spin-relaxation rate [2, 3]. Lastly, also a bilayer graphene Josephson junction with a single magnetic hydrogen impurity in the normal region is studied. There, it is shown that signatures of YSR states can also be found in the charge transport, given by a strong and clear cut decrease of the Josephson supercurrent for resonant chemical potential values [3].

Chapter 6 covers a more technical aspect regarding the efficient numerical simulation of systems with a large local density of states in a limited spatial region of the full volume or area. Prime examples are topological insulators, where surface or edge states are exponentially confined to the surfaces and edges of the bulk material, or, in general, systems that have interfaces between different material components. Their numerical implementation can be improved by employing a non-uniform tight-binding method, which is introduced and developed in detail. Afterwards, the procedure is applied to two explicit examples and compared to standard uniform tight-binding simulations. We show that the numerical effort can be kept to a minimum, while increasing the accuracy of the computed quantities such as the LDOS of topological edge states or bandstructures of hybrid systems.

After studying a variety of different systems and setups, the main findings are summarized and highlighted in the following chapter. Moreover, a short outlook is given for possible future studies and open questions that still need further attention are addressed.

Appendices are left as a final chapter right after. Some sanity checks are performed in order to compare the results obtained from different calculation approaches and to check their correctness. Also, details of the numerical tight-binding implementation of Hamiltonians with cubic terms in momenta are given, which were important for the calculation of the anisotropic spin injection in Ref. [45].

2. Theoretical background

This chapter provides the necessary theoretical background for the following parts of this thesis. The reader will be first introduced into the models that describe topological insulator systems, where a full 3D model, as well as an effective surface model, are treated. Second, single-layer and bilayer graphene are discussed, including the modeling of adatoms which are chemisorbed on top af the carbon layers. Right after that, an introduction into superconductivity, together with all of its related physical effects and phenomena, which will be studied in this thesis, will follow. Finally, the reader will be introduced into the concept of spin relaxation.

2.1. Topological insulators

Since the discovery that topological states can emerge due to spin-orbit coupling [5, 6, 10] in real material systems, research on topological materials has evolved into a prominent part of condensed matter physics. Topological insulators are a material class whose constituents are classified by a non-trivial topological invariant $\mathbb{Z}_2$, and that host edge or surface states [9] inside of a bulk energy gap between conduction and valence bands. There are a variety of ways to compute the $\mathbb{Z}_2$ invariant, depending on the system that is considered. For detailed explanations on this topic, see Refs. [9, 46, 47] and the references therein. In essence it is a quantized number that does not change for smooth perturbations of the Hamiltonian without a gap closing and that is linked to the properties of the corresponding bulk bands [11, 48, 49]. If a material has a non-trivial topological invariant, in contrast to, for example, vacuum, then the band gap needs to close around the edge or surface of the material in order to assure a continues transformation between the different states. This closing of the band gap leads to the formation of surface or edge states, which are predicted to possess numerous special physical properties. A key feature of these states is that they have a linear dispersion and can be described by an effective Dirac Hamiltonian in the low-energy regime [7, 9]. Moreover, the spin of these states is locked to their momentum and they are predicted to be very robust against backscattering [7, 23]. Up to now, thousands of material compounds have been predicted to be topological insulators [13] and even machine learning algorithms [50] are being employed to find new candidates. Most prominent examples of topological insulators are the bismuth-based materials Bi_2Se_3, Bi_2Te_3, and $Bi_{2-x}Sb_xTe_{3-y}Se_y$ [11, 51, 52], as well as the quantum-well-based HgTe systems, which can be 2D or 3D topological insulators depending on the quantum well thickness [12, 53]. The first material class is predicted to exhibit surface states that are located inside large energy gaps ranging hundreds of meV [11], which could be an

(a) Bi_2Se_3

$M = 0.28\,\text{eV}$	$A_1 = 2.2\,\text{eV Å}$
$C = -0.0068\,\text{eV}$	$A_2 = 4.1\,\text{eV Å}$
$B_1 = 10\,\text{eV Å}^2$	$D_1 = 1.3\,\text{eV Å}^2$
$B_2 = 56.6\,\text{eV Å}^2$	$D_2 = 19.6\,\text{eV Å}^2$

(b) Toy model parameters

$M = 1\,\text{eV}$	$A_1 = -1\,\text{eV Å}$
$C = 0\,\text{eV}$	$A_2 = -1\,\text{eV Å}$
$B_1 = 1\,\text{eV Å}^2$	$D_1 = 0\,\text{eV Å}^2$
$B_2 = 1\,\text{eV Å}^2$	$D_2 = 0\,\text{eV Å}^2$

Table 2.1: Hamiltonian parameters for Eq. (2.1).

advantage for experimental applications. But these materials often suffer from strong disorder, which leads to large metallic bulk conductivity [54–56]. HgTe systems on the other hand can be built with high quality possessing long phase-coherence lengths of a few microns [25]. But the drawback of these systems is that their surface states are submerged inside the bulk valence band [25, 57], such that one always needs to check for bulk effects in actual experiments. In the following sections of this thesis both kinds will be considered. Therefore, we will next introduce the models which allow us to describe and study these systems theoretically.

2.1.1. 3D BHZ model

In order to model topological insulator systems based on Bi_2Se_3 in many of the following numerical simulations, we employ the well-established 3D Bernevig-Hughes-Zhang (BHZ) model [11, 33], which is given in the basis $\{|p1_z^+\uparrow\rangle, |p2_z^-\uparrow\rangle, |p1_z^+\downarrow\rangle, |p2_z^-\downarrow\rangle\}$ by

$$\begin{aligned} H_{\text{BHZ}} = &\left(\epsilon(\boldsymbol{k}) - \mu\right) \mathbb{1}_{4\times4} \\ &+ \begin{pmatrix} M(\boldsymbol{k}) & A_1 k_z & 0 & A_2 k_- \\ A_1 k_z & -M(\boldsymbol{k}) & A_2 k_- & 0 \\ 0 & A_2 k_+ & M(\boldsymbol{k}) & -A_1 k_z \\ A_2 k_+ & 0 & -A_1 k_z & -M(\boldsymbol{k}) \end{pmatrix}, \end{aligned} \tag{2.1}$$

with

$$\epsilon(\boldsymbol{k}) = C + D_1 k_z^2 + D_2(k_x^2 + k_y^2), \tag{2.2}$$

$$M(\boldsymbol{k}) = M - B_1 k_z^2 - B_2(k_x^2 + k_y^2), \tag{2.3}$$

$$k_\pm = k_x \pm \mathrm{i} k_y. \tag{2.4}$$

The basis corresponds to the relevant bulk band orbitals which give rise to topological surface states via band inversion. This model is a low-energy approximation that takes into account the lowest conduction and highest valence bands of the bulk material. In order to obtain concrete system parameters, the Hamiltonian spectra were fitted to DFT calculations (see, for example, Ref. [33]). The parameter values, which will be used throughout this thesis, can be found in Tab. 2.1. We use the standard values for Bi_2Se_3 and simplified toy model parameters in order to make also general predictions, independently of a special material compound configuration.

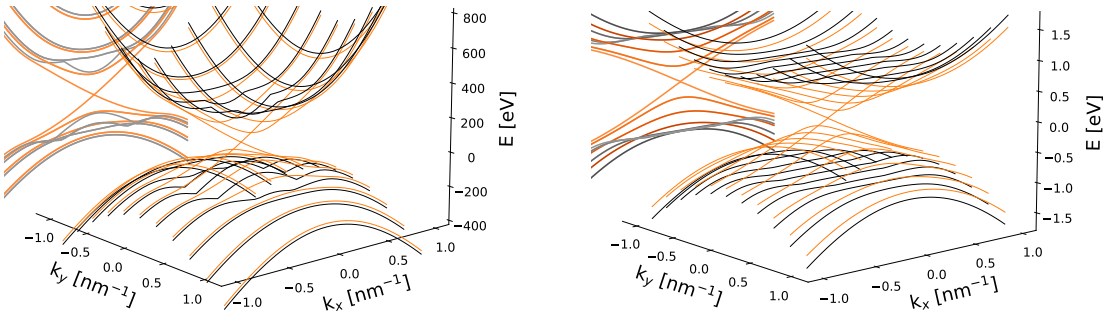

(a) Bandstructure for Bi_2Se_3.

(b) Bandstructure for toy model values.

Figure 2.1: Bandstructure plots computed with the BHZ model [Eq. (2.1)] and the parameters of Tab. 2.1. Black (orange) lines correspond to bulk (surface) bands.

Note that Eq. (2.1) describes a trivial insulator if $M/B_2 < 0$ and a topological insulator for a sign change in M [58]. In Figs. 2.1 (a) and (b) the bandstructures plots for the parameters listed in Tab. 2.1 are shown. The spectra were computed for slab geometries with infinite x- and y-dimensions. Black colored bands correspond to the bulk conduction and valence bands, while the orange colored spectra indicate the topological surface states. For better visibility, also a quasi-1D projection is shown on a vertical plane. While the toy model parameters lead to a particle-hole symmetric spectrum, the values for Bi_2Se_3 incorporate the anisotropy induced by the crystallographic quintuple layers. Moreover, the spectrum has two degenerate Dirac cones, one for each surface of the slab geometry. The degeneracy could be easily lifted by applying an electric field along the z-direction, such that the Dirac cones experience different gating potentials.

2.1.2. 3D TI nanowires

By cutting a macroscopic TI sample into a wire geometry, where the circumference becomes smaller than the phase-coherence length of the surface states, it is possible to form TI nanowires with a quantized single Dirac cone on their surface. This procedure is typically done by chemical etching [24, 25] or by growing wires from a seed or core material [59]. In the case of HgTe, nanowires with a width of hundreds of nanometers can be constructed due to a phase-coherence length of a few micrometers. For bismuth-based systems the diameter of nanowires is typically limited to much smaller values, as these systems contain usually many defects and impurities [60, 61].
For the description of such nanowires we use two models. The first option is to employ Eq. (2.1) simply choosing fixed width and height dimensions. This will then lead to quantization of the surface spectrum, where only a single Dirac cone is left. The second possibility is to resort to an effective 2D surface state model, which neglects the presence of the bulk bands and only incorporates the topological surface spectrum. This model will become very important in the simulation of TI nanowire Josephson junctions, where the full 3D model is computationally too expensive.

The surface states [23, 24, 62, 63] can then be described with an effective 2D Dirac Hamiltonian

$$H = \hbar v_{\mathrm{F}} \left[\hat{k}_x \sigma_x + \hat{k}_s \sigma_y \right], \tag{2.5}$$

where σ_i denotes the Pauli spin matrices. The surface is parametrized by cylindrical coordinates, with x being the longitudinal coordinate in the wire direction and s the azimuthal coordinate around the circumference in the interval $[0; 2\pi R]$, with R being the radius of the nanowire. Therefore, $\hat{k}_x$ is the momentum along the nanowire axis, while $\hat{k}_s$ is the momentum around the wire circumference. Due to the topological nature of the surface states, where spin is coupled to momentum, one has to take into account a very subtle, but important, point. If a surface state electron travels once around the wire perimeter, the spin of the electron experiences a rotation by 2π. Therefore, the electron will pick up a Berry phase of π [23], which renders the boundary condition of the wave functions to antiperiodic, i.e.,

$$\Psi(s) = \exp(-\mathrm{i}\pi)\Psi(s + C) = -\Psi(s + C), \tag{2.6}$$

where $C = 2\pi R$ denotes the circumference of the wire. Moreover, and as already mentioned above, the angular momentum $\hat{k}_s$ can only assume quantized values $k_s = 2\pi l/C$. The eigenfunctions of the effective Dirac Hamiltonian Eq. (2.5) can then be written as [64, 65]

$$\begin{aligned} \Psi(x, s) &= \exp(\mathrm{i}k_x x) \exp(\mathrm{i}k_s s) \chi_{k_x,l} \\ &= \exp(\mathrm{i}k_x x) \exp\left(\mathrm{i}\frac{2\pi}{C} l \frac{C}{2\pi} \varphi \right) \chi_{k_x,l} \\ &= \exp(\mathrm{i}k_x x) \exp(\mathrm{i}l\varphi) \chi_{k_x,l}, \end{aligned} \tag{2.7}$$

where the antiperiodic boundary condition enters the angular momentum quantum number by a factor 1/2, such that $l = n - 1/2$ with $n \in \mathbb{Z}$. The variable φ denotes the azimuthal angle on the wire perimeter and $\chi_{k_x,l}$ is a two component spinor. The corresponding energy spectrum reads [64, 65]

$$E(k_x, l) = \pm\hbar v_{\mathrm{F}} \sqrt{k_x^2 + \left(\frac{2\pi}{C} \right)^2 \left(n - \frac{1}{2} \right)^2}. \tag{2.8}$$

Figure 2.2 (a) shows the surface spectrum of a TI nanowire given by Eq. (2.8). Note here the gap at $k_x = 0$, which is induced due to the Berry phase of π. The presence of this gap is problematic in some sense, as many interesting physical properties of TIs, like the feature of a perfectly conducting mode [23] or a 4π-periodic current-phase relation in Josephson junctions [66], require a spectrum with linear dispersion. In order to close the gap and to obtain linear bands, it is possible to exploit the well-known Aharonov-Bohm effect [67]. By applying a magnetic field parallel to the nanowire axis, the surface states will pick up an additional Aharonov-Bohm phase [23, 62], because

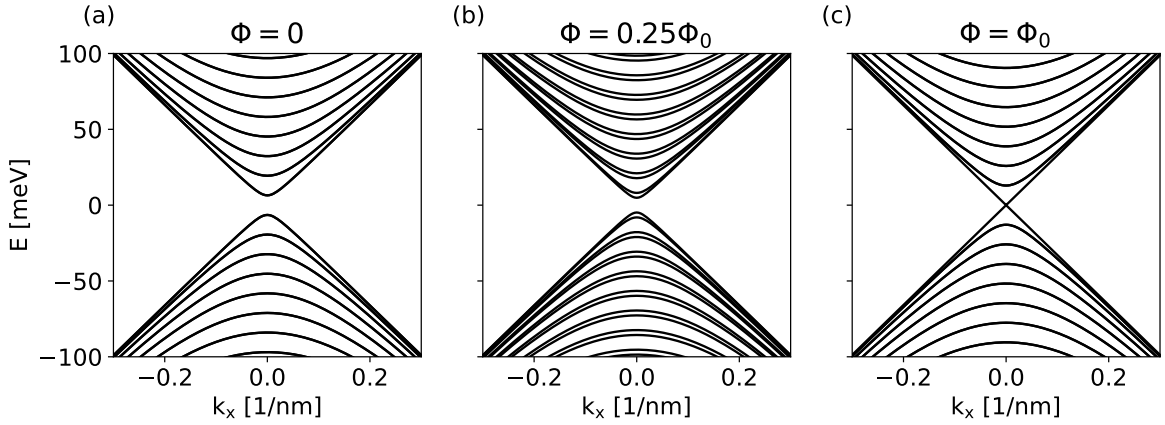

Figure 2.2: Bandstructure of topological insulator nanowire surface states given by Eq. (2.11) for different values of the applied axial magnetic flux.

of their confinement to the wire surface. This magnetic field can be incorporated into the Hamiltonian as

$$H = \hbar v_{\mathrm{F}} \left[\hat{k}_x \sigma_x + \left(\hat{k}_s - \frac{e}{\hbar} A_\varphi \right) \sigma_y \right], \tag{2.9}$$

with $A_\varphi = \Phi / C$ being the corresponding vector potential and Φ the flux through the wire cross-section. The Hamiltonian can be further rewritten in terms of the respective derivative operators as

$$H = -\mathrm{i}\hbar v_{\mathrm{F}} \left[\partial_x \sigma_x + \left(\frac{2\pi}{C} \right) \left(\partial_\varphi + \mathrm{i} \frac{\Phi}{2\Phi_0} \right) \sigma_y \right], \tag{2.10}$$

where $\Phi_0 = e/2h$ is the superconducting flux quantum. The corresponding eigenspectrum reads

$$E(k_x, l, \Phi) = \pm \hbar v_{\mathrm{F}} \sqrt{k_x^2 + \left(\frac{2\pi}{C} \right)^2 \left(n - \frac{1}{2} + \frac{\Phi}{2\Phi_0} \right)^2}. \tag{2.11}$$

From this expression it is clear that whenever the flux Φ is equal to an integer multiple of Φ_0, there exists a zero energy state where no gap is present and a linear spectrum is obtained. In Fig. 2.2 (c) the bandstructure for $\Phi = \Phi_0$ is plotted. Increasing the magnitude of the magnetic field lifts the degeneracy of the twofold degenerate subbands, while the size of the Berry gap is slowly decreasing; see Fig. 2.2 (b) for an example value of $\Phi = 0.25\Phi_0$. At $\Phi = \Phi_0$ the gap is completely closed, before it starts to open up again for larger field strengths until it regains its maximum value at $\Phi = 2\Phi_0$. From an earlier theoretical work [23] it is expected that the conductance will oscillate with a period of $\Phi = 2\Phi_0$, as the perfectly conducting mode in a linear spectrum has perfect spin polarization and no backscattering is allowed. For a gapped surface spectrum, this spin polarization is weakened and backscattering increases. This periodic modulation of the energy spectrum has been probed experimentally [24], where the conductance was measured with respect to the applied axial magnetic field. In Figs. (2.3a) and (2.3b) the spectra for $\Phi = 0$ and $\Phi = \Phi_0$, respectively, are colored according to the

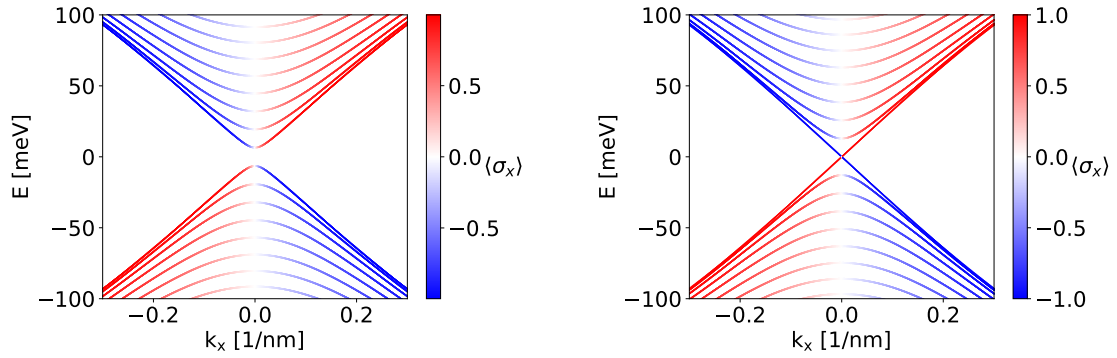

(a) $\Phi = 0$ (b) $\Phi = \Phi_0$

Figure 2.3: Bandstructure of the effective 2D TI surface model. The bands are colored according to their σ_x spin expectation value along the nanowire axis. For $\Phi = \Phi_0$ perfect spin polarization is present in the linear bands.

spin expectation value along the nanowire axis direction. For the latter case a perfect spin polarization can be observed in the linear branches, while it is certainly weakened without applied flux. It should be highlighted that the spin of the effective 2D model is only a so-called pseudo-spin and not the physical one. The Hamiltonian is only used to model the low-energy spectrum of the topological material. In the full 3D BHZ model, given by Eq. (2.1), the real spin of surface states is aligned along the azimuthal direction, but the properties with respect to transport signatures are still equivalent.

2.2. Single-layer and bilayer graphene

2.2.1. Single-layer graphene

The discovery of graphene by Geim et al. [14] in 2004 started intensive research on 2D materials and also led to advances regarding topological insulators [5, 6]. Graphene is a purely 2D hexagonal layer of carbon atoms, exhibiting novel physical properties like high carrier mobilities [15] and spin diffusion lengths reaching several microns [68–70], what makes it a perfect candidate for spintronic applications [71–73].
In Fig. 2.4 the graphene lattice is visualized schematically. It consists of two sublattices A and B, where each of them is a triagonal lattice structure [74]. The distance between two carbon atoms in one sublattice, i.e., the lattice constant inside a sublattice, is given by $a = 0.246$ nm. The basis vectors of the graphene lattice read

$$\boldsymbol{a_1} = (a, 0) \quad \text{and} \quad \boldsymbol{a_2} = \left(\frac{a}{2}, \frac{\sqrt{3}a}{2}\right), \tag{2.12}$$

while the basis atoms are located at

$$(0, 0) \quad \text{and} \quad (0, a_{cc}). \tag{2.13}$$

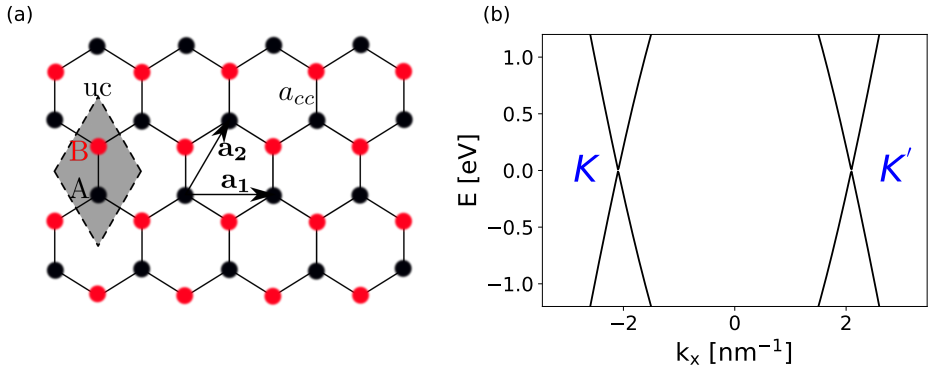

Figure 2.4: (a) Schematic plot of the graphene lattice structure. The sublattice A (B) is shown in black (red), while the unit cell is shown as the grey shaded region. (b) Bandstructure of graphene in the low-energy regime. The linear bands are visible at the K and $K^{'}$ points.

The carbon-carbon bond length is $a_{cc} = a/\sqrt{3} = 0.142$ nm. The real space tight-binding Hamiltonian describing the graphene structure is given by [74]

$$H_{\mathrm{G}} = -\sum_{m,n,\sigma} (t\delta_{\langle mn\rangle} + \mu\delta_{mn}) c^{\dagger}_{m\sigma} c_{n\sigma} + h.c., \tag{2.14}$$

where $t = 2.6$ eV describes the nearest-neighbor hopping between two carbon atoms, symbolized by $\delta_{\langle mn\rangle}$, and μ denotes the chemical potential. Furthermore, $c^{\dagger}_{m\sigma}$ and $c_{m\sigma}$ correspond to standard creation and annihilation operators acting on electrons at site m with spin $\sigma \in [\uparrow, \downarrow]$, respectively.

2.2.2. Bilayer graphene

Bilayer graphene consists of two single-layer graphene sheets that are stacked on top of each other. Due to the hexagonal lattice structure in a graphene layer, bilayer graphene offers two stacking orders, where the first one is the so-called AA stacking order. Here every carbon atom in the top layer sits exactly on top of a carbon atom in the bottom layer. The second configuration is the AB (Bernal) stacking order, which is shown in Fig. 2.5 (a). Here the carbon atoms in the top layer are shifted with respect to the bottom layer such that an atom of the A_2 sublattice sits on top of a B_1 atom. Moreover the B_2 carbon atoms are located over the center of the hexagonal carbon cells in the bottom layer. The AB stacking configuration will be further studied in later chapters of this thesis. In order to describe this bilayer material, one can employ the tight-binding Hamiltonian in the conventional McClure-Slonczewski-Weiss parameterization [75–78],

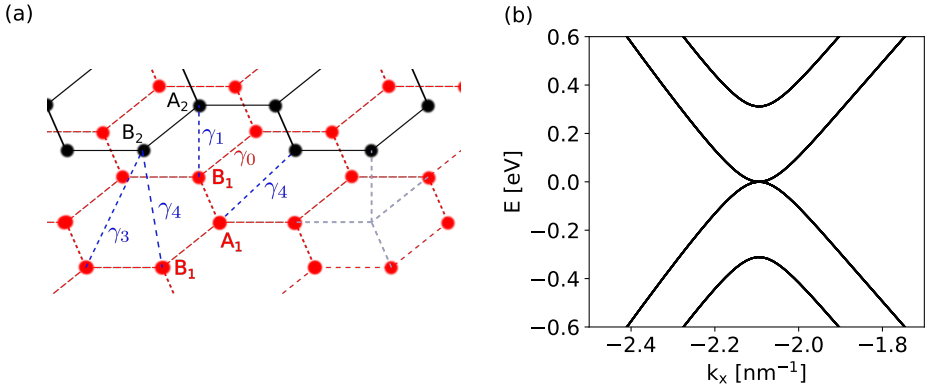

Figure 2.5: (a) Schematic plot of the bilayer graphene lattice structure in the Bernal stacking configuration. For better visibility the top (bottom) carbon layer is shown in black (red). (b) Bandstructure of AB stacked bilayer graphene at the K point. Adapted from Ref. [3].

which is given by

$$\begin{aligned} H_{\mathrm{BLG}} = &- \sum_{m,n,j,\sigma} (\gamma_0 \delta_{\langle mn \rangle} + \mu \delta_{mn}) c^{\dagger}_{j,m,\sigma} c_{j,n,\sigma} \\ &+ \gamma_1 \sum_{m,\sigma} (c^{\dagger}_{B_1,m,\sigma} c_{A_2,m,\sigma} + \mathrm{h.c.}) \\ &+ \gamma_3 \sum_{m,\sigma} (c^{\dagger}_{A_1,m,\sigma} c_{B_2,m,\sigma} + \mathrm{h.c.}) \\ &+ \gamma_4 \sum_{m,\sigma} (c^{\dagger}_{A_1,m,\sigma} c_{A_2,m,\sigma} + c^{\dagger}_{B_1,m,\sigma} c_{B_2,m,\sigma} + \mathrm{h.c.}), \end{aligned} \tag{2.15}$$

where $c^{\dagger}_{j,m,\sigma}(c_{j,n,\sigma})$ creates (destroys) an electron in sublattice $j \in [A_1, B_1, A_2, B_2]$ at site m with spin $\sigma \in [\uparrow, \downarrow]$. Parameters in Eq. (2.15) are fixed as follows. The intralayer nearest-neighbor hopping between two carbon sites is given by $\gamma_0 = 2.6\,\mathrm{eV}$. Top and bottom carbon layers are separated by a distance $c = 0.335\,\mathrm{nm}$, where B_1 and A_2 carbon sites are coupled by a $\gamma_1 = 0.34\,\mathrm{eV}$ interlayer hopping [77]. Furthermore we consider the additional interlayer hoppings $\gamma_3 = 0.28\,\mathrm{eV}$ (connecting A_1 and B_2 carbon sites) and $\gamma_4 = -0.14\,\mathrm{eV}$ (connecting B_1 and B_2, as well as A_1 and A_2 carbon sites). Finally, μ denotes again the chemical potential of the system. In Fig. 2.5 (b) the corresponding bandstructure is shown at the K point in the low energy regime. Linear bands of the single graphene layers are no longer observable, but instead a smooth touching point of conduction and valence band is present at zero energy. Furthermore, bilayer graphene offers the great feature to tune the size of the band gap via an external electric field [79–81], making it also a highly suitable for semiconductor devices.

2.2.3. Impurity models for graphene systems

The interesting physical properties of graphene are predicted for clean and pristine lattice structures. Obviously, real samples in experiments will never have such a perfect crystal structure. There will always be vacancies, defects, lattice deformations, and also impurity atoms present. Hydrogen atoms, for example, can be intentionally deposited onto graphene in order to modify its physical properties in the process of hydrogenation [82, 83]. Such impurities strongly affect the measurable physical quantities like spin relaxation [84, 85], local strength of the spin-orbit coupling [86–90], or electrical transport properties [91]. In the following chapters of this thesis the influence of impurities with magnetic exchange interaction, as well as spin-orbit active adatoms, will be studied in detail. Therefore well-established models for impurities on single-layer and bilayer graphene will be reviewed in this section.

The focus will rest on adatoms that are chemisorbed on top of a carbon atom, i.e., hydrogen or fluorine. Such impurities have been extensively studied [86, 87, 90], introducing the effective impurity potential

$$V_{\mathrm{imp}} = V^{(0)} + V_{\mathrm{s}}^{(1)} + V_{\mathrm{s}}^{(2)}. \tag{2.16}$$

The first term describes the onsite (ϵ) and hopping (ω) terms that connect the impurity with the carbon site at which it is localized. It can be written in real-space tight-binding form as

$$V^{(0)} = \sum_{\sigma} [(\varepsilon - \mu) d_\sigma^\dagger d_\sigma + \omega d_\sigma^\dagger c_{0\sigma}], \tag{2.17}$$

where the creation and annihilation operators $c_{i\sigma}^\dagger$ and $c_{i\sigma}$ act on the carbon sites, while $d_\sigma^\dagger$ and d_σ only act on the impurity site. The second term reads

$$\begin{aligned} V_{\mathrm{s}}^{(1)} &= -J\, \mathbf{s}\cdot\mathbf{S} = -J(\sigma_x \otimes \Sigma_x + \sigma_y \otimes \Sigma_y + \sigma_z \otimes \Sigma_z) \\ &= -J \begin{pmatrix} 1 & 0 & 0 & 0 \\ 0 & -1 & 2 & 0 \\ 0 & 2 & -1 & 0 \\ 0 & 0 & 0 & 1 \end{pmatrix}. \end{aligned} \tag{2.18}$$

Note that this term encodes the exchange interaction between the itinerant electron spin $\mathbf{s}$ and the impurity 1/2-spin $\mathbf{S}$ [85]. The orbitals in the electronic wave function are thereby extended and are given by

$$\Psi^{(1)} = (\Psi_{\uparrow\Uparrow}, \Psi_{\uparrow\Downarrow}, \Psi_{\downarrow\Uparrow}, \Psi_{\downarrow\Downarrow})^\top. \tag{2.19}$$

Note that the index $\sigma \in [\uparrow, \downarrow]$ corresponds to the itinerant electron spin, while the index $\Sigma \in [\Uparrow, \Downarrow]$ denotes the impurity spin. The full orbital representation will be important later on when we study the supercurrent flow in bilayer graphene Josephson junctions with an impurity in the system. For the purpose of computing the spin-relaxation rates in the presence of magnetic impurities, a simpler Hamiltonian with a reduced

number of orbitals can be employed. By looking at Eq. (2.18) it becomes clear that the only spin components that are coupled by $V^{(1)}$ are given by $\Psi^{(1)} = (\Psi_{\uparrow\Downarrow}, \Psi_{\downarrow\Uparrow})^T$. The reduced effective interaction Hamiltonian is then determined to be [2]

$$\tilde{V}_{\mathrm{s}}^{(1)} = -J \begin{pmatrix} -1 & 2 \\ 2 & -1 \end{pmatrix}, \tag{2.20}$$

or in real space tight-binding notation (neglecting the orbitals introduced by the impurity spin)

$$\tilde{V}_{\mathrm{s}}^{(1)} = J\big(d_\uparrow^\dagger\, d_\uparrow + d_\downarrow^\dagger\, d_\downarrow\big) - 2J\big(d_\uparrow^\dagger\, d_\downarrow + d_\downarrow^\dagger\, d_\uparrow\big). \tag{2.21}$$

The last term of Eq. (2.16) is only present for impurities that induce local spin-orbit coupling effects in the close vicinity of the adatom. It explicitly reads

$$\begin{aligned} V_{\mathrm{s}}^{(2)} = & \frac{\mathrm{i}\Lambda_{\mathrm{I}}^{\mathrm{A}}}{3\sqrt{3}} \sum_{m\in \mathrm{C_{nnn}}} \sum_{\sigma} c_{0\sigma}^\dagger \left(\hat{s}_z\right)_{\sigma\sigma} c_{m\sigma} + \mathrm{h.c.} \\ & + \frac{\mathrm{i}\Lambda_{\mathrm{I}}^{\mathrm{B}}}{3\sqrt{3}} \sum_{\substack{m,n\in \mathrm{C_{nn}} \\ m\neq n}} \sum_{\sigma} c_{m\sigma}^\dagger\, \nu_{mn} \left(\hat{s}_z\right)_{\sigma\sigma} c_{n\sigma} \\ & + \frac{2\mathrm{i}\Lambda_{\mathrm{R}}}{3} \sum_{m\in \mathrm{C_{nn}}} \sum_{\sigma\neq\sigma'} c_{0\sigma}^\dagger \left(\hat{\boldsymbol{s}} \times \boldsymbol{d}_{0m}\right)_{z,\sigma\sigma'} c_{m\sigma'} + \mathrm{h.c.} \\ & + \frac{2\mathrm{i}\Lambda_{\mathrm{PIA}}^{\mathrm{A}}}{3} \sum_{m\in \mathrm{C_{nnn}}} \sum_{\sigma\neq\sigma'} c_{0\sigma}^\dagger \left(\boldsymbol{d}_{0m} \times \hat{\boldsymbol{s}}\right)_{z,\sigma\sigma'} c_{m\sigma'} + \mathrm{h.c.} \\ & + \frac{2\mathrm{i}\Lambda_{\mathrm{PIA}}^{\mathrm{B}}}{3} \sum_{\substack{m,n\in \mathrm{C_{nn}} \\ m\neq n}} \sum_{\sigma\neq\sigma'} c_{m\sigma}^\dagger \left(\boldsymbol{d}_{mn} \times \hat{\boldsymbol{s}}\right)_{z,\sigma\sigma'} c_{n\sigma'}\,, \end{aligned} \tag{2.22}$$

where $\hat{\boldsymbol{s}}$ is the vector of the Pauli matrices. The parameter ν_{mn} is -1 $(+1)$ if the spin hopping via a carbon atom from lattice site n to m (n $\rightarrow$ C $\rightarrow$ m) is oriented (counter)clockwise. Moreover the unit vector connecting sites n an m is given by

$$\boldsymbol{d}_{mn} = \frac{\boldsymbol{R}_m - \boldsymbol{R}_n}{|\boldsymbol{R}_m - \boldsymbol{R}_n|}. \tag{2.23}$$

Strengths of the different spin-orbit coupling types are given by the Λ factors. Figure 2.6 illustrates a schematic plot of all spin-orbit coupling terms entering Eq. (2.22). The first two terms are *intrinsic* (I) spin-orbit coupling terms acting between next-nearest neighbors in the respective sublattices A and B [86]. In the third term *Bychkov-Rashba* (R) spin-orbit coupling between spins of nearest-neighbor carbon atoms is included. *Pseudospin inversion asymmetry* (PIA) (breaking of the sublattice symmetry due to the impurity on top of a carbon atom) is responsible for the emergence of the last two terms.

In this thesis the effect of hydrogen (H) and fluorine (F) adatoms will be studied in more detail. The parameters of V_{imp} [Eq. (2.16)] for those adatoms are shown in

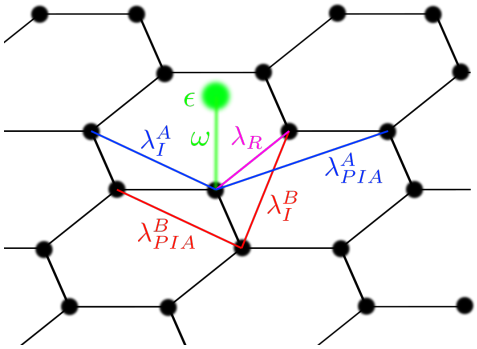

Figure 2.6: Schematic illustration of the locally induced spin-orbit coupling terms of $V_{\mathrm{s}}^{(2)}$ in Eq. (2.22). The impurity is shown in green and sits on top of a carbon site. Spin-orbit coupling hoppings corresponding to different sublattices are shown in different colors.

Tab. 2.2 [85–87]. There we differentiate between parameters for single-layer graphene (SLG) and bilayer graphene (BLG). For the latter two distinct impurity positions in the top layer can be identified for the AB stacking configuration. Those are denoted as dimer and non-dimer positions, where the first corresponds to an impurity sitting on top of an A_2 carbon atom, while the second labels an adatom on top of a B_2 atom.

	[eV]			[meV]				
impurity/layers/position	ϵ	ω	J	Λ_I^A	Λ_I^B	Λ_R	Λ_{PIA}^A	Λ_{PIA}^B
F on SLG	-2.2	5.5	0.5	0	3.3	11.2	0	-7.3
H on SLG	0.16	7.5	-0.4	−0.21	0	0.33	0	0.77
H on BLG (dimer)	0.25	6.5	-0.4	−0.21	0	0.33	0	0.77
H on BLG (non-dimer)	0.35	5.5	-0.4	−0.21	0	0.33	0	0.77

Table 2.2: Parameters for V_{imp} [see Eq. (2.16)], taken from Refs. [85–87].

2.3. Mesoscopic transport – Landauer-Büttiker formalism

In the following chapters of this dissertation we are interested in the quantum transport properties of nanostructures. More specifically, the considered systems will be studied in the mesoscopic regime, where the system dimension is assumed to be smaller than the coherence length l_ϕ. In this regime quantum interference plays an important role due to the fact that motion of particles occurs phase coherently. One of the central physical observables is the electrical conductance. Contrary to the macroscopic regime, where

Ohm's law is applicable, the conductance in the mesoscopic transport regime depends on the number of quantized modes. In order to treat such systems, Landauer [92, 93] suggested that the conductance of nano devices can be related to scattering features of nanostructures. There, the system is assumed to consist of a scattering region, which is contacted by a certain number of reservoirs, called leads. The leads serve as waveguides for incoming and outgoing modes, which are coupled by the scattering region. Thereby, the wave functions are related to each other by the scattering matrix S, which contains the transmission and reflection amplitudes. In principle, the conductance is then given by the transmission probabilities of each quantized mode in the system. For example, the conductance of a two-terminal system at finite temperature can be calculated by

$$G = \frac{e^2}{h} \int dE \left(-\frac{\partial f(E)}{\partial E} \right) T(E), \tag{2.24}$$

with $f(E)$ being the Fermi distribution function. The transmission is given by [94]

$$T(E) = \sum_{\alpha,\beta} T_{\beta\alpha}(E), \tag{2.25}$$

where α denotes the modes in lead 1 and β the modes in lead 2. If the leads contain spin-degenerate modes one adds a factor of 2 into Eq. (2.24). The transmission $T(E)$ is computed in the Python package Kwant [34] by employing the so-called wave function approach. Via computationally efficient algorithms the scattering states, as well as the scattering matrix S, of complicated and high dimensional problems can be calculated. The quantity S contains information about reflection and transmission amplitudes of the scattering problem and one can then extract $T(E)$ from it. An equivalent approach to get access to $T(E)$ would be the non-equilibrium Green's function formalism [95, 96]. Note that this method is employed in Sec. 3.4 to calculate the transmission for a specific problem analytically and to compare it with the numerical Kwant solution. At zero temperature Eq. (2.24) simplifies to the summation over the single transmission probabilities and for a clean system [$T_{\beta\alpha}(E) = 1$ for all α and β] this quantity simply corresponds to the number of open channels N, such that the conductance is given by

$$G = \frac{e^2}{h} N. \tag{2.26}$$

Therefore it is quantized to multiples of the conductance quantum e^2/h and changes step like by changing the Fermi energy, which opens or closes conducting channels.

2.4. Superconductivity

Since the discovery of the superconducting state by Onnes in 1911 [97], in which the electrical resistance of a material vanishes below a certain transition temperature, the scientific interest and progress in the related field has considerably increased. From a theoretical point of view, the Bardeen-Cooper-Schrieffer (BCS) theory [98] of elemental

superconductors has paved the way for a detailed microscopic understanding of different intriguing physical effects. The BCS theory allows to explain the vanishing resistance by considering the minimization of the free energy due to electron-phonon coupling.
In this thesis we want to examine the influence of superconductivity on the properties of topological insulators and graphene systems. Therefore, in the following we first introduce the basic theoretical modeling of such hybrid systems and then introduce the reader to all of the relevant related phenomena, which will be studied in the proceeding chapters.

2.4.1. Bogoliubov-de Gennes Hamiltonian

A well-established method of treating superconductivity in s-wave superconductors is by employing the Bogoliubov-de Gennes (BdG) equation [99]. It is a wave function equation and its form resembles that of the Schrödinger equation, but one now has to consider electron and hole orbitals at the same time. The equation is an analogue to the mean-field expression [7] employing field operators, which is derived from a model of superconductivity that takes the phonon mediated attractive interaction into account [100]. Note that this mean-field approach is not particle conserving and in certain cases, for example to study non-equilibrium transport situations [101], more advanced techniques have to be employed. However, for the systems considered in this thesis, the BdG approach is completely sufficient.
Therein, the electron and hole components of the wave functions are coupled by the superconducting pair potential $\hat{\Delta}(\boldsymbol{r}) = \Delta(\boldsymbol{r})\mathrm{i}\sigma_y$, where the equation reads

$$H_{\mathrm{BdG}}\Psi = E\Psi \tag{2.27}$$

$$\begin{pmatrix} H_{\mathrm{e}} & \hat{\Delta}(\boldsymbol{r}) \\ -\hat{\Delta}(\boldsymbol{r})^{\dagger} & H_{\mathrm{h}} \end{pmatrix} \Psi = E\Psi \tag{2.28}$$

$$\begin{pmatrix} H_{e} & \hat{\Delta}(\boldsymbol{r}) \\ -\hat{\Delta}(\boldsymbol{r})^{\dagger} & -H_{\mathrm{e}}^{\dagger} \end{pmatrix} \Psi = E\Psi. \tag{2.29}$$

Assume that the electron Hamiltonian H_{e} is given by a simple 2x2 matrix, representing spin up and down components. Then the wave functions of the superconducting quasiparticles are given by a four-component spinor in the so-called Nambu basis

$$\Psi = \begin{pmatrix} \psi_{\uparrow}^{\mathrm{e}} \\ \psi_{\downarrow}^{\mathrm{e}} \\ \psi_{\uparrow}^{\mathrm{h}} \\ \psi_{\downarrow}^{\mathrm{h}} \end{pmatrix}, \tag{2.30}$$

with spin-resolved electron and hole-components $\psi_{\uparrow}^{\mathrm{e}}, \psi_{\downarrow}^{\mathrm{e}}, \psi_{\uparrow}^{\mathrm{h}}$, and $\psi_{\downarrow}^{\mathrm{h}}$, respectively. In the case of the 3D BHZ Hamiltonian [Eq. (2.1)] the BdG Hamiltonian will be an 8x8 matrix, with accordingly eight-component spinors as eigenfunctions. Note that there is another useful and frequently used Nambu basis, which can be obtained by performing

a unitary transformation [7] of Eq. (2.29) with

$$U = \begin{pmatrix} \sigma_0 & 0 \\ 0 & \mathrm{i}\sigma_y \end{pmatrix}. \tag{2.31}$$

In the new Nambu basis

$$\tilde{\Psi} = \begin{pmatrix} \psi^{\mathrm{e}}_{\uparrow} \\ \psi^{\mathrm{e}}_{\downarrow} \\ \psi^{\mathrm{h}}_{\downarrow} \\ -\psi^{\mathrm{h}}_{\uparrow} \end{pmatrix}, \tag{2.32}$$

the transformed BdG equation reads

$$\begin{pmatrix} H_{\mathrm{e}} & \Delta(\boldsymbol{r})\sigma_0 \\ \Delta(\boldsymbol{r})^{\dagger}\sigma_0 & -\mathbb{T}H_{\mathrm{e}}^{\dagger}\mathbb{T}^{-1} \end{pmatrix} \Psi = E\Psi, \tag{2.33}$$

where $\mathbb{T} = \mathrm{i}\sigma_y\mathbb{C}$ is the time-reversal operator.

2.4.2. Superconducting proximity effect

Bringing an s-wave superconductor in close proximity to another normal-conducting material can induce an effective superconducting pair potential $\hat{\Delta}$ in the latter, even though this part is itself actually not superconducting. This is the superconducting proximity effect [102–104]. Theoretically such systems are also modeled by the BdG Hamiltonian of Eq. (2.29), where the effectively induced gap is put as the pairing potential. For our purposes we are interested in graphene and topological insulators like HgTe or Bi_2Se_3, which are proximitized by an s-wave superconductor like niobium. This superconductor has many experimental advantages, for example, a high critical field value for thin films and in-plane magnetic fields, as well as the possibility to achieve good interface qualities. Throughout this thesis we assume that hybrid systems are constructed using this material which has a superconducting gap of $\Delta_{\mathrm{Nb}} \approx 1$ meV [105]. Out of simplicity we assume proximity-induced gaps, which are smaller or equal than the gap of the s-wave superconductor. For a more sophisticated approach to study the emergent superconducting state in such hybrid systems one would need to perform self-consistent calculations of the induced gap, which is beyond the scope of this work.

2.4.3. (Crossed) Andreev reflection

The superconducting proximity effect can be viewed as a direct consequence of another phenomenon emerging at N/S-interfaces [102–104]. In the normal-conducting part of the system electrons with an energy inside the superconducting gap can propagate through the system. When such electrons approach the interface with the superconducting part of the system, no states are available on the S side because of the pairing potential Δ that gaps out the spectrum. Therefore, the only scattering possibilities are to be either back reflected as an electron or to be reflected into a hole state; the latter process is known as Andreev reflection [106–108]. In order for that to take place,

a Cooper pair has to be formed by the incoming electron along with a second electron of the N part such that an outgoing hole state is left behind. Figure 2.8 (a) schematically visualizes this effect. The same mechanism can also occur for free hole carriers in the normal region, which are then Andreev reflected into back-moving electrons while Cooper pairs in the S are destroyed. Due to this process, superconducting pairing correlations are carried into the normal part of the system, inducing the superconducting proximity effect [104].

Scattering at such a N/S-interface can be described by the Blonder-Tinkham-Klapwijk (BTK) [109] model, where the following derivation of the Andreev reflection amplitude mainly follows the lecture notes of F. Dolcini in Ref. [110]. The superconducting pairing is assumed to be a simple step-like function $\Delta(x) = \theta(x)\Delta_0 \exp(\mathrm{i}\varphi)$, where Δ_0 is the pairing amplitude and φ the phase of the macroscopic superconducting wave function. Then, by employing the BdG notation one can write for the single-electron Hamiltonian $H = -\frac{\hbar^2}{2m}(\hat{k}_x^2 + \hat{k}_y^2) + (-\mu + U(x,y))$ the equation

$$\begin{pmatrix} H & \theta(x)\Delta_0 \exp(\mathrm{i}\varphi) \\ \theta(x)\Delta_0 \exp(-\mathrm{i}\varphi) & -H \end{pmatrix} \begin{pmatrix} u(x,y) \\ v(x,y) \end{pmatrix} = E \begin{pmatrix} u(x,y) \\ v(x,y) \end{pmatrix}, \tag{2.34}$$

where $U(x,y) = U_0\delta(x)$ models an interface barrier, and $u(x,y)$ and $v(x,y)$ are denoted as the quasiparticle coherence factors. Note that for simplicity we assume a simple spinless electron system with a parabolic dispersion. The junction is pointing along the x-direction, such that the full energy E will be a sum of longitudinal E_x and transverse E_y energies. Therefore, we can define an effective chemical potential $\mu' = \mu - E_y$. Eventually one wants to find the scattering amplitude for the electron to hole conversion process, which can be done by the standard mode matching technique. In the N region the eigenfunctions correspond to four decoupled solutions, which are right- and left-moving electron and hole states, respectively. These are given by

$$\psi_{\pm}^{\mathrm{e}} = \begin{pmatrix} 1 \\ 0 \end{pmatrix} \exp(\pm \mathrm{i} k_x^{\mathrm{e}} x) \exp(\mathrm{i} k_y y) \tag{2.35}$$

and

$$\psi_{\pm}^{\mathrm{h}} = \begin{pmatrix} 0 \\ 1 \end{pmatrix} \exp\big(\pm \mathrm{i} k_x^{\mathrm{h}} x\big) \exp(\mathrm{i} k_y y), \tag{2.36}$$

with the dispersion relations

$$E(k_x, k_y, \mu) = \pm \frac{\hbar^2}{2m} \left(\left(k_x^{\mathrm{e/h}}\right)^2 + k_y^2 \right) \mp \mu. \tag{2.37}$$

The respective momenta are obtained by inverting these dispersion relations and read

$$k_x^{\mathrm{e}} = \sqrt{\frac{2m}{\hbar^2}(E+\mu) - k_y^2}, \tag{2.38}$$

$$k_x^{\mathrm{h}} = \sqrt{\frac{2m}{\hbar^2}(\mu - E) - k_y^2}. \tag{2.39}$$

In Fig. 2.7 (a) the electron and hole spectra are shown with a color coding that corresponds to their charges, given by $Q_{k/q} = (|u_{k/q}|^2 - |v_{k/q}|^2)(-e)$ [100] and where k and q denote the momenta in the N and S regions, respectively. Also, the eigenstates are marked for the example energy of $E = 0.5$ meV. We set $\hbar^2/(2m) = 1$ meV nm^2.
In the S the pairing potential is no longer zero, such that electron and hole orbitals are coupled. The quasiparticle solutions are

$$\xi_{\pm}^{\mathrm{e}} = \begin{pmatrix} u_0 \exp\left(\mathrm{i}\frac{\varphi}{2}\right) \\ v_0 \exp\left(-\mathrm{i}\frac{\varphi}{2}\right) \end{pmatrix} \exp(\pm \mathrm{i} q_x^{\mathrm{e}} x) \exp(\pm \mathrm{i} q_y y), \tag{2.40}$$

$$\xi_{\pm}^{\mathrm{h}} = \begin{pmatrix} v_0 \exp\left(\mathrm{i}\frac{\varphi}{2}\right) \\ u_0 \exp\left(-\mathrm{i}\frac{\varphi}{2}\right) \end{pmatrix} \exp\left(\pm i q_x^{\mathrm{h}} x\right) \exp(\pm \mathrm{i} q_y y), \tag{2.41}$$

with the corresponding energy dispersion (only positive branch)

$$E(q_x, q_y) = \sqrt{\left(\frac{\hbar^2}{2m}\left(\left(q_x^{\mathrm{e/h}}\right)^2 - q_y^2\right) - \mu\right)^2 + \Delta_0^2}. \tag{2.42}$$

For energies above the gap ($E > \Delta_0$), the quasiparticle momenta are again obtained by inverting these dispersion relations, they finally have the form

$$q_x^{\mathrm{e}} = \sqrt{\frac{2m}{\hbar^2}\left(\sqrt{E^2 - \Delta_0^2} + \mu\right) - q_y^2}, \tag{2.43}$$

$$q_x^{\mathrm{h}} = \sqrt{\frac{2m}{\hbar^2}\left(\mu - \sqrt{E^2 - \Delta_0^2}\right) - q_y^2}. \tag{2.44}$$

Moreover, the quasiparticle coherence factors are given by

$$u_0 = \sqrt{\frac{\Delta_0}{2E}} \exp\left(\ \frac{1}{2} \operatorname{arccosh}\left(\frac{E}{\Delta_0}\right)\right), \tag{2.45}$$

$$v_0 = \sqrt{\frac{\Delta_0}{2E}} \exp\left(-\frac{1}{2} \operatorname{arccosh}\left(\frac{E}{\Delta_0}\right)\right). \tag{2.46}$$

In Fig. 2.7 (b) the energy spectrum for positive and negative energies is shown for a gap size of $\Delta = 0.25$ meV.
In case of energies below the superconducting gap ($E < \Delta_0$), it is important to note that the momenta and coherence factors obtain an imaginary component. The expressions are then modified to

$$q_x^{\mathrm{e}} = \sqrt{\frac{2m}{\hbar^2}\left(\mathrm{i}\sqrt{E^2 - \Delta_0^2} + \mu\right) - q_y^2}, \tag{2.47}$$

$$q_x^{\mathrm{h}} = \sqrt{\frac{2m}{\hbar^2}\left(\mu - \mathrm{i}\sqrt{E^2 - \Delta_0^2}\right) - q_y^2}, \tag{2.48}$$

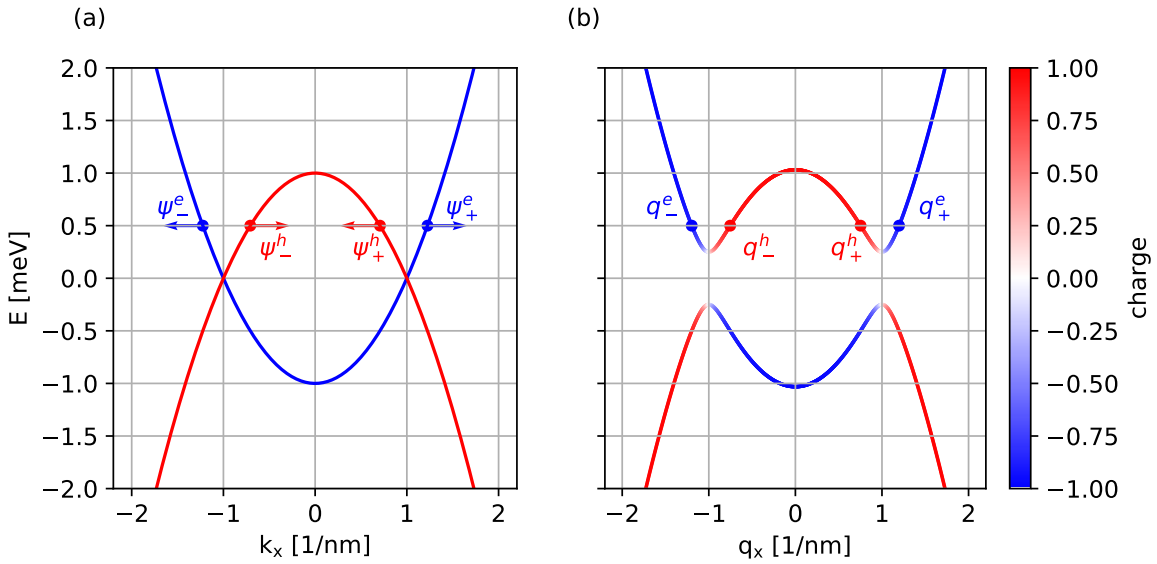

Figure 2.7: (a) Energy spectrum of the BdG Hamiltonian in Eq. (2.34) for $\Delta_0 = 0$ and $\mu = 1$ meV, electron and hole bands are visualized by a color coding of their charge. (b) Energy spectrum in the superconducting state with $\Delta_0 = 0.25$meV.

and

$$u_0 = \sqrt{\frac{\Delta_0}{2E}} \exp\left(\mathrm{i}\frac{1}{2} \arccos\left(\frac{E}{\Delta_0}\right)\right), \tag{2.49}$$

$$v_0 = \sqrt{\frac{\Delta_0}{2E}} \exp\left(-\mathrm{i}\frac{1}{2} \arccos\left(\frac{E}{\Delta_0}\right)\right). \tag{2.50}$$

Assume now that we have an interface between these N and S regions at $x = 0$. By employing the wave function matching procedure at the interface, one can derive the reflection (r_{ji}) and transmission (t_{ji}) amplitudes from state i to state j.
We start the mode matching by defining the incoming state as a pure electron wave function

$$\Psi_{\mathrm{in}} = \frac{1}{\sqrt{2\pi\hbar v_{\mathrm{e}}}} \psi^{\mathrm{e}}_+, \tag{2.51}$$

where the wave function is normalized by the electron velocity $v_{\mathrm{e}} = 1/\hbar|dE/dk_{\mathrm{e}}|$. This is important to assure unitarity [111] of the relevant scattering matrix S. Next, the reflected wave function in N is defined as a superposition of electron and hole components, which are also normalized by their velocities. The wave function is given by

$$\Psi_{\mathrm{refl}} = \frac{r_{\mathrm{ee}}}{\sqrt{2\pi\hbar v_{\mathrm{e}}}} \psi^{\mathrm{e}}_- + \frac{r_{\mathrm{he}}}{\sqrt{2\pi\hbar v_{\mathrm{h}}}} \psi^{\mathrm{h}}_+. \tag{2.52}$$

Finally, the transmitted wave function on the S side consists of a right-moving electron- and hole-like state, i.e.,

$$\Psi_{\mathrm{trans}} = \frac{t_{\mathrm{ee}}}{\sqrt{2\pi\hbar w_{\mathrm{e}}}} \xi^{\mathrm{e}}_+ + \frac{t_{\mathrm{he}}}{\sqrt{2\pi\hbar w_{\mathrm{h}}}} \xi^{\mathrm{h}}_-, \tag{2.53}$$

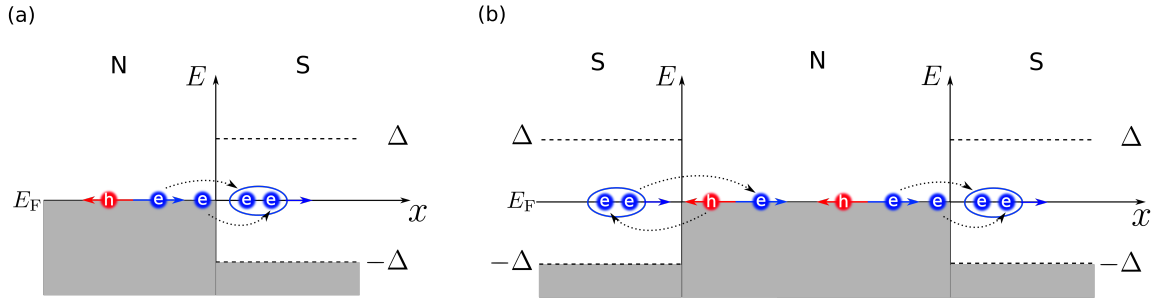

Figure 2.8: Schematic plot of Andreev reflection in (a) and the formation of Andreev bound states in (b).

where the velocities in the superconductor are denoted as $w_{\mathrm{e/h}}$. At the interface $x = 0$ these wave functions, along with their derivatives, need to be matched in order to get linear equations for the entries of the scattering matrix. Thereby, the Andreev approximation [106], where the chemical potential is taken to be much larger than the energy and the superconducting gap, i.e., $\mu \gg E, \Delta_0$, can be applied. It greatly simplifies the analytical computation as all of the relevant momenta can be assumed to be equal, with $k_x^{\mathrm{e/h}} \approxeq q_x^{\mathrm{e/h}}$. For a detailed derivation, the reader is referred to Ref. [110]. Moreover, for the following purposes it is enough to set the interface barrier strength to zero ($U_0 = 0$) and to consider only energies inside the superconducting gap ($E < \Delta_0$), such that the Andreev reflection amplitude is given by

$$r_{\mathrm{he}} = \frac{v_0}{u_0} \exp(-\mathrm{i}\varphi) = \exp\left(-\mathrm{i} \arccos\left(\frac{E}{\Delta_0}\right)\right) \exp(-\mathrm{i}\varphi) \equiv \exp(-\mathrm{i}\chi) \exp(-\mathrm{i}\varphi), \quad (2.54)$$

where the Andreev reflection probability $|r_{\mathrm{he}}|^2$ for $E < \Delta_0$ is equal to 1. The reflection amplitude of an incoming hole state that is scattered into an outgoing electron state reads

$$r_{\mathrm{eh}} = \exp(-\mathrm{i}\chi) \exp(\mathrm{i}\varphi). \quad (2.55)$$

These results play an important role in the analytical treatment of normal and superconducting hybrid systems, and will reappear in some of the proceeding parts of this thesis.

In a two terminal N/S-system the outgoing states can only move into the N lead. By attaching a second normal lead onto the structure to form a N/S/N-system, more scattering events become accessible. Normal back reflection and Andreev reflection are still present, but now also normal transmission from electron (hole) to electron (hole) states between the two N reservoirs is possible. Additionally, electrons (holes) can scatter into holes (electrons) between the spatially separated N leads [39–42]. This process is then called crossed Andreev reflection and has also been measured experimentally [112].

2.4.4. Josephson junctions

Extending a N/S-interface by one further superconductor, or sandwiching a normal-conducting material between two superconductors in order to form a S/N/S system [see Fig. 2.8 (b)], can induce the flow of a supercurrent between the S reservoirs, which does not originate from an applied voltage. Such a setup is called a *Josephson junction*, named after Brian David Josephson who realized in 1962 that the spatial overlap between the order parameters of two superconductors can drive a current due to a gradient in their superconducting phases [113, 114].
Microscopically the current is driven by *Andreev bound states* (ABS) [115, 116]. From the process of Andreev reflection we know that an electron in N can be reflected as a hole at one N/S-interface, by simultaneously injecting a Cooper pair into the S. This hole will phase-coherently retrace the path of the initial electron and eventually hit the second S/N-interface. There the hole is again converted into an electron by Andreev reflection, where a Cooper pair is destroyed in the S. Consecutively performing this process will carry a current from one S reservoir to the other and ABS are formed in the junction. In case of clean interfaces and no scattering inside the junction, the condition to form ABS between left (L) and right (R) superconducting reservoirs is given by the Bohr-Sommerfeld-quantization [117]

$$2\pi n = \oint d\phi = \int_{\mathrm{L}}^{\mathrm{R}} \pm\boldsymbol{k}^{\pm}\cdot\boldsymbol{dl} \pm \frac{e}{\hbar}\int_{\mathrm{L}}^{\mathrm{R}} \boldsymbol{A}\cdot\boldsymbol{dl} + \phi^{R}_{\substack{\mathrm{eh}\\\mathrm{he}}} + \int_{\mathrm{L}}^{\mathrm{R}} \pm\boldsymbol{k}^{\mp}\cdot\boldsymbol{dl} \mp \frac{e}{\hbar}\int_{\mathrm{L}}^{\mathrm{R}} \boldsymbol{A}\cdot\boldsymbol{dl} + \phi^{L}_{\substack{\mathrm{he}\\\mathrm{eh}}}. \quad (2.56)$$

This equation assumes a semiclassical picture, where electrons and holes propagate as point-like particles on straight lines between the two superconductors. The first term denotes the dynamical phase that is accumulated by electrons (upper signs) or holes (lower signs) which propagate from L to R. Additionally, the particles will pick up an Aharonov-Bohm phase if a magnetic field is acting on the system. This phase corresponds to the second term and will play an important role in Sec. 4.6, where we study the influence of an axial magnetic field on the supercurrent in topological insulator nanowire Josephson junctions. When these electrons and holes hit the right superconducting reservoir, they will be Andreev reflected where the phase $\phi^{\mathrm{R}}_{\substack{\mathrm{eh}\\\mathrm{he}}} = -\chi - \varphi_{\mathrm{R}}$ will be accumulated [see Eq. (2.54)]. Finally, the same phases will be acquired when the reflected particles move from R to L, where $\phi^{\mathrm{L}}_{\substack{\mathrm{he}\\\mathrm{eh}}} = -\chi + \varphi_{\mathrm{L}}$. In order to get bound states and to assure uniqueness of the wave functions, all of the accumulated phases have to be equal to an integer multiple of 2π.
By applying again the Andreev approximation and in the absence of an external magnetic field, Eq. (2.56) simplifies to the well-known expression for ABS energies in a clean system, i.e.,

$$E(\Delta\varphi) = \pm\Delta_0 \cos\left(\frac{\Delta\varphi}{2}\right), \quad (2.57)$$

with $\Delta\varphi = \varphi_{\mathrm{L}} - \varphi_{\mathrm{R}}$. The spectrum is plotted in Fig. 2.9 (a). The current, which is carried by the ABS from one superconducting lead to the other, is then given by the derivative of the filled ABS spectrum ($E \leq 0$) with respect to the phase difference

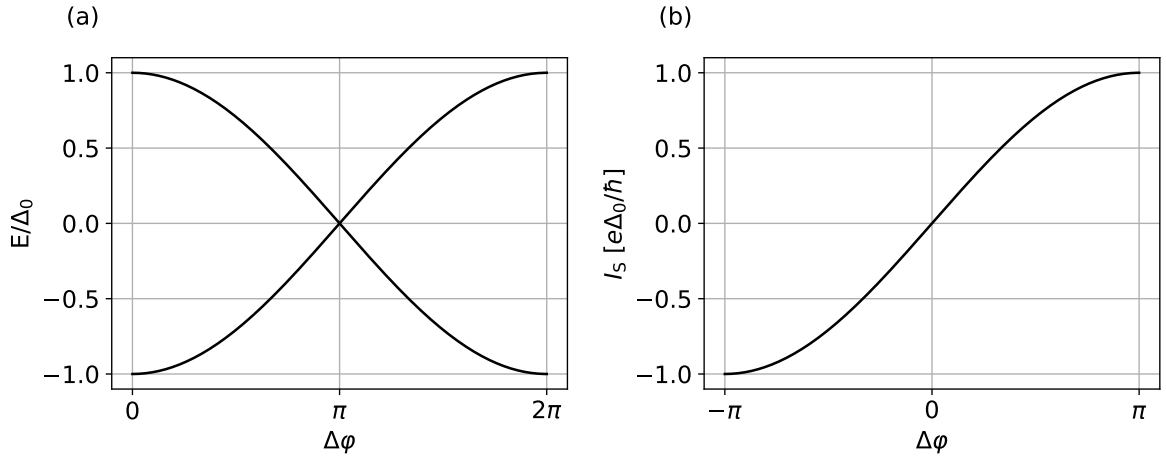

Figure 2.9: (a) Andreev bound state spectrum for a clean S/N/S-junction, see Eq. (2.57). (b) Phase dependence of the corresponding supercurrent in Eq. (2.58) that is mediated by the ABS.

across the junction [115]. For a clean junction, the current simply reads

$$I_{\mathrm{S}}(\Delta\varphi) = \frac{2e}{\hbar}\frac{dE(\Delta\varphi)}{d\Delta\varphi} = \frac{e\Delta_0}{\hbar}\sin\left(\frac{\Delta\varphi}{2}\right). \tag{2.58}$$

The current corresponding to the ABS spectrum of Eq. (2.57) is shown in Fig. 2.9 (b).

2.4.5. Yu-Shiba-Rusinov states

The ABS of the previous section emerge due to free states in a normal material that is sandwiched between two superconducting reservoirs. Another type of bound states appears in superconducting systems if the pairing potential can interact with magnetic exchange interactions. These states are called Yu-Shiba-Rusinov (YSR) bound states, and are named after the three physicists who independently performed pioneering work on this subject [118–123]. Such states can appear if magnetic impurities are adsorbed at superconducting materials. For a simple 2D electron gas with a single impurity site, and taking the spin as a classical quantity, Shiba [119] could derive the energies of the YSR states as

$$E(J) = \pm\Delta_0\frac{1-((J/2)S\pi\rho(E_F))^2}{1+((J/2)S\pi\rho(E_F))^2}, \tag{2.59}$$

where J is the magnetic exchange energy, S is the spin and $\rho(E_{\mathrm{F}})$ the density of states at the Fermi level. The equation shows that the YSR energies lie inside the superconducting gap and crucially depend on the strength of the magnetic exchange interaction. Recently, these states have become a topic of big scientific interest due to the possibility of generating Majorana bound states. By constructing chains of magnetic impurities on the surface of bulk superconductors, it is expected that these systems can host Majorana end states [124–126]. Moreover, in chapter 5 we show that

YSR states can also strongly modify spin-relaxation rates and therefore play also an important role in spintronics.

2.5. Spin-relaxation theory – Elliott-Yafet mechanism

Since the Stern-Gerlach experiment in 1922 [127], which showed the spatial quantization of angular momentum and its correct interpretation by Goudsmit and Uhlenbeck [128] as the signature of the spin of a particle, this quantum-mechanical property has led to the discovery and explanation of a diverse number of physical effects. One of the most famous manifestations of the spin is magnetism [129], where spins are aligned parallel in certain regions of a material. The spin of atomic nuclei can serve as a probe of the structure of organic molecules in nuclear magnetic resonance experiments [130] and it is standardly used in medicine with magnetic resonance imaging. More recently in physics, spin-momentum locking has attracted a lot of scientific attention due to the possibility of constructing topologically non-trivial systems. Also great efforts are being made in order to use spins for storing and processing information in computers with spin qubits [131]. Therefore, from a fundamental point of view, but also in sight of those possible applications, it is important to know how spins behave in macroscopic systems.

An important quantity is given by the spin-relaxation time τ, which tells how long spins can propagate in a material before they scatter and dephase. This means that τ serves as a limit for the transport of information in spintronic devices before it gets lost and therefore, spin relaxation should be weak. Up to now four spin-relaxation mechanisms [132] were proposed, where in this thesis only the *Elliott-Yafet* spin relaxation [43, 44] will be considered. It is a scattering mechanism that is in a sense similar to Fermi's golden rule and describes spin relaxation for scattering of electron spins at single impurities or phonons [132]. These impurities should either induce local spin-orbit coupling or have a magnetic exchange coupling in order to allow for spin scattering. An important feature of the spin-relaxation time τ_n for the Elliott-Yafet mechanism is the direct proportionality to the momentum relaxation time τ_p [133]. Moreover, Yafet [44] showed with first-order perturbation theory that the normal state spin-relaxation rate $1/\tau_n$ is related to the superconducting relaxation rate via

$$1/\tau_s \sim \langle (u_{\mathbf{k}} u_{\mathbf{q}} \pm v_{\mathbf{k}} v_{\mathbf{q}})^2 / \tau_n \rangle, \tag{2.60}$$

where u and v are again the quasiparticle coherence factors of the involved scattering states and $\langle \cdots \rangle$ stands for thermal broadening. Depending on whether local SOC (even w.r.t. time-reversal symmetry) or local magnetic moments (odd w.r.t. time-reversal symmetry) are induced by impurities, the spin-relaxation rate either decreases (minus sign) or increases (plus sign) when lowering the temperature. Therefore, performing such measurements can give insight into the dominant underlying spin-scattering impurities.

Given a microscopic model Hamiltonian one can compute spin-relaxation rates with well developed theoretical recipes [133–135]. Spin-relaxation rates in the superconducting state can be calculated in the presence of thermal smearing generalizing Fermi's golden rule, i.e.,

$$\frac{1}{\tau_s} = \frac{\iint_{\mathrm{BZ}} \mathrm{d}\mathbf{k}\,\mathrm{d}\mathbf{q}\; |\langle \mathbf{k},\uparrow|\mathbb{T}|\mathbf{q},\downarrow\rangle|^2\, \delta(E_\mathbf{k} - E_\mathbf{q}) \left(-\frac{\partial f}{\partial E_\mathbf{k}}\right)}{\frac{\hbar\pi}{A_{\mathrm{uc}}\eta} \int_{\mathrm{BZ}} \mathrm{d}\mathbf{k} \left(-\frac{\partial f}{\partial E_\mathbf{k}}\right)}, \tag{2.61}$$

with the Fermi-Dirac distribution $f = [\exp(E_\mathbf{k}/(k_\mathrm{B}T)) + 1]^{-1}$. Note that η denotes the impurity concentration and A_{uc} is the area of the lattice unit cell, so in our case it is given by the graphene unit cell. The necessary scattering amplitudes are obtained from the so-called T-matrix $\mathbb{T}$, which, in turn, is calculated from the local perturbation V and the retarded Green's function of the unperturbed system according to $\mathbb{T} = V(1-\mathbb{G}_0 V)^{-1}$. By computing $\mathbb{T}$, one also gets access to the perturbed Green's function, which contains information about the density of states and the bound state spectrum of the YSR states. For a full and detailed explanation of all the necessary steps we refer the reader to the Supplemental Material of Ref. [2].
In the following sections we will study the spin-relaxation rate $1/\tau$ in graphene systems, as these are predicted to be ideal platforms for spintronic devices. Particularly the influence of superconductivity will be examined in detail.

3. Numerical techniques

In the last decades numerical simulations have become more and more important for the understanding of complex problems that cannot be solved analytically. Also complicated quantum effects can be incorporated such that precise predictions for experiments can be made. It is a very fast developing field of science and, in combination with the quick technological progress of computer architectures, allows to treat realistic physical systems with high accuracy. In this chapter, the numerical tools are discussed that will be employed in the following chapters to study the systems of interest. We start by introducing the tight-binding method, which serves as basis for all of the proceeding simulations, and also treat useful tools for simulating large systems and the generation of correlated disorder. Then, we continue discussing how normal and superconducting topological insulator and graphene systems can be studied on the tight-binding level.

3.1. Tight-binding method

One of the standard techniques to numerically treat complex physical problems is the so-called tight-binding method [94]. Assume that we have a Hamiltonian that depends on certain orders of the momentum operator $\hat{k}$, i.e., $H(\hat{k})$. This continuous representation can then be treated with computer simulations by discretizing the problem and putting it onto a lattice. First, the momenta are replaced by their real-space counterparts, namely the spatial derivative operators

$$\hat{k}_i \to -\mathrm{i}\partial_i, \tag{3.1}$$

$$\hat{k}_i^2 \to -\partial_i^2, \tag{3.2}$$

where i denotes spatial coordinates. These derivatives are then approximated by applying the finite difference method [136]

$$\partial_i \Psi_i = \frac{\Psi_{i+1} - \Psi_{i-1}}{2a_i}, \tag{3.3}$$

$$\partial_i^2 \Psi_i = \frac{\Psi_{i+1} + \Psi_{i-1} - 2\Psi_i}{a_i^2}, \tag{3.4}$$

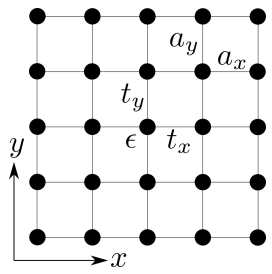

Figure 3.1: Plot of a 2D tight-binding lattice. The parameters ϵ, t, and a denote onsite and hopping energies, as well as lattice constants, respectively.

with a_i being the lattice spacing between the discrete grid points along the spatial direction i. For simplicity, assume we assume to have a 2D electron gas, where the Hamiltonian is given by $H = \hbar^2/(2m)\left(k_x^2 + k_y^2\right)$ and the Schrödinger equation $H\Psi = E\Psi$. Applying the above steps for each spatial dimension separately (with $a = a_x = a_y$), one gets

$$-\frac{\hbar^2}{2ma^2}\left[\Psi_{x+1,y} + \Psi_{x-1,y} + \Psi_{x,y+1} + \Psi_{x,y-1} - 4\Psi_{x,y}\right] = E\Psi_{x,y} \tag{3.5}$$

for each lattice point (x, y). From Eq. (3.5), it becomes possible to easily extract onsite and hopping terms, which construct the discrete lattice shown in Fig. 3.1. These are

$$\epsilon = 4\frac{\hbar^2}{2ma^2}, \tag{3.6}$$

$$t_x = t_y = -\frac{\hbar^2}{2ma^2}. \tag{3.7}$$

Considering that space is now treated by discrete lattice points and the fact that we obtain Eq. (3.5) for each of them, the Hamiltonian can be expressed by a Hermitian tight-binding matrix. The diagonal entries correspond to the respective onsite terms, while the off-diagonal terms give the hopping energies between the different grid sites. Exactly this procedure will be applied to all the following systems in order to simulate them numerically.

3.2. Dirac Hamiltonian on a lattice – fermion doubling problem

Treating the Dirac Hamiltonian in Eq. (2.5) numerically by discretizing it on a lattice will inevitably lead to the so-called fermion doubling problem [35–37]. Discretizing terms that are linear in momentum k with the finite difference approach results in a sinusoidal dispersion, such that artificial modes appear at the borders of the first Brillouin zone; see Fig. 3.2. These states can cause significant problems. For example, they can lead to artificial inter-valley scattering at delta barriers, and in turn falsify the results, in transport calculations. A well-known workaround is the inclusion of a Wilson mass term [137, 138], which gaps out the dispersion at large k values. The corresponding Hamiltonian reads

$$H = \hbar v_\mathrm{F}\left[k_x\sigma_x + k_y\sigma_y - \left(\alpha_x k_x^2 + \alpha_y k_y^2\right)\sigma_z\right], \tag{3.8}$$

where $\alpha_i = E_\mathrm{gap}a_i^2/(4\hbar v_\mathrm{F})$. The definition of α_i assures that we open a gap of size $2E_\mathrm{gap}$ at $k_i = \pm\pi/a_i$, between the positive and negative energy branches of the spectrum; the size of the gap is independent of the lattice constants a_i. If the Hamiltonian is

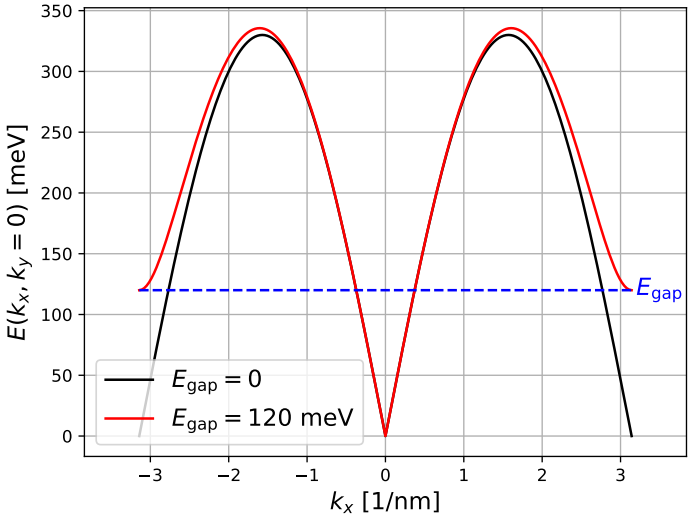

Figure 3.2: Spectrum of the Dirac Hamiltonian with the additional mass term given by Eq. (3.8) for $a = 1$ nm. At the borders of the first Brillouin zone, a gap opens and Fermion doubling is canceled for energies below E_{gap}.

discretized on a square lattice with $a = a_x = a_y$ (so that $\alpha = \alpha_x = \alpha_y$), the spectrum of Eq. (3.8) is then given by [139]

$$E(k_x, k_y) = \pm \frac{\hbar v_{\mathrm{F}}}{a} \sqrt{\sin(ak_x)^2 + \sin(ak_y)^2 + 4\frac{\alpha^2}{a^2}\left(\cos(ak_x) + \cos(ak_y) - 2\right)^2}. \tag{3.9}$$

In Fig. 3.2, the spectrum for $E_{\mathrm{gap}} = 120$ meV and $k_y = 0$ is plotted as a red curve. The opening of a gap at $k_x = \pm\pi$ is certainly observable, while the linear spectrum at $k_x = 0$ is preserved. Note, however, that one has to be aware that the additional mass term also affects physical properties like the spin polarization. Therefore, it is important to check if the addition of the mass term is justified for the respective calculations and does not cause unphysical modifications of the calculated quantities.
For certain topological materials, it is often important to also consider terms of higher order in k. One example is Bi_2Te_3, where hexagonal warping leads to a deformation of the Fermi contour and strongly impacts physical properties. The warping enters with cubic orders of k in the Hamiltonian, such that a quadratic Wilson mass term is no longer enough to get rid of Fermion doubling. However, it is still possible to study such a Hamiltonian on a discrete lattice. The numerical scheme is discussed in detail in App. A.6.

3.3. Magnetic fields in tight-binding models – Peierl's substitution

Many physical properties in different material classes can be probed by applying magnetic fields. For example, in weak-localization and weak-antilocalization experiments

it can be determined whether a material has spin-orbit coupling or not [140–143]. In this work, magnetic fields will also play an important role and it is therefore necessary to shortly discuss how these can be included in the tight-binding framework. The magnetic field $\boldsymbol{B}$ is determined by choosing a vector potential $\boldsymbol{A}$, as the two quantities are related by $\boldsymbol{B} = \nabla \times \boldsymbol{A}$. Then, after fixing a gauge, the standard procedure to include $\boldsymbol{B}$ in a discretized Hamiltonian is applying Peierl's substitution [144, 145]. Thereby, the vector potential enters the hopping terms as a phase factor, such that one gets

$$t = t(B = 0) \cdot \mathrm{e}^{-\mathrm{i}\frac{e}{\hbar}\int \boldsymbol{A}\cdot\boldsymbol{dl}}. \tag{3.10}$$

The phase in the exponential is simply a line integral of the vector potential along the hopping path. Accounting for the accumulation of phases in this way when an electron moves under the influence of a vector potential is analogous to performing minimal coupling $p \to p + e\boldsymbol{A}$ in the continuous limit (see, for example, Ref. [146]). Note that this method is only valid as long as the flux per lattice plaquette is smaller than a magnetic flux quantum $2\Phi_0$.

3.4. Numerical simulation of bulk systems

In this section, the basic numerical concept of simulating 2D systems like bulk materials is introduced. In computer simulations the system size is limited to a finite size and therefore there will always occur quantization effects, for example, of momenta, in certain directions. In order to circumvent this issue, it is possible to introduce periodic boundary conditions (PBC) along those finite system directions. As a simple example, let us consider a 2D system which is described by the Hamiltonian

$$H = \frac{\hbar^2}{2m}(k_x^2 + k_y^2), \tag{3.11}$$

while the eigenfunctions are given by

$$\Psi(x, y) \propto \exp(\mathrm{i}k_x x)\exp(\mathrm{i}k_y y). \tag{3.12}$$

In transport simulations, leads can be implemented by exploiting translational invariance in one spatial direction. This direction will be fixed to x, such that k_x is a good quantum number. However, the transverse y-direction will have a finite width W. According to the applied boundary conditions, the momentum k_y will be quantized. For hard-wall boundary conditions, the wave functions in the system must vanish at the boundaries and the transverse momentum will be given by $k_y = \pi n/W$ and n being a non-zero integer. In the case of PBCs, the quantized momenta can be obtained

considering

$$\begin{aligned} & \Psi(y) = \Psi(y+W) \\ \Leftrightarrow \quad & \exp(\mathrm{i}k_y y) = \exp(\mathrm{i}k_y(y+W)) = \exp(\mathrm{i}k_y y)\exp(\mathrm{i}k_y W) \\ \Leftrightarrow \quad & 1 = \exp(\mathrm{i}k_y W) \\ \Leftrightarrow \quad & 2\pi n = k_y W \\ \Rightarrow \quad & k_y = \frac{2\pi}{W} n, \end{aligned} \tag{3.13}$$

with $n \in \mathbb{Z}$. In Fig. 3.3 (a), this quantization is visualized at a fixed Fermi energy E_F. The continuous Fermi contour is cut at equally spaced k_y-values, with spacing $\Delta k_y = 2\pi/W$. That means, with increasing width W of the system, more k_y-values will be considered in the calculation. Those momenta correspond to higher subbands in the quasi-1D bandstructure. Moreover, the bandstructure is only important in the first Brillouin zone, which spreads from $-\pi$ to π. So only k_y-values in that range are important to consider. To get physical quantities of bulk materials, stemming from a continuous Fermi contour, it is necessary to integrate over the transverse momenta k_y. In tight-binding this can be done numerically, by adding a phase factor to the hopping that introduces the PBC

$$t_{y=W\to y=0} = t_y \exp(\mathrm{i}\phi). \tag{3.14}$$

The phase ϕ is chosen from the interval $[0; 2\pi]$. The integration is then performed over the phase ϕ. In the special case of $W = 1$, only the $k_y = 0$ mode is present, as $\Delta k_y = 2\pi$ and therefore the next transverse momentum will sit at the center of the second Brillouin zone. This means that different phases ϕ directly correspond to different k_y-values. For other values of W, already many subbands (many transverse momenta) can be present in the calculations. In those cases, the phase ϕ will shift the cut positions along the k_y-direction. More precisely, continuously changing ϕ from 0 to 2π will address all missing k_y-values between $k_y = 0$ and $k_y = 2\pi/W$. The momentum spacing Δk_y is not affected by the phase and so also all the momenta in higher intervals are addressed by the continuous shift. The calculation procedure is then as follows: For a certain width W one first sums over the contribution to the quantity of interest of the present subbands (modes) in the system for a fixed phase ϕ. Then the integration over ϕ of those contributions is performed.
A straightforward example is given by the computation of the 2D conductance of metallic electrons through an infinite barrier along the y-direction. In Fig. 3.3 (b), a sketch of the system is depicted . To be able to observe a few signatures in the conductance, we consider an infinite slab with height h, such that the Hamiltonian is given by

$$H_\mathrm{3D} = \frac{\hbar^2}{2m}(k_x^2 + k_y^2 + k_z^2). \tag{3.15}$$

The system has a width W with N_y lattice points and periodic boundary conditions in the y-direction. Furthermore, the length L of the system has only one lattice point, which will act as a barrier V. Also, the height h is discretized on N_z lattice points.

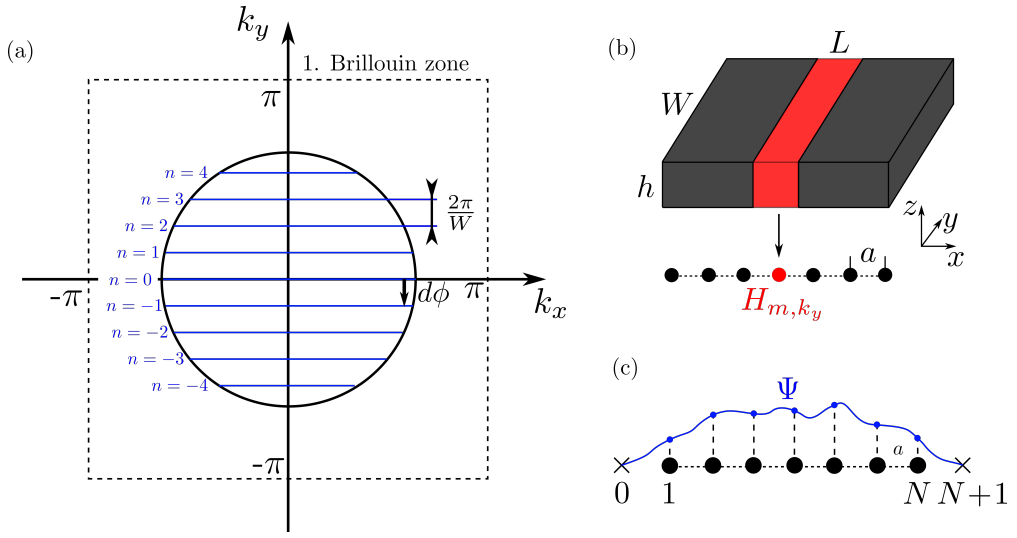

Figure 3.3: (a) Schematic plot of the quantization of momenta k_y for PBC. Instead of the circular Fermi contour, only discrete k_y-values shown in blue are allowed. Varying the phase ϕ will also address k_y-momenta between the blue lines. Adapted from Supplemental Material of Ref. [147]. (b) Plot of the test setup for the transmission computation. For the analytical calculation the setup is simplified to an effective 1D chain. (c) Visualization of the hard-wall boundary conditions. The wave functions have to vanish at positions 0 and $N + 1$.

The spectrum of the tight-binding implementation is then given by

$$E = 6t - 2t\cos(k_x a) - 2t\cos(k_y a) - 2t\cos(k_z a). \tag{3.16}$$

Due to the finite extensions in y- and z-direction, the corresponding momenta are quantized. It follows

$$E = 6t - 2t\cos(k_x a) - 2t\cos\left(n\frac{2\pi}{N_y}a\right) - 2t\cos\left(m\frac{\pi}{N_z+1}a\right), \tag{3.17}$$

with $t = \hbar^2/(2ma)$. For simplicity, the lattice constant in all spatial directions is fixed to $a = 1$ and also the hopping parameter is set to $t = 1$. Note that due to the PBC the momentum in y-direction is quantized differently than the one in z-direction. The height of the system has hard-wall boundary conditions. That means that the wave functions have to vanish at positions 0 and N_z+1, which are outside the computational lattice [148]. Therefore the effective length in z-direction is given by $N_z + 1$. This is depicted in Fig. 3.3 (c).
The numerical calculation of the transmission depending on the energy E through this system can be done as explained above. It is computed with

$$T(E) = \int_0^{2\pi} \frac{d\phi}{2\pi} \sum_{i=1}^{N} T_i(E, \phi), \tag{3.18}$$

where the summation is over all open subbands at energy E.
In order to check the computed results, it is useful to compare with an analytical solution. To obtain an analytical expression we employ the Fisher-Lee relation, which connects the transmission with Green's function [95, 96]. The setup is translationally invariant in the y-direction, so the transmission through the width W and height h is given by the sum of the transmission values through each of the N_y and N_z lattice rows. Therefore it is enough to just consider a simple 1D chain model. This system is also shown in Fig. 3.3 (b), where the scattering region is the lattice point marked in red.
The following derivation follows the lecture notes in Ref. [149]. The Hamiltonian of the isolated scattering region is given by

$$H_{m,k_y} = C_{m,k_y} + \frac{V}{a}, \tag{3.19}$$

where $C_{m,k_y} = 6t - 2t\cos(k_y a) - 2t\cos(m\pi a/(N_z+1))$ is incorporating the transverse components. At the end, we will sum over the contributions of different m modes and integrate out k_y.
To obtain Green's function, we need the self-energies of the leads. For the 1D chain, these are simply given by

$$\Sigma^1_{m,k_y} = \Sigma^2_{m,k_y} = -t\exp(\mathrm{i}k_x(E)a). \tag{3.20}$$

Next, one has to compute the broadening matrices, which are given as follows

$$\begin{aligned}
\Gamma^{1,2}_{m,k_y}(E) &= \mathrm{i}[\Sigma^{1,2}_{m,k_y}(E) - \Sigma^{1,2}_{m,k_y}(E)^\dagger] \\
&= \mathrm{i}[-t\exp(\mathrm{i}k_x(E)a) + t\exp(-\mathrm{i}k_x(E)a)] \\
&= \mathrm{i}t[-(\cos(k_x(E)a) + \mathrm{i}\sin(k_x(E)a)) + \cos(k_x(E)a) - \mathrm{i}\sin(k_x(E)a)] \\
&= 2t\sin(k_x(E)a).
\end{aligned} \tag{3.21}$$

This is further rewritten using the dispersion relation of our system, which is given by $E = C_{m,k_y} - 2t\cos(k_x(E)a)$. We substitute into the broadening matrix the momentum $k_x(E)a = \arccos\big(-(E - C_{m,k_y})/(2t)\big)$, which gives

$$\begin{aligned}
\Gamma^{1,2}_{m,k_y}(E) &= 2t\sin(k_x(E)a) \\
&= 2t\sin\left(\arccos\left(-\frac{E - C_{m,k_y}}{2t}\right)\right) \\
&= 2t\sqrt{1 - \frac{(E - C_{m,k_y})^2}{4t^2}} \\
&= \sqrt{4t^2 - (E - C_{m,k_y})^2}.
\end{aligned} \tag{3.22}$$

Green's function is now calculated as

$$\begin{aligned}
G_{m,k_y}(E) &= \left[E - H_{m,k_y} - \Sigma^1_{m,k_y} - \Sigma^2_{m,k_y}\right]^{-1} \\
&= \left[E - C_{m,k_y} + 2t\exp(\mathrm{i}k_x(E)a) - \frac{V}{a}\right]^{-1}.
\end{aligned} \tag{3.23}$$

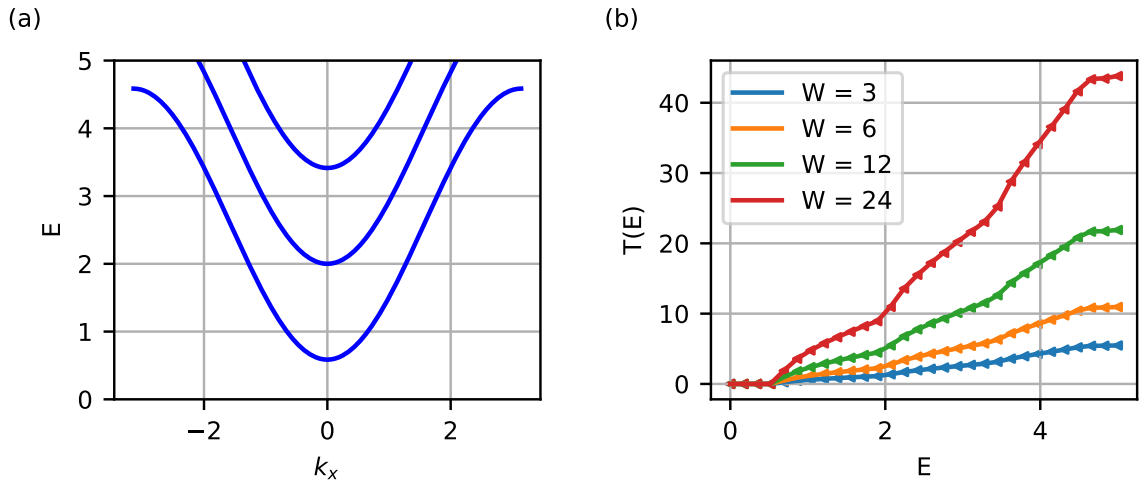

Figure 3.4: (a) Bandstructure computed from Eq. (3.17) with $N_y = 1$ and $N_z = 3$. For simplicity, lattice constant and hopping parameter were set to $a = 1$ and $t = 1$, respectively. (b) Calculated 2D transmission with respect to the energy. The numerical (analytical) results are shown as lines (triangular symbols). Both show very good agreement.

Now, one can plug in the dispersion relation such that

$$\begin{aligned} G_{m,k_y}(E) &= \left[2ti\sin(k_x(E)a) - \frac{V}{a}\right]^{-1} \\ &= [\mathrm{i}\Gamma_{m,k_y}(E) - \frac{V}{a}]^{-1} \\ &= \frac{1}{\Gamma_{m,k_y}(E)}\frac{1}{\mathrm{i} - \frac{V}{a\Gamma_{m,k_y}(E)}}. \end{aligned} \tag{3.24}$$

The transmission can then be computed employing the Fisher-Lee relation, summing over m, and integrating over k_y. It finally follows that

$$\begin{aligned} T(E)|_{W=1} &= \int_0^{2\pi} \frac{\mathrm{d}k_y}{2\pi} \sum_m \left[\Gamma_{m,k_y}(E) G_{m,k_y}(E) \Gamma_{m,k_y}(E) G_{m,k_y}(E)^\dagger\right] \\ &= \int_0^{2\pi} \frac{\mathrm{d}k_y}{2\pi} \sum_m \frac{1}{1 + \frac{V^2}{(a\Gamma_{m,k_y}(E))^2}}. \end{aligned} \tag{3.25}$$

The full transmission through a slab of width W is then simply

$$T(E) = \frac{W}{a} \cdot T(E)|_{W=1}. \tag{3.26}$$

Finally, we can compute the 2D transmission in our setup for different widths W. In Fig. 3.4 (a) the bandstructure for $N_y = 1$ is illustrated. There, only the $n = 0$

bands for $m = 1, 2, 3$ are allowed. The results for the transmission calculations are shown in Fig. 3.4 (b). The numerical transmission values are shown as lines, while the analytically obtained values are plotted with triangular symbols. Both methods agree very well. Exactly at the energies, at which a new subband stemming from the quantization in z-direction opens, the conductance starts to increase. Also the numerically calculated transmission scales linearly with the width as expected from the analytics.
This method can also be applied to compute quantum transport on TI surfaces which have a rough surface layer structure (see Chapter 4.1) or regions with a certain doping potential characteristic. This is not within the scope of this work, but was already applied in the Supplemental Material of Ref. [147].
Furthermore, another important quantity which can be studied by means of this methodology is the local density of states in bulk systems. It can also be computed by integrating over the introduced phase ϕ according to

$$\rho(x, y, z) = \int_0^{2\pi} \frac{d\phi}{2\pi} \sum_i^N \langle \Psi_{i,\phi}(x, y, z) | \Psi_{i,\phi}(x, y, z) \rangle \,. \tag{3.27}$$

This equation will play an important role in chapter 4.1, where we study scattering processes of topological surface states at surface steps and islands. There, the equation will be used to identify possible signatures of surface states in Bi_2Se_3, which might be observable in actual experiments.

3.5. Correlated disorder on a lattice

One of the greatest challenges of properly simulating quantum transport is to consider, on the one hand, a system that is as realistic as possible, while keeping, on the other hand, the numerical efforts to a minimum. Real samples that are studied in actual experiments are never perfectly clean and always contain impurities and defects, which impact the transport properties of the systems. Impurities typically increase the scattering potential, but they can also induce local magnetic exchange or spin-orbit interactions, which result in spin-dependent scattering [84]. Moreover, the scattering potentials often have a finite spatial extension and vary only over certain length scales. Therefore, this chapter explains an efficient and very powerful algorithm to generate disorder using a predefined spatial correlation function. This method was originally introduced in optics, but is also applicable to tight-binding calculations. It has a lot of practical features and advantages, which we will also discuss.

3.5.1. Spatial correlation function

In tight-binding calculations, disorder can be included adding disorder energy terms to some onsite energies. For some cases, it is sufficient to choose Anderson disorder (white noise), in which random numbers with a Gaussian distribution are generated in the interval $[-V, V]$, where V is the disorder strength. Contrary, real scattering potentials can

extend over certain length scales, like local defect areas or electrostatic/magnetic fields of impurities. But in certain numerical systems, also spatial correlations in the disorder potential can be desirable, for example, to prevent artificial inter-valley scattering in the case of the fermion doubling problem that arises when the Dirac Hamiltonian is put onto a lattice [150]. In order to generate spatially correlated disorder, one needs to define the so-called correlation function $C(|\boldsymbol{r}-\boldsymbol{r}'|) = \langle V(\boldsymbol{r})V(\boldsymbol{r}')\rangle$. In principle this function can take any form, i.e., a power law, exponential, or Gaussian dependence. The exact form that one needs to consider depends on the actual situation. For example, one resorts to a power law correlation function [151] in the case of porous materials. In the context of topological insulators, one finds a quite useful representation of a Gaussian correlation function (CF) [152] in the literature. Also for our purposes, we choose this definition, given by

$$C(|\boldsymbol{r}-\boldsymbol{r}'|)^{\mathrm{2D}} = K_0 \frac{(\hbar v_{\mathrm{F}})^2}{2\pi\xi^2} \exp\left(-\frac{r^2}{2\xi^2}\right) \tag{3.28}$$

for a 2D system and abbreviating $r = |\boldsymbol{r}-\boldsymbol{r}'|$. Note that the parameter ξ is denoted as the spatial correlation length and tunes the extend of the spatially correlated disorder regions. The advantage of this representation is that the disorder strength can be tuned by the dimensionless parameter K_0, for which previous studies [152] have already shown that values up to 0.2 correspond to weak disorder, values around 0.5 simulate intermediate disorder, and values larger than 1 give strong disorder. Here, it should be mentioned that this classification is valid for 2D systems only, in which $\hbar v_{\mathrm{F}} = 330\ \mathrm{meV}\cdot\mathrm{nm}$. For other systems, this interpretation could be different as the Fermi velocity might change.

3.5.2. Power spectral density (PSD)

For the following algorithm, it is necessary to introduce the power spectral density, which is just the Fourier transform of the CF. It allows for a simple tuning knob to determine the exact correlation in the generated disorder. In our case, we work with a Gaussian CF and one already finds analytical expressions for the PSD in Ref. [153], as well as for exponential CFs in the dimensions $D = 1, 2$, and 3. The PSD of Eq. (3.28) is given by

$$\mathrm{PSD}(k) = K_0(\hbar v_{\mathrm{F}})^2 \exp\left(-2(\pi k\xi)^2\right), \tag{3.29}$$

where k is the variable in Fourier space.
For the numerical simulations, we put the disorder on a discrete lattice and we thus need to adjust some parameters (the correlation length) depending on the lattice constant. The physical correlation length ξ will be expressed in the algorithm as

$$\xi_x = \xi/a_x \tag{3.30}$$
$$\xi_y = \xi/a_y. \tag{3.31}$$

This allows us to define different lattice constants along different spatial directions. Therefore, the discrete PSD can be rewritten as

$$\mathrm{PSD}(k_x, k_y) = K_0 \frac{1}{a_x a_y} (\hbar v_\mathrm{F})^2 \exp\left(-2\pi^2 \left((k_x \xi_x)^2 + (k_y \xi_y)^2\right)\right). \tag{3.32}$$

The generalization to a 3D system can be done choosing the same correlation function. The PSD will then change as the Fourier transform is now performed over a third dimension, and we get

$$\mathrm{PSD}(k_x, k_y, k_z)^{3\mathrm{D}} = K_0 \frac{1}{a_x a_y a_z} (\hbar v_\mathrm{F})^2 \sqrt{2\pi}\xi \exp\left(-2\pi^2 \left((k_x \xi_x)^2 + (k_y \xi_y)^2 + (k_z \xi_z)^2\right)\right). \tag{3.33}$$

Simulations with 3D models take more physical details into account, like bulk states in topological nanowires, but they are also computationally more expensive. Moreover, 3D disorder can be used to simulate more complex 2D surfaces like cones or constrictions [154] by interpolating between grid points in the 3D lattice and thereby cutting out the structured surface.

3.5.3. Thorsos (Monte-Carlo spectral) method

This approach was developed by Thorsos [155] and works, in principle, combining random numbers with the PSD. A very detailed introduction is given in Ref. [156] by Mack and will be adapted here. In real space, the lattice will have the finite length $L = a_x N_x$ and width $W = a_y N_y$, where a_i and N_i are the lattice constants and number of grid points along the two spatial directions, respectively. For simplicity, we only consider the 1D case, though the generalization to higher dimensions is straightforward. The disorder value on a lattice site along the x-direction can be calculated using a fast Fourier transformation (FFT), which is given by

$$V(x) = \mu_v + \frac{1}{L} \sum_{j=-N_x/2}^{N_x/2-1} F(k_j) \exp(\mathrm{i}2\pi k_j x), \tag{3.34}$$

where μ_v is the mean value of the disorder (in our case $\mu_v = 0$) and $F(k_j)$ is

$$F(k_j) = \sqrt{\mathrm{PSD}(k_j)} \begin{cases} \eta_1 + \mathrm{i}\eta_2, & j \neq 0, \pm N_x/2 \\ \eta_1, & j = 0, \pm N_x/2. \end{cases} \tag{3.35}$$

The variables η_1 and η_2 are random numbers, which we generate through a FFT of a set of random real numbers. In order to assure reproducible results, we further use the built-in random-number generator kwant.digest.gauss(input, salt='') of the Kwant package [34]. Note that in the context of Kwant the parameter *salt* has the same meaning as the *seed* in other random number generating schemes. For higher dimensions, Mack also specifies the boundary conditions that will result in a purely real disorder configuration U.

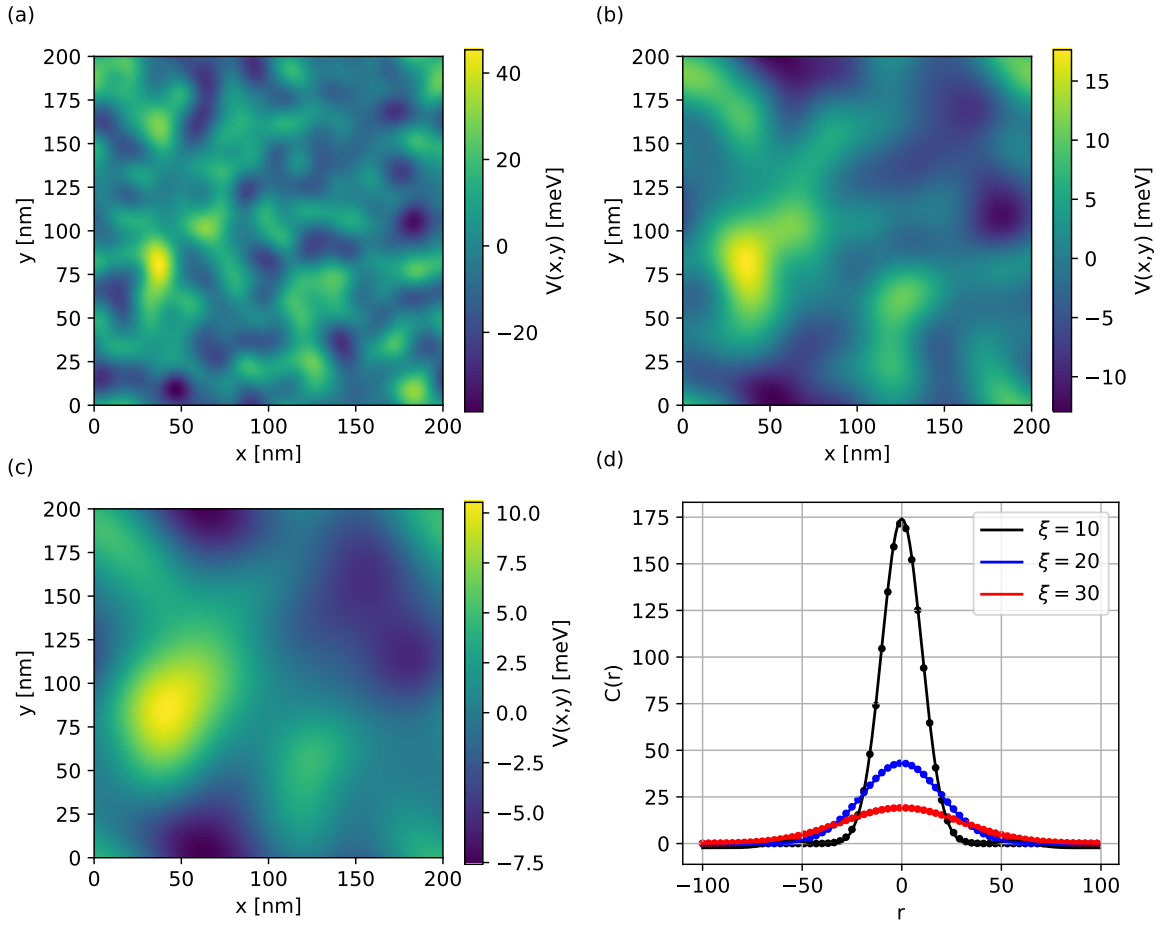

Figure 3.5: Example disorder configuration for a system with width $w = 200$ nm, length $L = 200$ nm, $K_0 = 1$, salt = 1, as well as (a) $\xi = 10$ nm, (b) $\xi = 20$ nm, and (c) $\xi = 30$ nm. (d) Comparison between the analytical correlation function (dots) given by Eq. (3.28) and the numerically calculated correlations (solid lines); the latter were averaged over $N_{\text{salts}} = 1000$ disorder configurations.

This method of generating random numbers with a certain spatial correlation brings along a lot of advantages, which are particularly handy in tight-binding calculations. First of all, the FFT steps are very fast due to the highly efficient implementation of available packages, such that one disorder configuration can be calculated in very short time steps (also in 3D). This is extremely important, as one needs to average over many disorder configurations to get rid of disorder-set dependent effects. Second, the scheme is also easily adjustable to different physical situations, meaning that the correlation function can be changed simply by modifying the PSD in the algorithm. Finally, the FFT assures that the generated disorder is periodic along all spatial directions. This is very convenient in systems with periodic boundary conditions, like in the case of the surface of a 3D topological insulator nanowire. The periodicity can be easily broken by taking only a subset of a larger disorder set.

Example

In Figs. 3.5 (a) – (c), examples of disorder configurations for different correlation lengths ξ are shown. Correlated regions are clearly visible, while also the periodicity can be seen at the edges of the samples. In order to check whether we can recover the predefined correlation function given by Eq. (3.28), we numerically check the correlation of the disorder sets and average over $N_{\text{salts}} = 1000$ configurations. Here, we follow Ref. [151] and use the formula

$$C(r) = \left\langle \frac{1}{N_{\text{salts}}} \sum_x (\tau_x - \mu_U)(\tau_{x+|r|\boldsymbol{e}_1} - \mu_U) \right\rangle_{\text{salts}}, \tag{3.36}$$

where $\langle ... \rangle_{\text{salts}}$ stands for the configuration averaging over different disorder sets. We evaluate it along one lattice row in the x-direction. The results are shown in Fig. 3.5 (d). We see a convincing agreement between the analytical form of the correlation function and the numerically computed correlation functions in the disorder sets.

3.6. Simulating superconducting systems

Properties of superconducting systems are more subtle to calculate than those of systems in the normal state. The reason for that lies in the presence of the superconducting gap. Many interesting physical effects originate from states that form inside this energy gap, i.e., Andreev bound states [115, 116] or Yu-Shiba-Rusinov states [118–123]. In the following parts, some numerical methods to study those states, as well as the corresponding supercurrent of Josephson junctions [113, 114], will be introduced.

3.6.1. Calculating Andreev bound states

Constructing a so-called Josephson junction by sandwiching a normal-conducting material between two superconducting electrodes can lead to the emergence of Andreev bound states (ABS). Charge carriers in the normal region can be consecutively Andreev

reflected at the N/S-interfaces. The energies of the ABS depend on the phase difference of the superconducting order parameters between the two ends of such a junction. In this work, three well-known schemes to numerically compute the Andreev spectra will be employed. We start with a short explanation of a straightforward method, namely performing exact diagonalization of the tight-binding Hamiltonian of a finite system.

Andreev bound states from diagonalization

The direct way to obtain the ABS spectrum of a Josephson junction is exact diagonalization of Hamiltonians of finite tight-binding systems. To be more precise, the Josephson junction is implemented with its geometric definitions and the superconducting leads are then implemented with long spatial extensions. It is useful to connect the ends of the superconducting regions with a hopping term, in other words to introduce periodic boundary conditions. In experiments, the phase difference is typically tuned by the application of a magnetic field through SQUIDs. The numerical system can now be assumed to be equivalent to such a structure and therefore the phase difference between the ends of the superconducting regions can be accounted for in terms of a Peierl's phase in the normal region. This is justified as the phase of the superconducting order parameters can be gauged away into the vector potential. The phase difference enters then as a hopping in the normal region that points along the junction direction, specifically as

$$t \exp\left(\mathrm{i}2\pi \frac{\Phi}{h/e}\right) = t \exp\left(\mathrm{i}\frac{\Delta\varphi}{2}\right),$$

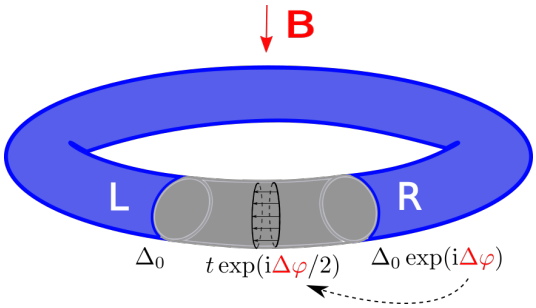

Figure 3.6: Schematic system for the calculation of ABS by diagonalization.

where Φ corresponds to the flux through the whole ring area shown in the schematic plot of Fig. 3.6. The above equation only shows the entry in the electron orbitals, for the hole orbitals the phase factor is its complex conjugate. Figure 3.6 shows an example system, which is chosen to be a normal TI nanowire between two superconducting leads. The implemented tight-binding system can be diagonalized with standard numerical procedures, where the eigenvalues of interest lie close to $E = 0$. Note that the spectrum converges better for longer superconducting (blue) regions, but the system size is obviously limited in diagonalization schemes.

Andreev bound states from the scattering matrix

The next method is applicable to Josephson junctions in which interface effects between the N and S regions can be neglected. In systems in that such effects are present and play a crucial role, it is still possible to incorporate them by hand, but they have to be understood in detail. Beenakker [115, 157] devised this method for Josephson junctions in which normal scattering only occurs far away from the interfaces. Moreover, the same approach is widely used to derive analytical expressions for ABS [158]. The general idea is to split the system into different scattering regions, as depicted in Fig. 3.7. The grey region corresponds to the disordered part of the junction. Incoming electron and hole wave functions are here connected to their outgoing counterparts by the normal-region scattering matrix S_N via

$$\Psi_\mathrm{out} = S_\mathrm{N}(E)\Psi_\mathrm{in}, \tag{3.37}$$

$$\begin{pmatrix} \psi^\mathrm{e}_\mathrm{out} \\ \psi^\mathrm{h}_\mathrm{out} \end{pmatrix} = \begin{pmatrix} S^\mathrm{e}(E) & 0 \\ 0 & S^\mathrm{h}(E) \end{pmatrix} \begin{pmatrix} \psi^\mathrm{e}_\mathrm{in} \\ \psi^\mathrm{h}_\mathrm{in} \end{pmatrix}, \tag{3.38}$$

where ψ_i^L and ψ_i^R contain electron and hole degrees of freedom. The Andreev reflection at the N/S-interfaces is emphasized by the Andreev scattering matrix S_A and connects the outgoing modes to the incoming ones by

$$\Psi_\mathrm{in} = S_\mathrm{A}(E)\Psi_\mathrm{out}, \tag{3.39}$$

$$\begin{pmatrix} \psi^\mathrm{e}_\mathrm{in} \\ \psi^\mathrm{h}_\mathrm{in} \end{pmatrix} = \begin{pmatrix} 0 & S^\mathrm{eh}_\mathrm{A}(E) \\ S^\mathrm{he}_\mathrm{A}(E) & 0 \end{pmatrix} \begin{pmatrix} \psi^\mathrm{e}_\mathrm{out} \\ \psi^\mathrm{h}_\mathrm{out} \end{pmatrix}. \tag{3.40}$$

Plugging Eq. (3.37) into Eq. (3.39) gives

$$\Psi_\mathrm{in} = S_\mathrm{A}(E)S_\mathrm{N}(E)\Psi_\mathrm{in}, \tag{3.41}$$

which further requires

$$\det(\mathbb{1} - S_\mathrm{A}(E)S_\mathrm{N}(E)) = 0. \tag{3.42}$$

Rewriting Eq. (3.41) in terms of the electron and hole components, we arrive at two coupled equations for the respective wave functions,

$$\psi^\mathrm{e}_\mathrm{in} = S^\mathrm{eh}_\mathrm{A}(E)S^\mathrm{h}(E)\psi^\mathrm{h}_\mathrm{in} \tag{3.43}$$

$$\psi^\mathrm{h}_\mathrm{in} = S^\mathrm{he}_\mathrm{A}(E)S^\mathrm{e}(E)\psi^\mathrm{e}_\mathrm{in}. \tag{3.44}$$

This leads then to the well-known defining expression for ABS in a Josephson junction, which is given by

$$\det\big(\mathbb{1} - S^\mathrm{eh}_\mathrm{A}(E)S^\mathrm{h}(E)S^\mathrm{he}_\mathrm{A}(E)S^\mathrm{e}(E)\big) = 0. \tag{3.45}$$

The bound state energies can be computed as the roots of this expression. However, it is still possible to derive an expression that is more useful and efficient for numerical applications. Heck et al. [159] showed that one can transform the problem into a simpler singular value decomposition. Initially, assume that the electron wave functions

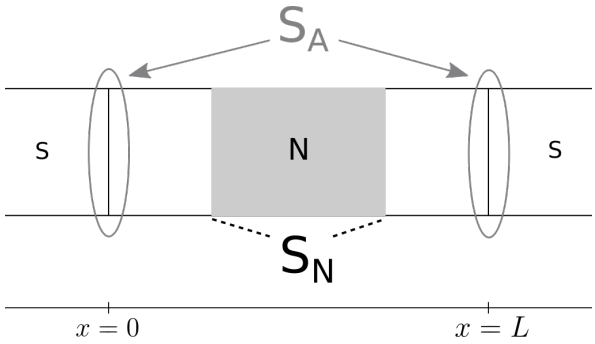

Figure 3.7: Schematic plot of the ABS calculation from the S matrix.

are connected to the hole wave functions by particle-hole symmetry. Then the normal scattering matrices of both types of particles are related by

$$S^{\mathrm{h}}(E) = S^{\mathrm{e}}(-E)^{\dagger}. \tag{3.46}$$

The energy dependence can be dropped, if we just consider the short-junction limit, which is valid for many experimental situations and entails that $S(E) \approx S(0) = S$. The Andreev reflection scattering matrix will transform into an off-diagonal form in the same basis

$$\begin{aligned} S_{\mathrm{A}}(E) &= \mathrm{i}\exp\left(-\mathrm{i}\arccos\left(\frac{E}{\Delta}\right)\right)\begin{pmatrix} 0 & R_{\mathrm{A}}^{\dagger} \\ R_{\mathrm{A}} & 0 \end{pmatrix} \\ &= \left(\sqrt{1-\left(\frac{E}{\Delta}\right)^2} + \mathrm{i}\frac{E}{\Delta}\right)\begin{pmatrix} 0 & R_{\mathrm{A}}^{\dagger} \\ R_{\mathrm{A}} & 0 \end{pmatrix}. \end{aligned} \tag{3.47}$$

Substituting these relations into Eq. (3.41), the equation can be recast as the following eigenproblem

$$A\psi_{\mathrm{in}}^{\mathrm{e}} = \frac{|E|}{\Delta}\exp(\mathrm{i}\chi)\psi_{\mathrm{in}}^{\mathrm{e}}, \tag{3.48}$$

where $A = 0.5 \cdot (R_{\mathrm{A}}S - S^{T}R_{\mathrm{A}})$. The phase χ is of no importance for the ABS energies and can be neglected. Further fixing the basis of modes such that the incoming ones are connected to the outgoing ones by time-reversal symmetry, the Andreev reflection matrix becomes diagonal

$$R_{\mathrm{A}} = \begin{pmatrix} \mathrm{i}\exp(\mathrm{i}\varphi_{\mathrm{L}})\mathbb{1}_{N_{\mathrm{L}}} & 0 \\ 0 & \mathrm{i}\exp(\mathrm{i}\varphi_{\mathrm{R}})\mathbb{1}_{N_{\mathrm{R}}} \end{pmatrix}, \tag{3.49}$$

with φ_i being the phases of the superconducting leads and N_i the number of open channels in these contacts. The eigenenergies of Eq. (3.48) correspond to the ABS energies and can be computed by a singular-value decomposition. This method is also very interesting for multiterminal Josephson junctions, like tri-junctions, which are becoming a topic of big interest in science due to the possibility of finding and generating Majorana fermions [160–162]. The Andreev reflection matrix R_{A} can then

simply be extended with more diagonal entries, which incorporate the additional phases and modes of more contacts. For a more detailed explanation, the reader is referred to Ref. [159].

Andreev bound states from the spectral density

The last method to numerically calculate the ABS spectrum of Josephson junctions is the spectral density method. This approach is very useful for systems, in which interface effects cannot be neglected. We will employ this method later on in the case of magnetic impurities in bilayer graphene Josephson junctions and TI nanowire junctions, which are only partially covered by s-wave superconductors. The drawback of this method is the same as for the diagonalization scheme, namely that the numerical cost is rising very fast with an increasing number of lattice sites.
The ABS spectrum can be extracted from the spectral density [163]

$$d(E) = \frac{1}{2\pi}\mathrm{Tr}[A(E)] = \frac{1}{2\pi}\mathrm{Tr}[\mathrm{i}(G^{\mathrm{r}}(E) - G^{\mathrm{a}}(E))], \tag{3.50}$$

by searching for peaks in the energy range of the superconducting gap $[-\Delta_0; \Delta_0]$. The retarded and advanced Green's functions read thereby as

$$G^{\mathrm{r}}(E) = ((E + \mathrm{i}\eta)\mathbb{1} - H - \Sigma)^{-1}, \tag{3.51}$$

$$G^{\mathrm{a}}(E) = G^{\mathrm{r}}(E)^{\dagger}, \tag{3.52}$$

where η is an infinitesimally small number and the self-energy Σ incorporates the influence of the superconducting leads. The Hamiltonian H is a matrix containing all onsite and hopping elements due to the tight-binding structure of the system.
Analogously, Σ is also a matrix with the same dimension and given by

$$\Sigma = \left(\begin{array}{c|c|c} \Sigma^{\mathrm{L}} & 0 & 0 \\ \hline 0 & 0 & 0 \\ \hline 0 & 0 & \Sigma^{\mathrm{R}} \end{array}\right), \tag{3.53}$$

with Σ^{L} and Σ^{R} being the self-energy matrices of the left and right superconducting leads, respectively. In Kwant, the tight-binding Hamiltonian H, as well as the lead self-energies, can be very easily extracted. Green's function is then calculated through matrix inversion for different phases inside the pairing terms of the superconducting leads.
At this point, a very important detail should be highlighted. The quantities that are computed by Kwant can only be directly plugged into Eq. (3.51) if the tight-binding system consists of a monoatomic lattice with one basis atom. For tight-binding setups with a polyatomic basis, i.e., graphene or bilayer graphene, the computed H needs to be modified in order to match the order of the entries in Σ. The reason for that additional step lies in the fact that the entries of the tight-binding Hamiltonian H are not spatially sorted, but instead according to the sublattice structure. The self-energies

Σ^{L} and Σ^{R} in turn have a pure spatial sorting of their entries.
As an explicit example, let us consider bilayer graphene, which will also be studied in a later chapter. Bilayer graphene has a sublattice structure with four basis atoms A_1, B_1, A_2, and B_2. The Hamiltonian matrix has the structure

$$H = \left(\begin{array}{c|c|c|c} H_{A_1A_1} & H_{A_1B_1} & H_{A_1A_2} & H_{A_1B_2} \\ \hline H_{B_1A_1} & H_{B_1B_1} & H_{B_1A_2} & H_{B_1B_2} \\ \hline H_{A_2A_1} & H_{A_2B_1} & H_{A_2A_2} & H_{A_2B_2} \\ \hline H_{B_2A_1} & H_{B_2B_1} & H_{B_2A_2} & H_{B_2B_2} \end{array}\right). \tag{3.54}$$

For the resorting of these entries we can exploit a functionality that the Kwant developers already incorporated. It allows for a shift of the Hamiltonian entries by providing a list of sorted site indices. Without loss of generality, we assume that our junction is pointing along the x-direction, while the y- and z-directions correspond to the transverse junction directions. The sites are first ordered according to their z-coordinate, then according to their y-coordinate, and finally according to their x-coordinate from smallest to biggest values. An example code to perform that step could look like this:

```
syst = make_system #build your system
syst = syst.finalized()
sites = syst.sites
n = len(sites)
sites = list(sites)
indices = np.linspace(0, n − 1, n)
site_index = np.asarray([x for _, x in sorted(zip(sites, indices),
    key = lambda pair : (round(pair[0].pos[0], 3), round(pair[0].pos[1], 3),
    round(pair[0].pos[2], 3)), reverse = False)])
```

The tight-binding Hamiltonian can then simply be sorted via

```
H = syst.hamiltonian_submatrix(to_sites = site_index, from_sites = site_index)
```

3.6.2. Josephson junctions – supercurrent calculations

The Andreev bound states in Josephson junctions carry a supercurrent from one superconducting lead to another. This current can be measured in experimental setups and

gives useful insight into the physics of specific junctions. Therefore, the calculation of this quantity is shortly recapitulated in this section.

Computing the supercurrent as derivative of the ABS spectrum

The most direct way to get access to the supercurrent in a Josephson junction is by considering the phase dependence of the ABS. If one has calculated the ABS spectra, then the current-phase relation can be computed by [115]

$$I(\Delta\varphi) = -\frac{2e}{\hbar}\sum_n \tanh\left(\frac{E_n(\Delta\varphi)}{2k_\mathrm{B}T}\right)\frac{\partial E_n(\Delta\varphi)}{\partial\Delta\varphi}. \tag{3.55}$$

The sum runs over all N Andreev bound states (with $E_n(\Delta\varphi) \leq 0$) in the junction and also smearing by finite temperature T is included, where k_B denotes the Boltzmann constant. This equation captures contributions from pure in-gap states. Current contributions that stem from processes outside the superconducting gap are not taken into account. It is also required to have knowledge of the ABS spectrum, which can be very complicated for certain physical setups. The next method might therefore be particularly useful in cases in which the ABS spectrum was not computed earlier. It allows us to directly compute the supercurrent in the Josephson junction.

Supercurrent from Green's function

The second method to numerically compute the Josephson current was developed by Furusaki and Tsukada in 1991 [164, 165]. In the context of Kwant, Ostroukh et al. [166, 167] implemented this procedure and provide an instructive *ipython notebook* that explains the basic functionalities of their code (see Supplemental Material of Ref. [166]). We are going to adapt parts of their code, as their implementation is very efficient in terms of numerical computation time. Still, one has to take care of a few details. First of all, it is necessary to adjust for systems with a spinful Hamiltonian such that traces over different orbitals are correctly performed. Second, modifications have to be incorporated if one wants to compute the supercurrent in tight-binding systems with a sublattice structure like graphene or bilayer graphene. For those systems, we modified the code such that it uses actual site positions instead of their tags. In summary, the method itself works as follows. The starting equation for the supercurrent calculation [165, 167] is given by

$$I_\mathrm{LR}(\Delta\varphi) = 2\frac{eK_\mathrm{B}T}{\hbar}\sum_{n=0}^{\infty}\sum_{\substack{i\in\mathrm{R}\\ j\in\mathrm{L}}}\mathrm{Im}\left(\mathrm{Tr}\left(H_{ji}G^\mathrm{r}_{ij}(\mathrm{i}\omega_n)\right) - \mathrm{Tr}\left(H_{ij}G^\mathrm{r}_{ji}(\mathrm{i}\omega_n)\right)\right), \tag{3.56}$$

with $\omega_n = K_\mathrm{B}T/\hbar(2n+1)\pi$ being fermionic Matsubara frequencies. Moreover H_{ji} and G^r_{ij} are the matrix elements of the tight-binding Hamiltonian H and the retarded Green's function G^r, evaluated between the lattice sites $j \in \mathrm{L}$ and $i \in \mathrm{R}$. L and R denote adjacent lattice rows in the normal part which are connected via a hopping along

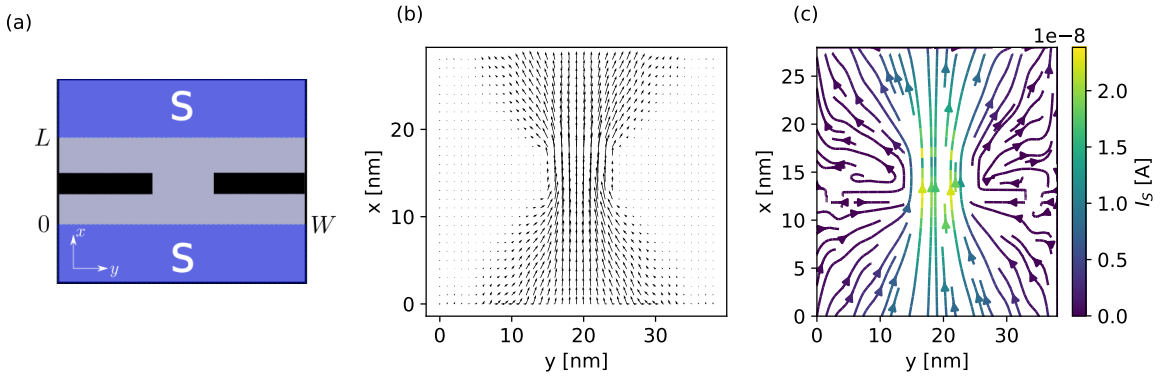

Figure 3.8: (a) Example system for visualization of local supercurrent flow. The Josephson junction consists of a two-dimensional electron gas with two strong barriers at the edges of the normal region. (b) and (c) illustrate the computed local supercurrent distribution with different plotting styles.

the junction direction. A schematic plot is shown in Fig. 5.9 in Sec. 5.3 for the explicit example of a bilayer nanoribbon Josephson junction. The supercurrent is determined by calculating the current flow between the sites in the system cuts L and R, and the following summation over all possible site contributions. Due to current conservation, the exact cut position in the system does not matter, but, for simplicity, in most cases it is chosen to be the center of the junction. In the summation of Matsubara frequencies one has to include enough terms in order to ensure proper convergence of the current. Equation (3.56) can be used to access the current-phase relation.
In experiments, it might not be possible to measure the CPR due to the complexity of device fabrication, but instead rather the critical current in dependence of some system parameter is studied. The critical current is the maximum of the CPR and is given by $I_c = \max_{\Delta\varphi} |I_{LR}(\Delta\varphi)|$. The supercurrent calculation via Green's function can be numerically quite costly for larger systems. However, it allows to include complicated physical effects like interactions between magnetic impurities in the junction and the superconducting leads, as well as interface effect and the influence of external magnetic fields. This will become very useful in the following chapters.

Another import advantage of the Green's function approach is that it can be used to locally resolve the supercurrent flow in the junction. This can be done by not tracing over the sites in the cuts L and R. Instead, the local current flow is stored and the calculation is repeated for each lattice column along the junction and each lattice row in the transverse lattice direction. A simple example is shown in Fig. 3.8 (a). There, we calculate the local current flow in a Josephson junction that is described by a simple 2D Schrödinger Hamiltonian as given by Eq. (3.11), which is written in the Bogoliubov-de Gennes form to include superconducting pairing. In order to give the current flow a few interesting signatures we consider two symmetric barriers at the edges of the system. These could be experimentally introduced through gates placed close to the junction. The system width is fixed to $W = 39$ nm, the length to $L = 29$ nm and the lattice

constant to $a = 1$ nm. For the tight-binding parameters we put the free electron mass into $t = \hbar^2/(2ma^2)$, set the superconducting pairing term to $\Delta = 0.05t$ and the chemical potential to $\mu = 0.02$ eV. Finally, we put strong onsite barriers at the centers of the edges with strength $V = 10t$, which will completely suppress the current flow in those regions. Employing Eq. (3.56) without tracing out the lattice dimensions, the local supercurrent distribution in the junction is calculated and plotted in Figs. 3.8 (b) and (c) with different plotting styles. It is immediately observable that the supercurrent is constrained to the center of the junction due to the highly gated regions at the edges.

3.7. Spin-relaxation rates from the S-matrix

The computation of spin-relaxation rates Γ in the case of local impurities is typically done by evaluating Eq. (2.61), which takes the T-matrix $\mathbb{T}$ into account. In order to calculate Γ numerically, it is useful to recall that the T-matrix is closely related to the scattering matrix S by [111]

$$S_{ij}(E) = \delta_{ij} - 2\pi \mathrm{i} T_{ij}(E), \tag{3.57}$$

where i and j label incoming and outgoing states, respectively. This quantity can be easily computed with the Kwant tool. Therefore, in the following, the numerical techniques for spin-relaxation calculations in the normal as well as in the superconducting case are introduced. Note that, despite the fact that we will discuss the details of the computation on the example of impurities on single-layer graphene below, the introduced methodology is general and applicable to any other system in the same way.

3.7.1. Normal-conducting state

Spin relaxation in single-layer graphene and bilayer graphene has already been extensively studied in the normal-conducting case [68, 84, 85, 135, 168–170], both experimentally and theoretically. Still, and in order to check the developed methodology in the superconducting case and to benchmark our implementation, the established Landauer formalism for spin-relaxation calculations in normal-conducting single-layer graphene will be shortly recapitulated. The results that will be obtained in the superconducting case in the next section should then converge to these normal-state results when sending the superconducting pairing Δ to zero. For this purpose, one can follow the method explained in Ref. [84], which will also serve as a basis for the superconducting case. Assume that we consider a graphene sample with a width W and a length L hosting a single impurity chemisorbed on top of a carbon atom, which allows for spin scattering. The different spin orbitals can either be coupled by local spin-orbit coupling or magnetic exchange interactions, which are given by Eq. (2.22) and Eq. (2.18), respectively. The spin-relaxation rate in the normal state can then be calculated from

$$\Gamma_n(\mu) = \tau_n(\mu)^{-1} = \frac{4t}{\hbar}\eta\frac{W}{a}\sum_{\sigma=\pm1}\sum_{i,j}(|t_{i\sigma,j-\sigma}|^2 + |r_{i\sigma,j-\sigma}|^2), \tag{3.58}$$

where $t_{i\sigma,j-\sigma}$ and $r_{i\sigma,j-\sigma}$ are the S-matrix elements for transmission and reflection of a spin-up into a spin-down state and vice-versa. The indices i and j label incoming and outgoing modes, while σ denotes the spin. In order to check our implemented tight-binding model, we initially reproduced the results of Ref. [84], where the spin-relaxation rate for an in-plane spin configuration was studied. These results and the details of the calculation are discussed in App. A.

Next, an important detail of the numerical calculation should be highlighted. By employing Eqs. (2.61) (for $\Delta = 0$) and (3.58), the same physical quantity should be

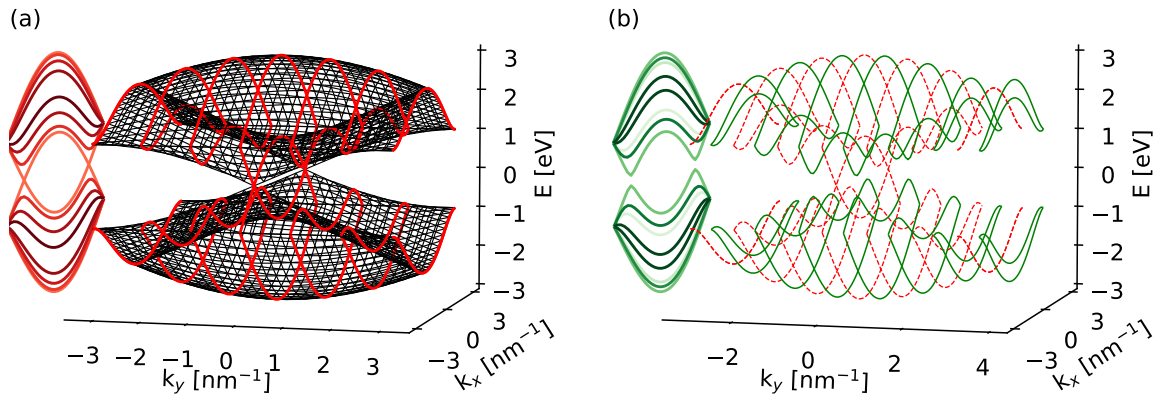

Figure 3.9: (a) Bandstructure of graphene plotted with black lines in the first Brillouin zone. The finite system width induces quantization of the transverse momenta k_y, those bands are shown with red contour lines. Additionally, the quantized bands are projected onto a vertical plane for better visibility. (b) Different transverse momenta k_y can be addressed by the introduced phase ϕ. The quantization condition changes such that the green bands are addressed for a certain value of ϕ. The red dashed lines correspond to the original $\phi = 0$ bands. Adapted from Supplemental Material of Ref. [2].

computed. Having a detailed look at Eq. (2.61), it becomes clear that the formula contains an integration over a continuous Fermi contour in the Brillouin zone. Therefore, the evaluation of Eq. (3.58) needs an additional numerical step to include the effects of a 2D Fermi contour instead of quantized subbands. The procedure is analogously implemented as already discussed in Sec. 3.4, where we introduced periodic boundary conditions that contain a phase $\phi \in [0; 2\pi]$. However, differently to above, we do here not integrate over the phase ϕ. Instead, we use a quantity that is associated with a single electron state, namely its relaxation time $\tau = 1/\Gamma$. The spin-relaxation rate is thereby taken as an averaged quantity over equally-spaced values of $\phi \in [0; 2\pi]$. This procedure is visualized in Fig. 3.9 for the special case of single-layer graphene.

In Fig. 3.9 (a), the 3D bandstructure of graphene is shown in black inside the first Brillouin zone. Due to the finite width of the numerical system, the transverse momentum k_y is quantized as discussed in Sec. 3.4. The quantized momenta are shown as red contour lines in Fig. 3.9 (a) and the bands are additionally projected onto a vertical plane. The linearly dispersing bands located at the K-points are obtained for each width W of the scattering region because we are using zigzag edges. Fixing a non-zero value for ϕ, those linearly dispersing branches are no longer present. The phase essentially changes the quantization condition such that the band cuts are shifted by dk_y. This is

illustrated in Fig. 3.9 (b) by green contour lines and the initially quantized bands are plotted as red dashed lines. Projecting the green contours again onto a plane highlights the opening of a band gap between the graphene conduction and valence bands. The shown bands correspond to different discrete k_y-values of the continuous Fermi contour at the Fermi energy. The numerical computation of the spin-relaxation rate is then performed by averaging over the number of considered phases ϕ and the relaxation rate needs to be normalized to the number of open modes N, which are involved in the spin scattering, for each phase.

The last problem that remains in the numerical simulation is the computation of the scattering matrix elements in Eq. (3.58) for different spins. This is discussed in detail in the next section for scattering of quasiparticles in superconducting systems. In case of normal-conducting electrons the general idea remains the same with a reduced number of orbitals.

3.7.2. Superconducting state

In the above considerations, the necessary ingredients for the numerical calculation of the spin-relaxation rates were introduced, without paying attention to superconductivity. The methodology explained up to now is, nevertheless, general and applicable to both normal-conducting and superconducting systems. Computing spin relaxation in the superconducting state is a bit more intricate than in the normal state. In the center of the calculation of the spin-relaxation rate $\Gamma_s(\mu)$ from the scattering matrix S stands the formula

$$\Gamma_s(\mu) = \tau_s(\mu)^{-1} = \frac{\frac{a}{L}}{\hbar} \frac{\int_{\Delta}^{\infty} \mathrm{d}E \, \left(-\frac{\partial f}{\partial E}\right) \sum_{i,o,\sigma} \left|S^{o,i}_{-\sigma,\sigma}(E,\mu)\right|^2}{\int_{\Delta}^{\infty} \mathrm{d}E \, \left(-\frac{\partial f}{\partial E}\right) \sum_{(i,\sigma)} \langle \Psi_{i,\sigma} | \Psi_{i,\sigma} \rangle} \tag{3.59}$$

$$= \frac{\eta \frac{4W}{\sqrt{3}a}}{\hbar} \frac{\int_{\Delta}^{\infty} \mathrm{d}E \, \left(-\frac{\partial f}{\partial E}\right) \sum_{i,o,\sigma} \left|S^{o,i}_{-\sigma,\sigma}(E,\mu)\right|^2}{\int_{\Delta}^{\infty} \mathrm{d}E \, \left(-\frac{\partial f}{\partial E}\right) \sum_{(i,\sigma)} \langle \Psi_{i,\sigma} | \Psi_{i,\sigma} \rangle}, \tag{3.60}$$

where $\eta = \sqrt{3}a^2/(4WL)$ is again the impurity concentration in graphene and the Fermi-Dirac distribution function is given by $f = [\exp(E/(k_\mathrm{B}T)) + 1]^{-1}$. The reader is referred to the Supplemental Material of Ref. [2], where the exact and detailed derivation of Eq. (3.60) can be found.
Comparing Eqs. (3.58) and (3.60) suggests that the superconducting calculation involves additional computational steps due to the thermal smearing. Instead of just computing the scattering matrix for a chemical potential like in the normal state, one now has to perform an integration over energy for each chemical potential value. This significantly increases the numerical cost and computation time. To keep again a balance of accuracy and computational cost, we perform the integration via a simple

Riemann summation from Δ until a cut-off of $\Delta + 25k_{\mathrm{B}}T$. Additionally, we split the integration range into two parts for a high resolution close the the band edge at Δ. The first interval covers Δ to $\Delta + 3.5k_{\mathrm{B}}T$ with 15 integration steps, while the second one consists of 25 integration steps until $\Delta + 25k_{\mathrm{B}}T$ is reached. This integration procedure will be used throughout the whole thesis for all spin-relaxation rate calculations.

Moreover, the evaluation of Eq. (3.60) incorporates the normalization to the thermally averaged DOS. Therefore, also the incoming modes need to be computed for each energy, which is again an additional effort in the case of superconducting systems. Nevertheless, Eq. (3.59) offers a general way to compute $\Gamma_s(\mu)$ from the scattering matrix and at different temperatures. Also, the employed tight-binding method allows us to easily include a variety of spatially dependent effects and to simulate, for example, the influence of magnetic and electric fields.

What still remains is to introduce the numerical concept of calculating the spin scattering matrix elements of superconducting quasiparticles. Note that Kwant offers the possibility to define a so-called conservation law when constructing the leads. This will separate the scattering matrix S according to the provided conservation law, for example, into different blocks that correspond to scattering between particle and hole orbitals through Andreev reflection. In order to develop a more general implementation scheme, which can also be used independently of Kwant, a different approach will be discussed in detail in the following.

Let us assume that we wish to study spin relaxation in superconducting graphene with a chemisorbed single impurity (i.e., hydrogen or fluorine) on top of a carbon site. The system can be described in a standard manner with the BdG Hamiltonian

$$\begin{aligned} H_{\mathrm{BdG}} &= \begin{pmatrix} H & \mathrm{i}\sigma_y\Delta \\ -\mathrm{i}\sigma_y\Delta & -H^* \end{pmatrix} \\ &= \begin{pmatrix} H_{\mathrm{G}} + V^{(0)} + V_{\mathrm{s}}^{(i)} & \mathrm{i}\sigma_y\Delta \\ -\mathrm{i}\sigma_y\Delta^* & -\left[H_{\mathrm{G}} + V^{(0)} + V_{\mathrm{s}}^{(i)}\right]^* \end{pmatrix}. \end{aligned} \tag{3.61}$$

The term H_{G} denotes the normal-state graphene Hamiltonian of Eq. (2.14), while $V^{(0)}$ and $V_{\mathrm{s}}^{(i)}$ describe the impurity as given by Eq. (2.16). The impurity is first assumed to introduce local spin-orbit coupling in its close vicinity, such that we need to consider $V_{\mathrm{s}}^{(2)}$ [Eq. (2.22)]. The BdG Hamiltonian can then be explicitly written as

$$H_{\mathrm{BdG}} = \left(\begin{array}{cc|cc} A & SO_{\uparrow\downarrow}^{\mathrm{ee}} & 0 & \Delta \\ SO_{\downarrow\uparrow}^{\mathrm{ee}} & B & -\Delta & 0 \\ \hline 0 & -\Delta^* & -A^* & -(SO_{\uparrow\downarrow}^{\mathrm{ee}})^* \\ \Delta^* & 0 & -(SO_{\downarrow\uparrow}^{\mathrm{ee}})^* & -B^* \end{array}\right), \tag{3.62}$$

where the wave functions are given in the Nambu basis

$$\Psi = \left(\Psi_{\uparrow}^{\mathrm{e}},\ \Psi_{\downarrow}^{\mathrm{e}},\ \Psi_{\uparrow}^{\mathrm{h}},\ \Psi_{\downarrow}^{\mathrm{h}}\right)^{\top}. \tag{3.63}$$

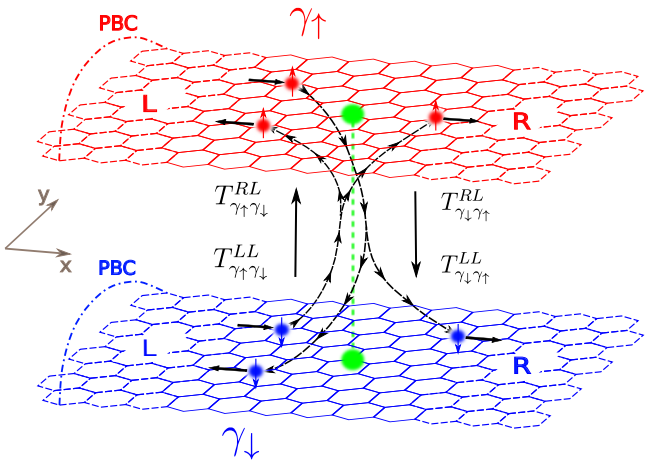

Figure 3.10: Schematic visualization of the numerical implementation of H'_{BdG} [Eq. (3.65)]. The two diagonal blocks of the Hamiltonian are put on two different computational grids, which are shown for $\gamma_\uparrow$ in red and $\gamma_\downarrow$ in blue. The impurity (shown in green) couples them by the induced local spin-orbit coupling terms. The scattering matrix elements are taken from the S-matrix that is calculated with Kwant. The relevant transport events are shown with vectorized lines. They correspond to transmission probabilities between the attached four leads. Moreover, the PBCs which are necessary for the phase averaging over ϕ are shown with dashed lines connecting the edges of the system. Adapted from Supplemental Material of Ref. [2].

Note that the terms A and B are short-hand notations for all terms that act between the same spin kinds. Contrary to that, the terms $SO^{\mathrm{ee}}_{\uparrow\downarrow}$ and $SO^{\mathrm{ee}}_{\downarrow\uparrow}$ incorporate all electron spin-orbit terms that couple different spins.

This representation is still not adequate to separate the quasiparticle spin degrees of freedom. The Bogoliubov quasiparticles are given by electron and hole orbitals that are coupled by the superconducting pairing term Δ. A much more convenient form can be obtained employing a simple unitary transformation, which is given by

$$U = \begin{pmatrix} 1 & 0 & 0 & 0 \\ 0 & 0 & 0 & 1 \\ 0 & 0 & 1 & 0 \\ 0 & 1 & 0 & 0 \end{pmatrix}. \tag{3.64}$$

The Hamiltonian H_{BdG} is then transformed according to

$$H'_{\mathrm{BdG}} = U^{-1} H_{\mathrm{BdG}} U = \left(\begin{array}{cc|cc} A & \Delta & 0 & SO^{\mathrm{ee}}_{\uparrow\downarrow} \\ \Delta^* & -B^* & -(SO^{\mathrm{ee}}_{\downarrow\uparrow})^* & 0 \\ \hline 0 & -(SO^{\mathrm{ee}}_{\uparrow\downarrow})^* & -A^* & -\Delta^* \\ SO^{\mathrm{ee}}_{\downarrow\uparrow} & 0 & -\Delta & B \end{array}\right). \tag{3.65}$$

Additionally, the wave function is now given in the transformed Nambu basis

$$\Psi' = U\Psi = \left(\Psi^{\mathrm{e}}_{\uparrow},\ \Psi^{\mathrm{h}}_{\downarrow},\ \Psi^{\mathrm{h}}_{\uparrow},\ \Psi^{\mathrm{e}}_{\downarrow}\right)^{\top}, \tag{3.66}$$

where we explicitly define the quasiparticle basis $(\gamma_\uparrow, \gamma_\downarrow)^\top$ with

$$\gamma_\uparrow = \left(\Psi^{\mathrm{e}}_{\uparrow},\ \Psi^{\mathrm{h}}_{\downarrow}\right)^{\top} \quad \text{and} \quad \gamma_\downarrow = \left(\Psi^{\mathrm{h}}_{\uparrow},\ \Psi^{\mathrm{e}}_{\downarrow}\right)^{\top}. \tag{3.67}$$

The above transformation effectively separates the BdG Hamiltonian in two blocks. The first block in the upper left part describes quasiparticles with spin up, while the lower right block incorporates quasiparticles with spin down. The off-diagonal blocks, introduced by spin-orbit coupling, couple those two spin components.

Recognizing this special structure of the Hamiltonian offers the possibility for an efficient implementation scheme, which allows for an easy way to extract the spin scattering matrix elements. The general idea is shown in Fig. 3.10. In the numerical implementation two computational graphene lattice structures are generated. On each of the two grids, one of the two quasiparticle blocks of H'_{BdG} is put. The red lattice corresponds then two $\gamma_\uparrow$ wave functions, while the blue lattice carries $\gamma_\downarrow$ quasiparticles. Summing up both grids gives the physical graphene lattice with its full orbital degrees of freedom. The impurity on top of the graphene structure marks a special location in the system, which contains components present on both computational grids and additionally induces local spin-orbit coupling in its close vicinity according to Eq. (2.22). These terms are responsible for a coupling of the two computational lattices and therefore induce local spin scattering of the superconducting quasiparticles. In Fig. 3.10, these scattering events are visualized with black curves connecting the two grids. For the numerical simulation, in total four leads are attached to the system, i.e., two left (L) and two right (R) leads for $\gamma_\uparrow$ and $\gamma_\downarrow$ modes. All the necessary scattering processes in Eq. (3.60) are given by transmission probabilities between those four leads with different spin species. They are denoted as $T^{RL}_{\gamma_\uparrow\gamma_\downarrow}$, $T^{RL}_{\gamma_\downarrow\gamma_\uparrow}$, $T^{LR}_{\gamma_\uparrow\gamma_\downarrow}$, $T^{LR}_{\gamma_\downarrow\gamma_\uparrow}$, $T^{LL}_{\gamma_\uparrow\gamma_\downarrow}$, $T^{LL}_{\gamma_\downarrow\gamma_\uparrow}$, $T^{RR}_{\gamma_\uparrow\gamma_\downarrow}$, and $T^{RR}_{\gamma_\downarrow\gamma_\uparrow}$ in Fig. 3.10. These quantities can simply be obtained by computing the scattering matrix with Kwant.
Also, in Fig. 3.10, the above discussed PBCs are visualized on both lattices. They are introduced by a hopping from the system edges starting at $y = W$ to $y = 0$. Throughout this thesis, the graphene system is defined with zigzag edges to simplify the implementation of the PBC. The explicit form of the hopping is then given by

$$\begin{aligned}\mathrm{hop}^{\phi\text{-PBC}} = {} & \gamma^\dagger_{\uparrow,(x,W)} \begin{pmatrix} -t\mathrm{e}^{-\mathrm{i}\phi} & 0 \\ 0 & t\mathrm{e}^{-\mathrm{i}\phi} \end{pmatrix} \gamma_{\uparrow,(x,0)} \\ & + \gamma^\dagger_{\downarrow,(x,W)} \begin{pmatrix} t\mathrm{e}^{-\mathrm{i}\phi} & 0 \\ 0 & -t\mathrm{e}^{-\mathrm{i}\phi} \end{pmatrix} \gamma_{\downarrow,(x,0)} + \mathrm{h.c.},\end{aligned} \tag{3.68}$$

where now also the phase ϕ enters, which is necessary to address different values of k_y. Finally, a short summary of the different calculations steps follows below.

Summary of calculation steps

- Construct the superconducting system with two computational grids, one for each quasiparticle spin.
- Introduce PBC with the phase factor $\exp(\mathrm{i}\phi)$.
- Compute all spin scattering matrix elements [nominator in Eq. (3.60)] for energies in $[\Delta, \Delta + 25k_\mathrm{B}T]$, normalize the transmission probabilities by the number of propagating modes.
- Compute the DOS [denominator in Eq. (3.60)] for the same energies.
- Repeat this step for a number of different $\phi \in [0; 2\pi]$ and average over that number.
- Finally, integrate the nominator and denominator of Eq. (3.60) over the energy and compute the spin relaxation rate for a certain impurity concentration η.

Analogously, one can treat magnetic impurities that induce magnetic exchange interactions. The difference then only lies in the definition of Eq. (3.65), where instead of spin-orbit coupling terms, the magnetic exchange energies are included.

4. Quantum transport in normal and superconducting topological insulator systems

In this chapter, we examine quantum transport phenomena in topological insulator systems like slabs and nanowire geometries in the, first, normal conducting and, second, superconducting states. We start by studying the LDOS of topological states in presence of rough surface structures on TI slabs. Next, the bandstructure of Dirac states on inner and outer surfaces of core-shell nanowires is calculated and the interplay in conductance simulations between the two components is further elaborated employing an effective model. Moreover, the effect of an external magnetic field with an arbitrary angle to the nanowire axis on the surface spectrum is discussed. These findings are important for understanding properties of the full 3D model spectrum, which will be employed in the first section that covers superconducting effects, where crossed Andreev reflection is examined in detail in a TI nanowire T-junction. But, before making this crossover to superconducting hybrid systems, we consider a normal conducting TI nanowire with a broken rotational symmetry and a non-uniform cross-section area. Transport simulations show that resonant Dirac states emerge due to a magnetic and geometric confinement, which could be exploited to study the surface state spectrum experimentally. Finally, after considering CAR, we study Andreev bound states and the corresponding supercurrent in fully, as well as partially, proximitized TI nanowire Josephson junctions.

4.1. Scattering of surface states on surface steps

Realistic material samples, which are used in experiments, are never perfectly homogeneous. For the case of topological insulators it is known that the sample surfaces can develop rough landscapes. In atomic force microscopy measurements on Bi_2Te_3 samples, for example, the surfaces exhibit clear surface islands which consist of different quintuple layer thicknesses [171, 172]. As topological states are localized at the material surfaces, it is obviously of interest to answer the question whether these surface steps affect them or not. Theoretical studies have shown that step edges on the TI surface can influence the local density of states due to a difference in Dirac point energies on the step surfaces [173, 174] and also scattering on such steps has been studied [175]. Moreover, experimentalists have used triangular surface structures to trap Dirac fermions in quantum corals [176], thereby giving insight into the possible tuning

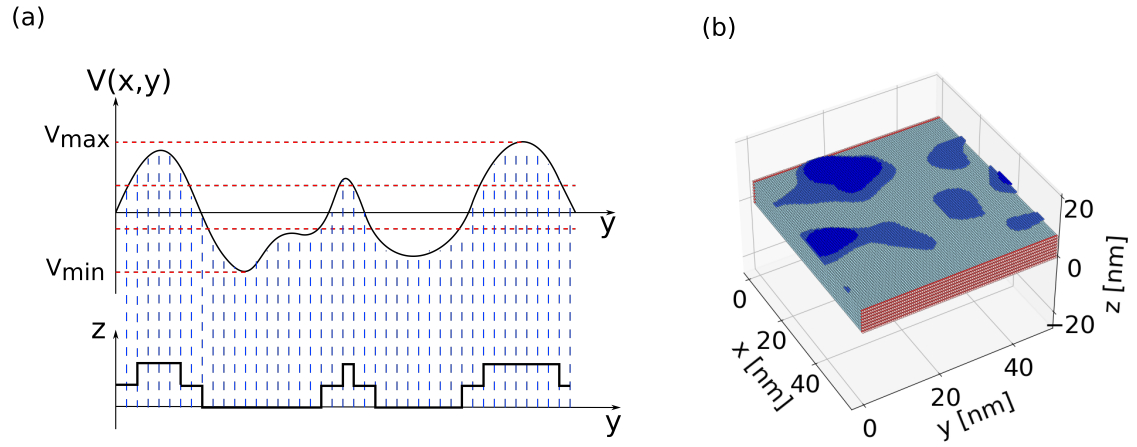

Figure 4.1: (a) Schematic plot of the surface profile generation. Gaussian correlated disorder is translated into surface islands. (b) Plot of an example system with surface islands. The corresponding LDOS is visualized in Fig. 4.2 (b).

of surface state properties.
In this section we want to numerically study the scattering behavior of topological states on randomly generated, but spatially correlated, surface islands. We will calculate the local density of states in the top layers and check how such structures influence the involved scattering states. These obtained results can serve for comparison with possible future experiments to find signatures of topological surface states. Note that further studies on scattering of topological states on surface structures can be found in the Bachelor thesis of Philipp Wutz [177].

4.1.1. Modeling of surface structures

As the samples in experiments are of micron size we expect that the top and bottom surface of the topological insulator will be more or less decoupled if the thickness is large compared to the surface state penetration depth. In order to get such a system with two decoupled Dirac cones on both surfaces, we are implementing the Hamiltonian of Eq. (2.1) with periodic boundary conditions along the transverse direction of the scattering region. This is simply done by adding a hopping that connects the two sides of the scattering region for all points along the z-direction. Additionally we will compute the LDOS of scattering states by attaching two leads to the longitudinal direction of the scattering region with the same boundary conditions.
Next, we need to introduce the desired surface islands. Here the method for generating a random set of spatially correlated disorder that was introduced in Chap. 3.5 can be employed. A schematic plot is shown in Fig. 4.1 (a). First one can generate a 2D disorder landscape of Gaussian correlated disorder that spans the same area as the scattering region. The disorder profile is then split into different intervals. This is done by searching for the maximum V_{max} and the minimum value V_{min}, where the range in

between defines our complete interval. If we want to get steps between three quintuple layers, we split it then into three equally spaced intervals [shown as red dashed lines in Fig. 4.1 (a)]. At each lattice point in the top surface of the scattering region, the potential value $V(x, y)$ determines how many lattice points will be removed. More precisely two (one) lattice points will be removed from the top surface, if $V(x, y)$ lies in the lowest (middle) interval. If $V(x, y)$ is located in the highest interval, no lattice point will be removed. By following this procedure a correlated island structure is generated at the top surface.

4.1.2. Local density of states at surface structures

The next step is to compute the LDOS of the scattering states in the scattering region. We employ Eq. (3.27) and integrate over the phase ϕ in the PBC. Initially the width, height and length of the setup are respectively set to $W = 50$ nm, $H = 7$ nm and $L = 60$ nm. Moreover, surface islands are generated according to the above method with two additional lattice layers inside the scattering region, such that the maximal height is 9 nm. The final system is shown in Fig. 4.1 (b). Note that in order to achieve a high resolution of the LDOS in the x-y plane, the lattice constants in those spatial directions are set to $a = 0.5$ nm, while it is set to $a_z = 1$ nm in the z-direction. In Fig. 4.2 (a) the corresponding bandstructure is plotted. Instead of a gapped spectrum due to the Berry phase in the case of TI nanowires, a linearly dispersing Dirac cone is observed. Actually the Dirac cone is two times degenerate, one originates from the top surface while the second one stems from the bottom surface. For the LDOS calculations we are just interested to see the scattering behavior at the top surface. Therefore, and for simplicity of visualization, the LDOS is summed in z-direction over the four top most lattice layers and plotted as a simple 2D plot. For the Fermi energy of $E_\mathrm{F} = 120$ meV [shown as green dashed line in Fig. 4.2 (a)] the calculated LDOS is shown in Fig. 4.2 (b). The phase integration was performed over 60 equally spaced integration steps. Note that the surface island structure of Fig. 4.1 (b) is certainly reproduced by the LDOS. The contours of each step layer are exhibiting a pronounced change in the LDOS magnitude. Particularly at the edges of layer steps an increased LDOS amplitude is observable. Contrary, at the regions directly before the steps, a decreased magnitude is present.

In order to exclude that these features depend on the explicit surface structure of small islands on top of a flat TI surface, we next consider a different geometry. Now the height of the flat TI leads is set to $H = 9$ nm, while the surface disorder is generated as "craters", where up to two lattice layers are removed. The explicit structure is plotted in Fig. 4.2 (c). Dark blue lattice points correspond again to the upper most layer, which is at the same height as the lead top surface. For a direct comparison, the corresponding LDOS for the same Fermi energy of $E_\mathrm{F} = 120$ meV is visualized in Fig. 4.2 (d). There it is even more clearly observable that the highest LDOS is located right at step edges, while shortly before those the magnitude drops considerably. Therefore, we can conclude that these signatures are a general property of surface modes for the employed

Bi_2Se_3 parameters.

To check if these signatures are also present for other TI compounds would require further calculations for other parameter sets. These computations are not in the scope of in this work, but would certainly be interesting for future considerations. By more detailed studies of these transport properties one could perhaps shine light on possibly observable signatures in real experiments. Particularly with scanning tunneling microscopy [178, 179] or near-field mid-infrared microscopy measurements [180] the local density of states can be probed with a high resolution across real surface structures. Comparing between such experiments and the numerical findings could hint at the presence of surface transport of TI samples.

4.2. Core-shell nanowires

Topological insulator nanowires grown from a seed material will form so-called core-shell structures [59, 181], where possible components can be, for example, a HgTe shell which surrounds a CdTe core. In experimental physics at the University of Regensburg the aim is to use BSTS-based TI shells on hexagonal GaAs cores in a variety of different experiments [182], see Fig. 4.3 (a) for a schematic plot. Such systems are also produced in context of semiconductor nanowires and they already attracted a lot of interest as they might be a platform for generating Majorana fermions [183]. A significant feature of such structures is that they do not only have one surface which is an interface to the trivial vacuum or air around it, but they also have an inner interface with the seed material that might offer an additional surface where protected helical states can emerge. Therefore, in contrast to nanowires introduced in Sec. 2.1.2 which have only a single quantized Dirac cone on their surface, the core-shell systems could exhibit very different Aharonov-Bohm interference signatures in transport experiments. Also, in combination with additional superconducting or ferromagnetic shells these platforms could show significantly different physical properties than the usual TI nanowires. In the following we are going to check with the full 3D BHZ model which kind of states appear if we put a whole in the center of a nanowire and how they react to an external axial magnetic field. These findings are then used as a basis to develop a simple effective 2D model that can be used for larger systems and to perform transport simulations in such setups. Further studies on TI core-shell nanowires with the employed models can be found in the Bachelor thesis of Alexander Setescak [184].

4.2.1. Bandstructure and local density of states – 3D model

Initially, the bandstructure of a core-shell nanowire will be studied. An exemplary tight-binding system is illustrated in Fig. 4.3 (b). For simplicity we assume the center of the nanowire to be filled with vacuum. We use the Hamiltonian given by Eq. (2.1) and construct an infinite lead with the simple model parameters shown in Tab. 2.1b. The outer width and height of the nanowire are fixed to $w_{\text{out}} = h_{\text{out}} = 40$ nm, while the

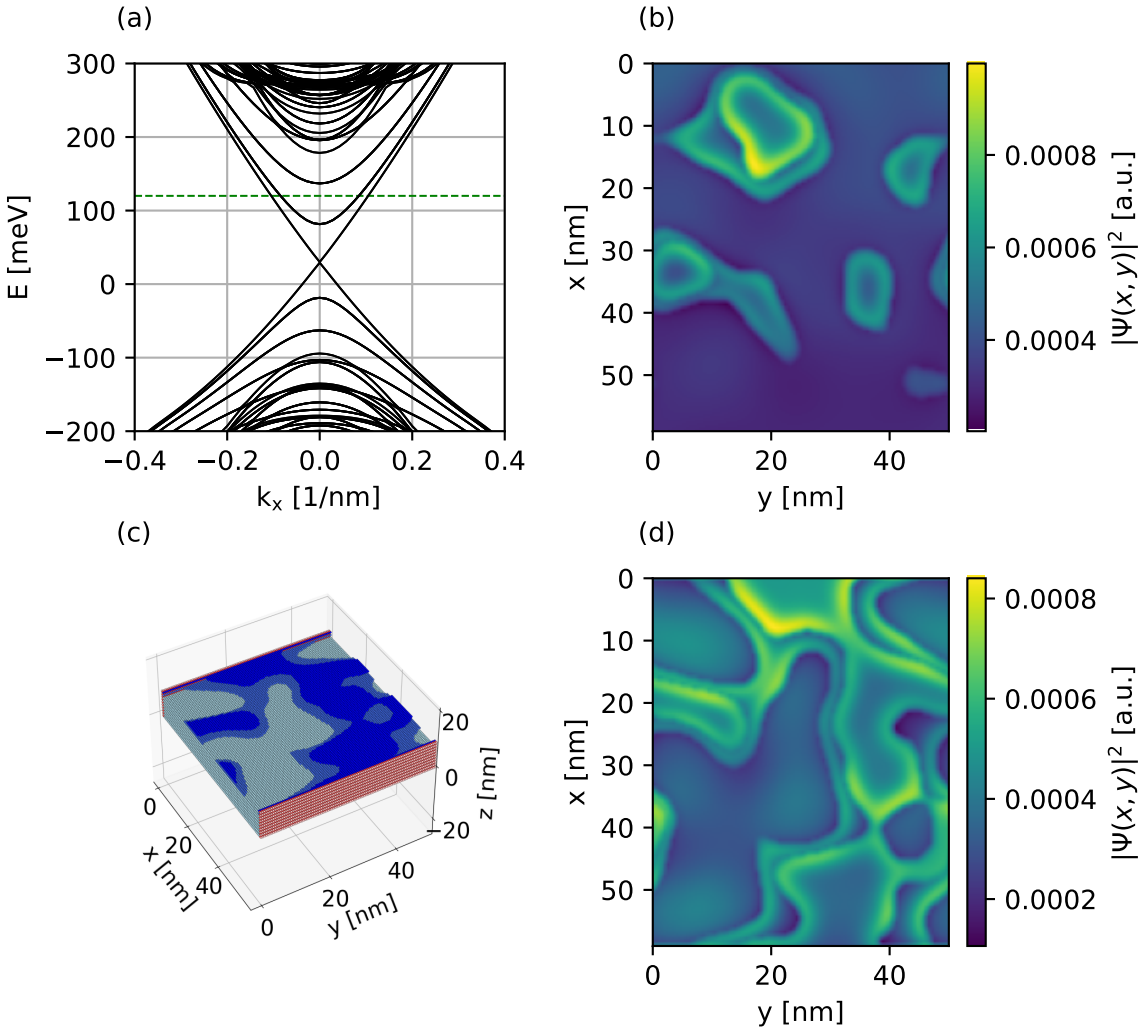

Figure 4.2: (a) Bandstructure of a TI lead with width $W = 50$ nm and height $H = 7$ nm and periodic boundary conditions along the transverse direction. The lattice constants along the x- and y-directions are set to $a = 0.5$ nm, while along z it is fixed to $a_z = 1$ nm. Due to the decoupling of top and bottom surface two degenerate Dirac cones are present on each of these surfaces. The green dashed line marks the Fermi energy $E_F = 120$ meV. (b) Local density of states summed over the 4 top most layers. The structure corresponds to the system shown in Fig. 4.1 (b). Panel (c) shows another surface disorder configuration with craters instead of islands, while in panel (d) the related LDOS is again visualized. Both calculated local density of states exhibit in front of surface steps a decrease, while at step edges it is enhanced.

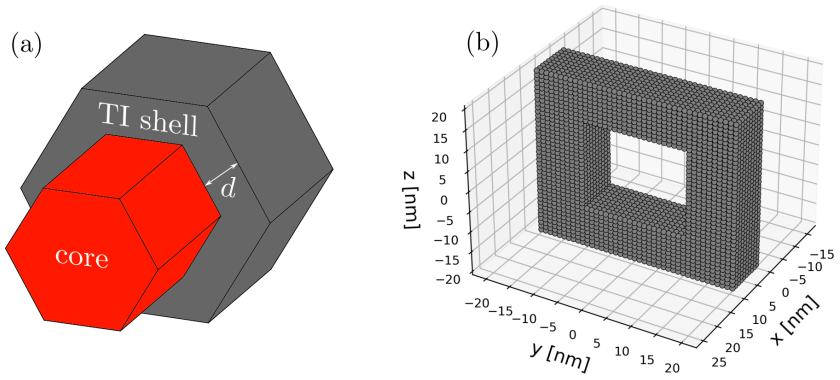

Figure 4.3: (a) Schematic plot of a hexagonal core-shell TI nanowire. The topological insulator encloses an insulating core material such that the TI has two surfaces where Dirac states can emerge. (b) Plot of the 3D tight-binding system. For simplicity vacuum is assumed as the core material.

inner width and height of the hole are chosen to be $w_{\text{in}} = h_{\text{in}} = 20$ nm. Considering a penetration depth of the outer surface states of $\lambda = 1$ nm the ratio between the flux penetrating the outer shell and the flux threading through the inner hole is roughly $\Phi_{\text{out}}/\Phi_{\text{in}} = (w_{\text{out}} - \lambda) \cdot (h_{\text{out}} - \lambda)/(w_{\text{in}} \cdot h_{\text{in}}) \approx 3.14$. The thickness of the shell is then 9 nm, such that hybridization effects of the states at the two surfaces are negligible.
Fig. 4.4 shows the computed bandstructure for the case of no applied axial magnetic field. In order to study the bandstructure of such a system it is very useful to plot the probability densities of the eigenmodes. More precisely we want to check, whether the modes are localized at a specific surface or if they are present at both surfaces. Therefore, Fig. 4.4 shows also the local density of states (LDOS) for the numbered modes at the Fermi energy E_{F}, which is visualized in green. According to the surface at which the corresponding modes are localized, the bands are then colorized in blue (red) if the wave function has a high LDOS at the inner (outer) surface. All of the bands are twice degenerate, but for convenience the LDOS of only one of those modes is visualized. Performing this analysis, it becomes clear that certain subbands should stem from a quantized Dirac cone located at the outer surface, while others originate from quantization of a Dirac cone localized at the inner surface.
In order to check this idea, it is reasonable to tune the axial magnetic field to certain values, such that either the flux through the inner hole Φ_{in} or the flux through the whole cross-section Φ_{out} is almost equal to half of a magnetic flux quantum $\Phi_m = h/e$. In Fig. 4.5 the case of $\Phi_{\text{out}} \approx \Phi_m/2$ is illustrated, corresponding to a magnetic field of $B_{\parallel} = 1.363$ T. Employing the same analysis as before, it is observable that the flux induces a closing of the outer surface Dirac cone, with an appearing linear dispersion and two times degenerate higher subbands. For the number 3 and 5 modes we get again degenerate bands. The bands stemming form the inner surface are single degenerate, which is due to a flux ratio of $\eta_{\text{in}} = \Phi_{\text{in}}/\Phi_m = 0.1593$.
As a last check a magnetic field of $B_{\parallel} = 4.3$ T is applied to the wire. This gives then

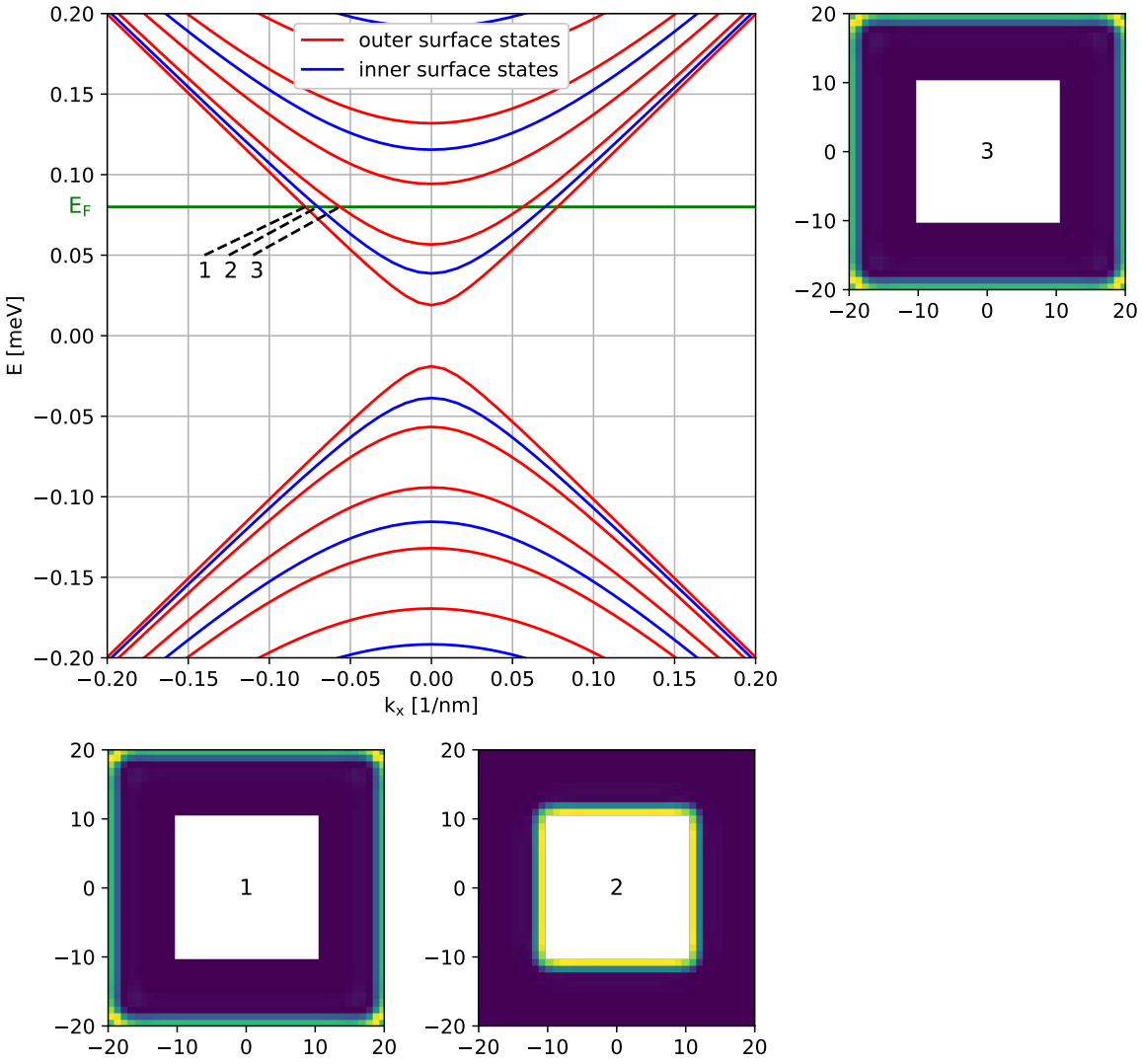

Figure 4.4: Bandstructure of a hollow TI shell with width $w_{\text{out}} = 40$ nm and height $h_{\text{out}} = 40$ nm, and local density of states displayed in the wire cross-sections. The hole in the center of the wire has the dimensions $w_{\text{in}} = h_{\text{in}} = 20$ nm. No axial magnetic field is applied parallel to the wire axis. The subbands are colored in blue (red) if the wave function is localized at the inner (outer) nanowire surface. The Fermi energy E_{F} is shown in green and the LDOS plots belong to the numbered modes in the bandstructure. Yellow in the LDOS plots corresponds to a high, while dark blue to a low density value.

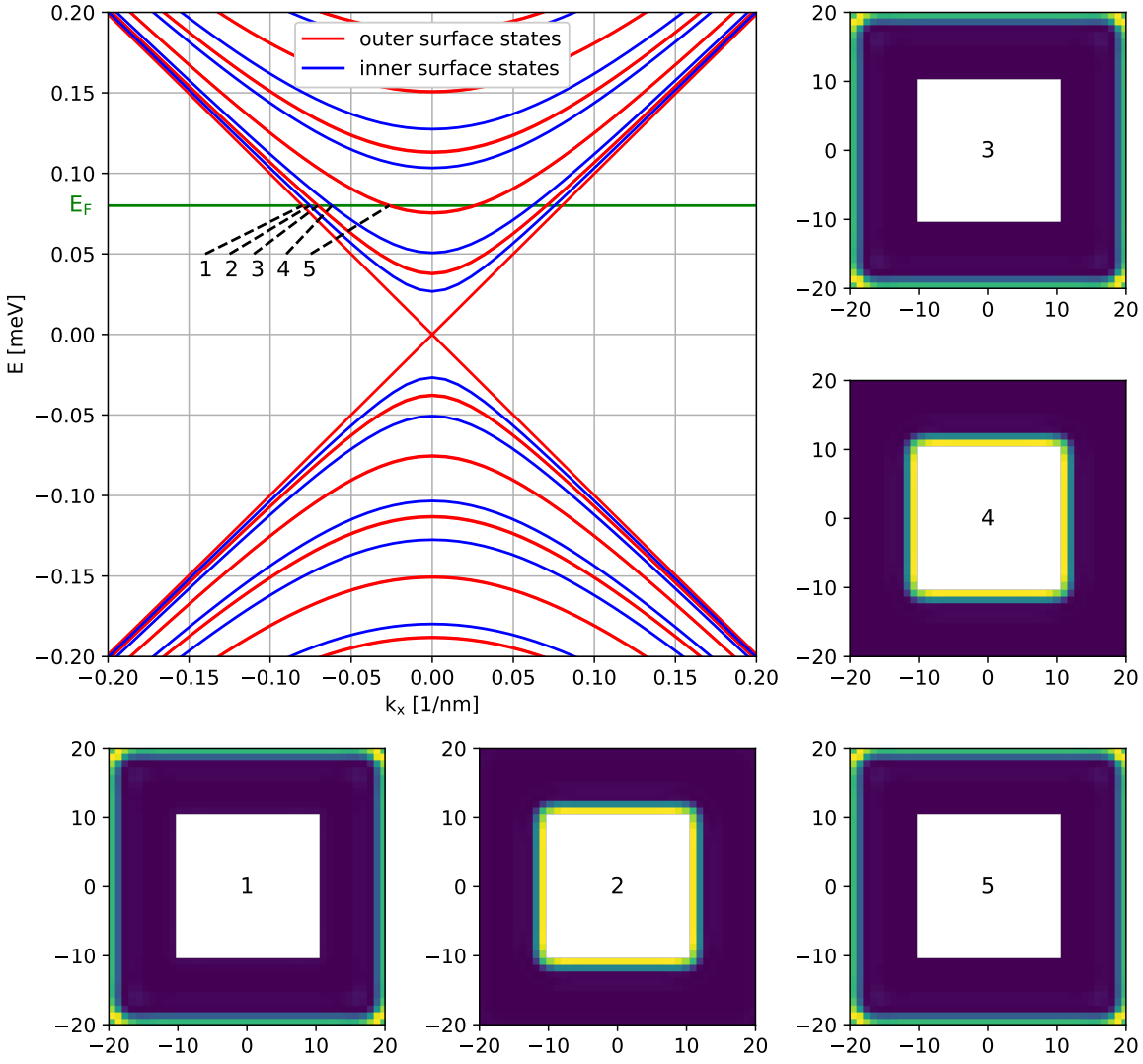

Figure 4.5: Bandstructure of a hollow TI shell with width $w_{\text{out}} = 40$ nm and height $h_{\text{out}} = 40$ nm, and local density of states displayed in the wire cross-sections. The hole in the center of the wire has the dimensions $w_{\text{in}} = h_{\text{in}} = 20$ nm. An axial magnetic field $B = 1.363$ T is applied parallel to the wire axis. The flux ratios of the outer and inner surfaces are $\eta_{\text{out}} = 0.5007$ and $\eta_{\text{in}} = 0.1593$, respectively. The subbands are colored in blue (red) if the wave function is localized at the inner (outer) nanowire surface. The Fermi energy E_{F} is shown in green and the LDOS plots belong to the numbered modes in the bandstructure. Yellow in the LDOS plots corresponds to a high, while dark blue to a low density value.

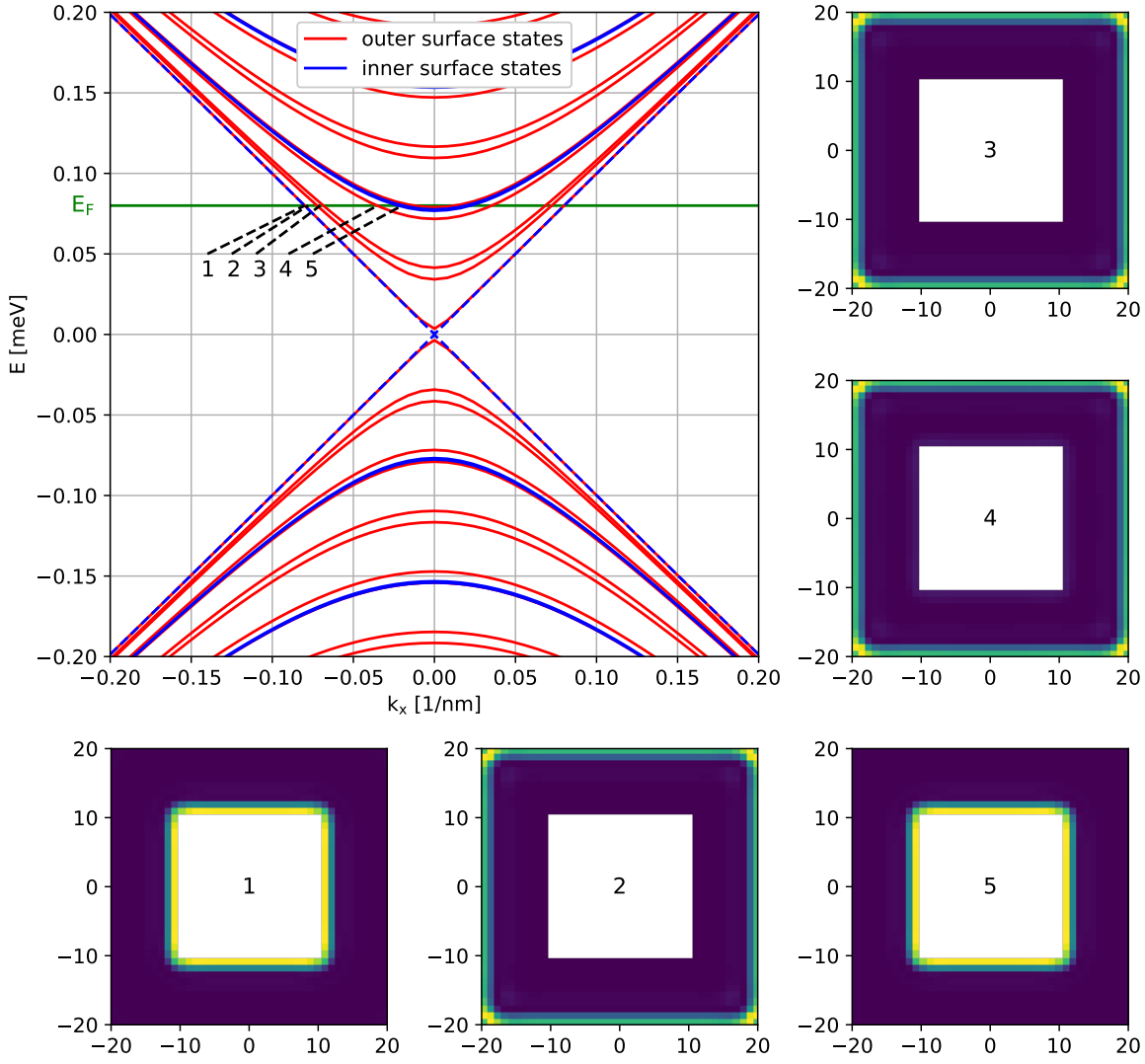

Figure 4.6: Bandstructure of a hollow TI shell with width $w_{\text{out}} = 40$ nm and height $h_{\text{out}} = 40$ nm, and local density of states displayed in the wire cross-sections. The hole in the center of the wire has the dimensions $w_{\text{in}} = h_{\text{in}} = 20$ nm. An axial magnetic field $B_{\parallel} = 4.3$ T is applied parallel to the wire axis. The flux ratios of the outer and inner surfaces are $\eta_{\text{out}} = 1.5798$ and $\eta_{\text{in}} = 0.5027$, respectively. The subbands are colored in blue (red) if the wave function is localized at the inner (outer) nanowire surface. The Fermi energy E_{F} is shown in green and the LDOS plots belong to the numbered modes in the bandstructure. Yellow in the LDOS plots corresponds to a high, while dark blue to a low density value.

flux ratios of $\eta_{\text{out}} = \Phi_{\text{out}}/\Phi_m = 1.5798$ and $\eta_{\text{in}} = 0.5027$, such that the Berry gap of the inner surface states should be almost closed and also the subbands of the outer surface modes should only be slightly split. Exactly this picture can be seen in Fig. 4.6. The linearly dispersing band of the inner states is shown as a dashed line for better visibility of the almost linear branch of the outer surface states. By checking again the LDOS of the modes, the simple picture of two Dirac states on both surfaces is confirmed.

4.2.2. Effective 2D surface model

The states on each of these surfaces, analogously to a single nanowire surface, should obey an effective 2D model. In order to perform transport simulations for realistic nanowire dimensions it is necessary to introduce such an effective model. The Hamiltonian, describing two decoupled Dirac shells, can be written down as

$$\begin{aligned} H^{\text{2D}}_{\text{c-s}} &= \begin{pmatrix} H^{\text{2D}}_{\text{in}} & 0 \\ 0 & H^{\text{2D}}_{\text{out}} \end{pmatrix} \\ &= \begin{pmatrix} -\mathrm{i}\hbar v_{\text{F}} \left[\sigma_x \partial_x + \sigma_y \frac{2\pi}{C_{\text{in}}} \left(\partial_s + \mathrm{i}\eta_{\text{in}}\right)\right] & 0 \\ 0 & -\mathrm{i}\hbar v_{\text{F}} \left[\sigma_x \partial_x + \sigma_y \frac{2\pi}{C_{\text{out}}} \left(\partial_s + \mathrm{i}\eta_{\text{out}}\right)\right] \end{pmatrix}. \end{aligned} \tag{4.1}$$

Note that even though we now also have a 4x4 matrix for the Hamiltonian, the numerical effort will still be considerably smaller, as we still have a 2D lattice. In the following, we are going to perform a test transport calculation for fixed radii of the inner and the outer surfaces. The tight-binding implementation is performed on a square lattice and for simplicity it is assumed that the nanowire has cylindrical symmetry. First, the parameters of the inner surface are fixed to a circumference of $C_{\text{in}} = 99$ nm and a lattice constant of $a_{\text{in}} = 1$ nm, giving the number of lattice points $N = 100$. Then, defining the shell thickness d, the parameters of the outer shell are calculated as

$$C_{\text{out}} = 2\pi(r_{\text{in}} + d) = 2\pi \left(\frac{C_{\text{in}}}{2\pi} + d\right) \tag{4.2}$$

$$a_{\text{out}} = \frac{C_{\text{out}}}{N}. \tag{4.3}$$

Also the flux through the inner surface Φ_{in} is chosen as the reference value.
The flux through the outer surface is then given by

$$\Phi_{\text{out}} = \Phi_{\text{in}} \cdot \frac{r^2_{\text{out}}}{r^2_{\text{in}}}. \tag{4.4}$$

In the spirit of the 3D bandstructure calculation above, we fix now the shell thickness to $d = 11.65$ nm. This value assures that the fluxes are related by $\Phi_{\text{out}} = 3\Phi_{\text{in}}$. To circumvent the Fermion doubling problem, we add a Wilson mass term to Eq. (4.1) with $E_{\text{gap}} = 60$ meV. For the transport simulation the length of the scattering region is fixed to $L = 200$ nm and an averaging over 20 Gaussian correlated disorder sets with amplitude $K_0 = 0.75$ and correlation length $\xi = 6$ nm is performed. In Fig. 4.7

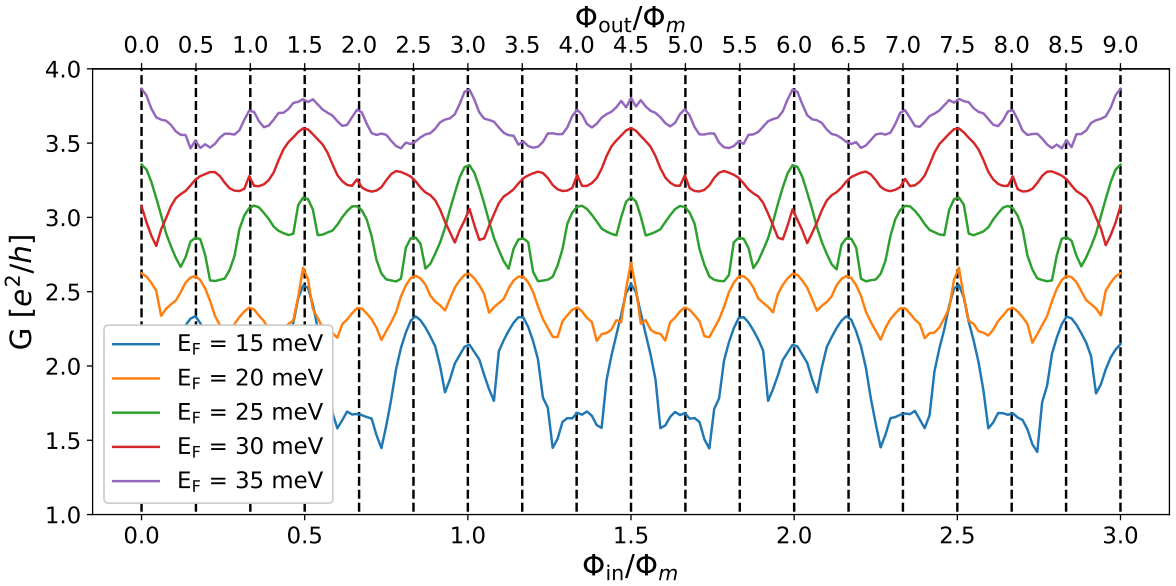

Figure 4.7: Conductance for a core-shell nanowire with respect to the applied axial magnetic field and for different Fermi energies. The inner wire circumference is set to $C_{\text{in}} = 99$ nm and the shell thickness to $d = 11.65$ nm, such that $C_{\text{out}} = 172.2$ nm.

the conductance is plotted with respect to the applied flux and for a few values of the chemical potential. In the figure the bottom axis corresponds to the flux ratio of the inner surface, while the top axis shows the outer flux ratio. The peak positions are independent of the Fermi energy E_{F} and they are marked by the vertical dashed lines. Their position corresponds to half integer multiples of the outer flux ration η_{out}. The overall periodicity seems to be mainly determined by the transport of the modes propagating on the inner surface, as the curves are Φ_m periodic with respect to the inner flux ratio η_{in}. The conductance therefore seems to be a superposition of transport signatures of outer and inner surface modes, just as expected.

In summary, the effective 2D model gives reasonable results. The spectrum consists of two initially decoupled Dirac cones with quantized subbands. In transport simulations, clear Aharonov-Bohm oscillations can be observed, where the periodicity obeys the predefined ratio of inner and outer surface areas. Whether this is a general transport behavior for arbitrary thicknesses d and checking for other core-shell transport signatures is left for further studies. Further considerations could involve to account for more realistic simulations with a filled insulating core instead of vacuum, coupled inner and outer surface modes or the Andreev reflection between those surface states at an N/S-interface in the presence of Majorana fermions.

4.3. TI nanowire in magnetic fields – extrinsic higher-order TIs

Many experiments rely on the behavior of physical observables under the application of external magnetic fields. In Secs. 2.1.2 and 4.2 we have already seen the effect of an axial magnetic field. The flux through the cross-section of the nanowire periodically tunes the spectrum, such that for half of a magnetic flux quantum the surface hosts a perfectly transmitted mode. Also by applying external magnetic fields perpendicular to the wire axis the surface state spectrum can be tuned, leading to the emergence of Landau levels and chiral edge states [185]. This effect will be exploited in a following chapter, were quantum transport in hybrid structures of superconductors and topological insulators will be studied. Additionally, for magnetic fields that pierce all of the nanowire surfaces in an angle, the appearance of 1D hinge states is predicted [38], where the system is then denoted as extrinsic higher-order TI. In this section the surface spectrum in such magnetic fields is discussed in detail for the special case of Bi_2Se_3.

First let us fix a gauge for the vector potential $\boldsymbol{A}$. The gauge is chosen such that the magnetic field has components that are pointing along the negative z-direction and the positive y-direction. Therefore, we choose the gauge

$$\boldsymbol{A} = \begin{pmatrix} B_z y + B_y z \\ 0 \\ 0 \end{pmatrix},$$

$$\boldsymbol{B} = \nabla \times \boldsymbol{A} = \begin{pmatrix} 0 \\ B_y \\ -Bz \end{pmatrix},$$

$$\alpha = \tan^{-1}\left(\frac{B_y}{B_z}\right),$$

$$B_z = \sqrt{B^2 - B_y^2},$$

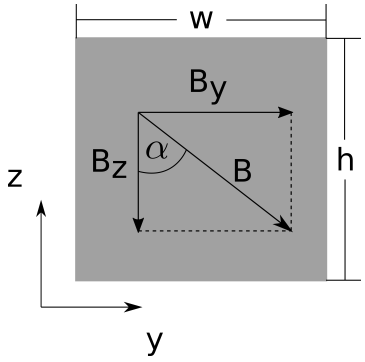

Figure 4.8: Cross-section of TI nanonwire and magnetic field definition.

where α is the angle between the y and z components of the magnetic field. Note that we will keep the magnitude of the magnetic field fixed and only rotate the field vector $\boldsymbol{B}$ around the nanowire axis. Figure 4.8 illustrates a schematic plot of the wire cross-section and the magnetic field components are shown. For the following considerations we are going to consider a rectangular nanowire with width $w = 30$ nm and height $h = 30$ nm. Also the magnitude of the magnetic field strength is fixed to $B = |\boldsymbol{B}| = 30$ T. The magnetic field is chosen quite large due to the small wire dimension, for larger wires the field strengths can be chosen much smaller in order to observe the following effects. First we are going to consider the effect of magnetic fields on the spectrum of such a TI nanowire, the results are shown in Fig. 4.9. Theoretically it is well known that an external magnetic field, which is perpendicularly piercing the

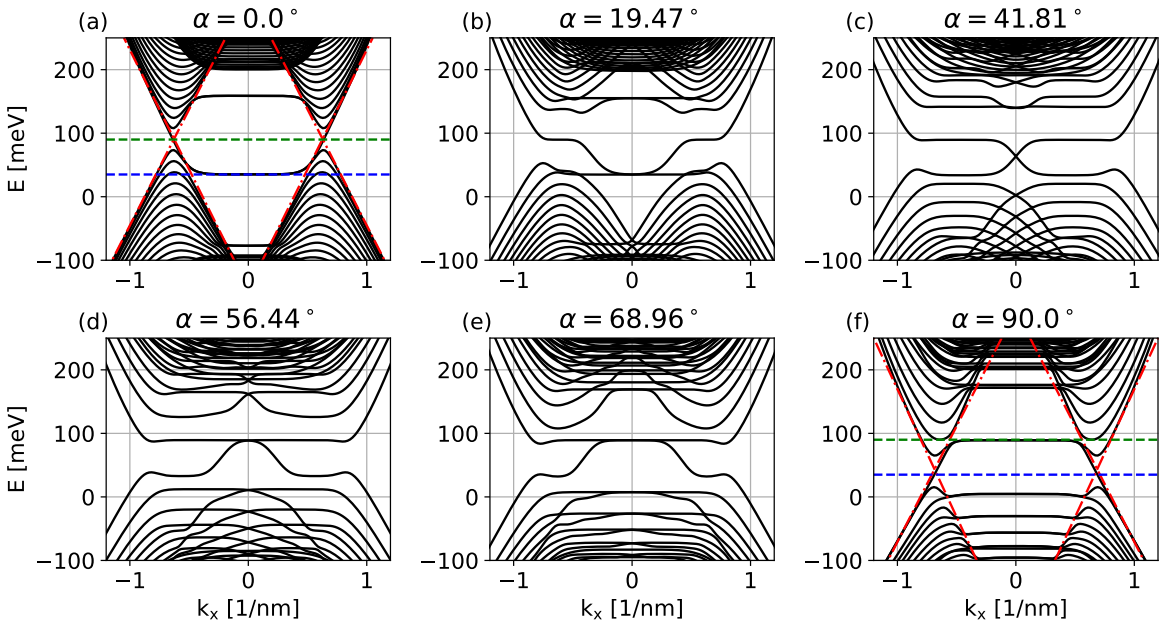

Figure 4.9: Bandstructure of TI nanowire for different magnetic field angles. Rotating $\boldsymbol{B}$ leads to formation of Landau levels on all nanowire surfaces. The blue (green) dashed lines in panels (a) and (f) mark the 0^{th}-Landau level on the $x-y$ ($x-z$)-surfaces.

top and bottom surfaces of a rectangular TI nanowire ($\alpha = 0$), is inducing the formation of localized Landau levels and chiral edge states [185] as soon as the magnetic length $l_B = \sqrt{\hbar/(eB)}$ becomes comparable to the wire width. This case is visualized in Fig. 4.9 (a). As the surface states can be described by an effective Dirac equation, the Landau level spectrum obeys the analogous expression that is derived in graphene. The Landau level energies are given by [186]

$$E_n = \sqrt{2e\hbar n}v_{\text{F}}\sqrt{B_\perp}, \tag{4.5}$$

where n is the Landau level index and $B_\perp$ is the magnetic field component which is perpendicular to the surface. The flat bands which are located symmetrically around $k_x = 0$ are the Landau levels. In Fig. 4.9 (a) the 0^{th}-Landau level is marked by the blue dashed line. At this point it should be stressed that the asymmetry of the spectrum with respect to the 0^{th}-Landau level stems from the anisotropy of the Hamiltonian with respect to the y- and z-directions in Bi_2Se_3. The x- and y-directions in the material are isotropic as these planes correspond to the crystallographic quintuple layers, while the z-direction is the stacking direction of those layers. Therefore the y- and z-directions are not equivalent and thus leads to a breaking of the spectrum symmetry. The red dashed lines are marking the chiral edge states which are propagating along the side surfaces of the nanowire. The other special magnetic field direction is the $\alpha = 90°$ (Fig. 4.9 (f)), where the magnetic field is pointing perpendicular to the side surfaces of the nanowire. Also here the flat Landau levels are emerging as expected, but now the 0^{th}-Landau level (marked with a green dashed line) is located much higher in

energy. This is also the effect of the crystallographic anisotropy, meaning that the Dirac point of the z-surface states lies lower in energy than the Dirac point of the y-surface states. For better visibility the green and blue dashed lines are shown in both angle configurations. The energy difference is roughly $\Delta E_0 \approx 55$ meV. By understanding these observations, it becomes quite clear what happens now if we start to rotate the field direction between these cases. Each of the surfaces will now have a component pointing perpendicularly out-of-plane, such that depending on the angle LLs will form on all surfaces. In Figs. 4.9 (b)-(e) bandstructures for different angles α are plotted. The slow field rotation visualizes the transition between the two LL configurations. At $\alpha = 41.81°$ the two LL species can be observed best. In order to check if the modes corresponding to the different regions in the spectrum behave as expected, one can again plot the LDOS of the wave functions in the wire cross-section. For the field configuration of panel (c) the spectrum is again plotted in Fig. 4.10 (a). The blue dashed lines are marking energies at which the LDOS were computed. Additionally, the relevant modes are labeled by letters and the LDOS in the wire cross-section are visualised in frames (b)-(f). The cross-sections correspond to the configuration in the schematic plot of Fig. 4.8. The bright spots represent a high LDOS value. First, frames (c) and (e) show a high LDOS on the y- and z-surfaces, respectively. This directly corresponds to the discussion above that the flat regions correspond to LL on these wire parts. Next, modes (b) and (f) correspond to 1D hinge states and they are certainly localized at the wire edges. The most interesting mode is d). Its wave function is strongly localized at the edge between the side and the top surface. Naively, one would expect that the Lorentz force would push the electrons away from this edge. But instead, one finds a mode which is emerging due to the different LL energies.
Note that the spectrum looks very similar to the result that is obtained in Refs. [187, 188]. The authors studied the topological insulator HgTe in an analogous magnetic field setup. Instead of a strong anisotropy in the material itself, the different LL energies are introduced due to an additional Zeeman term. However, the energy difference ΔE_0 is much smaller than in the above calculation. Nevertheless the authors make very interesting predictions for the quantum transport signatures. By locally contacting the edges of TI nanowires different conductance signatures should be observable which depend on small rotations of the magnetic field. These effects should also apply to materials with a strong anisotropy that is present inherently in the Hamiltonian.

In conclusion, an arbitrary angle between TI nanowire axis and external magnetic field leads to the emergence of 1d hinge states. The intrinsic anisotropy of the 3D Hamiltonian leads to an asymmetry in the Landau level spectrum, where Landau levels are energetically located at different reference energies for each nanowire surface.

4.4. Dirac particles in a magnetic box

One of the main features of Dirac particles with a linear dispersion is the suppressed backscattering and the possibility of Klein tunnelling [189]. Therefore, due to this

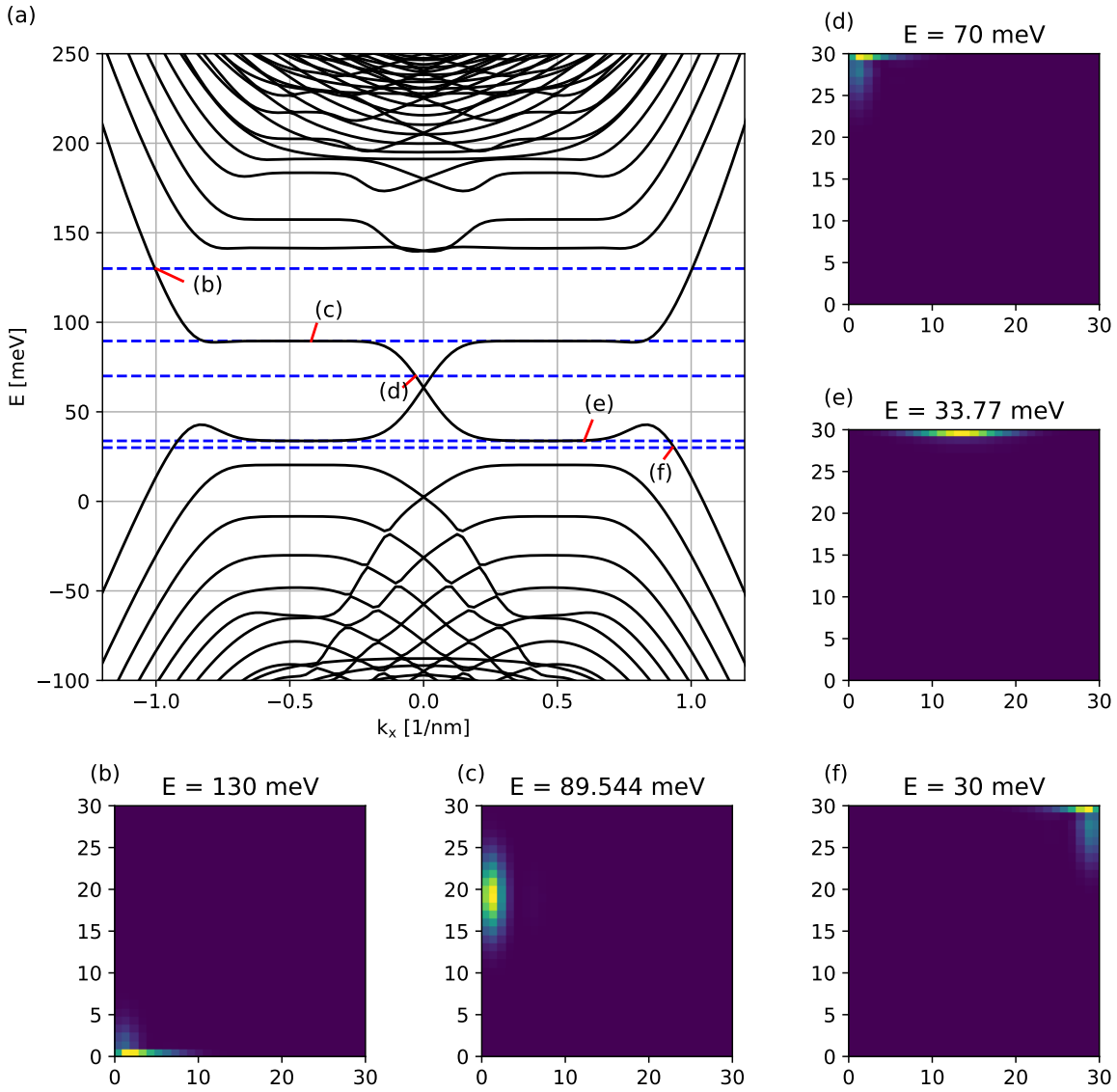

Figure 4.10: (a) Bandstructure of TI nanowire for a field angle of $\alpha = 41.81°$. (b) - (f) LDOS of the labelled modes of panel (a) plotted in the wire cross-section. 1D modes appear at the edges of the nanowire, which correspond to (b), (d), and (f). Contrary, (c) and (e) are localized Landau level electrons on the $x-z$ and $x-y$-surfaces, respectively.

property, it is conceptually hard to confine Dirac particles in a certain spatial area. However, such a confinement can be very useful to probe spectral properties of quantum states, i.e., in Fabry-Pérot interferometry experiments [190]. In topological insulator nanowires Osca et al. suggested in Ref. [191] a sequential gating setup to trap Dirac particles. Experimentally, it can be quite complicated to construct such local gates and to tune them into the right parameter regime. Another possibility to confine such states is the combination of magnetic fields and the actual surface geometry of the nanowire [64, 154], which, for example, allows to study Coulomb blockade. In Ref. [154] the considered system has a smoothly varying wire radius along the axial direction with a full rotational symmetry with respect to the wire axis. Intriguing quantum transport signatures can emerge in such systems due to the special surface geometry. Furthermore, M. Fürst could show in his Masterthesis [192] that Landau levels of Dirac fermions obtain very interesting spectral properties, which depend on the curvature of the surface.
Realistic samples, for example, HgTe, which are studied in the Weiss group at the University of Regensburg, are typically shaped a bit differently. In Fig. 4.11 (a) a scanning electron micrograph of a realistic sample is shown. Note that the wire is etched into a macroscopic slab geometry, where the actual wire is connected at its two ends by system parts which are continuously increasing in width. The wire has no rotational symmetry, as the resulting cross-section has a trapezoidal shape with a constant in-plane height. Additionally, for nanowires an axial magnetic field is necessary in order to induce the perfectly conducting mode by closing the Berry gap. Consequently, in such systems there will always be an out-of-plane magnetic field component at the sides of the nanowire constrictions.
In this section we want to study in detail the physics of such TI nanowire constrictions in a magnetic field parallel to the wire axis. Fig. 4.11 (b) is showing a schematic plot of the desired geometry. The setup consists of two wide TI nanowire leads with width W_{lead} which are coupled to a central nanowire with smaller width W_{center} and length L_{center} via two symmetric wire contractions with arc length L_{arc}. The height h is kept constant throughout the junction. Dr. Kozlovsky already devised an effective 2D implementation scheme of the depicted structure in his PhD thesis (see Ref. [64]) and studied it very thoroughly in a perpendicular magnetic field. Also, first simulations in an axial field showed very interesting features with quantized and flux dependent conductance lines (see Chap. 6.3.2 in Ref. [64]). Furthermore, M. Fürst could show in his Bachelor thesis [193] that analogous conductance features can be observed by employing a full 3D model. The origin of those transport properties will be examined in the following.

4.4.1. Modeling of a TI nanowire constriction

Two possible approaches are available to model the nanowire constriction in a tight-binding manner. First, the already mentioned code of an effective surface implementation of Dr. Kozlovsky will be employed. However, a broader geometric parameter range will be considered, which will clarify the basic working principle of a radially

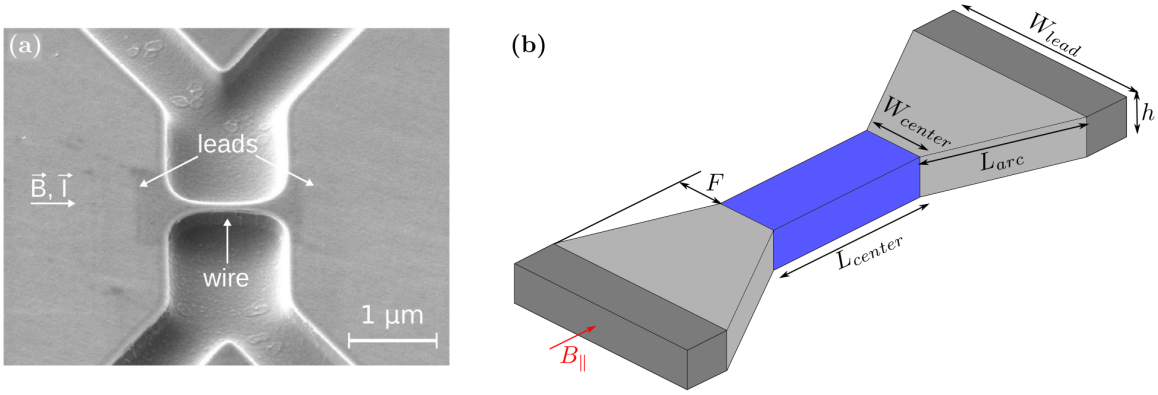

Figure 4.11: (a) Scanning electron micrograph of an experimental HgTe nanowire, which is etched into a macroscopic sample. Adapted from Ref. [25]. (b) Schematic plot of the considered TI nanowire constriction. A small diameter wire is symmetrically connected to two broader leads. An external magnetic field is applied parallel to the junction axis.

constrained nanowire junction. This scheme is not straightforwardly implemented, as it involves a local adjustment of hopping parameters. The procedure is necessary to be able to model with a 2D square lattice a spatially varying nanowire thickness. For more details of the methodology we refer the reader to Chap. 6.3 of Ref. [64]. As the first approach is technically a bit demanding, we also consider a second and more straightforward method in order to check for numerical artefacts. We will use the full 3D model, given by Eq. (2.1) with the toy model parameters of Tab. 2.1b and search in smaller systems for analogous transport features. The constriction shape is easily obtained by simply deleting sites of a full nanowire, which are lying outside the desired shape.

4.4.2. Results of conductance simulations

In the subsequent parts we will differentiate between two junction regimes. It turns out that one of the important geometrical quantities is the length L_{center} of the central nanowire segment. First, we will consider the case of *long* wires in the constriction, where the exact meaning of long will be clarified in the next paragraphs. Second, when the basic physics of these junctions were clarified, we will consider *short* central lengths. For the latter case, also the side faces of the contracting system parts contribute strongly to the observed quantum transport signatures.

Before starting to discuss specific junction geometries, we want to highlight an important model ingredient for the numerical simulations. In order to increase the conductance response for transport through the junctions we assume to have metallic leads (dark grey regions in Fig. 4.11 (b)). This assumption can be easily incorporated into the model by using highly doped leads, where the chemical potential in the reservoirs reads

$$\mu_L = \mu + \Delta\mu, \tag{4.6}$$

where $\Delta\mu$ is the energy offset compared to the chemical potential μ in the central and the contracting parts of the constriction. By considering a positive non-zero value for $\Delta\mu$ one can easily increase the kinetic energy of the lead modes, which probe the transport features of the constriction. This considerably increases the conductance in the energy range close to the Dirac point and gives insight into the present physics.

Long central segment – 2D model

Let us start the discussion by defining specific geometrical constriction parameters for the effective 2D model. The height of the whole junction is fixed to $h = 80$ nm, which is a standard value for HgTe nanowire systems [25], while the width of the leads and the central wire segment are set to $W_{lead} = 150$ nm and $W_{center} = 75$ nm, respectively. Contracting parts of the junction are defined by an arc length of $L_{arc} = 100$ nm and they are connected by a central homogeneous nanowire with length $L_{center} = 1000$ nm. This explicit geometry is resolved by a 2D square lattice with 302 lattice points around the circumference and 550 lattice points along the constriction direction. Finally, in the Hamiltonian we choose a Fermi velocity of $v_{\mathrm{F}} = 5 \cdot 10^5$ m/s and for the leads an energy offset of $\Delta\mu = 30$ meV with $\mu = 0$ and a Wilson mass strength of $E_{\mathrm{gap}} = 60$ meV.

In the following we will discuss the two terminal conductance through the above specified geometry with respect to two external parameters. The first of them is the externally applied magnetic field parallel to the junction axis. This field modifies the surface state spectrum by the Aharonov-Bohm effect and additionally produces out-of-plane magnetic field components at the contracting side faces. Secondly, we vary the Fermi energy in the whole system, which is measured with respect to the Dirac point. In this way, conductance maps are calculated as a function of both parameters. In case of a uniform nanowire the parameter variations will result in diamond shaped conductance features, which are periodic in flux and increase in conductance magnitude by raising the Fermi energy. However, these properties become strongly modified by constraining the nanowire.

In Fig. 4.12 (a) such a map is shown for the above introduced geometry. At low values of the magnetic field and in the full shown energy range one can still observe remnants of the uniform conductance diamonds. Still, inside those diamonds a conductance modulation with local maxima is appearing. Further increasing the magnetic field leads to periodic conductance peaks, which depend hyperbolically on the flux. Moreover, those conductance peaks are uniformly separated in energy. In the low energy range close to the Dirac point the conductance is almost fully suppressed, except at the isolated hyperbolic lines. Here it is remarkable that the lowest conductance line is slowly emerging at zero energy and then only dispersing with a positive slope. The higher lying conductance lines also have regions with a negative slope.

Naturally, the question arises wherein the origin of these features lies. Interestingly it turns out that the complicated structure can be boiled down to a simple particle in the box picture. We know from Sec. 2.1.2 that the surface state spectrum of a TI nanowire

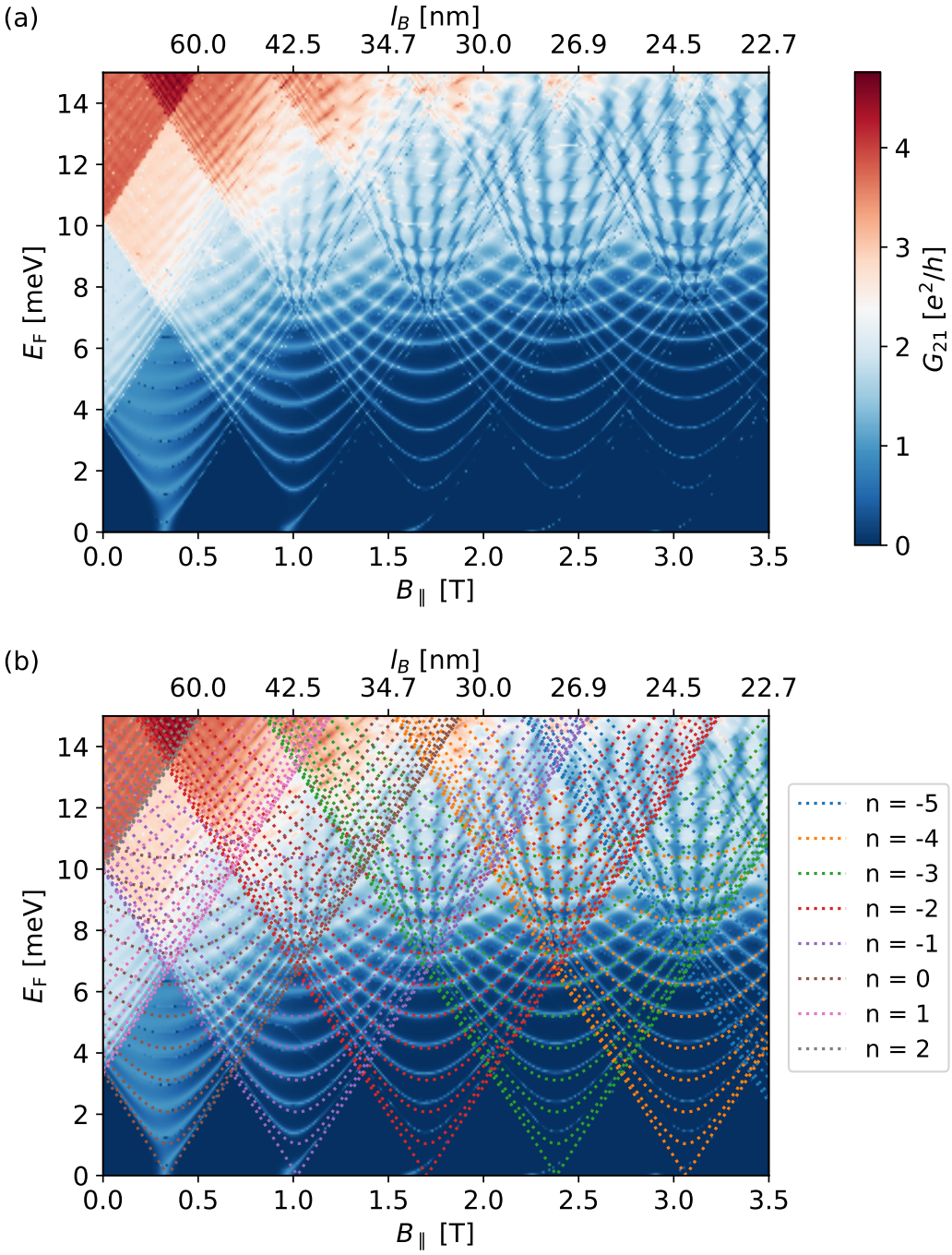

Figure 4.12: (a) Numerically calculated conductance through a TI nanowire constriction as a function of the Fermi energy E_F and an axial magnetic field $B_\parallel$. In (b) the resonances in the conductance are fitted by a quantized Dirac spectrum, which originates from a magnetic confinement of the surface states in the constriction. The system was implemented with a 2D effective surface model and the parameters are specified in the main text.

in an axial magnetic field is given by Eq. (2.11), which reads

$$E(k_x, l, \Phi) = \pm\hbar v_{\mathrm{F}} \sqrt{k_x^2 + \left(\frac{2\pi}{C}\right)^2 \left(n - \frac{1}{2} + \frac{\Phi}{2\Phi_0}\right)^2}. \tag{4.7}$$

As already mentioned, the axial magnetic field is inducing also out-of-plane magnetic field components at the side faces of the constriction. If those field components become strong enough, i.e., when the magnetic length l_B becomes comparable to the spatial extensions of the side faces, localized Landau levels can emerge at those surface regions. In Fig. 4.12 we also plot the magnetic length values as a second x-axis above the conductance maps. Note that those lengths do not correspond to the axial magnetic field $B_\parallel$, but instead to the out-of-plane field component $B_\perp = B_\parallel(W_{lead} - W_{center})/(2L_{arc})$ on the side faces. When the magnetic length becomes short enough, the emerging localized Landau levels can serve as strong magnetic barriers at each end of the central nanowire segment. This magnetic confinement leads then to a quantization of the longitudinal momentum k_x. For simplicity, we can assume that the longitudinal momenta become quantized according to hard-wall boundary conditions (see Sec. 3.4) with $k_x = \pi m/L^{'}$ and $m = 0, \pm1, \pm2, \pm3, ...$ With this assumption, the discrete energy levels are given by

$$E = \pm\hbar v_{\mathrm{F}} \sqrt{\left(m\frac{\pi}{L'}\right)^2 + \left(\frac{2\pi}{C}\right)^2 \left(n - \frac{1}{2} + \frac{\Phi}{2\Phi_0}\right)^2}. \tag{4.8}$$

The relevant length is assumed to be equal to the length of the central wire, i.e., $L^{'} = L_{center}$, and also the circumference of the central part with $C = 2(W_{center} + h)$ is considered for the values of the angular momenta. Using Eq. (4.8) we can compare the conductance map with these discrete energy levels for the above geometry. This comparison plot is shown in Fig. 4.12 (b). The figure shows again the computed conductance map which is overlaid by the calculated discrete energy levels, where the latter are shown as colored dotted lines. Each color therein corresponds to a different angular momentum quantum number. Additionally, each discrete energy branch in one colored cone structure stems from one fixed value of m, where the lowest linearly dispersing states are given by $m = 0$. By going up in energy, the upper energy levels are then obtained by increasing the value of m in integer steps.
Note that we also include $m = 0$ to fit these lowest linear conductance branches, even though in a simple 1D particle in a box picture such a state is not available. The difference in the constriction lies in the presence of the circumferential direction, such that the lowest state can have zero kinetic energy along the constriction direction. This state still has angular energy and circles therefore around the wire circumference, what results in the presence of a $m = 0$ state. What is even more remarkable and special about the lowest lying energy states is that only the part of the branch with positive slope is contributing to the conductance. States with negative slope are not observable in transport for $m = 0$, except if the energy is tuned to negative values. The explanation for this observation might be given by the assumption of Dr. Kozlovsky's

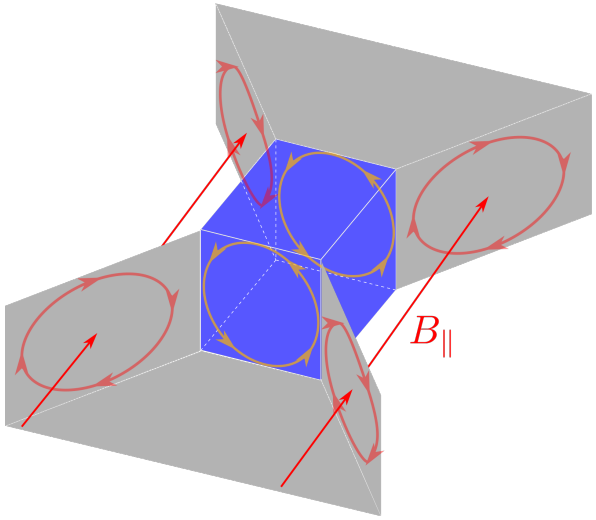

Figure 4.13: Induced chirality for the $m = 0$ states in the nanowire constriction. A specific current direction is favored due to the localized quantum Hall states.

PhD thesis (Ref. [64]), which is shown in Fig. 4.13. The argumentation for transport of only $m = 0$ branches with positive slope through the constriction lies in the formation of chiral states on the side faces, which circle those surfaces in a specific direction. This leads in the central wire segment to a preferred angular momentum direction, while the reversed circulation is suppressed. We take up this argument and further discuss the observed transport feature. In order to do that, we need to point out the close relation to the well known persistent currents in Aharonov-Bohm rings [194–197]. Currents are given by the derivative of the ring spectrum with respect to the applied flux through the circumference. For our constriction setup, the central wire part also corresponds to such a ring structure in a perpendicular magnetic field. The states with $m = 0$ do not have longitudinal kinetic energy in the axis direction. Therefore, the only energy contribution of those states lies in the angular momentum part. These energies are given by

$$E(n,\Phi)|_{m=0} = \pm\hbar v_{\mathrm{F}} \frac{2\pi}{C_{center}} \left(n - \frac{1}{2} + \frac{\Phi}{2\Phi_0} \right), \tag{4.9}$$

such that the resulting currents read

$$I = -\frac{\partial E}{\partial \Phi} = \mp\hbar v_{\mathrm{F}} \frac{2\pi}{C_{center}} \frac{1}{2\Phi_0} = \mp \frac{e v_F}{C_{center}}. \tag{4.10}$$

By tuning the magnetic flux at a fixed value of the Fermi energy E_{F} one should be able to switch between the two signs of the current which corresponds to different circumferential directions. In contrast to a typical Aharonov-Bohm ring structure, the quantum Hall states on the side faces suppress one circulation direction. The current direction, which is shown as orange lines in the central segment of Fig. 4.13, is probably the one which is mediating transport between the two leads, as it is in resonance with the chiral quantum Hall states on the side faces. Contrary, the counter rotating current

state is being suppressed due to the localization effect of the chiral states which strongly act against the central persistent current. Higher lying states with $m > 0$ have also kinetic energy along the constriction direction and are therefore not purely influenced by those quantum Hall states. These switch continuously between current directions if the flux is tuned from low to high values.
In order to show that this particle in a box picture in combination with the local quantum Hall states on the side faces is valid, we numerically compute the bound state energy spectrum as well as the related eigenfunctions of such a constriction. This is done by simply taking into account a finite system of the light grey and blue constriction parts of Fig. 4.11 (b) and by diagonalization of the tight-binding Hamiltonian matrix. In Fig. 4.14 we show again the computed conductance map of the above considered constriction in a low energy range with the calculated energy spectrum as orange dotted lines. The energies of states which are confined in the constriction match perfectly with the conductance peaks. Note that in the eigenspectrum also lowest branches ($m = 0$) with negative slopes are present, which are not leading to a conductance response.
To check whether these states correspond to localized quantum Hall states, we fix the magnetic field strength to $B_{\parallel} = 2.55$ T and show also the local density of states in arbitrary units for the eigenfunctions corresponding to the seven energies marked with white triangles. The two lowest energies are associated with states which have the quantum number $m = 0$ and a different angular momentum quantum number. These have a negative slope and do not contribute to conductance. Moreover, the flux dependence shows that by increasing the magnetic field strength the energy values are smoothly converging to $E = 0$. Just as expected, the first two LDOS panels exhibit that the corresponding eigenfunctions are strongly localized at the side faces of the constriction. Due to the localization no transport can be mediated by those states. Contrary, the next two states which lie higher in energy stem from one and the same angular momentum quantum number. Their longitudinal quantum numbers are $m = 0$ and $m = 1$ and from the simple particle in a box picture we expect an increasing number of nodes and local maxima in the LDOS plots. This is exactly what can be observed in the next two LDOS panels. While for $m = 0$ we have one single LDOS maximum in the central wire part, which is confined by the side faces and the effective magnetic barriers, one gets two maxima for $m = 1$. The next higher energy is again a $m = 0$ state with negative slope, therefore it is again localized at the side faces. Finally, the last states correspond to the quantum numbers $m = 2$ and $m = 3$ with three and four maxima in the LDOS panels, respectively. These findings are consistent with the picture of confined states inside the constriction.

Long central segment – 3D model

Before we go on and consider a short nanowire connection in the central part of the constriction, we check the above findings with the full 3D model of Sec. 2.1.1 and the simple model parameters of Tab. 2.1b. This serves as a consistency check in order to exclude possible artefacts which might arise due to the necessary numerical lattice transformation of the 2D effective surface implementation. In the full 3D model we

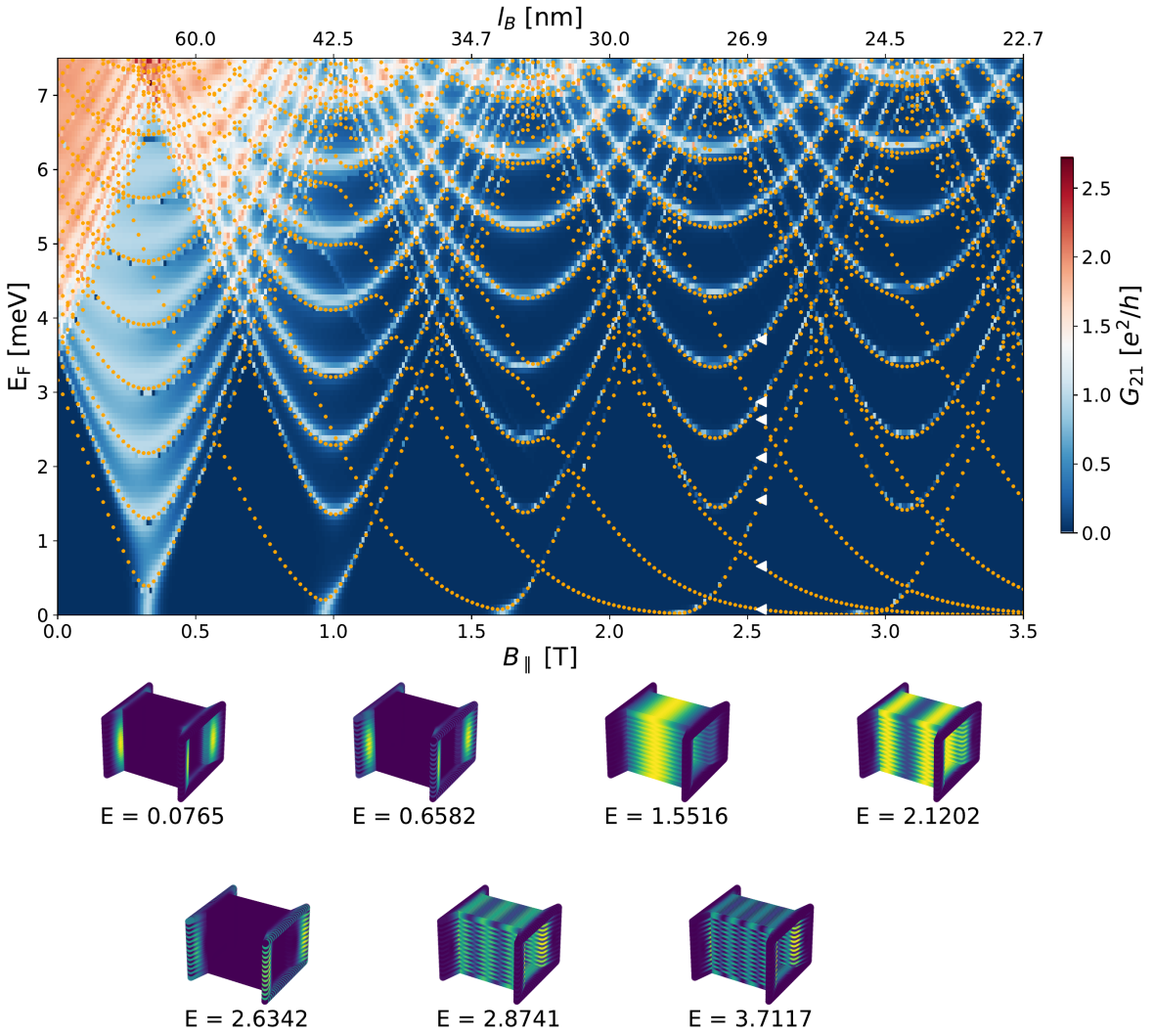

Figure 4.14: Comparison between conductance map and the eigenspectrum (orange dotted lines) of a finite constriction. The discrete conductance lines stem from bound states inside the constriction, where the lowest states with negative slope do not contribute to conductance. Those states correspond to localized quantum Hall states. In order to show this, also the LDOS of the eigenfunctions for the seven lowest eigenvalues (marked with white triangulars) at $B_\parallel = 2.55$ T are plotted. Contrary to states at higher energies and also to the lowest once with positive slope, which are localized in the central wire segment of the constriction, the lowest states with negative slope are localized at the side faces of the junction.

are limited by greater numerical cost such that we change the geometrical system parameters to a lead width of $W_{lead} = 30$ nm, a central width of $W_{center} = 10$ nm and a constant height of $h = 20$ nm. The system is discretized on a uniform cubic grid with lattice spacing $a = 1$ nm. Additionally to increase the effect of the magnetic barriers in our small constriction we choose an arc length of $L_{arc} = 10$ nm, meaning that we get a *hard* constriction that directly connects the lead width to the central nanowire segment. Therefore the side faces are always perpendicular to the applied axial field and experience the maximal out-of-plane field components. Finally, the central homogenous nanowire length is set to $L_{center} = 100$ nm and we use a lead energy offset of $\Delta\mu = 0.38$ meV. In Fig. 4.15 (a) the calculated conductance is again illustrated as a function of the applied magnetic field and the Fermi energy. Note that we need to use relatively large magnetic fields in order to thread a few flux quanta through the cross-section of the central segment due to the small constriction dimensions, but the qualitative features won't be different in larger systems. Analogously to the results obtained by the effective 2D model, the conductance is exhibiting discrete resonances with a hyperbolic flux dependence.
Also, the lowest resonance is only present with a positive slope and again we can fit Eq. (4.8) to the numerically calculated results. For the length of the confined region we set $L = 85$ nm and the flux ratio is defined by

$$\frac{\Phi_{\text{eff}}}{\Phi_0} = \frac{B_{\parallel}(W_{center} - \lambda_s)(h - \lambda_s)}{\Phi_0}, \tag{4.11}$$

where λ_s is the penetration depth of the surface states into the bulk. The fitted spectrum is shown in Fig. 4.15 (b) overlaid to the conductance map. The spectrum fits again perfectly the resonances, leading to the conclusion that the effective 2D model is reproducing correctly the physics in a 3D nanowire constriction.

Short central segment – 2D model

Finally, we want to study the effect of shortening the length L_{center} of the central wire segment. More precisely, we take into account the same constriction geometry as above, except that we set $L_{arc} = 150$ nm and $L_{center} = 10$ nm. Regarding the lattice points along the constriction direction, we change their number to 310. The conductance result is illustrated in Fig. 4.16, where also the bound state energies of Eq. (4.8) for the given geometry are plotted. Note that the conductance map shows similar features as Fig. 6.8 (a) of Ref. [64]. Due to the reduced length L_{center} the spacing between the discrete bound state energies for different quantum numbers m is increasing, such that only the lowest branch is visible in the considered energy range. It is evident that the particle in a box picture is no longer applicable to the very short wire segment. The energy branches do no longer fit the resonance lines, where remarkably the latter are bending towards zero energy for larger magnetic field values. Here, we want to point out that the value of L_{center}, at which the particle in a box picture breaks down, can be used as a threshold that separates the *long* from the *short* junction regime.
In order to answer the question, why the situation is changing for the shorter constriction, we extend the parameter range of the considered magnetic field strength and

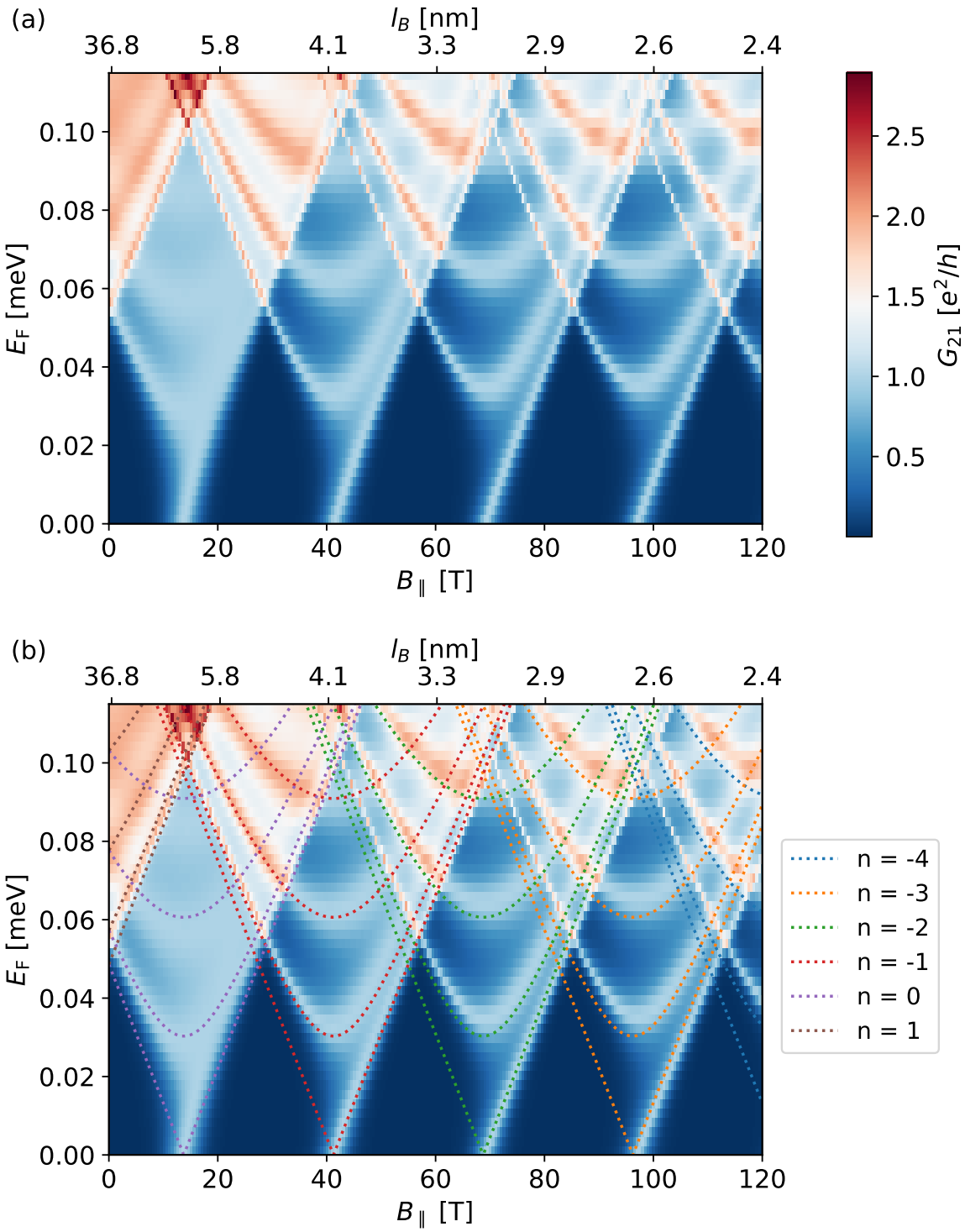

Figure 4.15: (a) Conductance as a function of the Fermi energy E_F and an axial magnetic field $B_\parallel$ for a TI nanowire constriction specified in the main text, which was implemented with the 3D BHZ Hamiltonian [Eq. (2.1)]. Discrete conductance resonances are observable, analogously to the effective 2D calculation. (b) Fit of bound state spectrum given by Eq. (4.8) to the conductance.

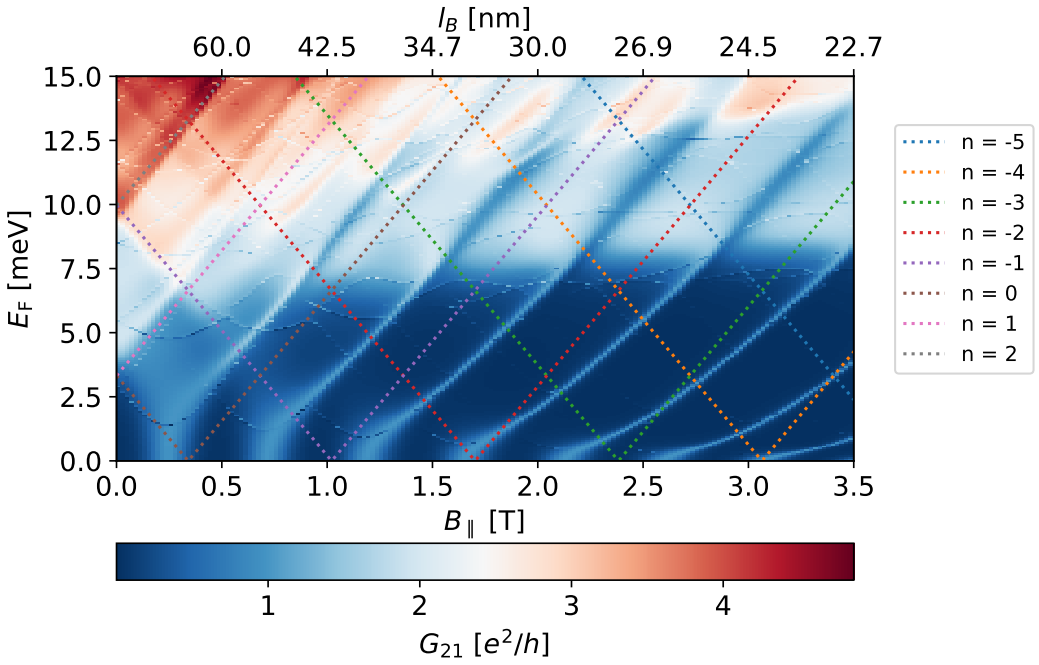

Figure 4.16: Conductance as a function of E_F and $B_\parallel$ for a constriction with a short central wire of length $L_{center} = 10$ nm. The expected bound state energies are shown in dotted lines. These are no longer fitting the observed conductance resonances.

Fermi energies. Figure 4.17 (a) is showing a conductance map for the full parameter set. At low values of E_F we see a periodic repetition of the single resonances which are bending smoothly towards $E = 0$. Additionally, at larger Fermi energies, one can certainly observe the emergence of three line like structures with positive slope. The origin of those features lies in the presence of the out-of-plane field components which pierce the side faces of the constriction. These surface components become very dominant in the considered geometry, as the central wire segment is short compared to their spatial extension. Therefore, the transport properties of the constriction are dominated by the quantum Hall physics which arise at the contractions. The out-of-plane magnetic field component leads to the formation of Landau levels, where in Dirac systems the respective level energies are known [186] to obey Eq. (4.5), such that

$$E_{LL} = \sqrt{2e\hbar n_{LL}} v_F \sqrt{B_{eff}} = \sqrt{2e\hbar n_{LL}} v_F \sqrt{B_\parallel \frac{F}{L_{arc}}}, \tag{4.12}$$

where $n_{LL} = 0, \pm 1, \pm 2, ...$ is the Landau level index. Energies of Landau levels are directly proportional to the square root of the perpendicular magnetic field, which pierces the Dirac surface states. In Fig. 4.17 (b) the expected Landau level energies of Eq. (4.12) are plotted in red, while only the $n_{LL} = 0$ level is shown in white for better visibility. The above emphasized line structures in the conductance map are perfectly fitted by Eq. (4.12). This observation shows that transport is mainly dictated by the side surfaces and the emerging Landau levels are strongly affecting the bound states

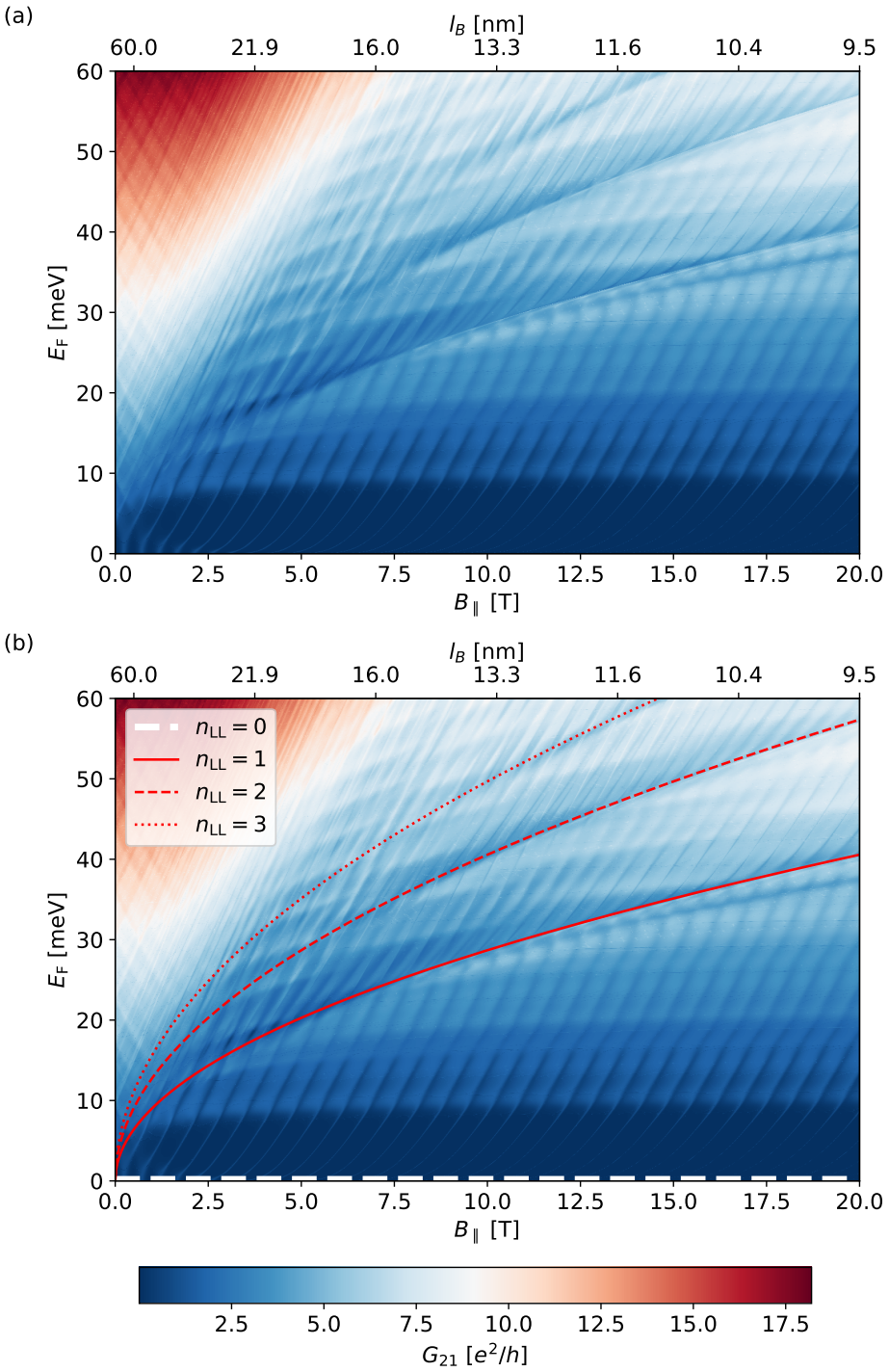

Figure 4.17: (a) Conductance as a function of E_F and $B_\parallel$ for the same constriction as in Fig. 4.16 with extended parameter spaces. In the conductance, line structures with positive slope are appearing. These are fitted in (b) by Eq. (4.12) with white ($n_{LL} = 0$) and red ($n_{LL} > 0$) colored line plots, which perfectly match the observed features.

in the central wire segment. Therefore, in such a TI constriction, transport in the low energy range should be mediated by states with a certain angular momentum and rotation direction. The exact angular momentum value can be tuned by the applied magnetic field.
Summarizing the above findings, we have shown that a geometrical confinement of Dirac surface states in combination with an axial magnetic field can lead to intriguing transport signatures. Two distinct regimes could be identified, which depend on the length of the central constriction part. For long nanowire segments, quantized Dirac states emerge in the junction, which can be probed by transport simulations and which can be described by a simple particle in a box picture. Furthermore, for short nanowires connecting the two contracting junction regions, transport is dominated by localized chiral quantum Hall states which emerge at the junction side faces. These observations might be employed in realistic experiments to probe the dispersion properties of topological surface states.

4.5. Crossed Andreev reflection in TI nanowire junctions

In recent years hybrid systems of topological insulators and s-wave superconductors attracted a lot of scientific interest due to the prediction that such systems might be ideal platforms to engineer Majorana fermions [9, 198–200]. But also many other interesting transport phenomena are expected to occur in these systems. One example is the possibility of perfect Andreev reflection at a N/S-junction in TI nanowires [65]. The Andreev reflection is here stabilized due to the presence of a phase winding in the superconducting pairing. The setup is in principle an application similar to the Majorana interferometer which was suggested by Fu and Kane [200]. Further exploiting this property of TI nanowires, also devices which allow perfect crossed Andreev reflection could be built. Such a system is studied in detail in this section.
Andreev reflection at a N/S-interface is a scattering process that relates electrons and holes. An incoming electron (hole) mode with an energy inside the superconducting gap can either be normal reflected as an outgoing electron or Andreev reflected into an outgoing hole mode [106]. Crossed Andreev reflection is an analogous process where the electron and hole modes are additionally spatially separated. This effect is very interesting for quantum computing as it is in a sense the reversed process of Cooper pair splitting. Cooper pair splitters could be used to generate entangled electrons [201–206] which in turn would be useful for secure information exchange. In order to build such devices a high Cooper pair splitting rate is necessary. Therefore also a high CAR rate might hint to physical systems where this process might be efficiently generated. CAR has already been studied in many theoretical proposals, where platforms were, for example, 2D materials such as graphene [40–42] or a 1D Kitaev chain [207], and it was also experimentally measured [112]. However, often CAR is accompanied by strong electron co-tunneling such that its signatures are hidden behind other transport features. In contrast, the below discussed setup allows for perfect CAR in certain pa-

rameter ranges, which could serve as a smoking gun signal in experimental realizations. Moreover, we show that CAR is also observable on a much broader parameter range, where the conductance features are also robust against a certain degree of disorder.
For TI nanowires it was shown that perfect Andreev reflection is possible under certain conditions [65]. By bringing a normal s-wave superconductor into contact with a TI nanowire an effective superconducting pairing can be induced in the topological surface states by the proximity effect [9, 208]. By further applying an axial magnetic field the system can be tuned into a topological superconducting regime. At roughly a flux of $\Phi = \Phi_0$ it is expected that a vortex forms at the N/S-interface. The winding in the superconducting phase leads to a shift of the quantized angular momenta, what leads to a stabilized superconducting pairing in the surface states. Moreover, for each value of the chemical potential μ, an odd number of Fermi points is present, what directly corresponds to a topologically non-trivial superconducting regime. By computing the Andreev conductance in such a N/S-junction a perfect conductance plateau is observable in the single mode regime. A drawback of TI systems is that it is usually hard to tune the Fermi energy close to the Dirac point and into the single mode regime. Therefore the authors of Ref. [65] suggest to introduce an additional out-of-plane magnetic field which induces quantum Hall states as was discussed in chapter 4.3. This magnetic field increases the energy range of the single mode regime to the range between the zeroth and the first Landau levels. Besides increasing the possibility of an experimental observation the magnetic field is also inducing chiral edge states at the sides of the nanowire. These states are spatially separated into counter propagating modes. Concluding from this observation it should be possible to use this property and construct a system which is spatially separating the incoming electrons from the outgoing holes into separated electrodes. The simplest setup that would allow for such a functionality is by adding an additional normal lead to the system and to form a T-junction with the nanowires. In the following the modeling of such a device is explained in detail and the conductance signatures are studied extensively employing a full 3D model. Note that the same setup was also studied using an effective 2D surface model in Refs. [1, 209]. The advantage of the latter lies in the lower computational cost and the possibility to study larger junction sizes, which are experimentally easier to realize.

4.5.1. T-junction model

In Fig. 4.18 (a) a schematic plot of the T-junction device is illustrated. Two normal-conducting leads are coupled in a T-shaped manner to a superconducting TI lead which is in close proximity to a normal s-wave superconductor, i.e., niobium. For the simulation the normal superconductor is neglected, only an induced effective pairing term is considered in the proximitized TI lead. The system is then implemented by the standard Bogoliubov-de Gennes Hamiltonian $H = \frac{1}{2}\Psi^\dagger \hat{H} \Psi$ with

$$\hat{H} = \begin{pmatrix} H_{\mathrm{BHZ}} & \Delta(\boldsymbol{r}) \\ \Delta^*(\boldsymbol{r}) & -\mathbb{T}^{-1} H_{\mathrm{BHZ}} \mathbb{T} \end{pmatrix}, \tag{4.13}$$

where H_{BHZ} is given by Eq. (2.1). The superconducting pairing term is non-zero in the

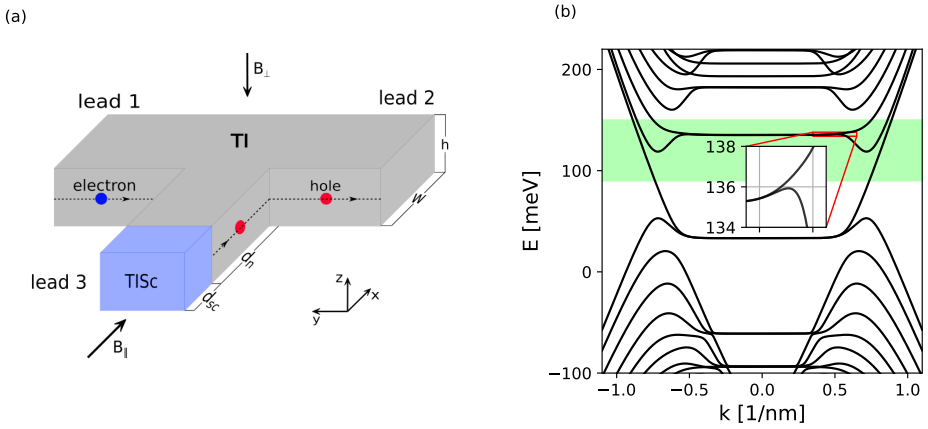

Figure 4.18: (a) Schematic plot of a T-junction. Two leads in the normal state serve as spatially separated reservoirs of electrons and holes while the superconducting lead induces the CAR process. (b) Bandstructure for a TI nanowire with width $w = 50$ nm, height $h = 10$ nm and an out-of-plane magnetic field strength $B_\perp = 20$ nm. Adapted from Ref. [1].

proximitized part of the TI nanowire and zero otherwise, such that it is defined as

$$\Delta(\boldsymbol{r}) = \Delta(r)\exp(\mathrm{i}\chi(y,z)) \tag{4.14}$$

and

$$\Delta(r) = \begin{cases} \Delta_0, & x < d_{\mathrm{sc}} \\ 0, & x > d_{sc}. \end{cases} \tag{4.15}$$

The pairing strength is fixed to $\Delta_0 = 0.25$ meV, which is taken from literature values [210–212]. As already mentioned above, two magnetic fields will be applied to the setup. The first magnetic field component $\boldsymbol{B}_\parallel$ is applied parallel to the superconducting wire axis and is used to tune the superconducting lead into a topologically non-trivial regime. The second component $\boldsymbol{B}_\perp$ is pointing along the z-direction and stands perpendicular to the whole device. Note that in the superconducting region this field component will be neglected as the normal s-wave superconductor will screen it due to the Meissner-Ochsenfeld effect [213]. The vector potential is fixed to the following gauge

$$\boldsymbol{A} = \boldsymbol{A}_\parallel + \boldsymbol{A}_\perp = \begin{pmatrix} 0 \\ -B_\parallel z/2 \\ B_\parallel y/2 \end{pmatrix} + \begin{pmatrix} 0 \\ -B_\perp x \\ 0 \end{pmatrix}, \tag{4.16}$$

such that the coordinate origin lies in the center of the superconducting lead. The magnetic field is also affecting the phase of the superconducting pairing $\chi(y,z)$, which becomes spatially dependent. At the N/S-interface [214] it is expected that a vortex emerges for a flux close to a superconducting flux quantum $\Phi = B_\parallel A_{\mathrm{wire}} = \Phi_0 = h/(2e)$.

The phase of the pairing term is then defined as

$$\chi(y,z) = \left\lfloor \frac{\Phi}{\Phi_0} \right\rfloor \begin{cases} \arctan\left(\frac{z}{y}\right), & \arctan\left(\frac{z}{y}\right) > 0 \\ 2\pi + \arctan\left(\frac{z}{y}\right), & \arctan\left(\frac{z}{y}\right) < 0 \end{cases} \tag{4.17}$$

where $\lfloor ... \rfloor$ denotes the floor function. The spatial dependence of the pairing amplitude can be neglected in our model as we are only interested in the transport behavior of the surface states. These states live only close to the wire surface, such that the spatial decay of the pairing magnitude into the bulk of the wire is of no importance for us. The winding of the phase is having two important effects. First of all it allows Andreev reflection for the perfectly conducting mode by introducing matching angular momenta of the electron and hole wave functions [65]. Moreover the vortex is stabilizing the superconducting state, which is disturbed by the axial magnetic field $B_\parallel$. The magnitude of the superconducting gap is continuously decreasing with increasing flux Φ through the wire cross-section [215]. The additional winding of the phase counteracts the influence of the vector potential.
The full 3D model is on the one hand computationally much more expensive as an effective 2D model, but on the other hand it also allows for the emergence of Majorana fermions at the N/S-interface. This will be particularly important in the next section in the case of conductance simulations in disordered devices.

4.5.2. Conductance signatures

For the transport simulations we fix the system parameters shown in Fig. 4.18 (a) to wire widths $w = 50$ nm and a device height of $h = 10$ nm. In all of the following conductance simulations the lattice constant was set to $a = 1$ nm. These dimension are already experimentally feasible [216] and still in a range such that calculations can be performed with a balanced numerical cost. The other length values are set to $d_{\mathrm{sc}} = 1$ nm and $d_{\mathrm{n}} = 20$ nm.

Strong magnetic field configuration – quantum Hall regime

First we consider the strong $B_\perp$ case in which the device is in the quantum Hall regime. If the magnetic length l_B becomes comparable to the width of the wires, localized Landau levels and edge states can form in the system. In order to enter this regime in our simulations we fix $B_\perp = 20$ T. At a first glance this value looks quite large, but it should be pointed out that nanowires in experiments usually have larger dimensions. This considerably reduces the necessary field strength to reach the quantum Hall state. The corresponding bandstructure is shown in Fig. 4.18 (b). Around $k = 0$ the flat Landau levels are observable while for larger k-values the chiral edge states are present. The green shaded region is visualizing the energy range in which we compute the conductance through the junction. The magnetic field is pointing downwards, therefore electrons entering the system from lead 1 will propagate along the side surface and hit eventually the N/S-interface at lead 3. Electrons entering from

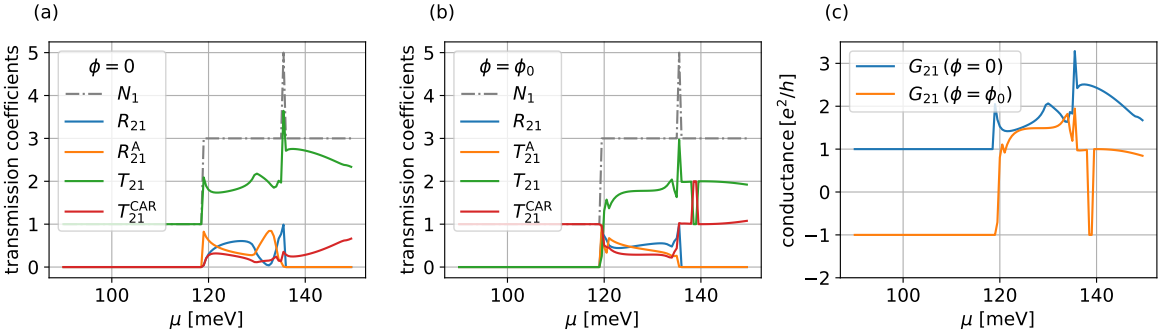

Figure 4.19: (a) and (b) show the different transport probabilities for a T-junction setup with wire widths $w = 50$ nm, height $h = 10$ nm and $B_\perp = 20$ T, corresponding to an axial flux of $\Phi = 0$ and $\Phi = \Phi_0$, respectively. (c) Conductance computed with Eq. (4.18) for both flux configurations. In the presence of a vortex perfect CAR is observed, which is measurable by a negative conductance signature. Adapted from Ref. [1].

lead 2 will mainly propagate along the back surface and move directly into lead 1. With Kwant we compute the S-matrix for the setup. Therein we have access to the various transport probabilities, which are given by normal reflection R, Andreev reflection R^{A}, normal transmission T and crossed Andreev reflection T^{CAR}. In actual experiments the measured quantity is the non-local conductance in which those transport probabilities are encoded. Therefore, we will also compute this quantity to make predictions for experimental setups. It is given by [217]

$$G_{21} = \frac{e^2}{h}\left(T_{21} - T_{21}^{\mathrm{CAR}}\right). \tag{4.18}$$

In Figs. 4.19 (a) and (b) the probabilities of the different transport events are plotted as a function of the chemical potential μ for the fluxes $\Phi = 0$ and $\Phi = \Phi_0$ ($B_\parallel = 4.6$ T), respectively. Also the total number modes N_1 in lead 1 are shown as dashed lines. Without an axial magnetic field $B_\parallel$, and therefore without a winding in the superconducting phase, the most dominant process is normal electron transmission T. Only in the energy range closely below the first Landau level normal back reflection R and Andreev reflection R^{A} are observable due to the presence of counter propagating modes on the side surfaces. The peak around $\mu = 135$ meV stems from a small up bending of the bands close to the first Landau level which is caused by the anisotropy of Bi_2Se_3. This is visualized as an inset in Fig. 4.18 (b). In contrast to this trivial transport signature, introducing a flux of $\Phi = \Phi_0$ leads to a CAR plateau in the single mode regime. Further approaching the first Landau level results again in the emergence of other transport probabilities and for higher energies again normal electron transmission is dominating. The jump between T and T^{CAR} around $\mu = 138$ meV is a numerical artefact. The axial flux is not exactly tuned to a superconducting flux quantum due to the finite penetration depth of the surface states into the bulk. The curves would become smooth by an exact tuning of the flux which results in a perfect

interplay between the winding of the phase and the magnetic field. The smoking gun signature in an experiment for perfect CAR would be a negative conductance plateau as illustrated in Fig. 4.19 (c). The flux through the wire cross-section induces perfect CAR in the single mode regime with $T^{\mathrm{CAR}} = 1$ and $T = 0$. By looking at Eq. (4.18) it is clear that a negative conductance signals the perfect conversion of an electron into a hole mode. Physically this means that an incoming electron from lead 1 is not leaving in lead 2. Instead, it forms along with an additional electron from lead 2 a Coopper pair which enters the superconducting lead 3. The missing electron from lead 2 results in a negative non-local conductance signal between leads 1 and 2.

Weak magnetic field configuration

Above the conductance was calculated as a function of the chemical potential μ for a fixed $B_\perp$ value in the quantum Hall regime. The drawback of the high out-of-plane field is that it might interact with the superconducting pairing and destroy it eventually, if the magnitude of $B_\perp$ becomes too large. Therefore it is also good to understand the conductance behavior at weaker field ranges for different doping regimes. As the parameter space is increasing due to the additional tuning of $B_\perp$, the system size is reduced by setting the wire widths to $w = 24$ nm. The other system parameters stay unchanged. Note that the general operational behavior of the device is not changing qualitatively with increasing or decreasing wire widths. Only the field ranges will scale with the system size. In Fig. 4.20 the non-local conductance G_{21} is plotted with respect to the chemical potential μ and the out-of-plane magnetic field $B_\perp$. More precisely, the results for an axial field of $B_\parallel = 9.58$ T ($\Phi = \Phi_0$) and $B_\parallel = 0$ ($\Phi = 0$) are shown in Figs. 4.20 (a) and (b), respectively. Blue (red) color coding corresponds to negative (positive) conductance and therefore to a dominating CAR (normal electron transmission) process. For small values of the chemical potential and increasing magnetic field the single mode regime with its plateau can be observed for both axial field configurations. At larger fields and higher chemical potentials normal electron transmission is the dominant process. However, remarkably also for low values of $B_\perp$, a certain parameter range is showing a high CAR rate in the two field cases. This is a very important observation, as it shows that the device can also operate with weak magnetic fields. This is always favourable for superconducting systems.
Due to that finding, we can now go back to our large system with wire widths $w = 50$ nm and study the conductance for a weaker perpendicular magnetic field of $B_\perp = 4$ T. The bandstructure of that parameter set is shown in Fig. 4.21 (a) where the energy range of interest is again shaded in green. The quantum Hall regime is not fully realized yet, Landau levels around $k = 0$ are only starting to form. Still, the influence of $B_\perp$ is strong enough to induce states that propagate preferably at the sides of the nanowires and will therefore hit the N/S-interface. The different scattering probabilities are illustrated in Figs. 4.21 (b) and (d) for $B_\parallel = 0$ ($\Phi = 0$) and $B_\parallel = 4.6$ T ($\Phi = \Phi_0$). For the latter, again a CAR plateau is observable in the single mode regime. However, compared to the strong field range from above, T^{CAR} stays the dominant scattering event even for large values of μ. This is also the case for no applied $B_\parallel$ and no winding

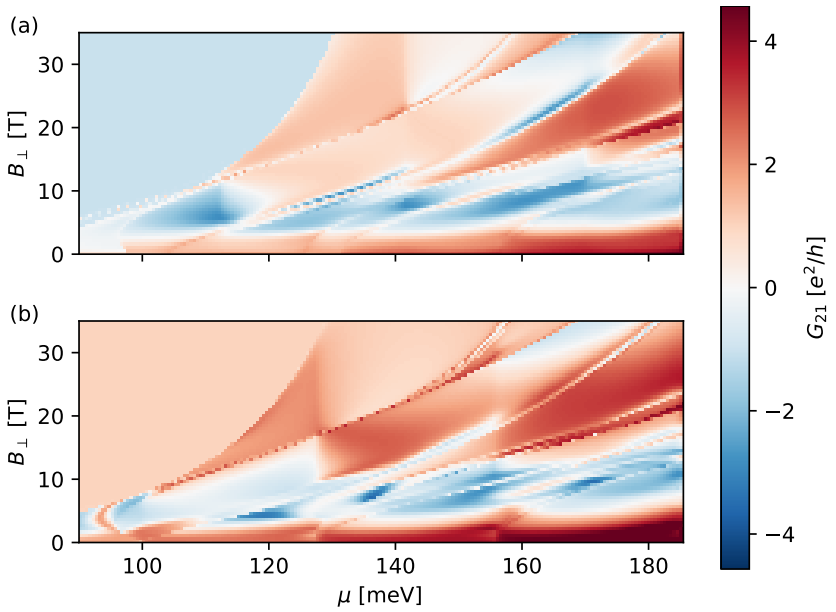

Figure 4.20: Conductance G_{21} with respect to the chemical potential μ and the applied perpendicular magnetic field $B_\perp$. In (a) a parallel field of $B_\parallel = 9.58$ T ($\Phi = \Phi_0$) is applied to the system, while in (b) $B_\parallel = 0$ ($\Phi = 0$). Adapted from Ref. [1].

in the phase of the pairing term. The non-local conductance, shown in Fig. 4.21 (c), is therefore also showing a strong negative conductance signature at high doping ranges. Moreover, the curves look very similar for both axial field configurations, meaning that the device can also be operated without the necessity of an in-plane field.

Disordered devices – robust CAR signature

In the clean limit the T-junction is showing clear CAR signatures for different parameter regimes. The question remains if these conductance features survive in presence of disorder. For the simulations and due to the relatively small diameter of the wires we chose to use white noise (short-range) disorder. The disorder potential is defined by the amplitude $V = K \cdot 0.41$ eV, where the onsite values are chosen from a standard normal distribution. The conductance is then calculated as the average of different disorder configurations. Typically many disorder samples are considered in averaging procedures, but as the 3D model is already quite computationally expensive the number of samples is fixed to 20. This number is high enough to get rid of the most dominant sample dependent conductance features. We consider the device of Fig. 4.20 with wire widths $w = 24$ nm in the presence of such disorder. As the disorder should also be included around the N/S-interface we set the distance parameters to $d_\mathrm{n} = 20$ nm and $d_\mathrm{sc} = 5$ nm. Additionally the distance between lead 1 and lead 2 is fixed to 45 nm to include possible scattering even before coming close to the N/S-interface. The conductance is computed for different disorder strengths K and for a perpendicular magnetic field strength of $B_\perp = 7$ T as a function of μ. This corresponds to a horizontal

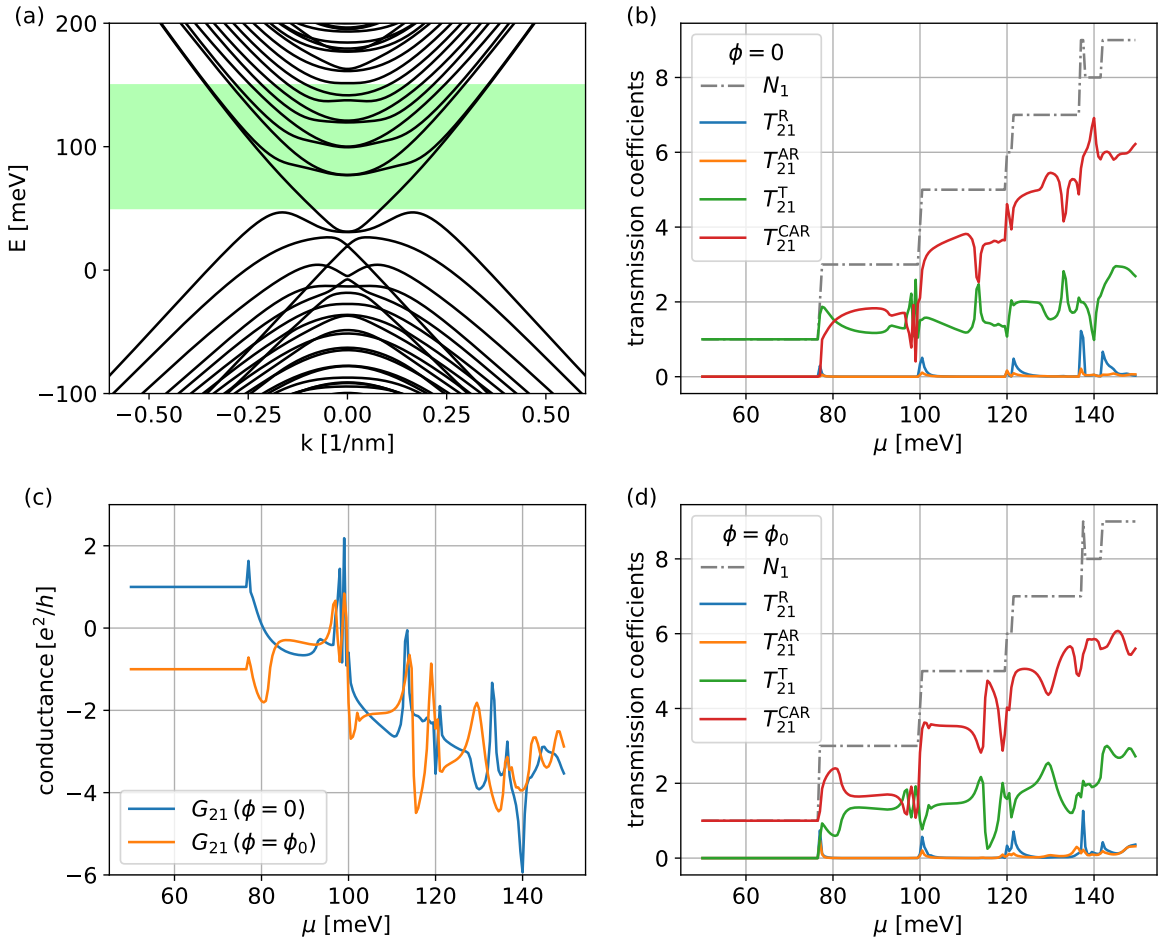

Figure 4.21: (a) Bandstructure of a TI nanowire with width $w = 50$ nm, height $h = 10$ nm and $B_\perp = 4$ T. The green shaded region marks the energy range of the conductance computation. (b) and (d) show the probabilities of the different possible scattering events in the T-junction. (c) shows the corresponding conductance calculated between leads 1 and 2. Adapted from Ref. [1].

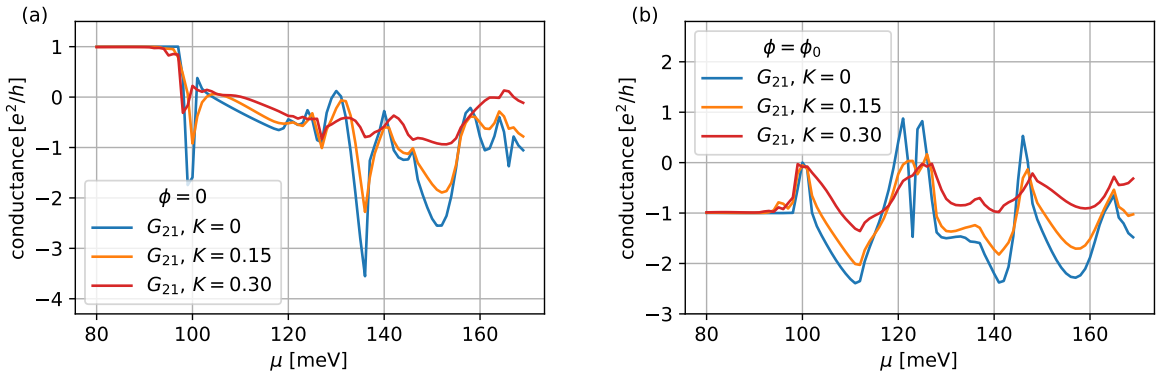

Figure 4.22: Conductance for a disordered T-junction as already studied in Fig. 4.20. The conductances were averaged over 20 disorder samples. The CAR signature of negative non-local conductance will survive a certain amount of disorder. Adapted from Ref. [1].

linecut in Figs. 4.20 (a) and (b). In Figs. 4.22 (a) and (b) the averaged conductances for the two axial field configurations are plotted. In both figures it is observable that the CAR rate is reduced with increasing disorder strength, but it survives until a certain magnitude of K. Furthermore, the conductance plateau in the single mode regime for small μ is robust against disorder and stays at +1 ($\Phi = 0$) or -1 ($\Phi = \Phi_0$).

Effect of Zeeman term

Up to now we only considered the orbital effect of the magnetic fields. Lastly, we are also going to consider the Zeeman effect which enters directly as an additional term in the Hamiltonian and scales with the magnitude of the magnetic field. This is particularly important in the case of Bi_2Se_3 and analogous compounds, because these materials typically have large g-factors. In the basis of the 3D BHZ model of Eq. (2.1) the Zeeman term is given by [218]

$$H_Z = \frac{\mu_B}{2} \begin{pmatrix} g_z^v B_z & 0 & g_P^v B_- & 0 \\ 0 & g_z^c B_z & 0 & -g_P^c B_- \\ g_P^v B_+ & 0 & -g_z^v B_z & 0 \\ 0 & g_P^c B_+ & 0 & -g_z^c B_z \end{pmatrix}. \tag{4.19}$$

The g-factors of magnetic fields parallel and perpendicular to the z-axis of the conduction band (c) and the valence band (v) are denoted as $g_z^{v/c}$ and $g_P^{v/c}$, respectively. Also the standard definition $B_\pm = B_x \pm \mathrm{i}B_y$ holds. We choose literature values of Ref. [219] for the necessary g-factors, which are set to $g_z^v = 29.90$, $g_z^c = 27.3$, $g_P^v = 18.96$ and $g_P^c = 19.48$. We consider again the same system as was studied in Fig. 4.20 with wire widths $w = 24$ nm. Fig. 4.23 (a) is showing the conductance for $B_\parallel = 9.58$ T, while (b) is illustrating the case of $B_\parallel = 0$. Comparing the results to those without a Zeeman term, the most important features are still present. For the case of an applied axial field the CAR signature become a bit smeared out. Particularly in the single mode regime

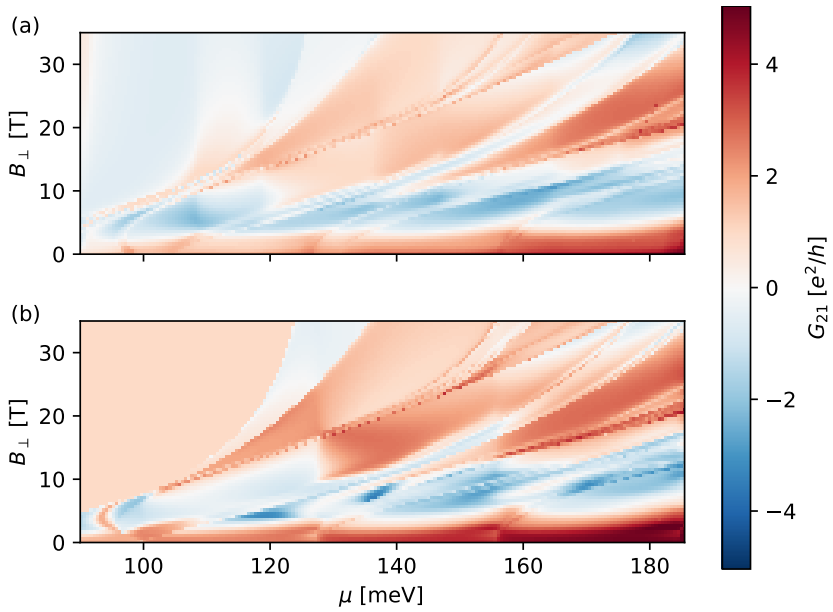

Figure 4.23: Conductance with respect to $B_\perp$ and μ for the same device as studied in Fig. 4.20 with an additional Zeeman term given by Eq. (4.19). The conductance signatures in the case of $B_\parallel = 9.58$ T are a bit smeared out, but still present over a large parameter range. Adapted from Ref. [1].

a parameter range with suppressed CAR starts to appear. But it should be stressed that the magnitude of the Zeeman term is quite large due to the high magnetic field strengths in the small diameter wires. For more realistic and larger wires the necessary magnitudes are much lower and therefore also the effect of the Zeeman term becomes much less pronounced.
In summary, we have extensively studied crossed Andreev reflection in a 3D TI nanowire T-junction for different setup conditions. CAR is highly tunable by the application of external magnetic fields, where a clear CAR signature is achievable by inducing a phase winding in the superconducting lead via an axial flux of $\Phi = \Phi_0$. Moreover, wide parameter ranges show high CAR rates even without the phase winding and for low values of the perpendicular magnetic field. The obtained results are robust to disorder and also only weakly affected by the Zeeman effect.

4.6. TI Josephson junctions

In this section we change the system of interest from the previous N/S/N-junction into a S/N/S-configuration. A topological insulator nanowire is sandwiched between two superconducting electrodes, thereby forming a Josephson junction. Theoretically, such systems have been studied with standard analytical approaches in Ref. [220], where, for example, the critical current is exhibiting maxima at odd integer multiples of the superconducting flux quantum, if an axial magnetic field is applied to the system. Moreover, the system is expected to host Majorana end states [214] for these flux values,

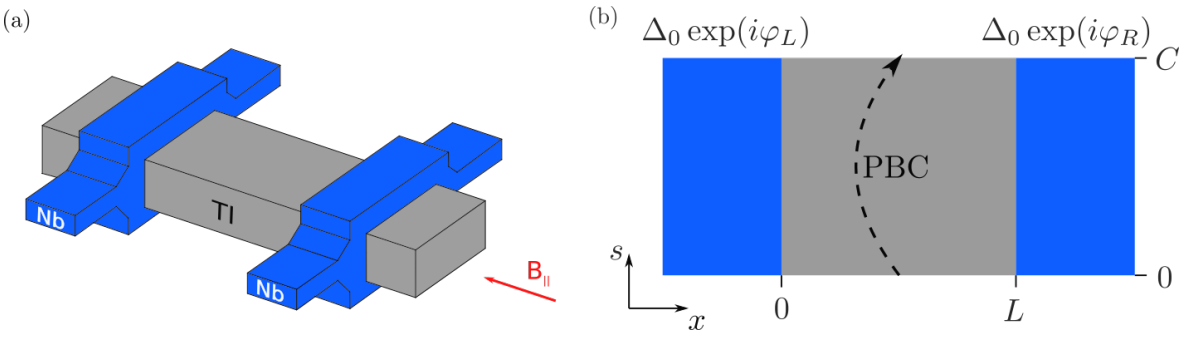

Figure 4.24: (a) Schematic plot of a TI nanowire that is proximitized over the whole circumference by two superconducting leads. An external magnetic field is applied parallel to the wire axis. (b) Unwrapped surface of the wire, which serves as the implemented geometry in the tight-binding simulations.

which should manifest as a 4π-periodic current-phase relation [220]. Experimentally, such setups are studied in the Weiss Group at the University of Regensburg, where an image of a HgTe Josephson junction is shown in Fig. 4.30. The wires are proximitized by superconducting niobium stripes from the top. Measurements of Shapiro steps [32] could already show that the samples contain a certain ratio of a 4π-periodic current. This hints in the direction that the supercurrent is carried to a large extent by surface states that propagate on the wire surface. In the following section we want to further study in detail the behavior the CPR and critical current under the influence of a tuned axial magnetic field with the numerical means that were introduced in Sec. 3.6.2. We start by first studying the CPR in a weak magnetic field for a TI nanowire that is fully proximitized by an external s-wave superconductor. Superconductivity is here assumed to be introduced homogeneously around the wire circumference. Afterwards, we depart from this ideal case by considering a more realistic local proximity effect in the wire circumference. There also the geometry is affecting the current flow in the junction and explains experimental findings. Note that the following hybrid systems were studied in strong collaboration with Dr. Fuchs, where we refer the reader to his thesis [209] for additional information.

4.6.1. Weak magnetic fields and fully proximitized surface

Let us start by considering a topological insulator nanowire that is proximitized by s-wave superconductors at its two ends. The superconductors are assumed to wrap around the circumference fully homogeneously, thereby introducing a constant and homogeneous pairing potential into the surface states. In Fig. 4.24 (a) the system is schematically illustrated. The system is modelled by the effective surface Hamiltonian given by Eq. (2.10), which is further incorporated into the BdG Hamiltonian

[Eq. (2.33)]. The latter then reads

$$\begin{pmatrix} -\mathrm{i}\hbar v_\mathrm{F}\left[\partial_x\sigma_x + \left(\partial_s + \mathrm{i}\frac{2\pi}{C}\frac{\Phi}{2\Phi_0}\right)\sigma_y\right] & \Delta(\boldsymbol{r})\sigma_0 \\ \Delta(\boldsymbol{r})^\dagger\sigma_0 & \mathrm{i}\hbar v_\mathrm{F}\left[\partial_x\sigma_x + \left(\partial_s - \mathrm{i}\frac{2\pi}{C}\frac{\Phi}{2\Phi_0}\right)\sigma_y\right] \end{pmatrix}\Psi = E\Psi, \tag{4.20}$$

where $C = 2(w+h)$ is the wire circumference and Φ the flux through the cross-section. The superconducting pairing is defined as

$$\Delta(\boldsymbol{r}) = \begin{cases} \Delta_0\exp(\mathrm{i}\varphi_L) & \text{for } x < 0, \\ 0 & \text{for } 0 <= x <= L, \\ \Delta_0\exp(\mathrm{i}\varphi_R) & \text{for } x > L. \end{cases} \tag{4.21}$$

In Fig. 4.24 (b) the induced pairing and the numerical geometry is visualized as an effective 2D plot of the unwrapped wire surface. The setup is the same as in Ref. [220], where the authors studied the Josephson junction purely analytically. We want to gain a more precise insight by employing the numerical tight-binding methodology, which was introduced in Sec. 3.6.2. The system depicted in Fig. 4.24 (b) is implemented by discretizing Eq. (4.20) on a square lattice with grid spacing $a = 5$ nm. The axial magnetic field enters via Peierl's substition into the hopping around the wire circumference according to Eq. (3.10). For the following discussion we fix the wire width and height to $w = 120$ nm and $h = 80$ nm, respectively. The wire circumference is therefore $C = 400$ nm, while the length is set to $L = 25$ nm. We choose a superconducting pairing strength of $\Delta = 0.25$ meV, which is a standard literature value for systems that are proximitized by niobium [210–212], and consider a temperature of $T = 0.05$ K. Finally, the chemical potential is set to $\mu = 22$ meV and the Wilson mass term is given by the gap energy $E_\mathrm{gap} = 50$ meV.

Next, we are interested in the influence of an external axial magnetic field on the supercurrent in the system. In order to study this quantity, we compute the current-phase relation for different flux values Φ in the wire cross-section by employing Eq. (3.56). The flux will be determined by the dimensionless ratio $\eta = \Phi/(2\Phi_0)$. Note that we also consider the orbital effect of the magnetic field inside the proximitized superconducting wire parts, such that we also put Peierl's phase in these regions. In Fig. 4.25 numerically computed CPRs for different flux values are shown. For $\Phi = 0$ the CPR exhibits a skewed shape, which corresponds to a junction with high transparency. At $\Delta\varphi = \pm\pi$ the curve is weakly smoothed due to the finite temperature. By slowly increasing the axial magnetic field strength, the CPR starts to change its form quite drastically. First of all, the magnitude of the critical current $I_\mathrm{c}(\Phi) = \max_{\Delta\varphi}|I_\mathrm{s}(\Delta\varphi, \Phi)|$ is being reduced very quickly with rising flux. Further increasing η would eventually fully suppress the supercurrent flow in the junction. Moreover, the curves start to exhibit small peaks with regular oscillations on top of the standard sinusoidal shape. The positions of the local maxima depend on the flux value and also start to vanish again for larger field strengths.

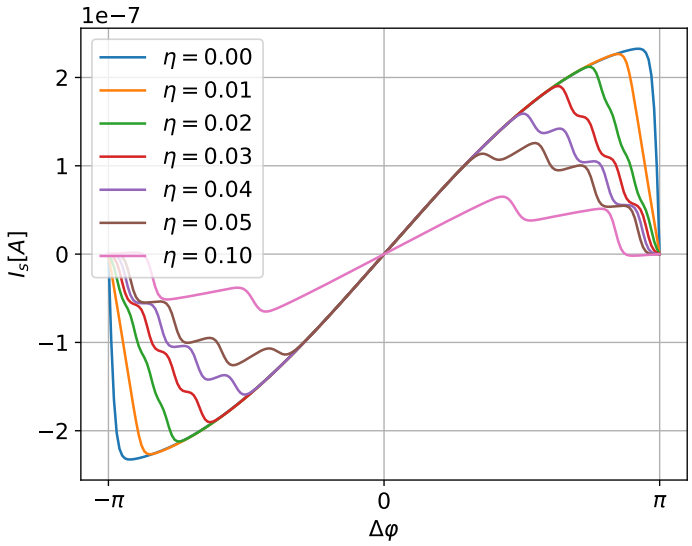

Figure 4.25: Current-phase relations computed utilizing Eq. (3.56) for a fully proximitized topological insulator nanowire Josephson junction illustrated in Fig. 4.24. The system parameters were fixed to $w = 120$ nm, $h = 80$ nm, $L = 25$ nm, $a = 5$ nm, $T = 0.05$ K, $\mu = 22$ meV and $\Delta_0 = 0.25$ meV. With increasing magnetic flux the CPR changes its shape. Smaller peaks appear and the overall current magnitude is reduced.

Naturally the question arises, what is responsible for these interesting features. In order to answer this question it is useful to calculate the ABS spectrum of such a Josephson junction. We perform this task in two ways. The first procedure will be the numerical diagonalization of a finite tight-binding system that corresponds to the studied Josephson junction. Here we employ the theory, which was introduced in Sec. 3.6.1. The junction is thereby implemented with the same geometrical values, except that the full system has a length of 4999 nm, such that each of the superconducting leads has a length of 2487 nm. An additional hopping in the wire axis direction connects the two ends of the superconducting leads. Thereby, the setup takes the form of a torus, where an exemplary system is shown in Fig. 3.6. A final modification is applied to the center of the normal-conducting region. Here we add the phase factor in the hopping in x-direction, which contains the superconducting phase difference.

The second approach to determine the ABS spectrum is an analytical calculation. We follow the approach of Pientka et al. in Ref. [158] and employ Beenakkers scattering matrix theory discussed in Sec. 3.6.1 in order to derive an expression for the ABS. The detailed derivation can be found App. A.1, whereas here we highlight only the important physical effect one has to consider. It concerns the third term in Eq. (2.56), which stems from Andreev reflection at the interfaces of the normal and the superconducting regions. The orbital magnetic field leads to a modification of the phase of the Andreev reflection if it also penetrates the superconductors. An analogous effect has recently been studied in Ref. [158] in planar Josephson junctions with a Zeeman term in the

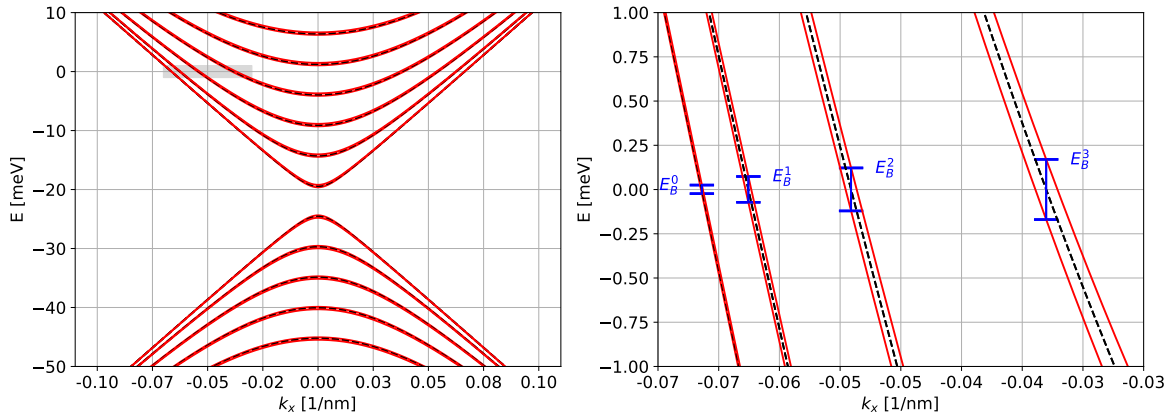

Figure 4.26: (a) Bandstructures of the normal-conducting region of the Josephson junction setup used for the results shown in Fig. 4.25. The black dashed lines correspond to $\eta = 0$, while the red lines represent the flux ratio $\eta = 0.04$. (b) Zoom into the shaded region of (a), where the splitting energies E_B^n of different subbands are shown in blue.

superconducting leads. In the case of TI nanowires a longitudinal B-field has the same effect as such a Zeeman term, namely the splitting of the spin up and spin down bands. The phase factor becomes then $\chi_\pm = \arccos\left((E_k^n \pm E_B^n)/\Delta\right)$. Here E_B^n takes the value of the Zeeman term E_Z. In the case of TI nanowires the splitting is not constant for all subbands, which are labelled by the angular momentum quantum number n. Instead, we have a strong dependence on the chemical potential μ and the respective band index number. The magnitudes of the splitting energies can be calculated by

$$E_B^n = E_k^n(\Phi) - E_k^n(\Phi = 0). \tag{4.22}$$

In Fig. 4.26 (a) the bandstructure of the normal-conducting TI region of the above studied Josephson junction is plotted. For the chemical potential of $\mu = 22$ meV we have four open subbands at $E = 0$, where each of them is twice degenerate (black dashed lines). Applying a flux ratio of $\eta = 0.04$ splits the degeneracy (red lines) and the subbands start to separate with E_B^n. For better visibility an inset of the grey shaded region in Fig. 4.26 (a) is shown in Fig. 4.26 (b). The splitting energies E_B^n are marked in blue, where the energy is measured from $E = 0$. One can clearly observe that the energies differ strongly in each of the subbands and we obtain four splitting energies for our system.

With all of the above considerations the energies of the ABS read

$$E_{\mathrm{ABS}}^n = \pm\Delta \cos\left[\frac{1}{2}\arccos\left(r^2\cos\left(2\theta_-^n\right) + (1-r^2)\cos(\Delta\varphi)\right) - \theta_+\right] \mp E_B^n, \tag{4.23}$$

where r denotes a normal reflection amplitude and $\theta_\pm = (k_\mathrm{e} \pm k_\mathrm{h})\frac{L}{2}$ enter as angles of the dynamical propagation in the junction. The above equation makes it clear that the ABS energies will be shifted in energy by the amount of $\mp E_B^n$, which scales directly with the magnetic field strength.

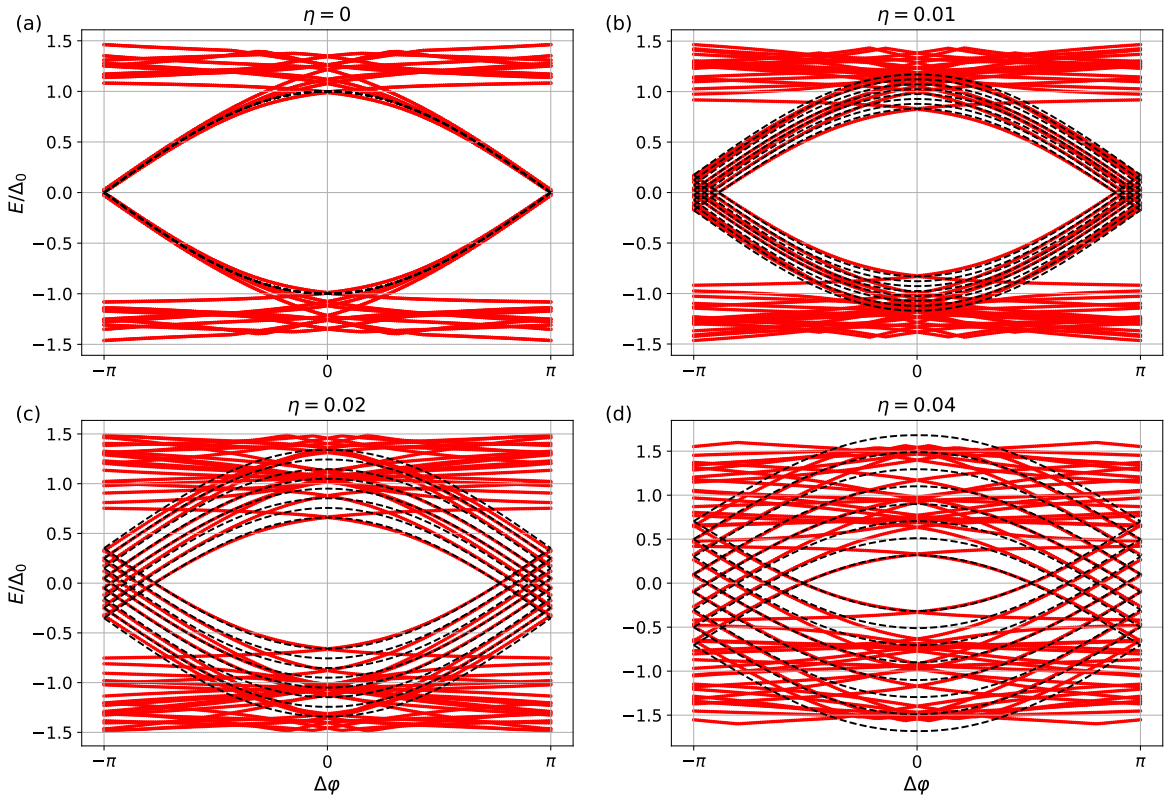

Figure 4.27: Comparison of ABS spectra obtained by numerical diagonalization of a finite tight-binding system (red dots) and by evaluating Eq. (4.23) (black dashed lines). Both approaches give perfectly agreeing results. The system parameters are the same as those for the data of Fig. 4.25.

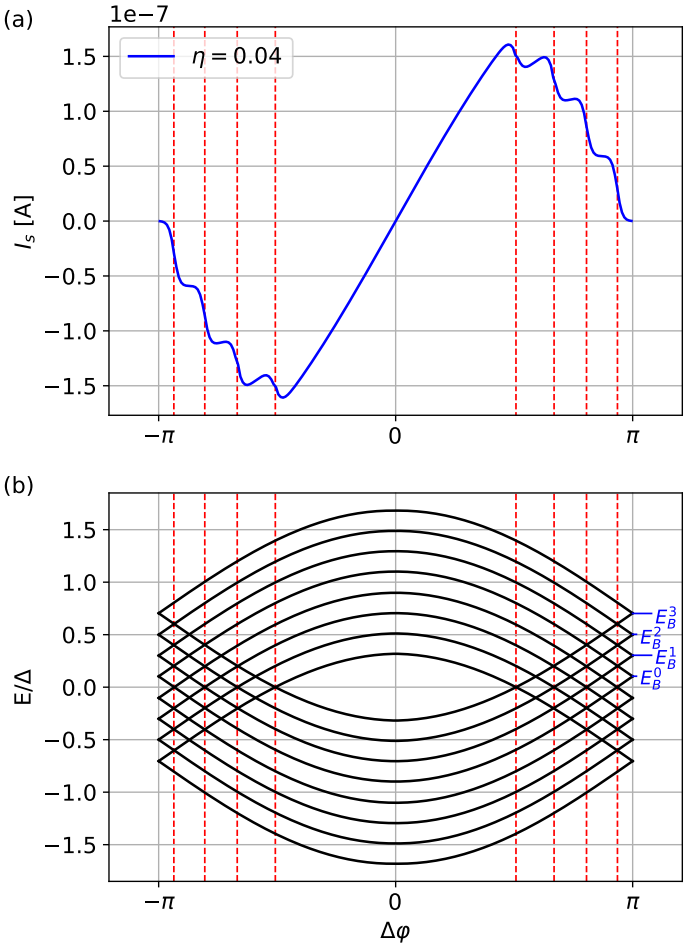

Figure 4.28: Comparison between (a) current-phase relation and (b) the corresponding ABS spectrum for $\eta = 0.04$. The red dashed lines mark the zero energy crossings in the ABS spectrum.

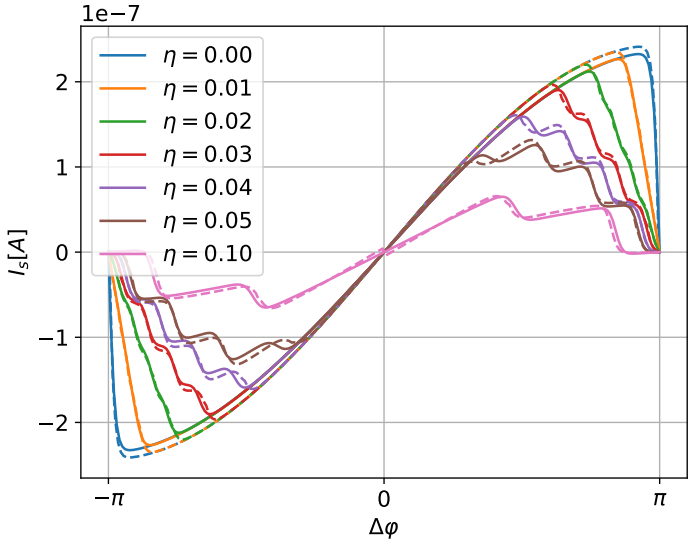

Figure 4.29: Comparison of current-phase relations for different flux ratios, which were calculated numerically with Eq. (3.56) and analytically using Eq. (3.55) shown in continuous and dashed lines, respectively.

In Fig. 4.27 the ABS spectra for different values of η are illustrated. All of the panels certainly show that the analytical (black dashed lines) and numerical (red dots) results agree perfectly. Panel (a) illustrates the spectrum for no axial magnetic field. The ABS energies are four times degenerate and show the expected cosine-like dependence on the phase difference. Also, in the numerical results the superconducting band gap edge is observable at $E/\Delta_0 = 1$. By slowly increasing the magnetic flux ratio to $\eta = 0.01$, $\eta = 0.02$ and $\eta = 0.04$ the degeneracy of the ABS spectrum is slowly lifted, where bands are shifted in energy by E_B^n. Moreover, the size of the superconducting gap is at the same time decreasing. This will eventually lead to a vanishing supercurrent flow. The reason for that lies in the pair breaking effect of the orbital magnetic field and is in agreement with previous studies like Ref. [215], where the stability of the superconducting gap in such TI systems was studied. Due to the shift of ABS energies in positive and negative energy directions, non-degenerate zero energy crossings appear. These crossings are responsible for the emergence of the oscillations and local peaks on top of the sinusoidal CPR shape. In Fig. 4.28 this is shown in more detail. Panel (a) illustrates the current-phase relation for $\eta = 0.04$, while in (b) the corresponding analytical ABS spectrum is plotted. To highlight the direct relation between the zero energy crossings and the maxima in the CPR, their positions are marked by red dashed lines in both panels. The CPR is the sum of all derivatives of the ABS curves with respect to the phase difference $\Delta\varphi$ for $E < 0$. So whenever there is a change in slope at a zero energy crossing, the current is first reduced before the weight of another ABS state is adding up again.

Finally, this result can be further checked by directly computing the current-phase re-

lation from the analytical ABS spectrum given by Eq. (4.23). The temperature dependent supercurrent can be computed from the ABS spectrum by considering Eq. (3.55). In Fig. 4.29 the numerical CPRs are plotted in continuous lines, while the analytical results are shown as dashed lines in the corresponding colors for different values of η. For all cases we see a very good agreement between the two approaches.
Up to now, we have seen that the orbital magnetic field can modify the accumulated phases and therefore also leads to oscillations in the CPR. Moreover, the axial magnetic field leads to a quick decay of the superconducting gap in TI nanowires which are fully proximitized by an external s-wave superconductor. By breaking the rotational symmetry in the wire surface, it was shown in Ref. [215] that the superconducting gap will prevail also for larger field strengths. In real experiments the symmetry is either broken by local lattice defects and impurities, or by the sample construction itself. This will be discussed further in the next section.

4.6.2. Periodic supercurrent oscillations in axial magnetic fields

In this section realistic TI Josephson junctions will be studied and we will construct a model that can explain flux-periodic supercurrent oscillations, which are observed in experiments of the Weiss group at the University of Regensburg. Let us start by giving important details about the studied samples. HgTe nanowires serve as the basis for the construction of the Josephson junctions. The wire structure is first etched into a HgTe slab sample. Therefore, the bottom surface sits on top of a GaAs substrate. For simplicity of the fabrication process of Josephson junctions, the external superconducting contacts are deposited from the top. In the experiments niobium is used as the external s-wave superconductor. It is deposited as stripe like structures with thickness between 60 and 120 nm, while the stripe width is usually in a range of 600 nm. The bottom surface cannot be directly contacted, such that the wire circumference is only partially proximitized. In Fig. 4.30 (a) a scanning electron micrograph top view image of a real HgTe Josephson junction is shown (provided by the Weiss group), while in 4.30 (b) a schematic 3D plot of the system can be seen for better visibility. In the experiments, differential resistance maps were measured for the TI Josephson junctions with respect to an applied DC current along the junction and an axial magnetic field $B_\parallel$. Contrary what was discussed in the section before, the induced flux was tuned to high multiples of the superconducting flux quantum Φ_0. Interestingly, the observed switching current (the current at which the junction gains a finite resistance) exhibited in some of the measured samples flux-periodic oscillations. An example measurement is shown in Fig. 4.30 (c). The peaks are marked with vertical dashed lines and remarkably, the peaks are distributed at integer multiples of half of a superconducting flux quantum. Analogous measurements in semiconductor nanowires [166, 221, 222] have also shown current oscillations with a regular period of a full superconducting flux quantum. These can be explained by standard Aharonov-Bohm interference effects. Oscillations with half of that period can not be directly explained by that theory, such that more junction details need to be considered.
In the following, we will again use the Green's function technique of Sec.3.6.2 to obtain

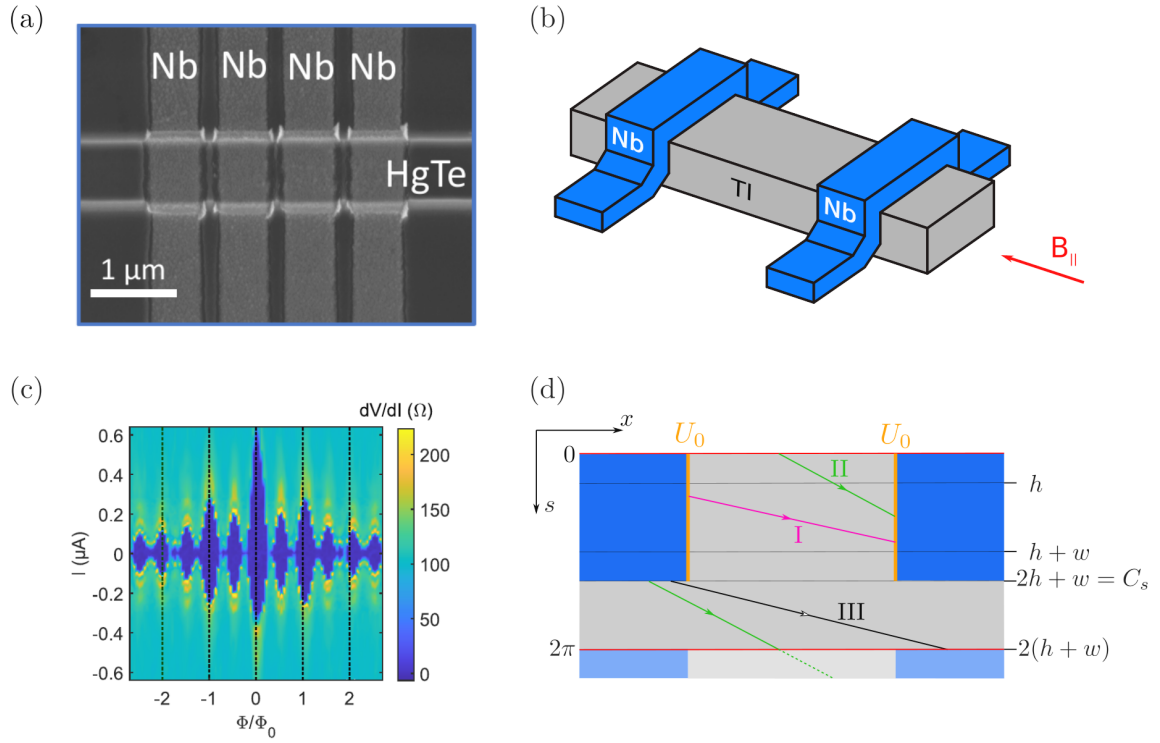

Figure 4.30: (a) Scanning electron micrograph top view of a HgTe nanowire Josephson junction. Niobium is deposited on the top as stripes with a width of a few hundred nanometers and perpendicularly to the nanowire axis. (b) Schematic 3D plot of the nanowire Josephson junction. The superconducting niobium is only partially contacted to the wire surface. (c) Experimental measurement of a differential resistance map. The switching current shows flux-periodic oscillations with a period of $\Phi_0/2$, (d) Schematic 2D plot of the unwrapped wire surface. Superconducting regions are shaded in blue, while normal-conducting parts are colored in grey. The edges marked in red symbolize periodic boundaries. Adapted from Ref. [4].

the current-phase relation for varying axial magnetic fields and based on that compute the critical current as $I_\mathrm{c}(\Phi) = \max_{\Delta\varphi} |I_\mathrm{s}(\Delta\varphi, \Phi)|$. We therefore assume that the critical current has analogous properties as the switching current of the experiments, at least in regards of the flux periodicity. In order to capture the specific geometry of the realistic HgTe Josephson junctions, we start by modifying the model of the previous section. First, we redefine the superconducting pairing potential. Instead of a homogeneously induced gap around the wire perimeter, as given by Eq. (4.21), we now take into account the partial coverage of the wire surface by the external niobium contacts. The superconducting pairing potential then reads

$$\Delta(\boldsymbol{r}) = \begin{cases} \Delta_0 \exp(\mathrm{i}\varphi_L) & \text{for } x < 0 \text{ and } 0 < s < C_s, \\ \Delta_0 \exp(\mathrm{i}\varphi_R) & \text{for } x > L \text{ and } 0 < s < C_s, \\ 0 & \text{otherwise,} \end{cases} \tag{4.24}$$

where C_s is the length of the superconducting coverage around the wire circumference. Due to the partial surface coverage, the superconducting niobium is forming an open ring structure around the wire circumference. Therefore the phases of the pairing potential will experience a local phase modulation around the wire circumference. As the simplest approximation, we assume that the external flux is completely screened in the superconducting electrodes, such that the phases are given by [100, 223, 224]

$$\varphi_{L/R} = \pm\frac{\Delta\varphi}{2} + 2eAs/\hbar, \tag{4.25}$$

where $A = \Phi/C$ is the vector potential of the axial magnetic field. Plugging in the vector potential, we arrive at

$$\varphi_{L/R} = \pm\frac{\Delta\varphi}{2} + 2\pi\frac{\Phi}{\Phi_0}\frac{s}{C}. \tag{4.26}$$

The superconducting phases therefore vary locally by moving around the wire circumference and are directly tuned by the externally applied flux. This assumption is an essential ingredient for finding $\Phi_0/2$ periodic supercurrent oscillations. Next, we will introduce a local barrier at the interface between the normal junction part and the superconducting contacts. From the experimental measurements it is known that the flux periodic oscillations are typically observable in samples with a low transparency. In order to include this observation in our model, we define

$$U(x, s) = U_0\Theta(s)\Theta(w + 2h - s)[\delta(x) + \delta(x - L)]. \tag{4.27}$$

This serves as a phenomenological parameter, which incorporates the very complicated and divers physical scattering properties of a realistic junction. The position of such a barrier is justified by the actual fabrication process of the junctions. Before niobium is deposited on top of the HgTe material, a CdTe capping layer needs to be etched away [32]. If the capping layer is not removed completely in this process, the remains can serve as an interface scattering barrier. This justifies the local barrier position,

which is the second important ingredient in our model. Fig. 4.30 (d) visualizes the essential details of the effective surface implementation of the TI Josephson junction. The plot illustrates the unwrapped surface of the junction. In blue are shown the proximitized surface regions which are affected by an induced superconducting gap, while grey regions correspond to normal-conducting surface elements. Note that the red lines are marking the cut along the junction direction, such that the blurred structure below is a periodic continuation of the upper surface edge. This model is then discretized and implemented in Kwant, such that the critical current can be calculated numerically by Eq. (3.56). In order to have a good balance between numerical cost and experimental system sizes we fix the following setup parameters. The wire dimensions are set to width $w = 300$ nm and height $h = 80$ nm, while the length of the Josephson junction is $L = 200$ nm. The effective surface Hamiltonian is discretized and implemented on a square grid with lattice spacing $a = 4$ nm. As we want to simulate surface states of HgTe, we fix the Fermi velocity to $v_\mathrm{F} = 5{\cdot}10^5$ m/s. Also, due to the usage of niobium as s-wave superconductors, we choose an induced superconducting gap of $\Delta = 0.8$ meV. This value is in good agreement with experimental estimates for the HgTe samples (see Refs. [4, 32]), but the exact value is of no importance for the flux periodicity of the current. The value only tunes the magnitude of the current amplitude. Moreover, the chemical potential is set to $\mu = 30$ meV, such that we are still in a converged energy range with a high number of open channels. Increasing the Fermi energy would also increase the current magnitude due to the rising number of accessible subbands. Finally, in order to get rid of the Fermion doubling problem we employ a Wilson mass term (see Sec. 3.2) with $E_\mathrm{gap} = 60$ meV. Before we study the Josephson junction with partially proximitized surface regions, we also want to discuss the flux dependence of the critical current in a homogeneously proximitized nanowire. In case of a fully proximitized circumference like shown in Fig. 4.24 (a), the superconducting phase φ is no longer varying around the circumference. Due to the closed superconducting shell, the winding of the phase has to be quantized, such that the wave function is single valued by a full rotation of 2π. Figure 4.31 (a) shows the calculated critical current as a function of the applied flux ratio. For this setup no periodic oscillations are observable. Instead, I_c is monotonously decaying with increasing flux. This observation matches the findings of Ref. [215], where the authors show a quick breakdown of the superconducting gap due to pair breaking effects of an axial magnetic field. Some measured samples in the experiment exhibited such a monotonously decaying critical current. Therefore, we assume that in these samples the superconducting proximity effect is present in the whole wire circumference.

However, the flux modulation changes drastically, if only partial proximitization is being considered. In Fig. 4.31 (b) the computed critical current for this system configuration is plotted. More precisely, the critical current is calculated with respect to the applied axial magnetic flux and for different values of the local barrier U_0. For a clean system with $U_0 = 0$, the critical current amplitude is maximal and Φ_0 periodic in flux. By increasing the magnetic flux, the current is initially strongly decaying and then, after saturating at a quasi plateau, it starts to increase again before it reaches its new maximum at Φ_0. Then, with increasing barrier strength, the current magni-

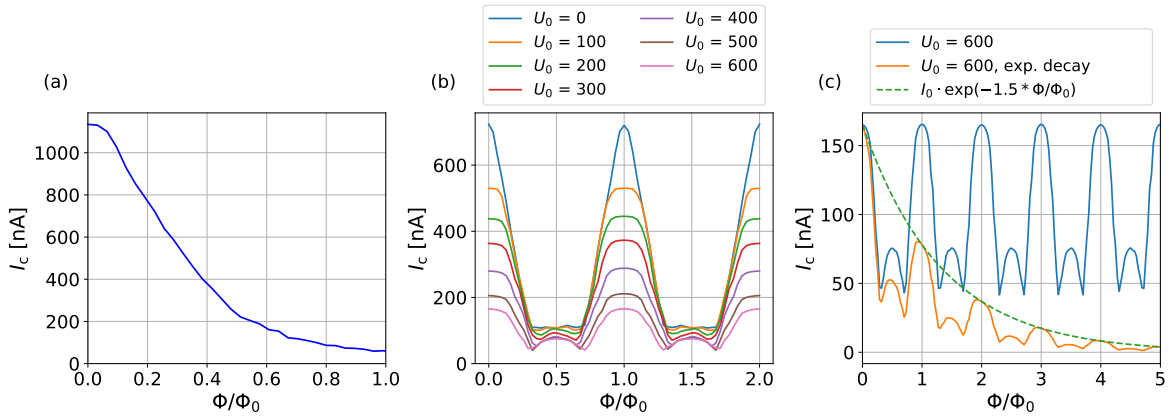

Figure 4.31: Numerically calculated critical currents as a function of an applied axial magnetic flux for different Josephson junction configurations. In (a) we assume a fully proximitized nanowire circumference, which exhibits monotonous decay of I_c with increasing flux strength. Panel (b) shows the critical current for a partially proximitized nanowire surface and for different local barrier strengths. Note that the barrier strength is given in units of $[U_0] = \text{meV nm}$. With increasing magnitude of U_0 the overall amplitude decreases until a $h/(4e)$-periodic current remains. (c) shows again the critical current for $U_0 = 600$ meV nm of (b). The monotonous decay of I_c which is observed in the experiment can be fitted by assuming an explicit flux dependence of the induced superconducting pairing strength (orange curve). Panel (c) is adapted from Ref. [4].

tude is decreasing very strongly at integer multiples of Φ_0. Contrary, at odd integer multiples of $\Phi_0/2$, the current is staying almost unaffected. At the strongest barrier value of $U_0 = 600$ meV nm additional peaks at $\Phi = (2n+1)\Phi$ ($n \in \mathbb{Z}$) are present. For better visibility, this curve is again plotted in Fig. 4.31 (c) (blue curve) over a broader flux range. We see that the magnitude of the critical current is periodically oscillating and, in contrast to the experimental measurements, not decreasing with increasing flux. The reason for that lies in the fact that the BdG spectrum of the partially proximitized nanowire is $2\Phi_0$ flux periodic due to the choice of the superconducting phase which depends directly on the vector potential $\boldsymbol{A}$ [see Eq. (4.26)]. The model neglects yet that also the amplitude of the superconducting pairing potential, i.e., Δ_0, depends explicitly on the applied flux. For simplicity, we assume that the pairing term mainly affects the amplitude of the computed supercurrent, such that we define

$$\Delta_0(\Phi) = \Delta_0 \exp(-\alpha\Phi/\Phi_0), \tag{4.28}$$

where α is a constant that determines how fast the gap and therefore the current I_c decays to zero. In Fig. 4.31 (c) we plot also the exponentially scaled critical current with $\alpha = 1.5$. This value reproduces the decrease in current magnitude of the experimental measurement shown in Fig. 4.30 (c). Also note the matching feature that in both curves the third peak exhibits a larger magnitude than the second one. The difference in current magnitude between numerics and experiment is around a factor of four. This discrepancy can be explained by the low chemical potential which is used in the

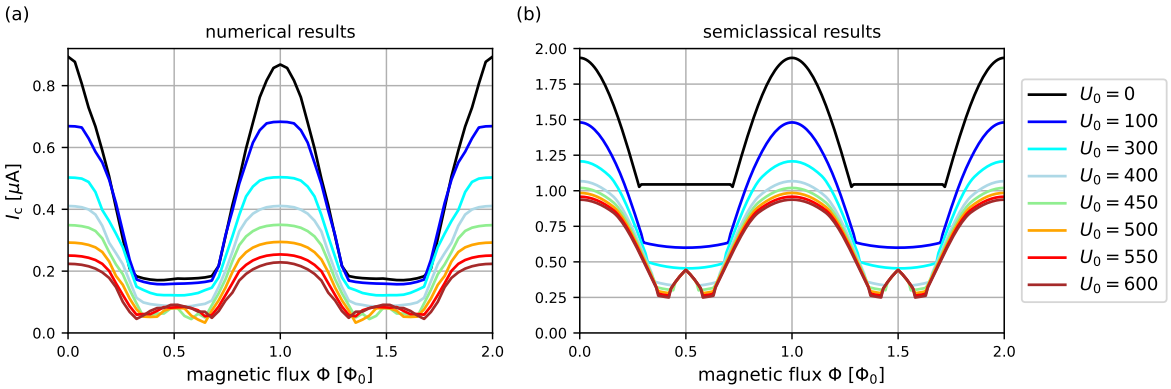

Figure 4.32: Comparison between numerically and analytically computed critical currents in a partially proximitized TI nanowire Josephson junction. The latter was provided by Dr. Fuchs. Note that U_0 is given in units of $[U_0] = \text{meV}\,\text{nm}$. Adapted from Ref. [4].

simulations. By using a larger Fermi energy, more modes can contribute to the current and in turn increase the amplitude. However, one would also need to reduce the lattice constant and thereby increase the numerical effort.

We see that the employed model captures the essential flux-periodicity of the supercurrent quite well. The origin of such a critical current curve can be explained by a semiclassical picture, which was studied in detail by Dr. Fuchs in Ref. [209]. Here we will only shortly emphasize the most important points of the computation. For more details of the analytical calculation, we refer the reader to the PhD thesis of Dr. Fuchs in Ref. [209] with its detailed explanations.
The current is computed via [167]

$$I = \frac{1}{2\pi}\int \mathrm{d}s \int \mathrm{d}k_s\, i(s,k_s) = \frac{k_\mathrm{F}}{2\pi}\int \mathrm{d}s \int \mathrm{d}\theta \cos(\theta) i(s,\theta), \tag{4.29}$$

where θ is the angle between the angular momentum k_s and the Fermi momentum k_F. Essentially, the analytical calculation is then based on the summation of three basic current contributions $i(s,\theta)$. Each of these terms corresponds to different types of semiclassical paths of particles, which move through the Josephson junction as Andreev bound states and carry current from one superconducting lead to the other. These are visualized in Fig. 4.30 (d), where type I paths correspond to the direct propagation between the superconducting surface regions. Type III paths cross the normal-conducting bottom surface and connect the edges of the superconducting areas, which are not affected by the local barrier U. Finally, type II paths are a mixture of the previous two types, where start or end points are lying on the distinct superconducting edges. Out of these three categories, the type III paths are the essential ones to obtain a $\Phi_0/2$ flux periodicity. It explicitly stems from the flux tuned phase difference at the start and end points, given by Eq. (4.26), in combination with an additional Aharonov-Bohm phase

which is accumulated by travelling through the Josephson junction. The corresponding ABS energies read [209]

$$E = \pm\Delta_0\sqrt{1 - \tau\sin^2\left(\tfrac{1}{2}\Delta\varphi - \gamma\right)}, \tag{4.30}$$

where γ is the flux induced accumulated phase of a classical trajectory. It reads

$$\gamma = \frac{e}{\hbar}\int_\Gamma \mathrm{d}\boldsymbol{s}\cdot\boldsymbol{A} = n\pi\frac{\Phi}{\Phi_0}. \tag{4.31}$$

In a clean junction with a high transparency τ, the type III current contribution is much lower compared to the other two path types, such that this periodicity is not directly observable. The current magnitude can be increased by considering higher Fermi energies, such that modes with high angular momenta become accessible. This finding is also in accordance with experimental measurements, where an external gate could induce the $\Phi_0/2$ periodicity (see Ref. [4]). The key point, why these oscillations become observable, lies in the presence of the local barriers U_0. These considerably reduce the current contributions of type I and II paths by gapping out the corresponding Andreev bound states. What remains are the type III paths, which are not or only weakly affected by the local barriers.

A direct comparison between numerics and analytics is shown in Fig. 4.32 for a junction with the same parameters as above, except a shorter length of $L = 100$ nm. Note that qualitatively, both approaches give consistent results. By increasing the barrier strength, the current peaks at integer multiples of Φ_0 are considerably decreased, while additional current peaks between them emerge. However, a clear mismatch is present in the overall current magnitude. The numerical approach gives much smaller current amplitudes than the semiclassical method. There are two main reasons for this discrepancy. On the one hand, the semiclassical approach is computed for the pure short junction limit. In the numerical calculations, also length dependent effects are included. Test computations showed that reducing the junction length L in the numerics considerably increases the current amplitude. Then, on the other hand, the semiclassical approach assumes a constant pairing potential Δ_0 for all Andreev bound states. Due to the partial proximitization along the wire circumference, this is no longer the case. Each quantum confined surface state will in fact experience its own effectively induced gap, stemming from the difference in angular momentum. In the numerical approach this information is included and we can easily show this by the direct computation of the corresponding ABS spectra. Fig. 4.33 shows ABS spectra which were calculated by the diagonalization procedure introduced in Sec. 3.6.1. Due to the large computational effort, we reduced the width of the nanowire to $w = 120$ nm and increased the lattice constant slightly to $a = 5$ nm, while keeping the other geometric parameters as above. The overall length of the finite system is set to $L = 6000$ nm. Moreover, in order to increase visibility of the spectral properties, we reduced the number of ABS states by lowering the chemical potential to $\mu = 22$ meV. The eigenenergies in all three panels were normalized by the pairing amplitude Δ_0. First, let us discuss the spectra shown in

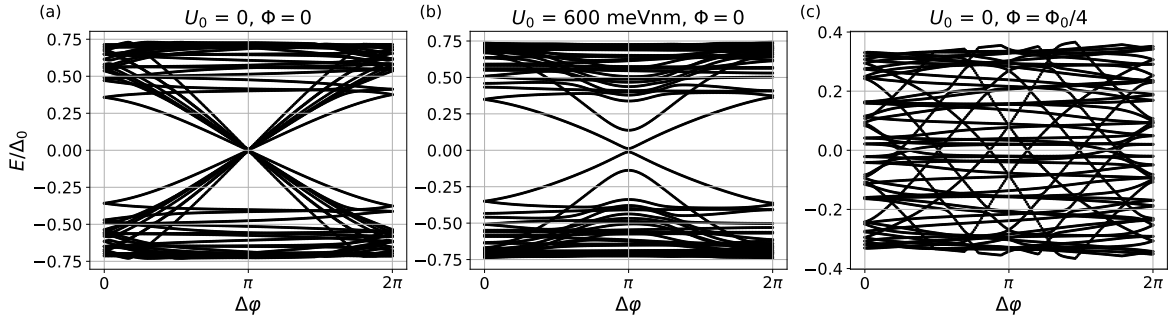

Figure 4.33: ABS spectra of a partially proximitized TI nanowire surface for different barrier strengths and flux values. Panels (a) and (b) are adapted from Ref. [4].

Fig. 4.33 (a) for no applied flux and no barriers in the system. Here it is only assumed that the top and the two side surfaces of the nanonwire experience superconducting pairing. As we are considering a clean system, the ABS energies should obey the known expression $E(\Delta\varphi) = \Delta_i \cos(\Delta\varphi/2)$ and we see that each of the ABS branches can be fit by such an expression. Note that at zero phase difference the ABS energies are equal to the induced pairing strength and obviously this value differs for each of the present states in the computed spectra. Exactly this property is missing in the analytic calculations. These features remain also in the presence of a non-zero barrier, which is shown in Fig. 4.33 (b). The barrier gaps out the ABS branches at $\Delta\varphi = \pi$, but leaves the rest of the spectrum intact. For completeness, in Fig. 4.33 (c) the barrier is again put to zero, while a weak magnetic field is applied parallel to the nanowire axis. The orbital effect of the magnetic field is weakening the induced gap values Δ_i. At the same time, one can certainly observe that the spectrum becomes much more complicated and ABS branches are shifted with respect to each other.

Finally, in order to check the semiclassical picture from above numerically, we can compute the local supercurrent density on the surface. Here we employ the methodology which was introduced in Sec. 3.6.2. In Fig. 4.34 local supercurrent densities are illustrated for different values of the magnetic flux. The system configuration is the same as in Fig. 4.31 (c) with $U_0 = 600$ meV nm, such that we are probing different flux values along the blue curve. For each of the considered critical current values we extract the corresponding absolute value of the phase difference and define our tight-binding system with these fixed parameters. The case without local barriers is illustrated in Fig. 4.34 (a) as a benchmark example. The highest supercurrent density is located at the top surface, what is to be expected on the partially proximitized surface. Then, by introducing the strong barriers, the current density on the top surface is almost completely erased and only the bottom surface is hosting supercurrent flow (see panel (b)). Next, we switch on the axial magnetic field and plot in panels (c) to (f) the calculated densities for four varying flux values. In (c) one can clearly observe that the current is flowing on the bottom surface from the upper edge of the left partially superconducting reservoir to the right lower edge of the other lead, just as expected from the locally varying phase around the wire circumference. It matches the semiclas-

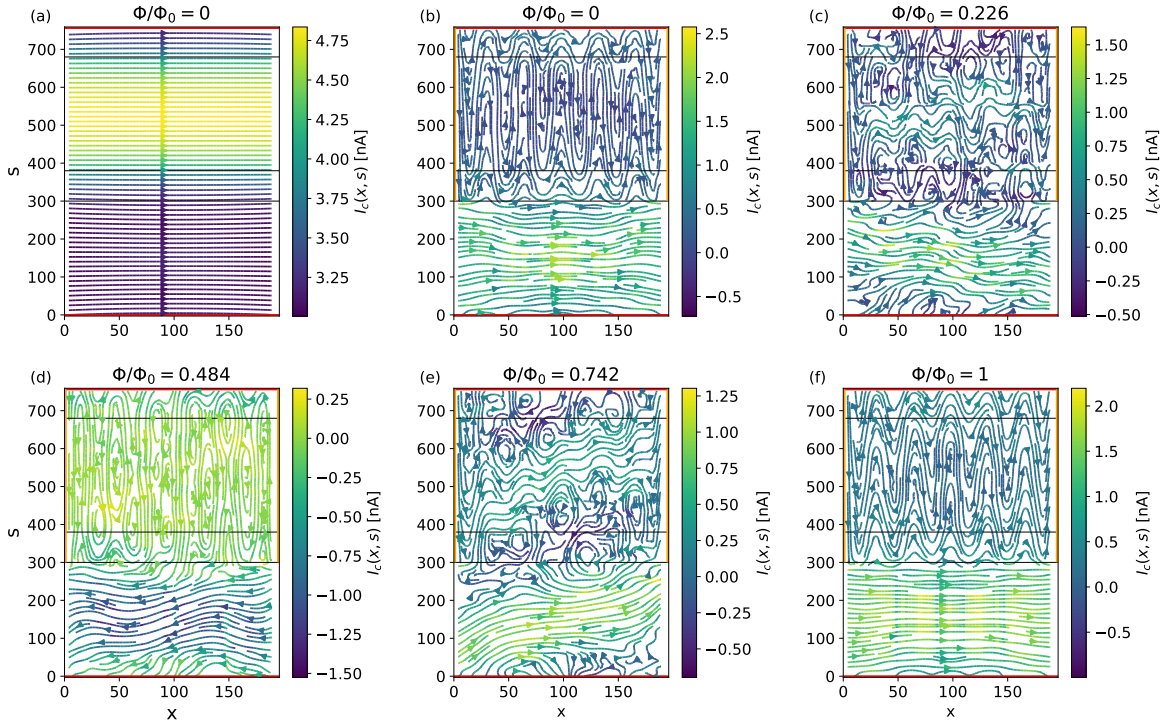

Figure 4.34: Local supercurrent density for different applied axial magnetic fluxes. In (a) the barrier strength U_0 is set to zero, the highest current density is located at the top surface. Panels (b) to (f) show the supercurrent density with barrier strength $U_0 = 600$ meV nm and for increasing flux strength. With a non-zero barrier, the highest density is located at the bottom surface. Edges with periodic boundary conditions are marked in red, while the local barriers are shown in orange.

sical picture of the type III paths (compare with Fig. 4.30 (d)). By further increasing the magnetic flux to almost half of a flux quantum Φ_0 the current direction is reversed and flowing more straightly, while for $\Phi \approx 0.75\Phi_0$ in (e) the current direction is again reversed and flowing between opposite edges as in (c). Lastly, with a full flux quantum applied to the wire cross-section, the current is again flowing straightly on the bottom surface between the two superconducting reservoirs. This observation makes sense, as in Eq. (4.30) the effective phase difference

$$\Delta\varphi^{'} = \Delta\varphi + 2\gamma = \Delta\varphi + 2\pi n\frac{\Phi}{\Phi_0}, \tag{4.32}$$

is periodic in Φ_0.

In this section we have shown that flux periodic supercurrent oscillations can occur in TI nanowires which are partially covered by an external s-wave superconductor. The current modulation stems from a flux induced phase variation around the wire circumference and the suppression of current contributions with a different flux-periodicity via local barriers at the N/S-interfaces. Numerics, as well as semiclassical calculations, show consistent results for the developed model and explain the experimental measurements to a large extend. The discussed features are a signature of dominant surface transport and highlight therefore the topological nature of HgTe nanowires.

5. Transport and bound states in superconducting single-layer and bilayer graphene

We start this chapter by studying in detail the emergence of locally bound Yu-Shiba-Rusinov states induced by a magnetic hydrogen impurity that is sitting on top of superconducting bilayer graphene. This is of great importance, as these states are responsible for the modification of the spin-relaxation behavior in the superconducting state. We show that the spectral weight, given by the resonance width of a magnetic impurity in the normal DOS, is directly related to the energy separation of the YSR energies and the superconducting band gap edge. This in turn directly affects the temperature dependence of the spin-relaxation behavior. Moreover, we show that signatures of the magnetic resonances can also be directly observed in setups like Josephson junctions which are easier to realize experimentally.

5.1. Yu-Shiba-Rusinov states in superconducting bilayer graphene

In section 2.4.5 we already introduced YSR states as bound states that are localized in the close vicinity of superconducting regions which experience magnetic exchange interactions. The YSR spectra for a hydrogen adatom, as well as for fluorine, in superconducting single-layer graphene were computed analytically by Dr. Kochan in Ref. [2]. Here we will focus on the special case of a magnetic hydrogen adatom that is chemisorbed to the top layer of superconducting bilayer graphene. Contrary to single-layer graphene, this material offers the possibility of studying the YSR states with an impurity at two geometrically distinct positions. These are the so-called dimer and non-dimer sites, where the first one corresponds to carbon atoms in the A_2 sublattice and the latter to sites in the B_2 sublattice in Fig. 2.5 (a). Such a system can be treated numerically in several ways. First one could employ the kernel polynomial method that approximates the DOS with Chebyshev polynomials [225–228]. By computing the DOS in the range of the superconducting gap and spatially close to the impurity, one has to look for peaks in this interval. Those peaks directly correspond to the YSR eigenenergies. Note that Kwant already offers the possibility to employ this method by the implemented KPM package. The second way of computing the YSR spectra is by exact diagonalization of a finite system. Here one has to simply look for eigenenergies

inside the superconducting gap, i.e., in the interval $[-\Delta;\Delta]$.

We chose to use diagonalization of a finite tight-binding system with hard-wall boundary conditions, because this also gives us access to the eigenfunctions of the YSR states. The bilayer graphene substrate is implemented by the Hamiltonian given in Eq. (2.15). We want to point out that for the computation of the YSR states we set $\gamma_3 = 0$ and $\gamma_4 = 0$. There are two reasons for this simplification. On the one hand, we need to treat a finite tight-binding system with many sites in order to achieve converged YSR spectra. Therefore, sparsity of the Hamiltonian matrix is of great importance in order to reduce the computational cost. On the other hand, we performed spin-relaxation simulations with the full BLG model of Eq. (2.15) and the simplified model with only γ_1 as the interlayer hopping (the results are shown in the sections below). The results differ only marginally, hinting that γ_3 and γ_4 are not important for the observed physical features. The impurity is introduced by considering $V^{(0)}$ of Eq. (2.16) and the reduced magnetic exchange Hamiltonian given by Eq. (2.20). The relevant parameters for the hydrogen impurity with respect to the dimer and non-dimer positions are given in Tab. 2.2. Finally, superconductivity is introduced by adding the s-wave pairing Hamiltonian

$$H_s = \Delta \sum_m \left(c^\dagger_{m,\uparrow} c^\dagger_{m,\downarrow} + c_{m,\downarrow} c_{m,\uparrow} \right), \tag{5.1}$$

where we assume that the BLG substrate is in close proximity to a normal s-wave superconductor. At the impurity site we assume for simplicity the same pairing strength as in the bilayer system, but note that also differing gap configurations can easily be considered.

The above model is then implemented with Kwant to obtain the tight-binding Hamiltonian. The bilayer graphene system is constructed with width $W = 601a$ and length $L = 601a$. The impurity is located on top of either a dimer or a non-dimer site in the center of the BLG system. This assures that the spatial distance between the system boundaries and the impurity site is as large as possible, while we are still in a regime that is computationally treatable. This is important to achieve a converged result with respect to the system size. Whether the impurity "knows" about the presence of the system boundaries or not depends on the superconducting coherence length $\xi = \hbar v_\mathrm{F}/\Delta$, which should be much smaller than the impurity-boundary distance. Therefore, we additionally need to artificially enlarge the superconducting pairing term and fix it to $\Delta = 50$ meV. This value assures convergence of the YSR spectra, while still exhibiting the qualitative features that are present for a realistic gap size, i.e., $\Delta = 1$ meV.

Numerical diagonalization of the tight-binding Hamiltonian matrix is then performed by employing the open source software package Octave [229]. It can efficiently handle large sparse real matrices while keeping the necessary memory usage of the computer to a minimum. Furthermore, the numerical results can be directly compared to analytically calculated YSR eigenenergies provided by Dr. Fuchs. A detailed discussion of

the calculation procedure can be found in his PhD thesis (see Ref. [209]). The computed YSR spectra are plotted in Fig. 5.1 (a) with respect to the chemical potential in the system. The spectrum corresponding to a dimer (non-dimer) impurity is plotted in black (blue), where the numerical and analytical results are shown in continuous and dotted lines, respectively. Here we want to highlight that the results obtained by the two approaches match almost perfectly. At a first glance, it is clear that the two impurity configurations exhibit completely different spectral properties. First of all, the dimer impurity shows two distinct resonance peaks around the doping levels of $\mu = -0.1$ eV and $\mu = 0.08$ eV. Contrary to that, a non-dimer impurity shows a broad resonance range in the full considered parameter range of μ. In order to show that the numerically studied system parameters are sufficient to capture the relevant YSR features, we also show purely analytical results for $\Delta = 1$ meV in Fig. 5.1 (b). Comparing panels (a) and (b) we see that the spectra are qualitatively the same. This is important for the spin-relaxation calculations in the next sections, as we are there using the realistic gap value of $\Delta = 1$ meV. The properties of the YSR spectra in the two impurity configurations described above can now be related to the normal state bilayer DOS which is perturbed by a certain impurity concentration. Dr. Kochan was able to show in Ref. [3] in a detailed derivation that the following statement holds true: Whether the energies of YSR states are closely located at the edge of the superconducting continuum or inside the superconducting gap, can be computed by the relation

$$E_{\mathrm{YSR}} = \pm \frac{|\Delta|}{\sqrt{1 + 4J^2/\Gamma_c^2}} = \pm \frac{|\Delta|}{\sqrt{1 + 4\tau_{\mathrm{life}}^2/\tau_{\mathrm{Larmor}}^2}}. \tag{5.2}$$

Note that the above equation is valid for systems whose chemical potential μ is tuned closely to magnetic resonant peaks in the perturbed DOS with resonance width Γ_c. For the two resonances ($\mu_\pm$) in case of the dimer hydrogen impurity above, it should then hold that

$$\mu \in [\mu_\pm - \Gamma_{c\pm}/2; \mu_\pm + \Gamma_{c\pm}/2]. \tag{5.3}$$

From Eq. (5.2) it is now possible to conclude that whenever the normal state resonance lifetime $\tau_{\mathrm{life}} = \hbar/\Gamma_c$ is much smaller than the Larmor precession time $\tau_{\mathrm{Larmor}} = \hbar/|J|$, the corresponding YSR energy will lie closely at the edge of superconducting gap $\pm\Delta$. Contrarily, when the opposite relation between the two quantities holds, the YSR energies will lie deep in the superconducting gap.

This finding can now be directly probed by the results shown in Figs. 5.1 (a) and (b). In Fig. 5.1 (c) the normal state DOS, perturbed by an impurity concentration of $\eta = 0.7\,\%$, is visualized (provided by Dr. Kochan). We see that for dimer site impurities the DOS is exhibiting two sharp and distinct resonance, while the non-dimer impurities have a very broad resonance range. Connecting this observation into Eq. (5.2), one would directly expect that for a dimer impurity the corresponding YSR energies would lie closely in the center of the superconducting gap ($E = 0$) when the doping approaches the resonance peaks of Fig. 5.1 (c). Analogously, seeing the broad resonance range of non-dimer impurities in the normal phase DOS, it can be expected that

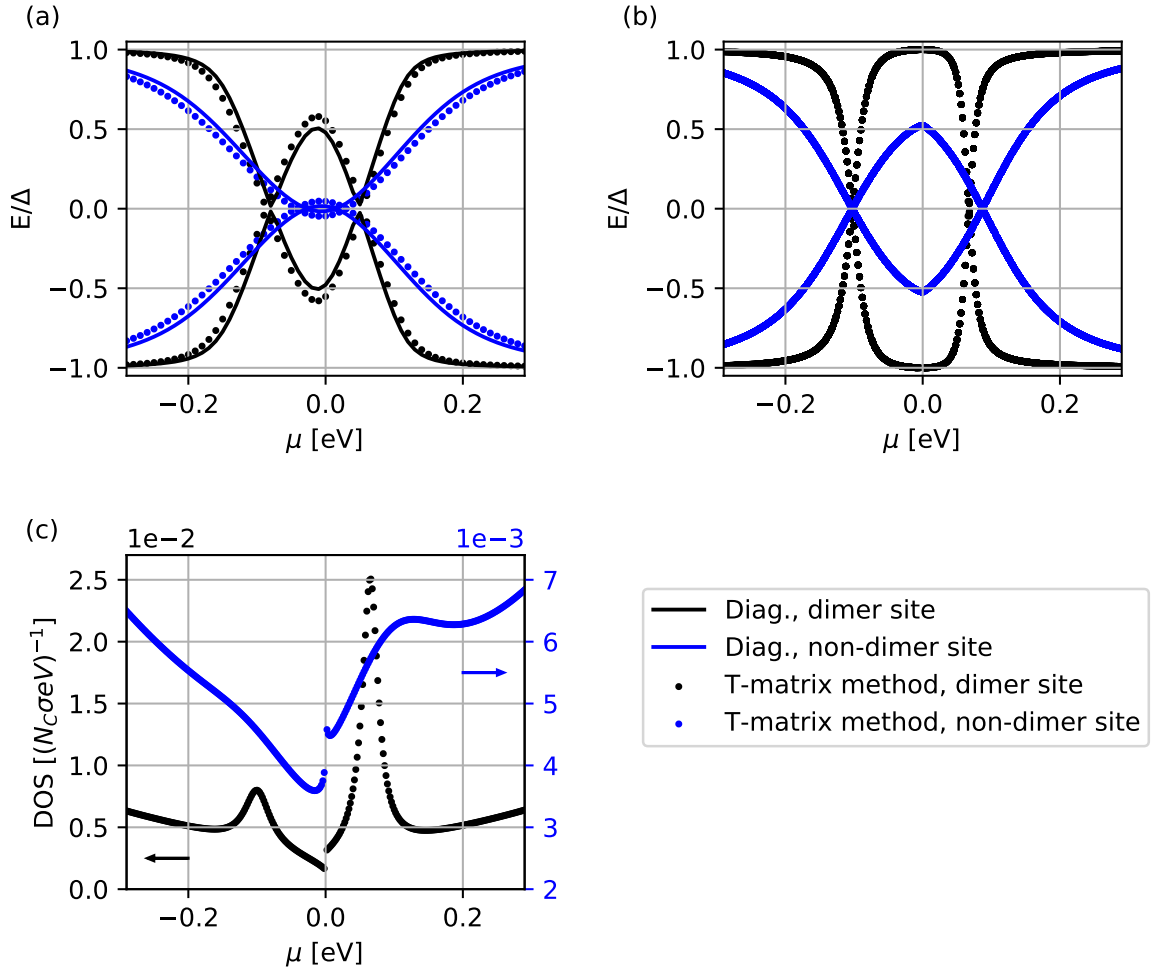

Figure 5.1: YSR eigenenergies and normal state DOS for a magnetic hydrogen impurity located at either the dimer (black) or non-dimer (blue) sites in superconducting BLG. (a) Numerically computed YSR spectrum (continuous lines) for a finite BLG system with width $W = 601a$ and length $L = 601a$ and an assumed gap size of $\Delta = 50$ meV. The energies are normalized by the gap size. The dimer site impurity exhibits two resonance peaks close to $\mu = -0.1$ eV and $\mu = 0.08$ eV, while the non-dimer impurity shows a broad resonance region. The dotted lines are analytic results provided by Dr. Fuchs. Note that analytics and numerics match almost perfectly. (b) Analytic results of YSR energies for a realistic gap size of $\Delta = 1$ meV. The qualitative features of panel (a) stay unchanged. (c) Normal state DOS (per carbon atom and spin) also versus chemical potential μ for an impurity concentration of $\eta = 0.7\,\%$ (provided by Dr. Kochan). The resonance peaks correspond directly to the YSR resonance widths. Adapted from Ref. [3].

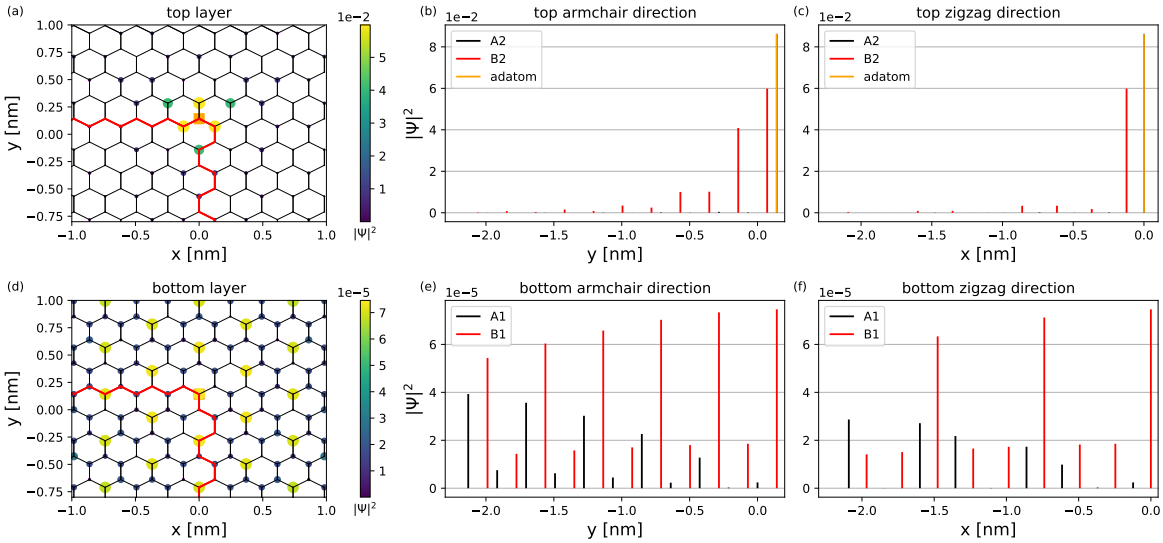

Figure 5.2: Probability density of a YSR state corresponding to a hydrogen impurity located at a dimer site (A_2 sublattice, shown as a orange square) for the same system parameters as in Fig. 5.1 (a) at $\mu = -0.1$ eV. In (a) $|\Psi|^2$ is illustrated in the top layer, while in (d) the bottom layer is shown. Note that the YSR state is mainly localized at non-dimer sites (B_2 sublattice). This is further shown in panels (b), (c), (e) and (f) for cuts along armchair and zig-zag lattice rows. Adapted from Ref. [3].

the YSR energies lie deep in the superconducting gap for the full shown doping range. Here we want to point out that this is a very important finding which is closely related to the spin-relaxation effects that will be shown in the next sections, where the most interesting features are observable in such resonance regions.

Next we can also study the YSR eigenfunctions. Analytically, these states are not very easy to compute. The advantage of the numerical diagonalization approach lies in the fact that we more or less get eigenfunctions for free. Furthermore, we know from the spectrum that the system parameters used in the numerics capture the main features of realistic parameters. Therefore, we also expect that the properties of the wave functions will not change too much for a smaller gap size. In Fig. 5.2 (a) and (d) the local probability density of a hydrogen impurity, which is chemisorbed at a dimer site (so on a carbon atom in the A_2 sublattice), is plotted in the top and bottom layer, respectively. The system parameters are set to the same values as those that were used for Fig. 5.1. The chemical potential is chosen to be $\mu = -0.1$ eV, such that it is tuned into the magnetic resonance peak where the YSR energy is located inside the superconducting gap. The impurity position is visualized as an orange square symbol. First, note the trigonal symmetry of the local density of states which stems from the underlining bilayer lattice structure. By having a detailed look at the density distribution in the two layers, it becomes clear that the YSR state is mainly localized at non-dimer sites in the B_2 top and the B_1 bottom sublattices. This is more clearly illustrated in Figs. 5.2 (b) and (c) for the top layer and in panel (e) and in (f) for the

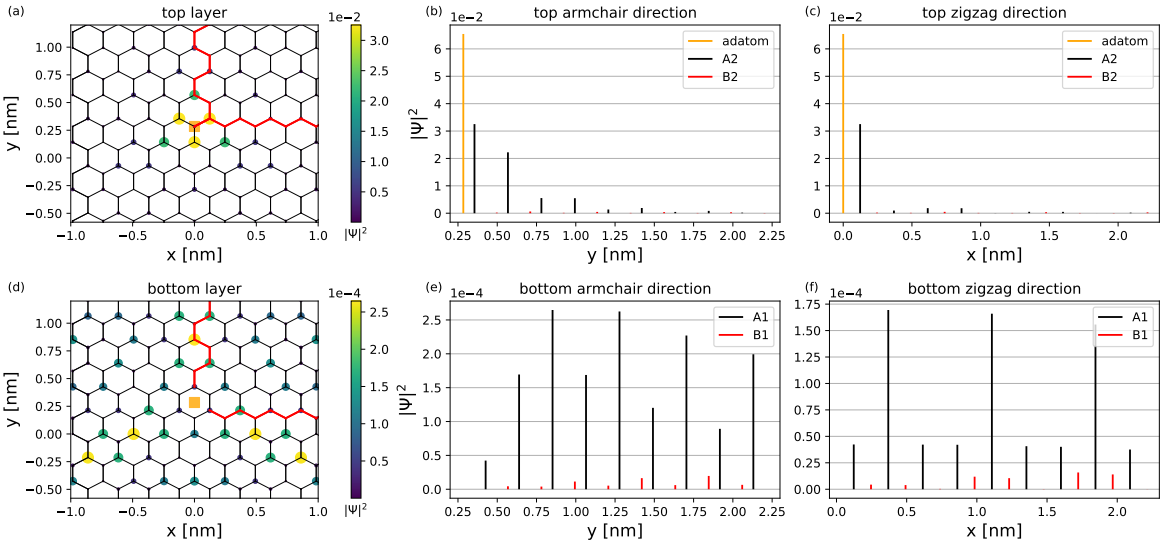

Figure 5.3: Probability density of a YSR state corresponding to a hydrogen impurity located at a non-dimer site (B_2 sublattice, shown as a orange square) for the same system parameters as in Fig. 5.1 (a) at $\mu = -0.1$ eV. In (a) $|\Psi|^2$ is illustrated in the top layer, while in (d) the bottom layer is shown. Note that the YSR state is mainly localized at non-dimer sites (A_2 sublattice). This is further shown in panels (b), (c), (e) and (f) for cuts along armchair and zig-zag lattice rows. Adapted from Ref. [3].

bottom layer, where $|\Psi|^2$ is plotted along the armchair and zig-zag lattice directions. Also the bound state is much stronger localized in the top than in the bottom layer.

The same considerations can be made for a hydrogen impurity that is adsorbed onto a non-dimer site. The local DOS in the top and bottom layers is plotted in Fig. 5.3 (a) and (d), respectively. Contrary to the dimer impurity from above, the probability density is now mainly localized at dimer sites (A_2 sublattice) in the top layer and at non-dimer sites (A_1) in the bottom layer. Again we plot this observation more clearly along armchair and zig-zag lattice directions in panels (b) and (c) in the top layer, as well as in panels (e) and (f) for the bottom layer. Similarly to the first case, the YSR state has a much larger LDOS in the top layer. Still, in the bottom layer $|\Psi|^2$ is an order of magnitude larger than for a dimer impurity.

These observations suggest that in materials with a sublattice structure the YSR spectrum and also the corresponding eigenfunctions will manifest very differently depending on the position at which an impurity will be adsorbed. This could offer the possibility to tune functionalities of spintronic and also electronic devices whose physical properties depend on those states in the superconducting state. In the following sections we will show this explicitly by studying spin-relaxation rates in superconducting single-layer and bilayer graphene. For the latter material, we then also consider Josephson junctions and show that there as well strong differences in the current transport can

be observed depending on the impurity position.

5.2. Spin-relaxation mediated by impurities in single-layer and bilayer graphene

In this section we want to study in detail the effect of the emerging YSR states discussed above on the spin relaxation in superconducting single-layer and bilayer graphene. We will start the discussion with single-layer graphene. In this material, no distinct impurity positions are present. Instead we will consider two different kinds of impurities, i.e., hydrogen and fluorine. Both of them exhibit completely different spectral resonance features in case of magnetic exchange coupling and will therefore also serve as a probe of the influence of YSR states on spin relaxation. Nevertheless, we will first assume that both impurities induce local spin-orbit coupling in their close vicinity and compute the spin-relaxation rate with respect to different temperatures.

5.2.1. Single-layer graphene

Graphene is predicted to have spin diffusion lengths of micron size [230]. It is therefore a material of high interest for spintronic applications. Despite the fact that graphene itself has only very weak intrinsic spin-orbit coupling due to the light carbon atoms, this drawback can be compensated by inducing stronger SOC via proximitizing it with other materials like TMDCs or by adding single adatoms. In the following we are going to study the latter case. More precisely, we will examine in detail the effect of superconductivity on the spin-relaxation rates and how this quantity is tuned by single impurities in SLG. This will be done by using Kwant and by following the detailed calculation manual given in Sec. 3.7. Doing so, one can calculate the spin-relaxation rate $1/\tau_s$ of superconducting systems from the scattering matrix S. This quantity will be studied as a function of the chemical potential and for different temperatures. Temperature effects are incorporated in two ways. On the one hand, thermal smearing is included in the calculation of the spin-relaxation rate given by Eq. (3.60). On the other hand, we employ the standard interpolation formula for the BCS temperature dependence of the superconducting pairing potential, which reads [231] as

$$\Delta(T) = \Delta_0 \tanh\left[1.74\sqrt{T_\mathrm{c}/T - 1}\right]\Theta(T_c - T), \tag{5.4}$$

where we get $T_c = \Delta_0/(1.76 \cdot K_\mathrm{B}) = 6.953\,\mathrm{K}$ [100] for a gap size of $\Delta_0 = 1\,\mathrm{meV}$.

Spin-orbit active impurity

Let us start by considering an adatom which is chemisorbed on top of a carbon atom in single-layer graphene. This adatom is assumed to induce local spin-orbit coupling in its close vicinity according to the impurity model given by Eqs. (2.17) and (2.22) and as visualized in Fig. 2.6. We will consider two explicit impurity examples, namely hydrogen and fluorine adatoms, where the exact parameters are given in Tab. 2.2. In

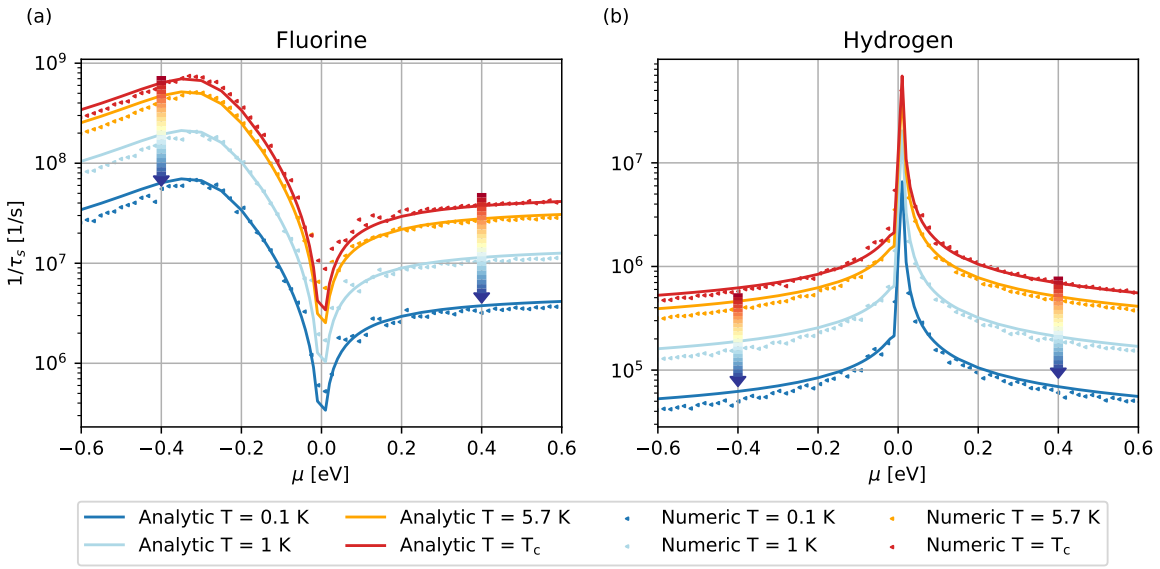

Figure 5.4: Spin-relaxation rate in single-layer graphene mediated by a fluorine adatom in (a) and a hydrogen adatom in (b), which was calculated as a function of the chemical potential μ and for different temperatures T. The impurity is assumed to introduce local spin-orbit coupling according to Eqs. (2.17) and (2.22). In both panels, we compare the numerically calculated values (dots) extracted from the S-matrix to the analytic results (continuous lines) obtained by Dr. Kochan by employing the T-matrix method. Note that both results match almost perfectly. In (a) we used an impurity concentration of $\eta = 280$ ppm and in (b) we set $\eta = 220$ ppm, where for the numerical calculation the scattering region has width $W = 299a$ and length $L = 5a$. Adapted from Ref. [2].

Fig. 5.4 the numerically computed spin-relaxation rates $1/\tau_s$ are plotted as colored dots as a function of the chemical potential μ in the system and also for various temperatures. The scattering region was chosen to have a width $W = 299a$ and a length $L = 5a$, where the impurity is then placed on top of a carbon atom in the center. The necessary phase-averaging procedure introduced in Sec. 3.7 is performed for 20 equally distributed phase values of ϕ in $[0; 2\pi]$. Moreover, those results are compared to analytic values (shown as correspondingly colored continuous lines) which are provided by Dr. Kochan. The analytical curves were computed by employing the standard T-matrix method [see Eq. (2.61)]. First of all, one immediately recognizes that both approaches match almost perfectly and this assures therefore the correctness of the obtained results. Rate features mediated by fluorine and hydrogen impurities in the normal phase ($T = T_c$) are also consistent with earlier studies in Ref. [84]. While fluorine shows an enhanced spin relaxation in the negative doping regime, hydrogen is more actively relaxing spins close to zero doping. By lowering the temperature, the magnitude of the superconducting pair potential $\Delta(T)$ is slowly enhanced. For both impurity types a reduction of the spin-relaxation rate, or equivalently an increase in the spin-relaxation time τ_s, by an order of magnitude can be observed for the transition of the normal phase into the full superconducting state. This is perfectly in line with the known Eliot-Yafet theory of spin relaxation (see Sec. 2.5).

Magnetic impurity

Next, we go on and study the same system as above in presence of fluorine and hydrogen impurities that exhibit magnetic exchange interactions, see Eq. (2.20). The computed results are shown in Fig. 5.5. The numerically calculated rates are shown as colored dots and analytical results are visualized by continuous lines in the corresponding color. Again, both approaches give almost identical results. The important observation in case of a magnetic impurity is now that in certain doping regions the spin-relaxation rate is not behaving as predicted by the Hebel-Slichter effect [232–234]. Instead of an increase in the spin relaxation over the whole range of chemical potentials, certain doping regions show a strong decrease of $1/\tau_s$. For fluorine this can be observed in the whole negative doping regime, while in the positive range the rate is increasing just as expected. Hydrogen is showing a strong reduction of spin relaxation in the low doping range and an increase for high values of μ. The reason for this behavior, contrary to the known theory, lies in the spectral properties of the YSR states. Fluorine has a magnetic resonance energy range in the negative doping regime, such that according to Eq. (5.2) here the YSR states will separate from the superconducting band gap edge and move into the gap (see Fig. 2 in Ref. [2] for the analytically computed DOS and YSR spectra). Analogously, hydrogen has magnetic resonances close to zero doping. Therefore, the chemical potential values for which the unexpected decrease of $1/\tau_s$ can be observed corresponds also to the ranges of μ where the YSR energies are spectrally separated from the superconducting quasiparticle energies. This separation in energy leads to a reduced overlap between the quasiparticles and YSR bound states, further leading to a reduced spin relaxation. In case of fluorine, this reduction is close to four

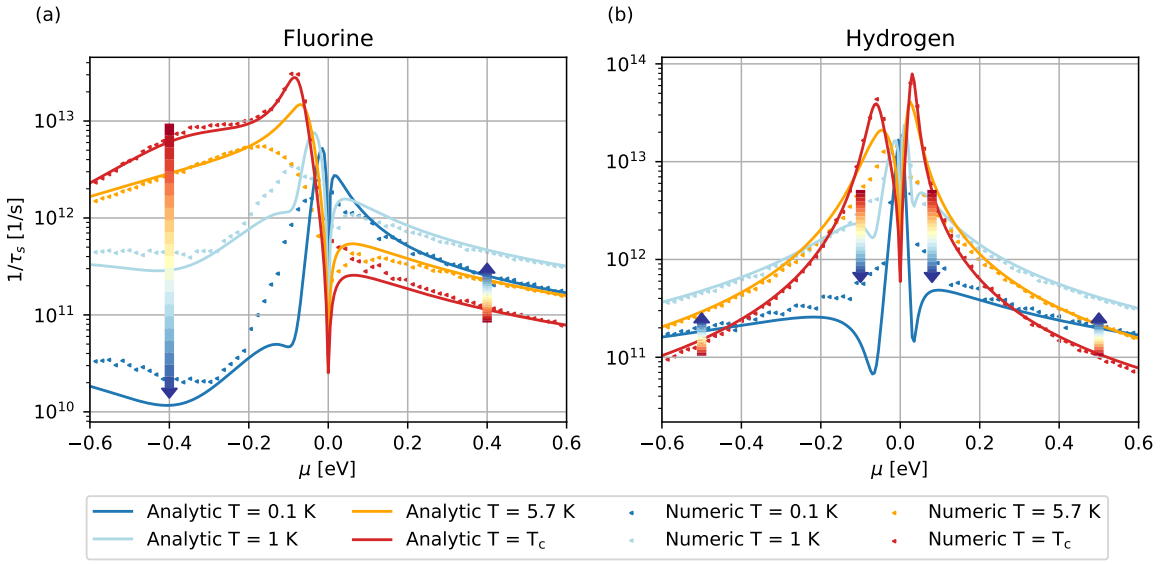

Figure 5.5: Spin-relaxation rate in single-layer graphene mediated by a fluorine adatom in (a) and a hydrogen adatom in (b), which was calculated as a function of the chemical potential μ and for different temperatures T. The impurity is assumed to exhibit magnetic exchange coupling according to Eqs. (2.17) and (2.20). In both panels, we compare the numerically calculated values (dots) extracted from the S-matrix to the analytic results (continuous lines) obtained by Dr. Kochan by employing the T-matrix method. Note that both results match again almost perfectly. In both panels we used an impurity concentration of $\eta = 280$ ppm, where for the numerical calculation the scattering region has width $W = 299a$ and length $L = 5a$. For doping levels that correspond to magnetic resonance energies of emerging YSR states, $1/\tau_s$ is showing a decrease instead of an increase, contrary to the known Hebel-Slichter effect. Adapted from Ref. [2].

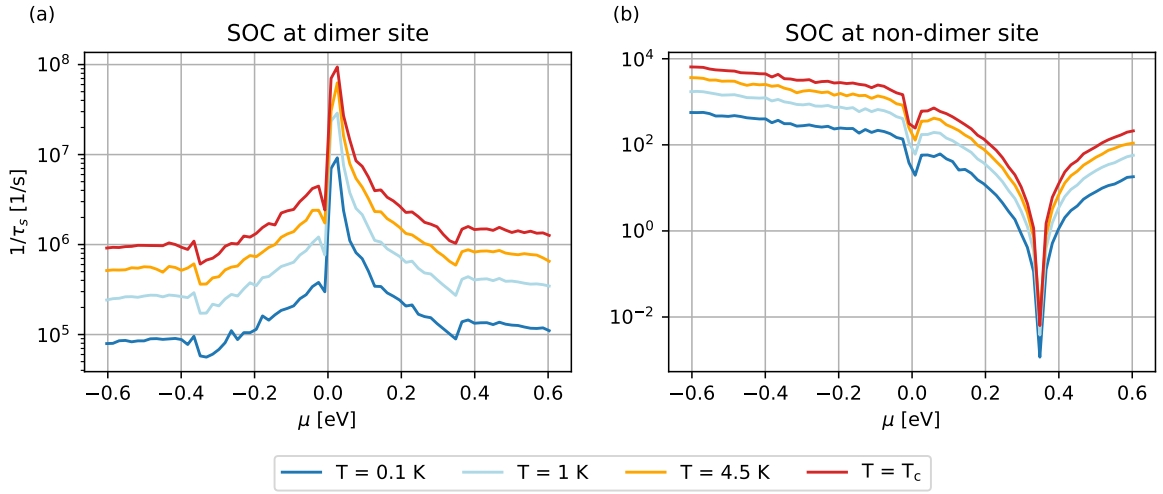

Figure 5.6: Spin-relaxation rate of BLG with a spin-orbit active hydrogen impurity that is chemisorbed at a dimer site (a) or a non-dimer site (b), which was calculated as a function of the chemical potential μ and for different temperatures. The scattering region has width $W = 131a$ and length $L = 4a$, such that $\eta = 0.0413$ %. The phase averaging over ϕ was performed for 20 equally spaced values in $[0, 2\pi]$. The spin-relaxation rate $1/\tau_s$ shows a decrease by an order of magnitude. Adapted from Ref. [3].

orders of magnitude and therefore an effect with strong impact on the spin-relaxation process.

5.2.2. Bilayer graphene

The above interesting findings naturally lead to the question whether an analogous effect is observable in bilayer graphene or not. From studying the YSR spectra in BLG in Sec. 5.1 for a hydrogen impurity we already know that the bound state spectrum strongly depends on the adatom position in the sublattice structure. Connecting this to the observations above, which showed a clear relation between the YSR energies and spin relaxation, we can expect big differences for dimer and non-dimer adatoms as well. In the following, this will be discussed in detail for the hydrogen impurity, first again for SOC and then for magnetic exchange interaction. Note that we will again put $\gamma_3 = 0$ and $\gamma_4 = 0$. In App. A.3, the spin-relaxation rate for this parameter configuration is compared to the complete model. Only minor differences are observable and therefore the simplified model is enough to capture the most important physical properties.

Spin-orbit active impurity

As for the case of single-layer graphene, let us start by studying spin relaxation in bilayer graphene with a hydrogen adatom that is assumed to induce local spin-orbit coupling as given by Eqs. (2.17) and (2.22). The computed spin-relaxation rates $1/\tau_s$

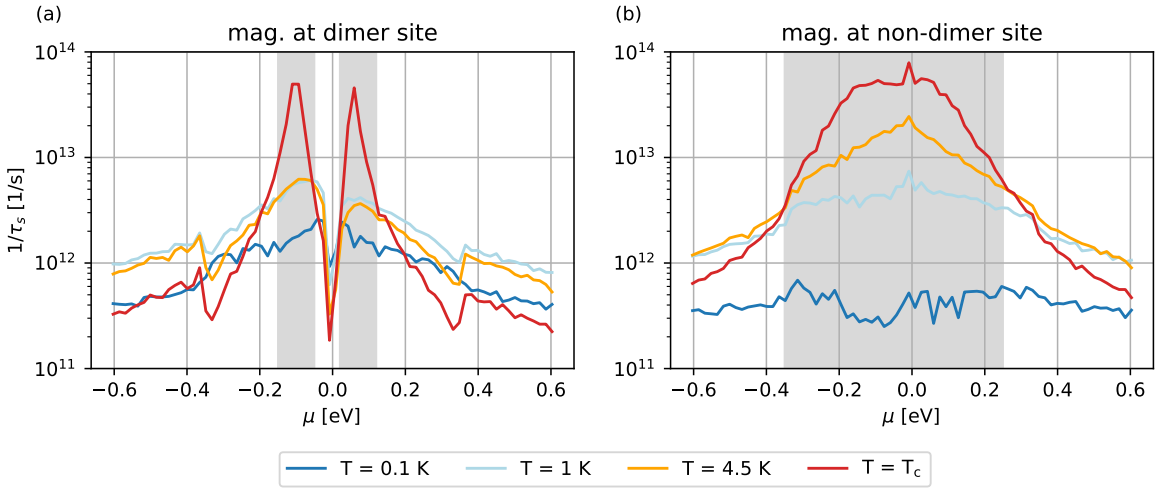

Figure 5.7: Spin-relaxation rate of BLG with a magnetic hydrogen impurity that is chemisorbed at a dimer site (a) or a non-dimer site (b) as a function of the chemical potential μ and for different temperatures. The scattering region has width $W = 131a$ and length $L = 4a$, such that $\eta = 0.0413$ %. The phase averaging over ϕ was performed for 20 equally spaced values in $[0, 2\pi]$. The spin-relaxation rate $1/\tau_s$ shows also a decrease for magnetic resonance doping levels. Furthermore the effect depends strongly on the impurity site. Adapted from Ref. [3].

as a function of the chemical potential μ and for different temperatures are shown in Figs. 5.6 (a) and (b) for a dimer and non-dimer impurity, respectively. Due to the bilayer structure with its fast increasing number of sites, one can not go to the same system size as for SLG. The size of the scattering region was set to a width $W = 131a$ and length $L = 4a$, resulting in an impurity concentration of $\eta = 0.0413$ %. The phase averaging was also performed over 20 equally spaced values in $[0; 2\pi]$ and the superconducting gap is fixed to $\Delta_0 = 1$ meV. The spin-relaxation rate for a dimer impurity (panel (a)) shows an equal curve compared to the SLG case in Fig. 5.4 (b), except two dips around $\mu \approx \pm 0.35$ eV. This value correspond to the γ_1 interlayer hopping, such that those dips might stem from a resonance that is connected to scattering events between the two layers. An analogous, but much more pronounced feature is observable in the case of a non-dimer impurity (panel (b)). A strongly reduced spin-relaxation rate is shown at $\mu = 0.35$ eV, where $1/\tau_s$ drops by four orders of magnitude. Also, the interlayer coupling is strongly affecting the spin scattering properties here. Regarding the evolution of $1/\tau_s$ with respect to the transition into the full superconducting state, a decrease by one order of magnitude can again be seen by lowering T from T_c to 0.1 K.

Magnetic impurity

Finally, we also consider a hydrogen impurity with magnetic exchange interaction on top of the BLG substrate. The system parameters remain the same as for the spin-orbit coupling case before. In Figs. 5.7 (a) and (b) the computed spin-relaxation rates for

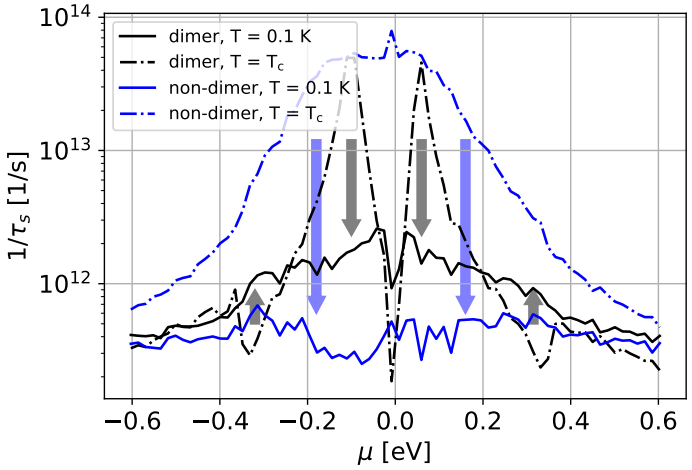

Figure 5.8: Comparison plot of spin-relaxation rates for a hydrogen impurity located at a dimer site (black) and a non-dimer site (blue) in the normal-conducting ($T = T_c$) and the superconducting ($T = 0.1$ K) phases. The emerging YSR bound states affect $1/\tau_s$ much more strongly if the impurity is adsorbed at a non-dimer site. Adapted from Ref. [3].

an adatom at a dimer and non-dimer site, respectively, are plotted. Analogously to the results of a spin-orbit active adatom at the dimer site, the magnetic dimer impurity also exhibits similar spin relaxation features as hydrogen on SLG. The interlayer coupling γ_1 is again introducing dips around $\mu = \pm 0.35$ eV, but the overall curves look similar to Fig. 5.5 (b). For high doping levels, the rate is also increasing with decreasing temperature. For small chemical potentials, particularly in close ranges around $\mu = -0.1$ eV and $\mu = 0.05$ eV, we can again observe a decrease of $1/\tau_s$. Linking this finding to the YSR spectra in Fig. 5.1 (b), the doping range where a decrease of the rate is exhibited again matches the discussion of Eq. (5.2). The separation of the YSR energies from the superconducting continuum leads to a reduced spin scattering and in turn to a smaller relaxation rate in the superconducting state.

Comparing next Fig. 5.7 (a) and Fig. 5.7 (b) for a magnetic non-dimer impurity in BLG, spin relaxation shows completely different properties. For T_c, an enhanced relaxation rate is calculated for a broad doping range around $\mu = 0$. The curves start to match the dimer impurity results only at higher values of μ. By lowering the temperature, a strong decrease of $1/\tau_s$ is again visible. The corresponding doping range matches exactly the wide magnetic resonances observed in the YSR spectrum and the perturbed normal phase DOS of Figs. 5.1 (b) and (c), respectively. This again underlines the reasonability of the relation between the emergence of YSR states and spin relaxation. Moreover we see that the effect can strongly depend on the actual impurity position if the substrate material owns a sublattice structure with geometrically distinct lattice sites. In case of bilayer graphene, the influence of YSR states localized at non-dimer impurities is much more pronounced than for dimer adatoms. This is more clearly visualized in Fig. 5.8,

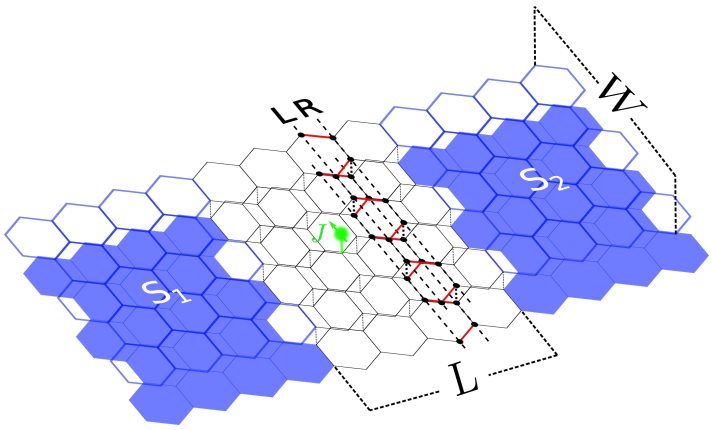

Figure 5.9: Schematic plot of a bilayer graphene Josephson junction with a single magnetic hydrogen impurity in the normal part (shown in green). L and R mark lattice sites where Eq. (3.56) is evaluated to calculate the supercurrent in the junction.

where the spin relaxation at temperatures $T = T_c$ and $T = 0.1$ K for the two adatom configurations are directly compared. The magnitude of $1/\tau_s$ is dropping more strongly (visualized by blue arrows) in case of an impurity located at a non-dimer site (blue lines). The reason for this difference might lie in the additional spatial overlap between the quasiparticle scattering states and the bound YSR states. In Figs. 5.2 and 5.3, the spatial probability densities of the computed YSR states are shown and we saw that they localize at different sublattices. In case of a dimer impurity this might be more favourable for spin scattering, while for a non-dimer impurity it could further reduce such scattering events. Still this needs a more thorough study and is left for future considerations.
Summing up, single impurities offer many possibilities to modify and tune the spin-relaxation rate in spintronic devices. Contrary to the known theory for superconducting systems, resonant doping levels can lead to a reduction of spin relaxation in case of magnetic impurities. The reason lies in the presence of locally bound YSR states which spectrally separate from the quasiparticle continuum for resonant chemical potential values. Features of these resonances can also be found in the charge transport of Josephson junctions. This will be examined in detail in the next section of this work.

5.3. Bilayer graphene Josephson junctions with magnetic impurities

In this section we want to discuss a different setup, where signatures of magnetic resonances which are introduced by single impurities play an important role, namely bilayer graphene Josephson junctions. We will focus again on a hydrogen impurity in the center of the normal region of a S/N/S-junction formed by a bilayer graphene ribbon with finite width W. Such systems are experimentally much easier to study than spin relaxation in bulk superconductors. In the following we will show that also

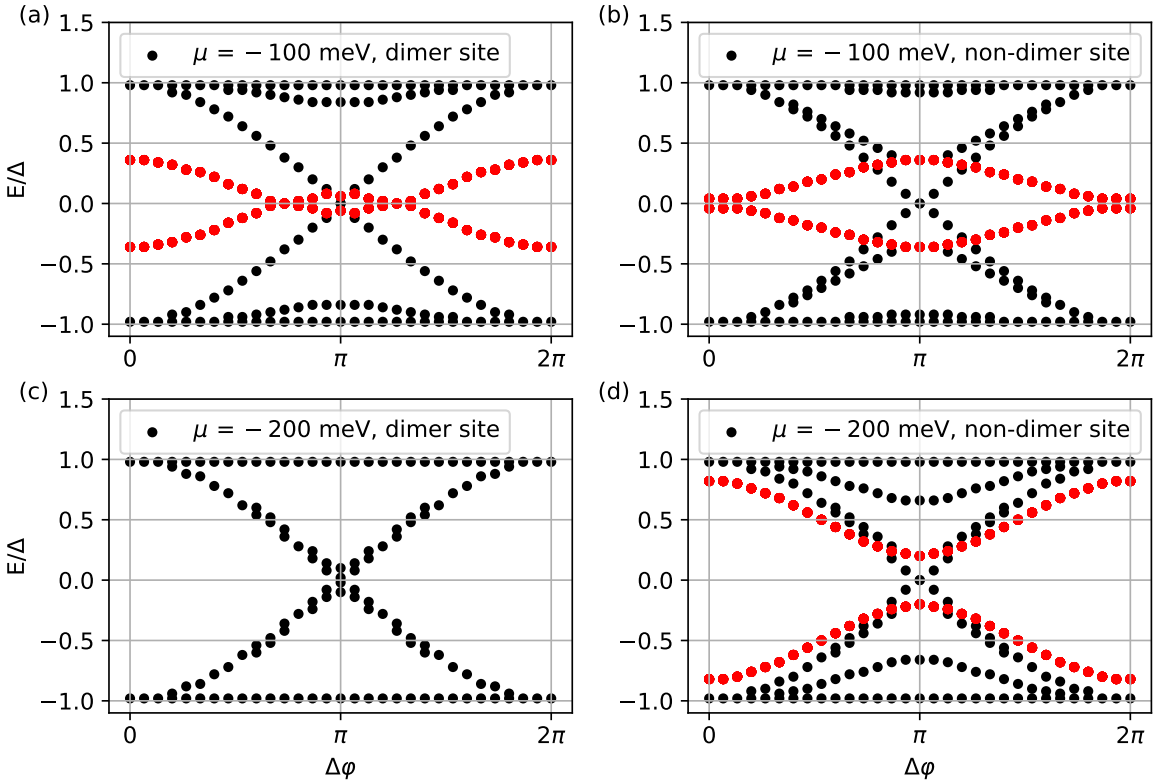

Figure 5.10: Andreev bound states computed for a bilayer graphene Josephson junction with width $W = 40a$, length $L = 10a$ and a single magnetic hydrogen impurity in the normal region. We consider the adatom to be either located at a dimer [panels (a) and (c)] or a non-dimer site [panels (b) and (d)]. Moreover, we assume two doping levels, namely $\mu = -100$ meV and $\mu = -200$ meV, which correspond to magnetic resonance energies known from the YSR spectra computed above. Also for Andreev bound states the influence of the magnetic exchange interaction leads to resonant energies which are shown in red. Adapted from Ref. [3].

in these simpler systems spectral features analogous to the above findings are present. The discussion starts by examining the ABS spectrum of such junctions and then continues with transport signatures in the supercurrent.

5.3.1. Andreev bound states

Let us assume we have a nanoribbon of bilayer graphene in AB stacking order with finite width $W = 40a$ and construct a Josephson junction from this material. The junction has length L, which is defined as the distance between two superconducting leads S_1 and S_2. In the leads, we define a superconducting pairing potential $\Delta_0 = 1$ meV which is induced by putting the BLG nanoribbon in close proximity to normal s-wave superconductors. A schematic plot of such a system is shown in Fig. 5.9, where the single hydrogen impurity is visualized as a green sphere on top of the bilayer structure.

In order to understand the signatures of the supercurrent flowing in such a system, which will be discussed in the next section, we will first compute the corresponding Andreev bound states. This is done by employing the spectral density method introduced in detail in Chap. 3.6.1. Note that this calculation procedure is actually necessary to capture the correct spectral properties which are strongly modified by the interplay of superconducting pairing and magnetic exchange interaction. If one would simply use the scattering matrix approach which is also discussed in Chap. 3.6.1, the computed ABS would be not correct. This methodology is missing the right interference effects of Δ and J terms. Still, it can be used to check if the spectral density method with its subtle sorting problem is implemented correctly by considering the case of $J = 0$, namely a trivial impurity that serves as a scattering center. Such test calculations can be found in App. A.4. Furthermore, it is no longer enough to use the simplified impurity model given by Eq. (2.20), which we used for the YSR spectra and the spin-relaxation calculations. For the ABS, and later also for the supercurrent computations, one has to consider the full set of orbitals corresponding to the electron and impurity spins, because now also the momentum relaxation processes contribute to the quantities of interest. This is done by simply employing Eq. (2.18).

In Fig. 5.10 we plot the ABS spectra as a function of the phase difference $\Delta\varphi$ across the BLG Josephson junction computed with Eq. (3.50) for different impurity positions and doping levels. Panels (a) and (c) correspond to an adatom sitting over a dimer site, while (b) and (d) are results for a non-dimer impurity. Also, both site configurations are considered at two values of the chemical potential, i.e., $\mu = -100$ meV and $\mu = -200$ meV. These values were chosen since we know from the discussion of the YSR states above that these energy values lie in magnetic resonance regimes of a hydrogen impurity on BLG (see Fig. 5.1). Starting with a dimer impurity, the ABS spectrum for $\mu = -100$ meV in (a) exhibits an energy branch that is separated from the superconducting continuum bands at $\pm\Delta$ also for zero phase difference (shown in red). This doping level corresponds to one of the sharp magnetic resonances of a dimer site hydrogen impurity (see Fig. 5.1 (c)). Contrary to that, if the chemical potential is tuned away from this resonance to the larger value of $\mu = -200$ meV in (c), no such exotic ABS band is present. The spectrum is only weakly gapped around a phase difference of $\Delta\varphi = \pi$, corresponding to standard scattering off a non-resonant impurity center.

Next, we change the impurity position to a non-dimer site and consider the same values of the chemical potential for ease of comparison. Analogously to the results shown in panel (a), we can observe for both doping levels in (b) and (d) resonant ABS bands colored in red which sit inside the superconducting gap. This also matches the observations for YSR spectra above, where the non-dimer impurity exhibited a very broad resonance regime over a wide doping range. Furthermore, for both impurity positions, the ABS spectra show enlarged mini gaps around $\Delta\varphi = \pi$ if the chemical potential is tuned into resonance. Therefore, we can also expect an influence on the magnitude of the supercurrent because the amplitude of the current is directly propor-

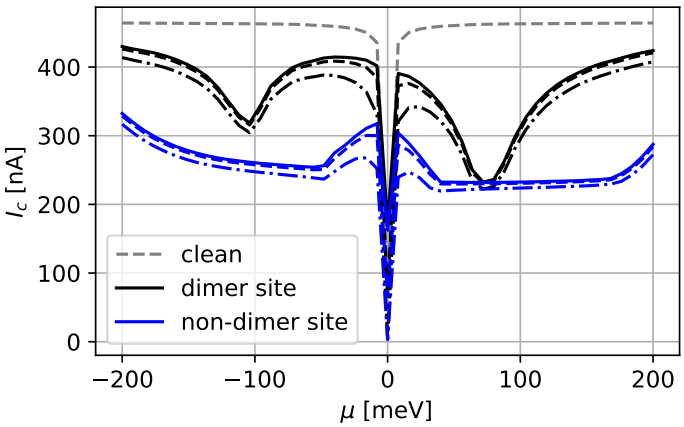

Figure 5.11: Critical current of a BLG Josephson junction with width $W = 40a$ and a magnetic hydrogen impurity located at either a dimer site (black curves) or a non-dimer site (blue curves) as a function of the chemical potential μ. Note that the full lines correspond to length $L = 10a$, the dashed lines to $L = 20a$ and the dashed-dotted lines to $L = 60a$. The grey dashed line is a benchmark that corresponds to a clean setup. For doping levels in magnetic resonance regimes we see a strong decay of the current amplitude. This matches the findings for the ABS spectra shown in Fig. 5.10. Adapted from Ref. [3].

tional to the derivative of the ABS spectrum with respect to the phase difference, i.e., $I(\Delta\varphi) \propto \sum_{\mathrm{ABS}} \partial E^{\mathrm{ABS}}(\Delta\varphi)/\partial\Delta\varphi$. That this assumption holds true is shown in the next section.

5.3.2. Supercurrent

Above we studied the ABS spectra of the BLG Josephson junction. Now we want to show that also in the experimentally measurable critical current, direct signatures of the magnetic resonances can be observed. In order to compute the critical current I_{c}, we employ the methodology of Sec. 3.6.2 and evaluate Eq. (3.56), except that we need to neglect here the prefactor of 2. The reason for that lies in the doubling of the orbital degrees of freedom to account for the impurity spin in its potential $V_{\mathrm{s}}^{(1)}$ [see Eq. (2.18)]. The current-phase relation is calculated between two lattice rows L and R by computing Green's function connecting the respective sites (see Fig. 5.9 for a schematic plot of the lattice cuts). After computing the CPR, the critical current is determined as its maximum $I_{\mathrm{c}}(\mu) = \max_{\Delta\varphi} |I_{\mathrm{LR}}(\Delta\varphi, \mu)|$. We also show a consistency check in App. A.5, where we directly compare the computed CPR with a ABS spectrum that was obtained by calculating the spectral density given in Eq. (3.50). In Fig. 5.11 the critical current for a magnetic dimer (non-dimer) hydrogen impurity is shown in black (blue). Note that we consider different lengths L of the normal BLG region to check for the length dependence. We see that for an increasing junction length the magnitude of the critical current is decreasing as expected. Also shown as a grey

dashed line is the critical current of a clean junction without an impurity, which serves as a benchmark for the adatom influence. Starting with a dimer site impurity, ones sees two sharp and clear dips in the critical current for doping values around $\mu = -100$ meV and $\mu = 80$ meV. These doping ranges correspond exactly to the magnetic resonance energies that were already significantly modifying the YSR spectra in bulk superconducting BLG. Moreover, we know from the section before that the ABS spectrum for a dimer impurity and a chemical potential of $\mu = -100$ meV exhibits a resonant ABS band with a reduced slope inside the superconducting gap. The reduced slope will result in a decreased contribution to the current, as it is directly proportional to the derivative of the ABS energies with respect to the phase difference $\Delta\varphi$. By tuning μ out of resonance, the impurity is only acting as a normal scattering center and weakly gaps out some of the ABS bands, such that the current is reduced by a smaller amount.

In case of a non-dimer adatom we see a very broad decay of the current amplitude over the complete range of computed chemical potential values. This is also in line with the findings of the sections above, where we always saw a broad magnetic resonance range for this impurity position. Comparing again with Figs. 5.10 (b) and (d) we see the resonant ABS bands for the given doping energies, which are responsible for the strong drop in current magnitude.
We can summarize that also in the case of well known Josephson junctions one can observe the interplay of superconducting pairing and magnetic exchange interactions introduced by single magnetic impurities.
In conclusion, we found that the spectral properties of YSR states located at magnetic impurities in bulk superconducting systems can be tuned by varying the chemical potential and their eigenenergies separate from the quasi-particle continuum spectrum, whenever the doping level is close to magnetic resonances in the perturbed normal state DOS. This spectral separation in turn leads to a strongly decreasing spin-relaxation rate, instead of the from theory expected increase (Hebel-Slichter peak). Moreover, due to the example of bilayer graphene it was shown that the effect depends on the exact impurity position for systems with a sublattice structure. Finally, also in Josephson junctions the magnetic exchange coupling leads to a reduction of the critical current for chemical potentials close to magnetic resonance energies. These platforms are experimentally easier to examine and could therefore serve as additional probes for the discussed observations.

6. Non-uniform tight-binding method

We have seen in Chap. 4 that it can be very useful and sometimes even necessary to employ full 3D models which are computationally very expensive. Moreover, for a quantitative comparison between certain parameter sets in simulations and real experiments which treat larger samples, the computational effort is analogously increasing with system size. Therefore there is a high demand for efficient simulation techniques. Particularly we are interested in the treatment of 2D or 3D topological insulator surface states with realistic models in tight-binding calculations. The computation contains a large amount of unimportant lattice points, namely the bulk of the system. Edge and surface states can only be obtained by taking into account the bulk of the material, despite the fact that for many cases these regions do not contribute important physics. But also in systems which contain interfaces between different material components, it is important to have a high resolution in the hybridization zone. Motivated by these points we introduce and discuss a general way of implementing tight-binding systems on a non-uniform lattice. The technique allows to efficiently shift grid points into spatial areas where a high lattice resolution is needed. Even though we are using the python package Kwant [34] in our simulations, we want to stress that our approach is applicable to any other open source tight-binding software or self-written code. The method will be applied to two examples. First the convergence of edge states in 2D HgTe quantum wells is examined, while in the second example we are employing the technique to a hybrid system of the 2D HgTe and a ferromagnetic metal.

Let us start with the general problem of naively applying the finite difference approach to a non-uniform lattice. By trying to apply the standard finite difference method given by Eqs. (3.3) and (3.4) onto a non-uniform lattice as plotted in Fig. 6.1, one arives at a non-hermitian tight-binding Hamiltonian. This can be easily shown by performing the discretization at the grid points y_j and y_{j+1} [see Eqs.(3.3) and (3.4)], where we get

$$\partial_j \Psi_j = \frac{\Psi_{j+1} - \Psi_{j-1}}{a_{j-1} + a_j}, \tag{6.1}$$

and

$$\partial_j \Psi_{j+1} = \frac{\Psi_{j+2} - \Psi_j}{a_j + a_{j+1}}. \tag{6.2}$$

The denominators are simply the sum of the adjacent lattice spacings. Obviously, the hopping from site y_j to y_{j+1} is not the hermitian conjugate version of the backward hopping from site y_{j+1} to y_j if $a_{j-1} \neq a_{j+1}$. This issue arises due to the non-trivial metric of the non-uniform lattice. However, the problem can be resolved by taking into account the considerations regarding hermiticity of the next section.

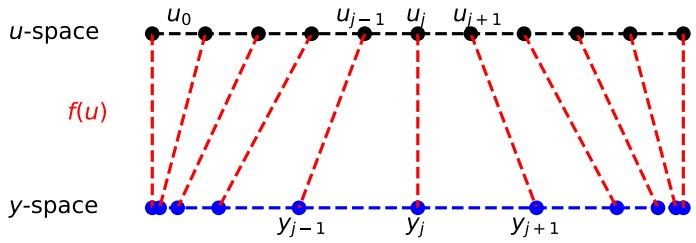

Figure 6.1: Schematic plot of the computational and physical spaces. The mapping $f(u)$ is shifting the equally spaced lattice sites in u-space onto the non-uniform y-grid, which corresponds to the physical space in which the Hamiltonian should be approximated.

6.1. Hermiticity with a non-trivial volume form

For the tight-binding implementation with lattice constant u_0 Kwant uses hermitian matrices $H^\dagger = H$. The hermiticity condition of H, $\langle\Psi|H\Phi\rangle = \langle H\Psi|\Phi\rangle$, is given in the continuum limit by the following scalar product, where we choose for simplicity a 2D example, which reads [154]

$$\langle\phi\,|\,H\psi\rangle = \int dx \int dy \phi^* H\psi = \langle H\phi\,|\,\psi\rangle\,. \tag{6.3}$$

However with a non-trivial volume form we get

$$\langle\phi\,|\,H\psi\rangle = \int dq_1 \int dq_2 g_1 g_2 \phi^* H\psi \tag{6.4}$$

with $g_i = |\partial \boldsymbol{r}/\partial q_i|$ $(i = 1, 2)$. From here we can only deduce that $H^\dagger = H$ if g_1 and g_2 are constant. Note that we define from now $q_1 = x$ and $q_2 = y$.
Written down in this form the tight-binding representation is in general not hermitian, but we can apply the following unitary transformation on the Hamiltonian and the wave functions [154]

$$\begin{aligned}\langle\phi\,|\,H\psi\rangle &= \int dx \int dy (\sqrt{g_x g_y}\phi^*) \left(\sqrt{g_x g_y} H \frac{1}{\sqrt{g_x g_y}}\right) (\sqrt{g_x g_y}\psi) \\ &= \int dx \int dy \tilde{\phi}^* \hat{H} \tilde{\psi},\end{aligned} \tag{6.5}$$

which renders the volume form trivial and results in a hermitian tight-binding form.

6.2. Non-unifrom grid

As we already mentioned, we want to have a non-unifrom grid with a denser set of grid points where a high resolution is needed. An example of such a grid is shown in

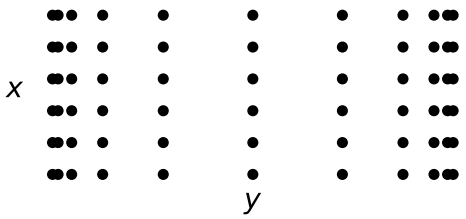

Figure 6.2: Example for a 2D non-uniform grid. The lattice constant in the x-direction is constant while the spacing in the y-direction is non-uniform.

Fig. 6.1. The method to change the grid is a simple mapping between the so-called *computational* space (coordinates parametrized by u, where u_0 is the lattice constant) and the *physical* space (coordinates parametrized by y). We define this mapping as

$$y_j = f(u_j)\,, \quad 1 \leqslant j \leqslant N. \tag{6.6}$$

In order to apply non-uniform mappings to partial differential equations, we need to know how the derivative operators behave under such transformations. For physical problems we usually need only the first and second derivative of a variable, which get transformed to

1^{st} derivative:

$$\partial_y = \frac{\partial}{\partial y} = \frac{\partial u}{\partial y}\frac{\partial}{\partial u} = \frac{1}{\frac{\partial y}{\partial u}}\frac{\partial}{\partial u} = \frac{1}{f'(u)}\partial_u, \tag{6.7}$$

2^{nd} derivative:

$$\partial_y\partial_y = \left(\frac{1}{f'(u)}\partial_u\right)\left(\frac{1}{f'(u)}\partial_u\right). \tag{6.8}$$

6.3. Example in 2D – discretization of momenta

We focus on an explicit example of a 2D lattice with a non-uniform grid spacing in one direction as illustrated in Fig. 6.2. In this case we can identify the non-trivial volume element as

$$g_y = g(u) = \frac{\partial y}{\partial u} = f'(u), g_x = 1. \tag{6.9}$$

Since the package Kwant uses a tight-binding implementation, we have to adjust the finite difference representation of a given Hamiltonian. As a first step we transform the momenta as $k_i \to -\mathrm{i}\partial_i$ and $k_i^2 \to -\partial_i^2$. After that we can discretize the derivatives resulting in the common finite difference form.

6.3.1. Finite difference – first derivative

For the parts of the Hamiltonian which are linear in momentum the tranformation gives us

$$\hat{k}_y = -\mathrm{i}\partial_y = -\mathrm{i}\frac{1}{f'(u)}\frac{\partial}{\partial u}. \tag{6.10}$$

This expression is not hermitian when we put it onto a lattice (the forward and the backward hoppings do not fulfill $t_{y\to y+1} = t^*_{y+1\to y}$, where t denotes the hopping energy shown in Fig. 3.1). But we can render it hermitian by applying the unitary transformation which we outlined in Sec. 6.1. Following the recipe, the scaled variables are given by

$$\begin{aligned}\hat{k}' &= \sqrt{f'(u)}\hat{k}\frac{1}{\sqrt{f'(u)}} \\ &= \sqrt{f'(u)}\left(-\mathrm{i}\frac{1}{f'(u)}\frac{\partial}{\partial u}\right)\frac{1}{\sqrt{f'(u)}} \\ &= -\mathrm{i}\frac{1}{\sqrt{f'(u)}}\partial_u\frac{1}{\sqrt{f'(u)}}. \end{aligned} \tag{6.11}$$

For all of the subsequent consideration we define the convenient short hand notations:

1. $d(u) = 1/\sqrt{f'(u)}$
2. $d(u_j) = d_j$ where j is the label of the lattice in y-direction, we neglect the x-direction in the notation
3. $\psi(u_j) = \psi_j$

Next we proof that the above transformation leads to a hermitian tight-binding matrix. First, we apply the finite difference method to two adjacent lattice points:

$$\hat{k}'_y\psi_j = [-\mathrm{i}d_j\partial_j d_j]\psi_j = -\mathrm{i}d_j\frac{d_{j+1}\psi_{j+1} - d_{j-1}\psi_{j-1}}{2u_0} \tag{6.12}$$

$$\hat{k}'_y\psi_{j+1} = [-\mathrm{i}d_{j+1}\partial_{j+1} d_{j+1}]\psi_{j+1} = -\mathrm{i}d_{j+1}\frac{d_{j+2}\psi_{j+2} - d_j\psi_j}{2u_0}. \tag{6.13}$$

Second, we can extract the hoppings, which read

$$t_{j\to j+1} = -\frac{\mathrm{i}}{2u_0}d_j d_{j+1}, \tag{6.14}$$

$$t_{j+1\to j} = \frac{\mathrm{i}}{2u_0}d_j d_{j+1}. \tag{6.15}$$

From these we see already that the transformed elements fullfil $t_{j\to j+1} = t^*_{j+1\to j}$ and therefore we can conclude that the tight-binding Hamiltonian is indeed hermitian.

6.3.2. Finite difference – second derivative

As mentioned, the recipe straightforwardly extends to the higher derivative. For the second derivative, we obtain we obtain

$$\hat{k}_y^2 = -\partial_y^2 = -\partial_y\partial_y = -\left(\frac{1}{f'(u)}\partial_u\right)\left(\frac{1}{f'(u)}\partial_u\right), \tag{6.16}$$

which is not hermitian. Hermiticity is again restored by applying the transformation

$$\begin{aligned}\hat{k}_y'^2 &= -\sqrt{f'(u)}\hat{k}_y^2\frac{1}{\sqrt{f'(u)}} \\ &= -\sqrt{f'(u)}\left[\left(\frac{1}{f'(u)}\partial_u\right)\left(\frac{1}{f'(u)}\partial_u\right)\right]\frac{1}{\sqrt{f'(u)}} \\ &= -\frac{1}{\sqrt{f'(u)}}\left(\partial_u\frac{1}{f'(u)}\partial_u\right)\frac{1}{\sqrt{f'(u)}}.\end{aligned} \tag{6.17}$$

This expression resembles the effective mass problem (see p. 214 of Ref. [96] or Ref. [235]) which is formulated as

$$H_{\text{kin}} = \frac{1}{2}\hat{p}\frac{1}{m(\boldsymbol{r})}\hat{p} \quad \text{and} \quad \hat{p} = -i\hbar\boldsymbol{\nabla}. \tag{6.18}$$

The considered Hamiltonian has a spatially dependent effective mass and its position representation reads

$$H = -\frac{\hbar^2}{2}\frac{\partial}{\partial x}\frac{1}{m(x)}\frac{\partial}{\partial x}, \tag{6.19}$$

which gives the following finite difference expression [96]

$$H\psi_j = -\frac{\hbar^2}{2}\left(\frac{2(\psi_{j+1}-\psi_j)}{m_{j+\frac{1}{2}}a_j(a_j+a_{j-1})} - \frac{2(\psi_j-\psi_{j-1})}{m_{j-\frac{1}{2}}a_{j-1}(a_j+a_{j-1})}\right). \tag{6.20}$$

This expression can be derived by applying the finite difference method to a lattice with spacing $a/2$. This will be shown in the following, where from now on we define $\partial_j\psi_j = \psi_j'$.

$$\begin{aligned}H\psi_j &= \left[-\frac{\hbar^2}{2}\partial_j\frac{1}{m_j}\partial_j\right]\psi_j \\ &= -\frac{\hbar^2}{2}\partial_j\frac{1}{m_j}\psi_j' \\ &= -\frac{\hbar^2}{2}\frac{\frac{1}{m_{j+\frac{1}{2}}}\psi'_{j+\frac{1}{2}} - \frac{1}{m_{j-\frac{1}{2}}}\psi'_{j-\frac{1}{2}}}{\frac{a_j}{2}+\frac{a_{j-1}}{2}} \\ &= -\frac{\hbar^2}{2}\frac{2}{a_j+a_{j-1}}\left[\frac{1}{m_{j+\frac{1}{2}}}\partial_{j+\frac{1}{2}}\psi_{j+\frac{1}{2}} - \frac{1}{m_{j-\frac{1}{2}}}\partial_{j-\frac{1}{2}}\psi_{j-\frac{1}{2}}\right] \\ &= -\frac{\hbar^2}{2}\frac{2}{a_j+a_{j-1}}\left[\frac{1}{m_{j+\frac{1}{2}}}\frac{\psi_{j+1}-\psi_j}{\frac{a_j}{2}+\frac{a_j}{2}} - \frac{1}{m_{j-\frac{1}{2}}}\frac{\psi_j-\psi_{j-1}}{\frac{a_{j-1}}{2}+\frac{a_{j-1}}{2}}\right] \\ &= -\frac{\hbar^2}{2}\left[\frac{2(\psi_{j+1}-\psi_j)}{m_{j+\frac{1}{2}}a_j(a_j+a_{j-1})} - \frac{2(\psi_j-\psi_{j-1})}{m_{j-\frac{1}{2}}a_{j-1}(a_j+a_{j-1})}\right]\end{aligned} \tag{6.21}$$

Analogously, we can apply this to our transformed finite difference expression. We write $d(u)^2 = 1/f^{'}(u)$ and get

$$\begin{aligned}
\hat{k}_y^{'2}\psi_j &= [-d_j(\partial_j d_j^2 \partial_j) d_j]\psi_j \quad \text{define: } A_j = d_j\psi_j \Rightarrow \partial_j A_j = A_j^{'} \\
&= -d_j \partial_j d_j^2 A_j^{'} \\
&= -d_j \frac{d_{j+\frac{1}{2}}^2 A_{j+\frac{1}{2}}^{'} - d_{j-\frac{1}{2}}^2 A_{j-\frac{1}{2}}^{'}}{\frac{u_0}{2}+\frac{u_0}{2}} \\
&= -\frac{d_j}{u_0}\left[d_{j+\frac{1}{2}}^2 \partial_{j+\frac{1}{2}}\left(d_{j+\frac{1}{2}}\psi_{j+\frac{1}{2}}\right) - d_{j-\frac{1}{2}}^2 \partial_{j-\frac{1}{2}}\left(d_{j-\frac{1}{2}}\psi_{j-\frac{1}{2}}\right)\right] \\
&= -\frac{d_j}{u_0}\left[d_{j+\frac{1}{2}}^2 \frac{d_{j+1}\psi_{j+1} - d_j\psi_j}{\frac{u_0}{2}+\frac{u_0}{2}} - d_{j-\frac{1}{2}}^2 \frac{d_j\psi_j - d_{j-1}\psi_{j-1}}{\frac{u_0}{2}+\frac{u_0}{2}}\right] \\
&= -\frac{1}{u_0^2}\left[-d_j^2\left(d_{j+\frac{1}{2}}^2 + d_{j-\frac{1}{2}}^2\right)\psi_j + d_j d_{j+\frac{1}{2}}^2 d_{j+1}\psi_{j+1} + d_j d_{j-\frac{1}{2}}^2 d_{j-1}\psi_{j-1}\right]. \qquad (6.22)
\end{aligned}$$

From the last expression we can again read off the onsite and the hopping terms

1. onsite term: $\epsilon_j = \frac{1}{u_0^2} d_j^2\left(d_{j+\frac{1}{2}}^2 + d_{j-\frac{1}{2}}^2\right)$
2. hopping term: $t_{j\to j+1} = -\frac{1}{u_0^2} d_j d_{j+\frac{1}{2}}^2 d_{j+1}$.

In order to show hermiticity we can again also apply the method to the $j+1$ site.

$$\begin{aligned}
\hat{k}_y^{'2}\psi_{j+1} &= [-d_{j+1}(\partial_{j+1} d_{j+1}^2 \partial_{j+1}) d_{j+1}]\psi_{j+1} \\
&= -d_{j+1}\partial_{j+1} d_{j+1}^2 A_{j+1}^{'} \\
&= -d_{j+1}\frac{d_{j+\frac{3}{2}}^2 A_{j+\frac{3}{2}}^{'} - d_{j+\frac{1}{2}}^2 A_{j+\frac{1}{2}}^{'}}{\frac{u_0}{2}+\frac{u_0}{2}} \\
&= -\frac{d_{j+1}}{u_0}\left[d_{j+\frac{3}{2}}^2 \partial_{j+\frac{3}{2}}\left(d_{j+\frac{3}{2}}\psi_{j+\frac{3}{2}}\right) - d_{j+\frac{1}{2}}^2 \partial_{j+\frac{1}{2}}\left(d_{j+\frac{1}{2}}\psi_{j+\frac{1}{2}}\right)\right] \\
&= -\frac{d_{j+1}}{u_0}\left[d_{j+\frac{3}{2}}^2 \frac{d_{j+2}\psi_{j+2} - d_{j+1}\psi_{j+1}}{\frac{u_0}{2}+\frac{u_0}{2}} - d_{j+\frac{1}{2}}^2 \frac{d_{j+1}\psi_{j+1} - d_j\psi_j}{\frac{u_0}{2}+\frac{u_0}{2}}\right] \\
&= -\frac{1}{u_0^2}\left[-d_{j+1}^2\left(d_{j+\frac{3}{2}}^2 + d_{j+\frac{1}{2}}^2\right)\psi_{j+1} + d_{j+1} d_{j+\frac{3}{2}}^2 d_{j+2}\psi_{j+2} + d_{j+1} d_{j+\frac{1}{2}}^2 d_j\psi_j\right] \qquad (6.23)
\end{aligned}$$

We see that the hoppings fulfill $t_{j\to j+1} = t_{j+1\to j}^*$ and therefore also the tight-binding Hamiltonian is hermitian.

6.4. Properties of mapping functions

To this point we did not specify $f(u)$. This mapping function between the computational space and the real space must fulfill at least two important properties. First of

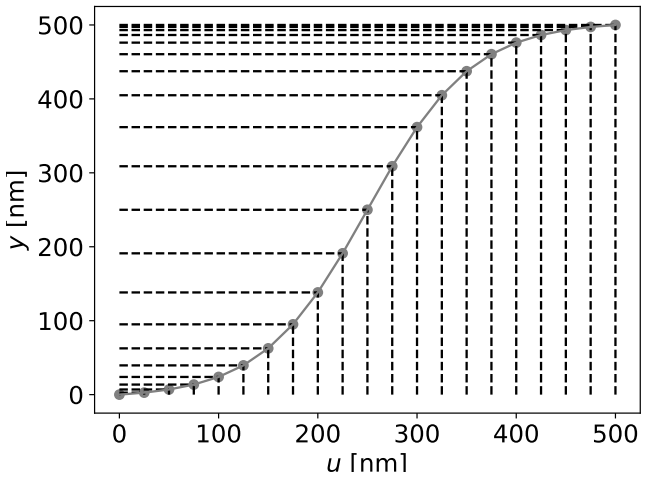

Figure 6.3: Example of the mapping function. The equally spaced grid points in u-space become shifted in y-space. The parameters were fixed to $W = 500$, $u_0 = 25$ and $s = 1.5$.

all, the physical width of the system should not change. We do not want to artificially stretch or shrink the system by the mapping, as this would change the physics in the system. That means the function has to obey the following boundary conditions

$$\begin{aligned} 0 &= f(u = 0) \\ W &= f(u = W), \end{aligned} \tag{6.24}$$

where W is the physical width of the system. The second property is that the derivative $f^{'}(u)$ is not allowed to vanish at any lattice point, as we must take the inverse of this function. A schematic of such a mapping is shown in Fig. 6.1. In the next chapters we are showing two examples, where we used the following example mapping

$$f(u) = \frac{W}{2} \coth\left(s\frac{\pi}{2}\right) \left[\tanh\left(s\left(\pi\frac{uu_0}{W} - \frac{\pi}{2}\right)\right) - \tanh\left(-s\frac{\pi}{2}\right)\right]. \tag{6.25}$$

The parameter s determines the strength of the stretching of the lattice spacing. If $s \to 0$, the grid transformation is almost zero and for large s the shifting of the grid points to the boundaries becomes more pronounced. The variable u runs over the label number of the grid points. An example for specific parameters is plotted in Fig. 6.3.

6.5. Examples

6.5.1. Density of scattering states in 2D BHZ model

In order to test the above theory it is reasonable to apply the procedure to a certain problem which would benefit by efficiently distributing lattice points in space. We consider a 2D topological insulator system with length $L = 400$ nm in the x-direction and

width $W = 500$ nm in y-direction that exhibits edge states, i.e., HgTe/CdTe quantum wells. This material class can be described by the well-established 2D BHZ Hamiltonian [236]. In the basis $|E1,\uparrow\rangle, |H1,\uparrow\rangle, |E1,\downarrow\rangle$ and $|H1,\downarrow\rangle$ it takes the form [236]

$$H_{\mathrm{BHZ}}^{\mathrm{2D}} = \begin{pmatrix} h(\boldsymbol{k}) & 0 \\ 0 & h(-\boldsymbol{k})^* \end{pmatrix}, \tag{6.26}$$

with

$$h(\boldsymbol{k}) = \begin{pmatrix} C - (B+D)\boldsymbol{k}^2 + M & Ak_+ \\ Ak_- & C + (B-D)\boldsymbol{k}^2 - M \end{pmatrix}. \tag{6.27}$$

We define $\boldsymbol{k}^2 = k_x^2 + k_y^2$ and $k_\pm = k_x \pm \mathrm{i}k_y$. The parameters are set to $C = 0$, $A = 364.5$ meV nm, $B = -686$ meV nm^2, $D = -512$ meV nm^2 and $M = -10$ meV, which correspond to a $d_{\mathrm{QW}} = 7$ nm thick HgTe/$\mathrm{Hg_{0.32}Cd_{0.68}Te}$ quantum well [53, 237, 238]. The general idea is to compare the local density of states (LDOS) of the edge scattering states for different lattice resolutions and check their convergence. The non-uniform tight-binding method is applicable to such a system, as the edge states are mainly localized at the edges of the system. In a standard tight-binding implementation an improved convergence with a higher number of equally spaced lattice points is paid by a big increase of the computational cost, despite the fact that the bulk is negligibly important. The non-uniform tight-binding method in turn does not increase the number of lattice points but shifts a certain portion of them closer to the edges, namely the regions where we need them. In Fig. 6.4 (a) the bandstructure of a 2D TI system with a lattice constant of $a = 2$ nm is plotted. The edge states correspond to the two linearly dispersing bands, while the upper and lower parabolic bands are the conduction and valence bands, respectively. Note that we applied an infinitesimally small out-of-plane magnetic field to lift the degeneracy of the edge states. Otherwise, the modes can be chosen as a random superposition of the pure edge state basis. These eigenstates are not desirable, as we want to look at the LDOS profile of a state that is purely localized at one edge.

For the following discussion the Fermi energy is set to $E_{\mathrm{F}} = 9$ meV, such that it lies inside the bulk band gap and only the edge states are present in the leads. Additionally, to get a spatial variation along the x-direction (direction of transport) we also introduce correlated disorder as described in Chap. 3. The advantage of correlated disorder is the possibility to adjust it for a non-uniform representation. It is necessary to have a direct comparison of the local density of states of the uniform and the non-uniform implementations. Therefore we fix the same disorder configuration for each of the simulations. We can achieve this by computing a densely resolved disorder set on a lattice with a small grid spacing of $a = 0.5$ nm. The disorder sets for the simulations with bigger or non-uniform lattice constants are then computed from this set by interpolation. Furthermore, we fix the disorder amplitude to $K_0 = 0.3$ and the correlation length to $\xi = 15$ nm. The non-uniform implementation will be performed on a computational grid with a lattice constant of $u_0 = 10$ nm and a scaling factor $s = 1.1$ for the lattice transformation given by Eq. (6.25). The computed scattering state probability densities are compared to uniform tight-binding simulations with the

big lattice constant of $a = 10$ nm and the small grid spacing of $a = 2$ nm. The corresponding disorder configurations are shown in Figs. 6.4 (b-d). Note that for all simulations the lattice constant in the x-direction a_x is fixed to 4 nm. This is done to prevent an influence of the longitudinal spatial direction and only probe the transverse resolution. While panels (b) for $a = 2$ nm and (c) for $a = 10$ nm in Fig. 6.4 show a uniform disorder distribution, panel (d) is illustrating the non-uniform case. In the latter, it is certainly observable that the lattice points, stretching from the edges of the system into the bulk, resolve the disorder with a higher resolution at the boundaries. Contrary, the bulk is sampled much less.
Next, we need to rescale the computed scattering states on the non-uniform lattice, as they correspond to transformed wave functions $\hat{\psi} = \sqrt{f'(u)}\psi$ and not directly to the physical wave functions ψ. Also, we have to account for the normalization of the states with respect to the number of lattice points in the transverse directions. The rescaling is then performed by the following relation

$$\psi = \sqrt{\frac{1}{u_0} \cdot \frac{1}{\frac{|f(u+u_0)-f(u-u_0)|}{2u_0}}}\hat{\psi} = \sqrt{\frac{2}{|f(u+u_0)-f(u-u_0)|}}\hat{\psi}. \tag{6.28}$$

Finally, we can put everything together and compute the LDOS of the states ψ in the scattering region. In Fig. 6.5 the probability densities with respect to the transverse y-direction for different positions along the transport direction (x-direction) are illustrated. The plots only show the local range close to one edge at $y = W$, as the scattering states for one propagation direction are localized at one system boundary. In all of the figures it is observable that for the uniform implementation with a large lattice constant of $a = 10$ nm (orange curves) the LDOS exhibits strong oscillations at the system boundaries with a bad convergence rate, compared to the small grid spacing and uniform implementation with $a = 2$ nm (blue curves). In contrast to that, the non-uniform implementation (red dots), with the same number of lattice points as the uniform $a = 10$ nm simulation, shows an almost perfectly matching LDOS when comparing to the $a = 2$ nm case. This is reasonable, as the smallest lattice constant located at the boundary is $a_s = 2.33$ nm, meaning that we have a comparable lattice resolution at the edges. The remarkable advantage is that we achieve a high convergence by just 20 % of the lattice points in the non-uniform implementation compared to the uniform case. For the exemplary positions along the x-direction, we plot in Fig. 6.5 the original probability density on the computational grid (green curves). The green curves are simply transformed into the red dots by mapping the computational coordinates onto the physical ones by Eq. (6.25).
Summing up, the non-uniform tight-binding implementation works as desired, improving the numerical convergence of spatial properties by using a reduced number of efficiently distributed lattice points.

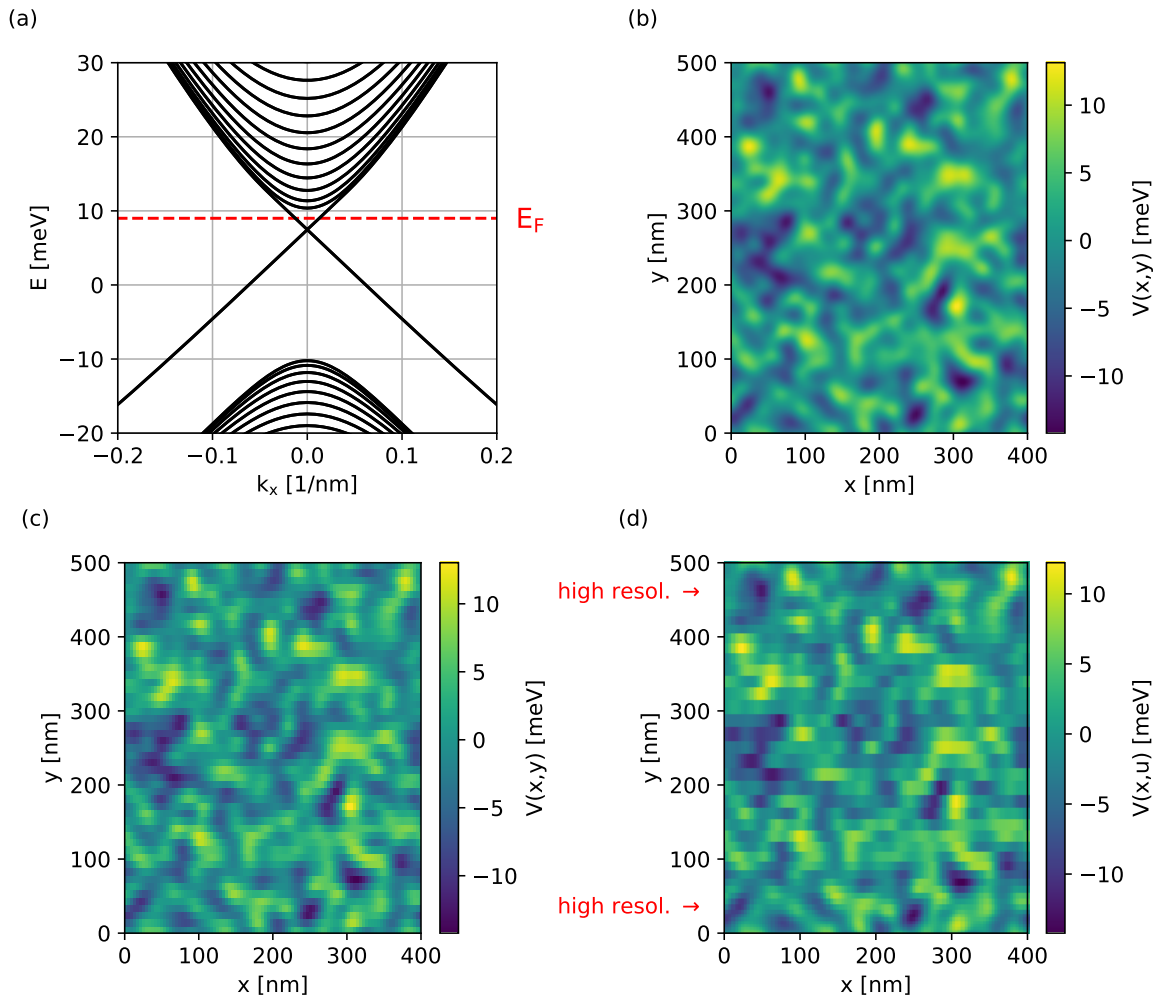

Figure 6.4: (a) Bandstructure of a 2D TI lead with width $W = 500$ nm and lattice constant $a = 2$ nm. The Fermi energy E_F is marked with a red dashed line. Panels (b) and (c) show uniformly sampled disorder configurations for lattice constants $a = 2$ nm and $a = 10$ nm, respectively. (d) Non-uniform disorder set that has a higher resolution at the system boundaries than in the bulk.

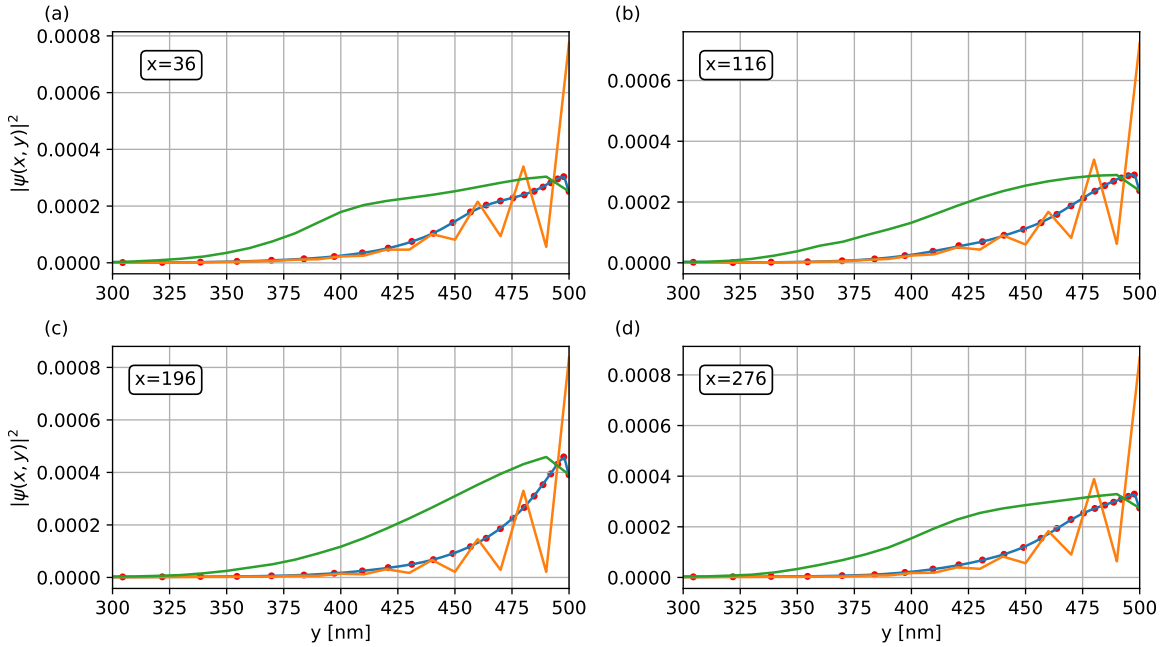

Figure 6.5: (a-d) Local densities of scattering states at different longitudinal x-positions. The orange (blue) curves corresponds to a uniform tight-binding simulation with lattice constant of $a = 10$ nm ($a = 2$ nm). The red dots are the LDOS computed on a non-uniform lattice with $s = 1.1$ in the employed lattice transformation given by Eq. (6.25). The red dots match with the densities in blue, obtained by the dense uniform grid. The green curves are the LDOS on the computational grid corresponding to the physical non-uniform grid. The green curves are mapped onto the red dots by transforming the transverse coordinates according to Eq. (6.25).

6.5.2. 2D TI/ferromagnetic metal hybrid

In order to test the non-uniform tight-binding in hybrid systems, where a part of the setup is implemented with a non-uniform grid, we explore the structure studied in Ref. [239] as another example. The system is a hybrid of a 2D topological insulator and a ferromagnetic metal (FM) with a magnetization $\boldsymbol{S}$. This physical setup provides interface states localized at the TI/FM boundary. Due to their localization this is a prime example to test our non-uniform numerical method. A schematic plot of the system is shown in Fig. 6.6 (a). The 2D TI is modelled by Eq. (6.26) with the same parameters as in the previous example, except that we choose here $D = 0$ to match the parameter set of Ref. [239]. The FM is modelled by a simple Stoner band model [240], where the Hamiltonian is given by

$$H_{\mathrm{FM}} = [-\mu_{\mathrm{FM}}^{\mathrm{eff}} + t_{\mathrm{FM}}(k_x^2 + k_y^2)]\sigma_0 \otimes \tau_0 + J_{ex}[\boldsymbol{S} \cdot \boldsymbol{\sigma}] \otimes \tau_0, \tag{6.29}$$

where the magnetization $\boldsymbol{S} = S(\sin(\theta)\cos(\varphi), \sin(\theta)\sin(\varphi), \cos(\theta))$ is a function of angles [see Fig. 6.6 (a)]. For simplicity we set $S = 1$. The matrices σ_i and τ_i act in spin and orbital space, respectively. The Hamiltonian parameter of the FM is fixed to $t_{\mathrm{FM}} = 5\ \mathrm{eV} \cdot \mathrm{nm}^2$. The coupling between the 2D TI region and the FM region is given by the hopping

$$t_{\mathrm{B}} = 0.35 \cdot \frac{t_{\mathrm{FM}}}{a_{\mathrm{B}}^2}\sigma_0 \otimes \tau_0. \tag{6.30}$$

The lattice constant a_{B} for the coupling hopping is the average between the smallest lattice constant at the boundary of the 2D TI and the lattice constant a_{FM} in the FM region. While the chemical potential of the TI region is fixed to zero, the chemical potential in the FM is chosen such that the upper band edge is fixed relative to the Dirac point of the TI. This can be done by defining

$$\mu_{\mathrm{FM}}^{\mathrm{eff}} = \mu_{\mathrm{FM}} + \frac{4}{a_{\mathrm{FM}}^2} t_{\mathrm{FM}}. \tag{6.31}$$

For the following calculations we fix the value $\mu_{\mathrm{FM}} = 8$ meV. This choice assures that we are in the pristine system configuration [239], where the Dirac point of the edge states is not submerged into the FM bands. In the TI region, we employ the mapping given by Eq. (6.25) and we fix $s = 0.8$. The mapping from the computational space onto the physical system is illustrated for the complete system in Fig. 6.6 (b). As the states of a metallic system are not localized in any specific region of the system, the Hamiltonian H_{FM} is discretized on a uniform lattice with lattice spacing a_{FM}. Note that the mapping function is not optimized yet, instead it is chosen such that the smallest lattice constant at the boundary of the non-uniform lattice is closely matching with a_{FM}. The computational grid is uniformly discretized with the lattice constant a_{TI}, which is fixed to 8 nm. The number of lattice points in the FM region, which are necessary to simulate a FM stripe with width W_{FM} and a lattice constant a_{FM}, is given by $N_{\mathrm{FM}} = W_{\mathrm{FM}}/a_{\mathrm{FM}} + 1$. These lattice points are separated by a_{TI} on the computational grid, but the values on each lattice site are scaled by a_{FM}. That is the reason, why the slope of the orange line in Fig. 6.6 (b) is not equal to 1. For simplicity,

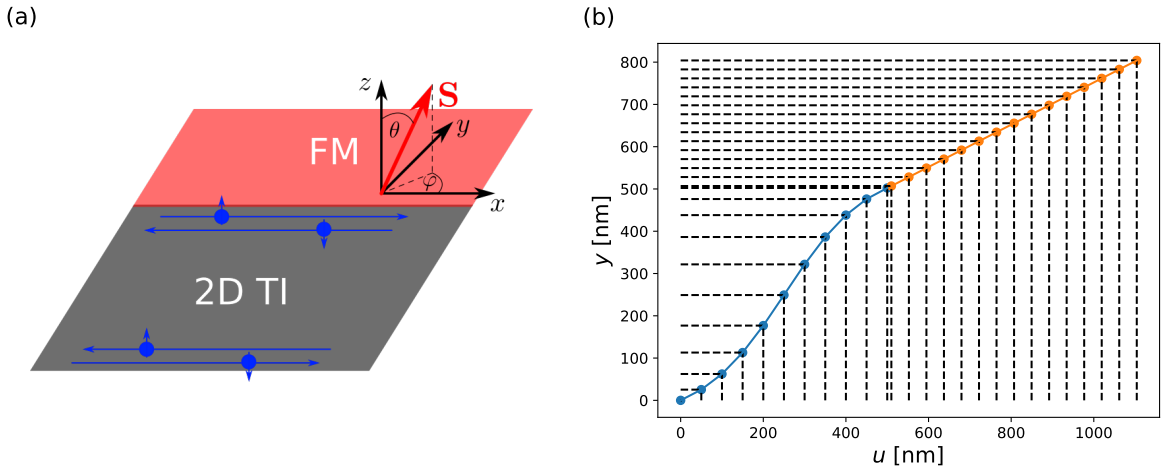

Figure 6.6: (a) Schematic plot of the TI/FM hybrid test system (adopted from Ref. [239]). The edge states (shown in blue) at the interface hybridize with the FM states and feel the influence of the magnetization $\boldsymbol{S}$. (b) Mapping procedure from the computational space u onto the physical space y. The discretization is chosen non-uniform in the TI and uniform in the FM.

the magnetization $\boldsymbol{S}$ is defined to point parallel to the z-direction and the exchange energy is set to $J_{ex} = -5$ meV.

In Fig. 6.7 (a), the bandstructure is displayed, where we choose a width of the TI region $W_{\mathrm{TI}} = 504$ nm and a width of the FM region $W_{\mathrm{FM}} = 300$ nm. The spectrum consists of the parabolic bands stemming from the FM region, bulk valence and conduction bands, as well as edge states, originating from the 2D TI. Compared with Fig. 6.4 (a), it is clear that the magnetization $\boldsymbol{S}$ is lifting the energetic degeneracy of the TI edges states. The states localized at the TI/FM-interface hybridize with the spin split bands of the FM. This can be visualized by calculating the spin expectation value for z-polarization $\langle \sigma_z \rangle$ and additional color coding (red $\uparrow$, blue $\downarrow$) of the respective bands in the spectrum [see Fig. 6.7 (b)]. The edge states at the TI boundary which are not connected to the FM remain with a linear dispersion. The states at the boundary between the TI and FM regions bend towards the parabolic FM bands and hybridize strongly with those if their spin quantum numbers match.

Next, we benchmark a non-uniform implementation with the standard uniform case. In Fig. 6.8 (a), the spectrum of the TI/FM hybrid structure is plotted for different configurations of the lattice implementation. The system widths are the same as in those calculations that we use in Fig. 6.7. The continuous blue line is the best converged, but simultaneously computationally the most expensive one, and corresponds to a uniform configuration with $a_{\mathrm{TI}} = a_{\mathrm{FM}} = 4$ nm. The worst implementation is illustrated by the dotted orange lines, where in the TI region, as well as in the FM region, uniform lattices with $a_{\mathrm{TI}} = 8$ nm and $a_{\mathrm{FM}} = 4$ nm are employed. Finally, the red dashed lines are computed using the non-uniform tight-binding scheme. The number of lattice points is

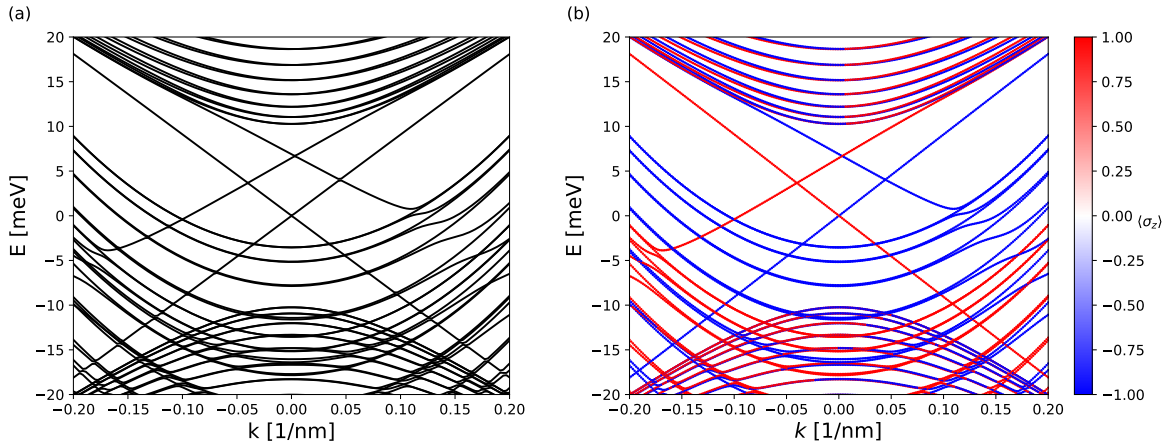

Figure 6.7: (a) Bandstructure of a TI/FM hybrid system for the widths $W_{\mathrm{TI}} = 504$ nm and $W_{\mathrm{FM}} = 300$ nm. The coupling between the TI and the FM induces, due to the presence of the exchange energy J_{ex}, a splitting of the spin polarized edge states. (b) The same bandstructure is plotted with the computed spin polarization along the z-direction.

the same as for the orange dotted lines, but the lattice points are efficiently shifted to the boundaries. It can be clearly observed in Fig. 6.8 (a) that the red dashed lines are lying closely to the blue continuous lines for the interesting interface states. Therefore the convergence of the spectrum of the interface states is increased considerably.
Next, we check the convergence of the local density of states. Figure 6.8 (b) displays the LDOS close to the TI/FM-interface for an energy of $E = 5$ meV. The corresponding states are marked in the bandstructure in Fig. 6.8 (a) by dots. Their colors correspond directly to the colors which are used for the LDOS plots. Also in the LDOS the increased convergence is observable. While the low resolved uniform lattice configuration (orange line) shows strong oscillations, the non-uniform implementation with an efficient lattice distribution is lying almost perfectly over the high resolved uniform implementation. Only the value exactly at the boundary site of the TI and FM regions is exhibiting a too small magnitude. The exact reason for this behavior still needs further checks in future studies. As a last remark, the green line is again the LDOS that is returned by Kwant on the computational grid.

Summing up, we conclude that the non-uniform tight-binding methodology showed a highly improved accuracy for the computed quantities in both of the above considered examples, while not increasing the computational effort. An efficient spatial distribution of lattice points leads to strongly improved results. This implementation scheme can be generally applied to analogous problems and might also help in studying, for example, 3D models, which are by nature very costly.

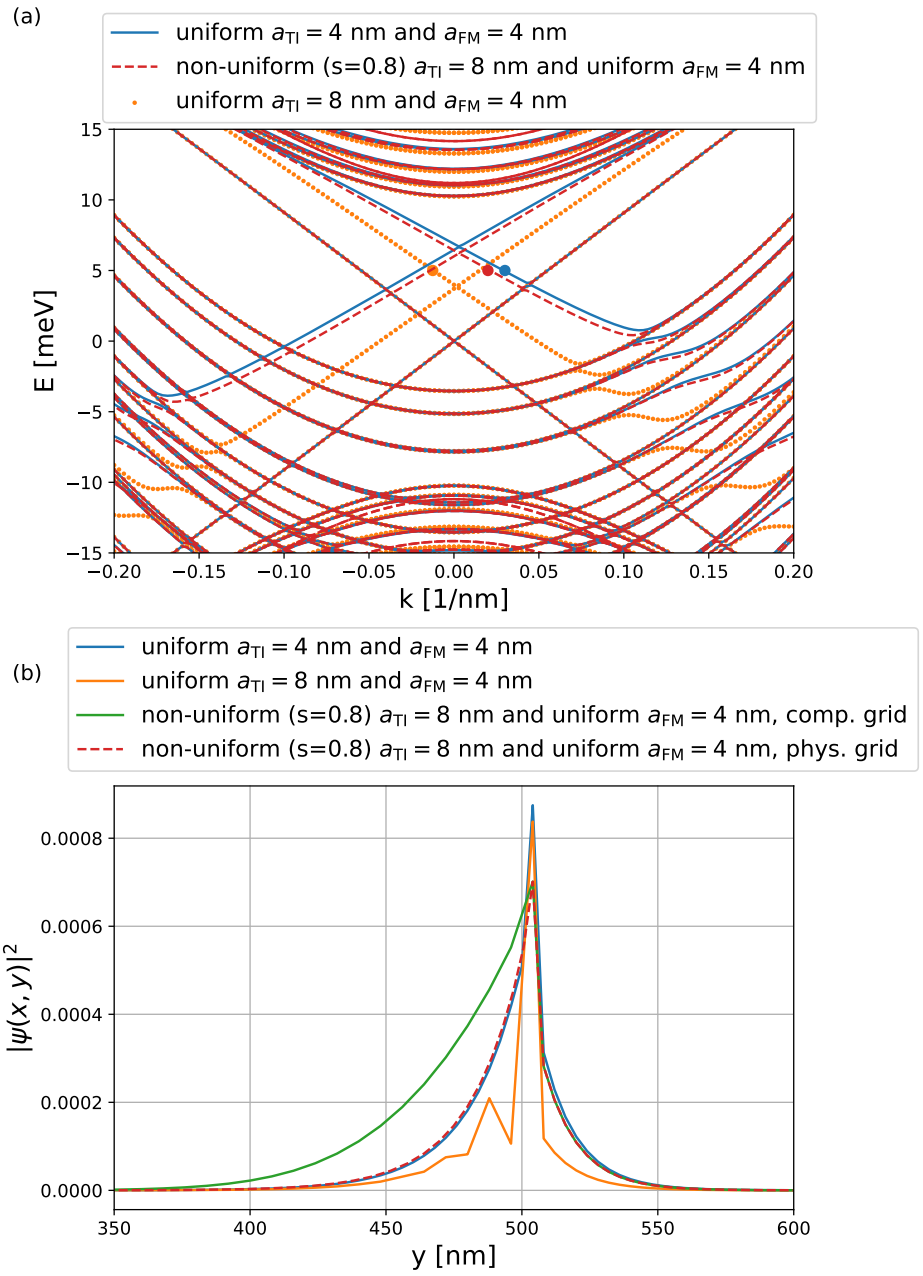

Figure 6.8: (a) Comparison of the TI/FM hybrid spectrum obtained by different lattice configurations. The non-uniform tight-binding method increases the convergence very closely to the uniform and dense grid. (b) Local density of states for the states marked with colored dots in the banstructures. Comparing the orange and red dashed lines we observe that convergence is highly improved with the non-uniform lattice implementation.

7. Conclusions and outlook

In this dissertation, we studied in detail charge and spin transport in normal-conducting, as well as in superconducting Dirac systems. The scattering behavior of topological states off surface steps in topological insulators was studied and transport in TI nanowires was examined in a divers number of system setups. Moreover, spin relaxation in superconducting single-layer and bilayer graphene was analyzed, while taking into account the emergence of locally bound Yu-Shiba-Rusinov states. The obtained results were then connected to properties of bilayer graphene Josephson junctions with a magnetic impurity in the normal region. Finally, a non-uniform tight-binding scheme was introduced to increase the efficiency in implementing systems with a non homogenous local density of states distribution, with TIs being a prime example. In the following, the main results of this thesis are recapitulated and summarized. Therein, short outlooks to further possible studies are given and remaining open questions are formulated.

Starting with the study of normal-conducting topological insulators, we first examined the scattering of Dirac states in Bi_2Se_3 systems which have step edges on their top surface. More precisely, we generated correlated island structures which are similarly present in realistic samples of bismuth based TIs. By computing the local density of states of the scattering states in the system, we saw that the highest density was located directly at the step edges between different lattice layers. Contrary, right before step edges the LDOS is reduced on the lower lattice layer and only weak but homogeneous values can be found between the islands.
The identification of topological surface states via signatures in the LDOS at step edges on the material surface would be certainly an interesting useful technique. Measurements of the state distribution at the surface can be performed via scanning tunnelling microscopy or mid-infrared near-field microscopy. Comparing the numerical simulations with experimental measurements on real samples could give hints on how to differentiate trivial from topological states, for example, by tuning the Fermi energy in the system or by applying certain magnetic field configurations. Further simulations should be performed to study the dependence of surface states on these parameters and also other materials like Bi_2Te_3 should be examined. The spectra of different TIs differ strongly concerning the size of the bulk bandgap and the anisotropy inside the crystal. These features also affect the properties of surface states at step edges and should be studied in more detail.
Next, we moved on from the slab geometry with two decoupled Dirac cones on the top and bottom surfaces by defining TI nanowires. In the wire configuration, for typical setups only one quantized Dirac cone is located at the surface and transport of these states can be modulated by applying a magnetic field parallel to the wire axis. However,

wires can also be grown in a core-shell structure, where the TI material is wrapped around an insulating core. In order to understand the spectrum of such nanowires we first studied in detail the bandstructure of a hollow TI shell by employing the 3D BHZ Hamiltonian. There vacuum was serving as the insulating core and it turned out that the spectrum consists of two separated Dirac cones on the inner and outer surfaces, as long as the thickness of the TI shell is not reduced to allow an overlap between the surface states. Inspired by this simple observation, we devised an effective Dirac Hamiltonian which captures the essential spectral information and performed transport simulations to predict signatures for future experimental measurements. By constructing wires with a certain ratio of inner and outer surface radii one is able to modify the periodicity of flux periodic conductance oscillations, due to the superposition of the Aharonov-Bohm effect of inner and outer surface modes.
Core-shell nanowires are a very fascinating platform to study Dirac physics. Compared to typical TI nanowires with a single Dirac cone on their surface, the bulk contribution to, for example, the conductance should be considerably reduced. At the same time, interesting effects arising from the topological states could be observable more clearly due to the presence of a second surface or interface Dirac cone located around the core material. From a theoretical point of view these systems offer a broad range of possible studies. It would be, for example, certainly interesting to examine the Andreev reflection behavior in a N/S-junction and to check if Majorana fermions emerge and how the two Dirac surfaces interact in transport. Also, constructing a Josephson junction with these wires could show interesting features in the current-phase relation and the Andreev bound state spectrum simply by tuning an axial magnetic field. Hopefully, future experiments can give insight into these fascinating Dirac platforms.
Afterwards we examined rectangular TI nanowires with a single surface Dirac cone and studied the emergence of 1D hinge states in a perpendicular magnetic field. Due to the anisotropy in the Bi_2Se_3 quintuple layers, which is included in the 3D BHZ model, Landau levels from at different energy values. This difference in energies results in a smooth deformation of the bandstructure by slowly rotating the magnetic field direction in the plane of the wire cross-section. Thereby, 1D hinge states can be induced and the system corresponds to an extrinsic higher-order TI.
As a last study in the normal-conducting regime, we considered nanowire constrictions, where the nanowire surface has a non constant radius along the wire axis. On the basis of interesting studies on shaped TI nanowires of Dr. Kozlovsky we picked up on still open questions and could identify many junction features when applying a magnetic field parallel to junction direction. The transport behavior can be classified by a geometry property, namely by the length of the central wire segment which connects the constricting system parts. Increasing the field strength leads to the formation of Landau levels on the side faces of the junction which experience an out-of-plane field component. Therefore the central part of the system acts like a box with quantized energy levels inside, where the lead modes can tunnel resonantly into. Depending on the length L_{center} of the central wire the separation of the discrete energy levels is either small (big L_{center}), leading to a large number of states in the box, or big due to a small length L_{center}, with only a few available states in the box. Furthermore, for the latter

case also Landau level features appear in the conductance because of the increasing influence of the side faces.
TI nanowire constrictions might offer the possibility to trap Dirac particles in a magnetically generated box and to probe the spectrum of these states in great detail. Here the question arises whether such junctions can be used as angular momentum filters of the TI states. Transmission is allowed by only a discrete set of quantized states in the setup, which also have a fixed angular momentum. Therefore it could be fascinating to use this setup as intermediate devices for experiments where a fixed angular momentum quantum number is useful for certain measurements. Still, this question needs more attention and further studies have to be performed in order to clarify this problem.

After extensive studies on normal-conducting TI systems, we switched to superconducting setups. As a first setup, we considered crossed Andreev reflection in a TI nanowire T-junction with one superconducting and two normal-conducting leads. Applying a magnetic field perpendicular to the junction induces the formation of chiral edge states, which allows for the spatial separation of incoming electrons and outgoing holes. Moreover, by applying an additional magnetic field parallel to the superconducting wire axis, CAR can be easily tuned and even switched on and off in the single mode regime. Also, advantageous for an experimental realization, CAR is observable dominantly in weak perpendicular magnetic field ranges and for energies far above the Dirac point.
Afterwards, TI nanowire Josephson junctions were studied. There we differentiated between the following two system configurations.
First, the TI nanowire was assumed to be fully proximitized around the wire circumference by an s-wave superconductor. Applying a weak axial magnetic field modifies the Andreev reflection, which is observable in the current-phase relation as discrete jumps with respect to the variation of the phase difference. These jumps are directly related to the surface state spectrum and could serve as a probe of the bandstructure in actual experiments.
Second, the setup is assumed to be in a partially superconducting state which is closer to the realization in experiments. This project was examined in close relation to experimental measurements performed in the Weiss group at the University of Regensburg. Low transparency HgTe Josephson junctions exhibit flux periodic supercurrent oscillations with a period half the superconducting flux quantum. Numerical simulations in combination with semiclassical analytical calculations of Dr. Fuchs could show that the oscillations originate from locally induced superconducting pairing in the TI nanowire surface. Additionally, interface barriers suppress large current contributions which cover up the $h/4e$-periodic components and eventually make those observable. These oscillations serve as another signature of clear surface transport in TI nanowires.

In the second main part of this thesis we switched the material class and considered superconducting single-layer and bilayer graphene. Initially the emergence of Yu-Shiba-Rusinov states at magnetic impurities on top of superconducting bilayer graphene was studied. The YSR energy spectrum was computed as a function of the chemical poten-

tial of the system and it was shown that the spectrum behaves differently for impurities which are located at either dimer or non-dimer sites. This finding can be directly related to the normal state DOS, where a doping level in a magnetic resonance regime leads to a change in the spectral properties of the YSR states. Furthermore, the eigenfunctions were studied and it was observed that these localize at different sublattices in the structure.
These findings have direct consequences on the spin relaxation of the superconducting quasiparticles. Therefore, spin-relaxation rates were computed for single-layer and bilayer graphene by employing a methodology which incorporates scattering matrix elements. The impurity in the system was assumed to either induce local spin-orbit coupling or a local magnetic exchange interaction, such that YSR states can form. The calculated spin-relaxation rates in case of local spin-orbit coupling decrease when lowering the system temperature, what matches perfectly with the known Elliot-Yafet spin-relaxation mechanism in superconducting systems. However, for magnetic impurities, the spin-relaxation rates exhibit also a drastic decrease in certain ranges of the chemical potential. This finding is in strong contrast with the known theory, where first an increase in the spin-relaxation rate is expected, after which it starts to decrease again (Hebel-Slichter peak). The anomalous behavior can be traced to the resonance doping ranges of the corresponding YSR states, while far away from these values the relaxation behaves as expected. This leads to the conclusion that the reduced overlap between the resonant YSR states, which lie inside the superconducting gap, and the quasiparticle states, which are located close to the gap energy, also leads to a reduced spin scattering. Consequently, one needs to be cautious when determining the microscopic source of spin relaxation.
Next, it was shown that also in the supercurrent of bilayer graphene Josephson junctions signatures of those resonances can be found. The locally induce magnetic exchange interaction affects the Andreev bound state spectrum for resonant values of the chemical potential, where a strong decrease in the critical current amplitude can be observed. These systems are experimentally easier to examine than spin relaxation in bulk superconductors and they could thereby serve as a first probe of the studied signatures in this thesis.
Regarding further possible studies, the emergence of ABS or YSR states in superconducting systems and in close relation to shaped TI nanowires, the effect of curvature on the ABS/YSR spectrum offers a fascinating possibility to tune their properties. Stretching, bending or putting a system under pressure along a defined direction will introduce a certain amount of positive or negative curvature at the material surface. This will obviously affect the localized YSR states, as well as the extended ABS, and therefore also their spectral properties. So curvature might be an interesting geometrical property to modify the transport behavior of surface states and could serve as a further possibility to study these special states in more detail.
Furthermore, in sight of the finding that the spin-relaxation rate induced by magnetic impurities in s-wave superconducting graphene behaves differently from the known theory for resonant doping levels, it might also be of interest to study this quantity for other pairing mechanisms. An example would be d-wave pairing, where the supercon-

ducting pairing depends on the momentum and therefore couples electrons and holes at different spatial positions. Such a pairing can analogously be treated with the devised calculation procedure of the spin-relaxation rate from the S-matrix. Maybe other relaxation signatures are present for different pairing mechanisms, which in turn would certainly be useful for many experiments as it could allow to differentiate between them.

The third and last part of this dissertation covered the theory of a non-uniform tight-binding implementation. Some systems exhibit physics which are localized in only a small region of the whole sample. Topological insulators for instance have states which are strongly localized to surfaces or edges, while the bulk of the system is not containing valuable information. In numerical tight-binding simulations one must therefore find a balance between accessible system size and convergence of the computed quantities, which is related to the used lattice constant. To raise the efficiency with a low number of lattice points while keeping the convergence to a maximum, we introduced a transformation methodology which efficiently distributes the available lattice points into the necessary spatial regions and keeps the tight-binding Hamiltonian in a hermitian form. By studying the convergence of, first, edge states computed with the 2D BHZ model and, second, interface states emerging in a 2D TI/FM hybrid system, we showed a big reduction of the computational cost while obtaining correct results. The methodology of a non-uniform tight-binding implementation might be particularly useful for simulating 3D systems, where the computational demands are even higher.

Finally, besides the in detail discussed topics of this thesis, many of the introduced methods have also been applied in studies which go beyond the scope of this work. First, in Ref. [45] spin-charge conversion conductance was examined numerically, where a spatial anisotropy can be observed due to special cubic spin-orbit coupling terms, which arise in a 2DEG at a $LaAlO_3|SrTiO_3$ interface [241]. Second, conductance features of topological surface states without quantization effects were examined in presence of randomly distributed but spatially correlated n- and p-doped surface areas. Results show two distinct conductance minima corresponding to Dirac points in each of the doped areas and the findings are in very good agreement with a different theoretical approach employed by Dr. Marganska Additionally, the observations could explain experimental measurements on the Gilbert damping factor in hybrid systems of a topological insulator and a ferromagnetic material. For more details the interested reader is referred to Ref. [147].

In summary, topological insulators and graphene are fascinating systems to study the effects of Dirac physics in condensed matter. These systems are ideal platforms for studying fundamental questions in physics due to the ability to tune the material properties in a divers number of ways. Even after two decades of intensive scientific research on these systems there are still new aspects and physical properties that can be discovered in these materials. Their special features also make them high ranking candidates for future applications and devices, where it is exciting to see what new characteristics might be found.

A. Appendices

A.1. Derivation of ABS in fully proximitized topological insulator nanowire Josephson junctions

In Ref. [158] Pientka et al. derive from Beenakkers scattering matrix formalism an expression for ABS with superconducting leads which display a Zeeman splitting of the bands. Here we can apply an analogous approach. The essence of Beenakkers method is discussed in Sec. 3.6.1, where the equations we need to consider are given by

$$\Psi^{\mathrm{out}} = S_{\mathrm{N}}\Psi^{\mathrm{in}}, \tag{A.1}$$
$$\Psi^{\mathrm{in}} = S_{\mathrm{A}}\Psi^{\mathrm{out}}, \tag{A.2}$$
$$\Psi^{\mathrm{in}} = S_{\mathrm{A}}S_{\mathrm{N}}\Psi^{\mathrm{in}}. \tag{A.3}$$

The bound state spectrum can then be found by demanding that

$$\det(\mathbb{1} - S_{\mathrm{A}}S_{\mathrm{N}}) \stackrel{!}{=} 0. \tag{A.4}$$

If there is no disorder coupling different modes, the problem is separable. We can show this by looking at the simple example of just four modes in the system. The first equation for scattering in the normal part of the system then reads

$$\Psi^{\mathrm{out}} = S_{\mathrm{N}}\Psi^{\mathrm{in}} \tag{A.5}$$

$$\begin{pmatrix} \Psi^{\mathrm{L}}_{\mathrm{e1}} \\ \Psi^{\mathrm{L}}_{\mathrm{h1}} \\ \Psi^{\mathrm{R}}_{\mathrm{e1}} \\ \Psi^{\mathrm{R}}_{\mathrm{h1}} \\ \Psi^{\mathrm{L}}_{\mathrm{e2}} \\ \Psi^{\mathrm{L}}_{\mathrm{h2}} \\ \Psi^{\mathrm{R}}_{\mathrm{e2}} \\ \Psi^{\mathrm{R}}_{\mathrm{h2}} \end{pmatrix}^{\mathrm{out}} = \begin{pmatrix} t_{\mathrm{e1}} & 0 & 0 & 0 & 0 & 0 & 0 & 0 \\ 0 & t_{\mathrm{h1}} & 0 & 0 & 0 & 0 & 0 & 0 \\ 0 & 0 & t'_{\mathrm{e1}} & 0 & 0 & 0 & 0 & 0 \\ 0 & 0 & 0 & t'_{\mathrm{h1}} & 0 & 0 & 0 & 0 \\ 0 & 0 & 0 & 0 & t_{\mathrm{e2}} & 0 & 0 & 0 \\ 0 & 0 & 0 & 0 & 0 & t_{\mathrm{h2}} & 0 & 0 \\ 0 & 0 & 0 & 0 & 0 & 0 & t'_{\mathrm{e2}} & 0 \\ 0 & 0 & 0 & 0 & 0 & 0 & 0 & t'_{\mathrm{h2}} \end{pmatrix} \begin{pmatrix} \Psi^{\mathrm{R}}_{\mathrm{e1}} \\ \Psi^{\mathrm{R}}_{\mathrm{h1}} \\ \Psi^{\mathrm{L}}_{\mathrm{e1}} \\ \Psi^{\mathrm{L}}_{\mathrm{h1}} \\ \Psi^{\mathrm{R}}_{\mathrm{e2}} \\ \Psi^{\mathrm{R}}_{\mathrm{h2}} \\ \Psi^{\mathrm{L}}_{\mathrm{e2}} \\ \Psi^{\mathrm{L}}_{\mathrm{h2}} \end{pmatrix}^{\mathrm{in}}, \tag{A.6}$$

while scattering at the N/S-interfaces gives

$$\Psi^{\text{in}} = S_{\text{A}}\Psi^{\text{out}} \tag{A.7}$$

$$\begin{pmatrix} \Psi^{\text{R}}_{\text{e1}} \\ \Psi^{\text{R}}_{\text{h1}} \\ \Psi^{\text{L}}_{\text{e1}} \\ \Psi^{\text{L}}_{\text{h1}} \\ \Psi^{\text{R}}_{\text{e2}} \\ \Psi^{\text{R}}_{\text{h2}} \\ \Psi^{\text{L}}_{\text{e2}} \\ \Psi^{\text{L}}_{\text{h2}} \end{pmatrix}^{\text{in}} = \begin{pmatrix} 0 & 0 & r^{\text{R1}}_{\text{ee}} & r^{\text{R1}}_{\text{eh}} & 0 & 0 & 0 & 0 \\ 0 & 0 & r^{\text{R1}}_{\text{he}} & r^{\text{R1}}_{\text{hh}} & 0 & 0 & 0 & 0 \\ r^{\text{L1}}_{\text{ee}} & r^{\text{L1}}_{\text{eh}} & 0 & 0 & 0 & 0 & 0 & 0 \\ r^{\text{L1}}_{\text{he}} & r^{\text{L1}}_{\text{hh}} & 0 & 0 & 0 & 0 & 0 & 0 \\ 0 & 0 & 0 & 0 & 0 & 0 & r^{\text{R2}}_{\text{ee}} & r^{\text{R2}}_{\text{eh}} \\ 0 & 0 & 0 & 0 & 0 & 0 & r^{\text{R2}}_{\text{he}} & r^{\text{R2}}_{\text{hh}} \\ 0 & 0 & 0 & 0 & r^{\text{L2}}_{\text{ee}} & r^{\text{L2}}_{\text{eh}} & 0 & 0 \\ 0 & 0 & 0 & 0 & r^{\text{L2}}_{\text{ee}} & r^{\text{L2}}_{\text{eh}} & 0 & 0 \end{pmatrix} \begin{pmatrix} \Psi^{\text{L}}_{\text{e1}} \\ \Psi^{\text{L}}_{\text{h1}} \\ \Psi^{\text{R}}_{\text{e1}} \\ \Psi^{\text{R}}_{\text{h1}} \\ \Psi^{\text{L}}_{\text{e2}} \\ \Psi^{\text{L}}_{\text{h2}} \\ \Psi^{\text{R}}_{\text{e2}} \\ \Psi^{\text{R}}_{\text{h2}} \end{pmatrix}^{\text{out}} . \tag{A.8}$$

Putting the respective scattering matrices into Eq. (A.4) and introducing a short hand notation, where $S_{\text{L/R}}$ denotes reflection at the left/right S/N-interface and $T_{1,2}$ contains the transmission amplitudes of the electron and hole modes 1/2 for moving through the N region, we get

$$\det\left(\mathbb{1} - \begin{pmatrix} 0 & S^1_{\text{R}} & 0 & 0 \\ S^1_{\text{L}} & 0 & 0 & 0 \\ 0 & 0 & 0 & S^2_{\text{R}} \\ 0 & 0 & S^2_{\text{L}} & 0 \end{pmatrix}\begin{pmatrix} T^1 & 0 & 0 & 0 \\ 0 & T'^1 & 0 & 0 \\ 0 & 0 & T^2 & 0 \\ 0 & 0 & 0 & T'^2 \end{pmatrix}\right) = 0, \tag{A.9}$$

$$\det\left(\mathbb{1} - \begin{pmatrix} 0 & S^1_{\text{R}}T'^1 & 0 & 0 \\ S^1_{\text{L}}T^1 & 0 & 0 & 0 \\ 0 & 0 & 0 & S^2_{\text{R}}T'^2 \\ 0 & 0 & S^2_{\text{L}}T^2 & 0 \end{pmatrix}\right) = 0, \tag{A.10}$$

$$\det\begin{pmatrix} \mathbb{1} & -S^1_{\text{R}}T'^1 & 0 & 0 \\ -S^1_{\text{L}}T^1 & \mathbb{1} & 0 & 0 \\ 0 & 0 & \mathbb{1} & -S^2_{\text{R}}T'^2 \\ 0 & 0 & -S^2_{\text{L}}T^2 & \mathbb{1} \end{pmatrix} = 0. \tag{A.11}$$

So in the end we get a determinant condition for each mode separately, leading to

$$\det\left(\mathbb{1} - S_{\text{L}}TS_{\text{R}}T'\right) \stackrel{!}{=} 0. \tag{A.12}$$

Analogously to Ref. [158], we define

$$\begin{aligned} S_{\text{R/L}}(\Delta\varphi) &= e^{\pm\text{i}\frac{\Delta\varphi}{2}\tau_z} S e^{\mp\text{i}\frac{\Delta\varphi}{2}\tau_z} \\ &= \begin{pmatrix} e^{\pm\text{i}\frac{\Delta\varphi}{2}} & 0 \\ 0 & e^{\mp\text{i}\frac{\Delta\varphi}{2}} \end{pmatrix}\begin{pmatrix} r_{\text{e}} & r_{\text{A}} \\ r_{\text{A}} & r_{\text{h}} \end{pmatrix}\begin{pmatrix} e^{\mp\text{i}\frac{\Delta\varphi}{2}} & 0 \\ 0 & e^{\pm\text{i}\frac{\Delta\varphi}{2}} \end{pmatrix}, \end{aligned} \tag{A.13}$$

$$S_{\text{R/L}}(\Delta\varphi) = \begin{pmatrix} r_{\text{e}} & r_{\text{A}}e^{\pm\text{i}\frac{\Delta\varphi}{2}} \\ r_{\text{A}}e^{\mp\text{i}\frac{\Delta\varphi}{2}} & r_{\text{h}} \end{pmatrix}, \tag{A.14}$$

where

$$r_{\mathrm{e/h}} = \pm r \exp\left(\mathrm{i}\chi_{\pm} \pm \mathrm{i}\varphi_{\mathrm{N}}\right), \tag{A.15}$$

$$r_{\mathrm{A}} = \sqrt{1-r^2}\exp(\mathrm{i}\chi_{\pm}), \tag{A.16}$$

$$\chi_{\pm} = \arccos\left(\frac{E \pm E_B^n}{\Delta_B}\right). \tag{A.17}$$

The parameter E_B^n is the flux induced energy splitting which was discussed in the main text. Further we include normal reflections at the interfaces, since the orbital magnetic field can lead to increasing reflection. As the scattering matrix S_{N} of the normal system we define

$$T = \begin{pmatrix} t_{\mathrm{e}} & 0 \\ 0 & t_{\mathrm{h}} \end{pmatrix} \qquad \text{with} \qquad t_{\mathrm{e/h}} = \exp\bigl(\mathrm{i}k_{\mathrm{e/h}}L\bigr). \tag{A.18}$$

We then plug these expressions into Eq. (A.12) and after some algebra we obtain the condition for ABS

$$\cos(2\chi_{\pm} + 2\theta_{+}) = r^2\cos(2\varphi_{\mathrm{N}} + 2\theta_{-}) + (1+r^2)\cos(\Delta\varphi), \tag{A.19}$$

where $\theta_{\pm} = (k_{\mathrm{e}} \pm k_{\mathrm{h}})L/2$ and $\Delta\varphi$ is the superconducting phase difference across the junction. Finally, we can neglect the phase φ_{N} of the normal reflection as this will only give a minor contribution in our clean setup and we write

$$\cos(2\chi_{\pm} + 2\theta_{+}) = r^2\cos(2\theta_{-}) + (1+r^2)\cos(\Delta\varphi). \tag{A.20}$$

For the bound states we can write the spectrum as

$$E_{\mathrm{ABS}}^n = \pm\Delta\cos\left[\frac{1}{2}\arccos\left(r^2\cos\bigl(2\theta_{-}^n\bigr) + (1-r^2)\cos(\Delta\varphi)\bigr) - \theta_{+}\right] \mp E_B^n. \tag{A.21}$$

A.2. Benchmark model for spin relaxation in graphene

For the exclusion of any errors due to a false implementation of the tight-binding system one can simply compare with known results. Particularly in the case of locally induced spin-orbit coupling, the implementation of the spin coupling terms in Eq. (2.22) needs careful checks. In Ref. [84] results for spin-relaxation rates in graphene with chemisorbed hydrogen and fluorine adatoms are discussed. More precisely, the effects of each of the SOC terms are studied separately. This allows us to check each component of our implemented model in great detail and assure its correctness. Note that the computed spin-relaxation rates are for an in-plane spin configuration of the incoming and outgoing scattering states along the x-direction. In turn, the implemented tight-binding model given by Eq. (2.22) is for an out-of-plane spin configuration. The transition amplitudes $S^x_{\sigma,-\sigma}$ [shorthand notation for the scattering matrix elements $t_{i\sigma,j-\sigma}$ and $r_{i\sigma,j-\sigma}$ of Eq. (3.58)] for in-plane spins can be calculated from the out-of-plane spin

transition amplitudes $S^z_{\sigma,-\sigma}$ by realizing that the eigenstates obey the relations

$$|1\rangle_x = \frac{1}{\sqrt{2}}\left(|1\rangle_z + |-1\rangle_z\right), \tag{A.22}$$

$$|-1\rangle_x = \frac{1}{\sqrt{2}}\left(|1\rangle_z - |-1\rangle_z\right). \tag{A.23}$$

The transition amplitudes are then given by

$$\begin{aligned} S^x_{1,-1} &= \langle 1| S |-1\rangle_x \\ &= \frac{1}{2}\left(\langle 1|_z + \langle -1|_z\right) S \left(|1\rangle_z - |-1\rangle_z\right) \\ &= \frac{1}{2}\left(\langle 1|_z S |1\rangle_z + \langle -1|_z S |1\rangle_z - \langle 1|_z S |-1\rangle_z - \langle -1|_z S |-1\rangle_z\right) \\ &= \frac{1}{2}\left(S^z_{1,1} + S^z_{-1,1} - S^z_{1,-1} - S^z_{-1,-1}\right), \end{aligned} \tag{A.24}$$

$$\begin{aligned} S^x_{-1,1} &= \langle -1| S |1\rangle_x \\ &= \frac{1}{2}\left(S^z_{1,1} + S^z_{1,-1} - S^z_{-1,1} - S^z_{-1,-1}\right). \end{aligned} \tag{A.25}$$

By using the correct combination of scattering matrix elements corresponding to the out-of-plane implementation, the in-plane spin transition amplitudes can be calculated. Analogously to Ref. [84], in Fig. A.1 the full relaxation rate along with the different spin-orbit coupling components are shown. The system parameters were fixed to a width of $W = 131a$ and a length of $L = 4a$. Note that the relaxation rate is independent of the exact length of the scattering region due to the fact that we only have a single impurity in the center. The region before and after the adatom can also simply be accounted as part of the translationally invariant leads. The phase averaging, which was introduced in Sec. 3.7, was performed over 30 equally spaced values in $[0; 2\pi]$. The calculated results for the full model, as well as for the different SOC components fit perfectly to the results discussed in Ref. [84]. As a final remark, note that the intrinsic components, shown in Figs. A.1 (d) and (h), are only non-zero for an in-plane spin configuration. For spin states that are polarized along the z-direction the intrinsic terms are only coupling equal spin kinds, such that no spin scattering is possible.

A.3. Comparison of different interlayer hopping configurations

In this section of the appendix the validity of the simplified bilayer graphene model with only γ_1 as the interlayer hopping which was employed in Sec. 5 is discussed. This is done by comparing the spin-relaxation results of the simpler model with $\gamma_3 = 0$ and $\gamma_4 = 0$ of the main text to computations using the full model. The computational effort increases only weakly when the additional interlayer hoppings are included, which makes an implementation easy at this point. Moreover, from the findings of Sec. 5

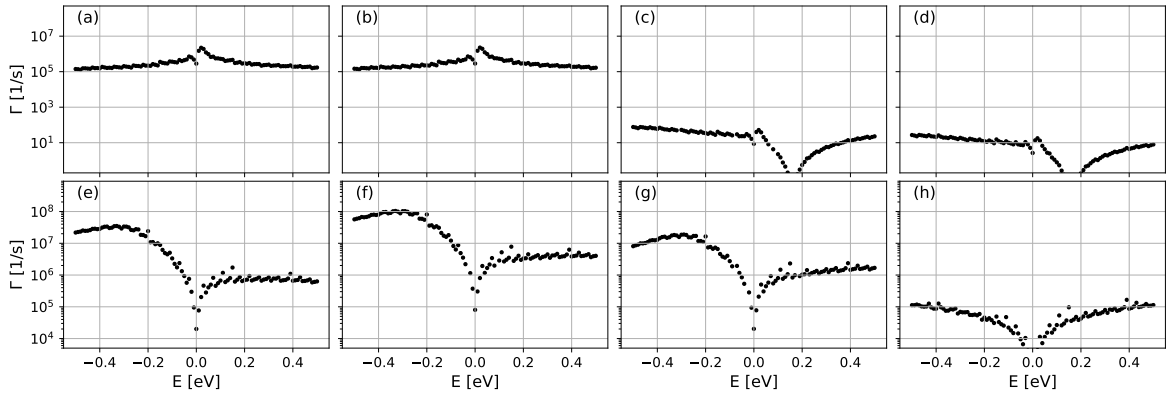

Figure A.1: Spin-relaxation rates for an in-plane spin configuration along the x-direction for a graphene system with width $W = 131a$ and length $L = 4a$. The impurity concentration is set to $\eta = 53$ ppm/carbon. The upper row corresponds to a hydrogen impurity, while the lower row shows results for fluorine. In (a) and (e) all SOC terms of Eq. (2.22) are used. Contrary, in (b) and (f) only PIA terms, in (c) and (g) only Rashba terms and in (d) and (h) only intrinsic SOC terms were used. The results fit perfectly with those of Ref. [84].

we know that the properties of $1/\tau_s$ are directly related to the magnetic resonance energies of impurities, which in turn determine the spectral properties of YSR states in bulk superconductors and ABS in Josephson junctions. Therefore, by comparing spin scattering calculations of the full model to the simplified ones, we can check for drastic changes also in the related quantities. In Fig. A.2 the spin-relaxation rates are plotted for the two model configurations as a function of the chemical potential for the temperatures $T = T_c$ and $T = 0.1$ K. We also compare both impurity kinds by considering a spin-orbit active (panels (a) and (c)) and a magnetic (panels (b) and (d)) hydrogen adatom that is located at dimer and non-dimer sites. The system and computation parameters are set as follows: Superconducting pairing is fixed to $\Delta = 1$ meV, the scattering region has a width of $W = 131a$ and the length is $L = 4a$ with a resulting impurity concentration of $\eta = 0.0413$ %. The phase averaging was performed over 20 equally spaced values in $[0, 2\pi]$. By comparing the computed curves in all four panels, we see immediately that only minor and no qualitative changes appear, such that the simplified model should capture all of the relevant physics.

A.4. ABS in bilayer graphene Josephson junction with J=0

In order to check the validity of our method for computing the ABS spectra by calculating the spectral density, we can directly compare the obtained results with the scattering matrix approach introduced in Sec. 3.6.1 if we put $J = 0$. For this system configuration the single hydrogen impurity will serve as a normal scattering center for

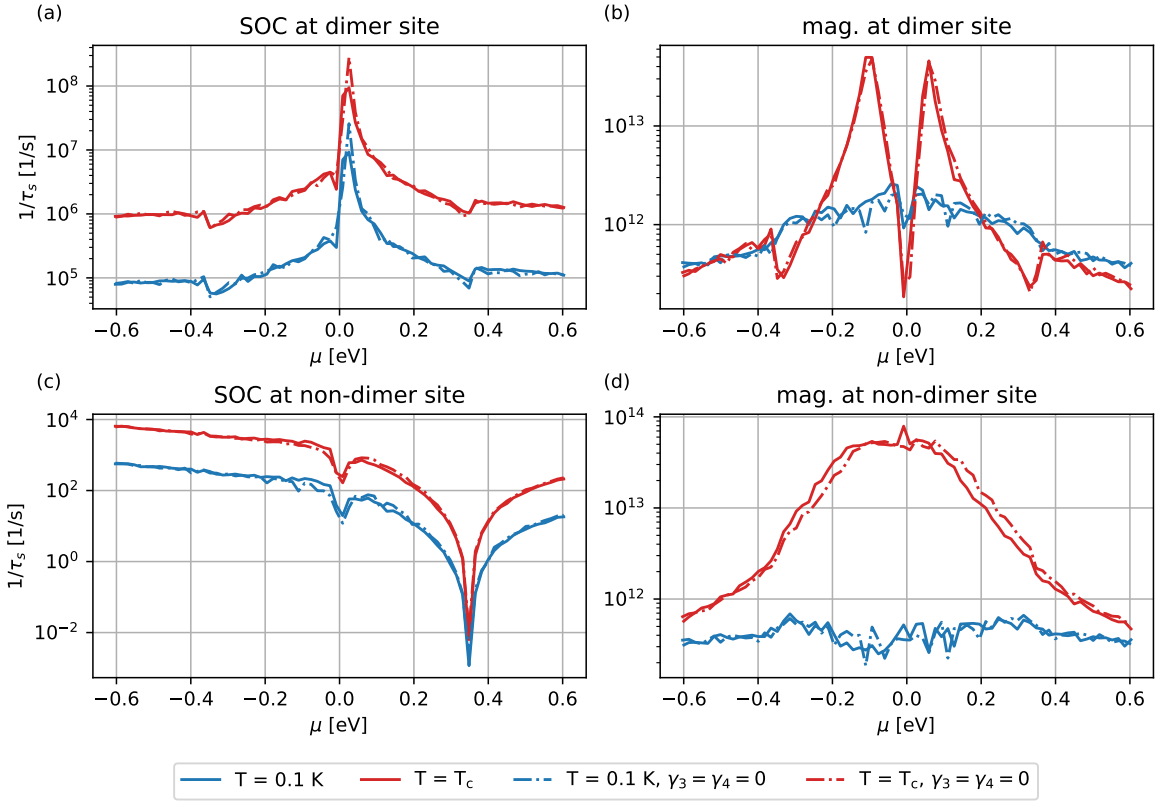

Figure A.2: Comparison of spin-relaxation rates $1/\tau_s$ as a function of the chemical potential μ for the two temperatures $T = T_c$ and $T = 0.1$ K obtained by the simplified BLG model ($\gamma_3 = 0$ and $\gamma_4 = 0$) and the full set of interlayer hoppings given by Eq. (2.15). A hydrogen impurity is considered to induce spin-orbit coupling [(a) and (c)], as well as magnetic exchange interactions [(b) and (d)], at dimer and non-dimer sites. The system and computation parameters are the same as those for Figs. 5.6 and 5.7 in the main text. The curves obtained by both models give qualitatively the same results. Adapted from the Supplemental Material of Ref. [3].

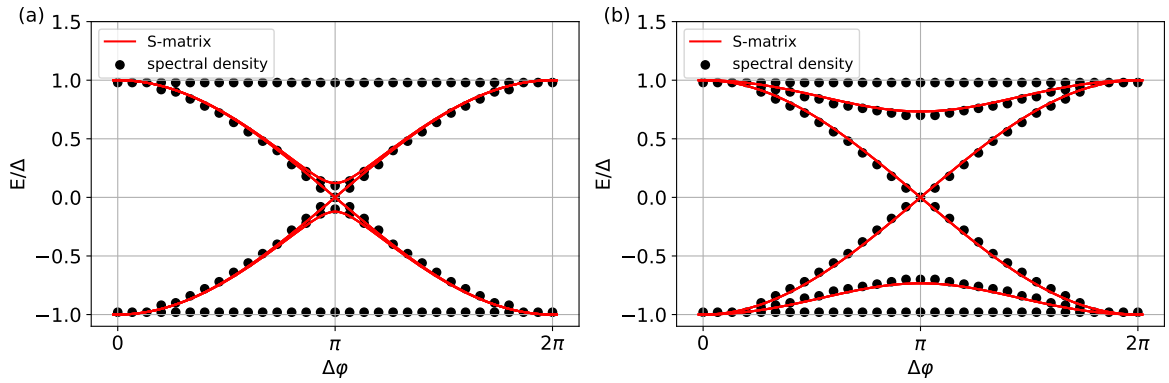

Figure A.3: Comparison of ABS spectra calculated by either the spectral density method (black dots) or the scattering matrix approach (continuous red lines) for (a) a dimer site and (b) a non-dimer site impurity. In the first case we used a chemical potential of $\mu = -100$ meV, while in the latter we put $\mu = 150$ meV and the superconducting pairing was set to $\Delta = 1$ meV. The system size is $W = 40a$ and $L = 10a$ and the magnetic exchange interaction was put to zero. Both methods give perfectly agreeing results. Adapted from the Supplemental Material of Ref. [3].

each value of the chemical potential μ. In Fig. A.3 the two approaches for calculating the ABS spectra are plotted, where the ABS spectra computed by the spectral density method are shown in black dots, and those obtained with the scattering matrix approach are plotted in red continuous lines. In (a), a hydrogen impurity is assumed to sit on top of a dimer site with $\mu = -100$ meV, while in (b) it is located at a non-dimer site with $\mu = 150$ meV. The ABS computed by the two approaches match perfectly, highlighting the correctness of the employed spectral density code.

A.5. Comparison of ABS and CPR in bilayer graphene Josephson junction

For a further consistency check of the spectral density code and also for the supercurrent computation via Green's function (see Sec. 3.6.2), we are in this appendix directly comparing a computed ABS spectrum obtained by the first method to a current-phase relation calculated with the second approach for a bilayer graphene Josephson junction. In Fig. A.4 (a) the CPR for a BLG Josephson junction with width $W = 40a$, length $L = 10a$, $\Delta = 1$ meV and a chemical potential of $\mu = -16$ meV is plotted. The curve shows two clear jumps around a phase differences of $\Delta\varphi = \pm 2$ which are marked with red dashed lines. These jumps typically occur in CPRs whenever the ABS spectrum has zero energy crossings, such that the bands in the ABS ground state change slope from negative to positive. The ABS energy spectrum, which is shown in Fig. A.4 (b), is computed by employing the spectral density method (for the same set of parameters). Exactly at phase differences $\Delta\varphi = \pm 2$ the ABS are exhibiting zero energy crossings

(also marked with red dashed lines). These matching features certainly highlight the correctness of both approaches.

A.6. Tight-binding implementation of hexagonal warping

This appendix serves as a general manual for the correct implementation of cubic momenta terms in a Hamiltonian and shows that fermion doubling for such components can be cancelled by employing an extended Hamiltonian which was devised by Marchand and Franz [242].

A.6.1. Hexagonal warping and finite difference representations

The spectra of surface states on topological insulators such as Bi_2Se_3 or Bi_2Te_3 do not only obey a linear Dirac equation. Instead, they exhibit strong hexagonal warping for higher energies. This effect is described by the inclusion of cubic momenta into the Hamiltonian [33, 243]

$$H'_{\text{warping}} = \hbar v_{\text{F}}(k_x\sigma_y - k_y\sigma_x) + \frac{W_2}{2}(k_+^3 + k_-^3)\sigma_z + V(x,y). \tag{A.26}$$

Here the usual definition of $k_\pm = k_x \pm \mathrm{i}k_y$ is used and the term $V(x,y)$ can describe any potential profile on the TI surface. In order to implement this Hamiltonian on a numerical grid using a tight-binding scheme one has to take care of the emerging Fermion doubling problem. Contrary to the case of a linear Dirac term it is no longer enough to add a second order Wilson mass term (see Sec. 3.2). Rather it becomes necessary to employ a 4x4 Hamiltonian derived by Marchand and Franz [242]. Additionally we rewrite the cubic term in terms of k_x and k_y,

$$H_{\text{warping}} = \hbar v_{\text{F}}(k_x\sigma_y - k_y\sigma_x) + W_2(k_x^3 - 3k_xk_y^2)\sigma_z + V(x,y). \tag{A.27}$$

This will be useful in the finite difference representation. The TI Hamiltonian is then given by

$$H_{\text{full}} = \begin{pmatrix} H_{\text{warping}} & H_{\text{c}} \\ H_{\text{c}} & -H_{\text{warping}} \end{pmatrix}. \tag{A.28}$$

The Hamiltonian component H_{c} is a coupling between two TI Hamiltonians, which can be thought of as top and bottom surface of a 3D TI slab. This coupling is defined as

$$H_{\text{c}} = C\left(k_x^2 + k_y^2\right)\sigma_0. \tag{A.29}$$

Note that the Hamiltonian A.28 resembles a standard BdG-Hamiltonian with a k-dependent superconducting gap. The chosen coupling [Eq. (A.29)] opens a gap at the borders of the first Brillouin zone, but is not coupling the bands at the Gamma point. In the following, the necessary finite difference expressions will be derived. These were analogously applied to cubic spin-orbit coupling terms which were studied in context of

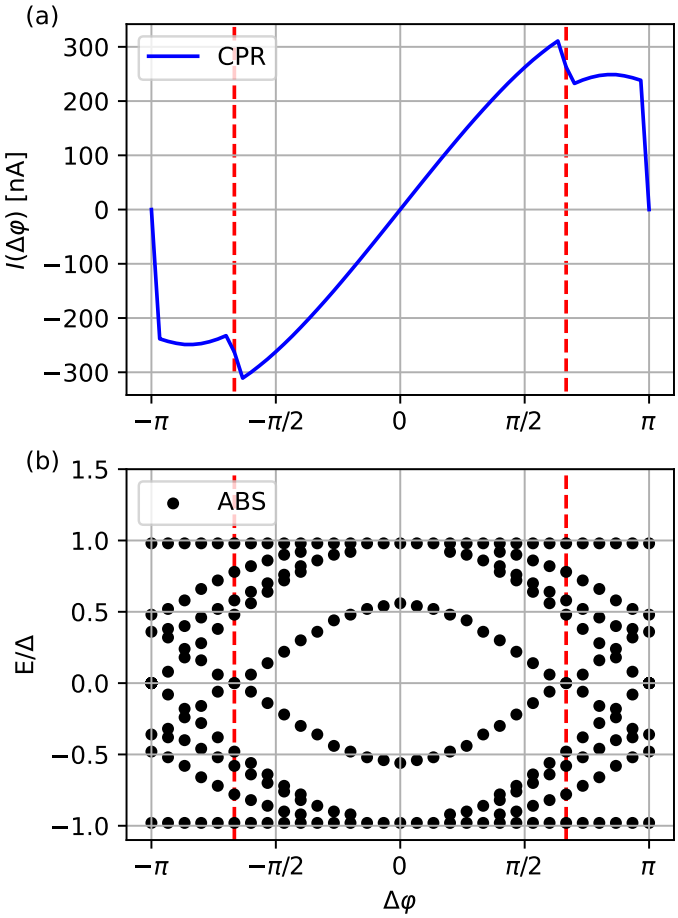

Figure A.4: Comparison of a current-phase relation computed with Eq. (3.56) and an ABS spectrum obtained by using Eq. (3.50). The Josephson junction has width $W = 40a$ and length $L = 10a$, where the chemical potential was fixed to $\mu = -16$ meV and $\Delta = 1$ meV. The CPR shows clear jumps at $\Delta\varphi = \pm 2$ (marked with red dashed lines) which stem from the zero energy crossings in the ABS at those values of the phase difference. Adapted from the Supplemental Material of Ref. [3].

anisotropic spin injection in Ref. [45]. The first and second derivatives are approximated by Eqs. (3.3) and (3.4). The finite difference expressions for the linear Dirac term are then given by

$$x \to x+1: \qquad t_x^1 = -\mathrm{i}\frac{\hbar v_\mathrm{F}}{2a_x}\tau_z \otimes \sigma_y, \tag{A.30}$$

$$y \to y+1: \qquad t_y^1 = \mathrm{i}\frac{\hbar v_\mathrm{F}}{2a_y}\tau_z \otimes \sigma_x. \tag{A.31}$$

The expressions for the cubic terms are a bit more complicated. First, the term $k_x^3 = \mathrm{i}\partial_x^3$ is discretized as

$$\begin{aligned}
\mathrm{i}W_2\partial_x^3\Psi_x &= \mathrm{i}W_2\partial_x^2[\partial_x\Psi_x] \\
&= \mathrm{i}W_2\partial_x^2\left[\frac{\Psi_{x+1}-\Psi_{x-1}}{2a_x}\right] \\
&= \mathrm{i}\frac{W_2}{2a_x}\partial_x\left[\frac{\Psi_{x+2}-\Psi_x}{2a_x} - \frac{\Psi_x-\Psi_{x-2}}{2a_x}\right] \\
&= \mathrm{i}\frac{W_2}{4a_x^2}\left[\frac{\Psi_{x+3}-\Psi_{x+1}}{2a_x} - \frac{\Psi_{x+1}-\Psi_{x-1}}{2a_x} - \frac{\Psi_{x+1}-\Psi_{x-1}}{2a_x} + \frac{\Psi_{x-1}-\Psi_{x-3}}{2a_x}\right] \\
&= \mathrm{i}\frac{W_2}{8a_x^3}\left[\Psi_{x+3} - 3\Psi_{x+1} + 3\Psi_{x-1} - \Psi_{x-3}\right].
\end{aligned} \tag{A.32}$$

This results then in the hopping terms

$$x \to x+3: \qquad t_{3x} = \mathrm{i}\frac{W_2}{8a_x^3}\tau_z \otimes \sigma_z, \tag{A.33}$$

$$x \to x+1: \qquad t_x^{31} = -\mathrm{i}\frac{3W_2}{8a_x^3}\tau_z \otimes \sigma_z. \tag{A.34}$$

Next, the second cubic term $-3W_2k_xk_y^2$ needs to be discretized. Here the derivatives act in two different spatial directions, so we end up with

$$\begin{aligned}
-3W_2k_xk_y^2\Psi_{x,y} &= -3W_2k_x\left[(-1)\frac{\Psi_{x,y+1}+\Psi_{x,y-1}-2\Psi_{x,y}}{a_y^2}\right] \\
&= -\mathrm{i}\frac{3W_2}{a_y^2}\left[\frac{\Psi_{x+1,y+1}-\Psi_{x-1,y+1}}{2a_x} + \frac{\Psi_{x+1,y-1}-\Psi_{x-1,y-1}}{2a_x}\right. && \text{(A.35)} \\
&\quad \left. -2\frac{\Psi_{x+1,y}-\Psi_{x-1,y}}{2a_x}\right]. && \text{(A.36)}
\end{aligned}$$

The respective hoppings read

$$x,y \to x+1,y+1: \qquad t_{xpy} = -\mathrm{i}\frac{3W_2}{2a_xa_y^2}\tau_z \otimes \sigma_z \tag{A.37}$$

$$x,y \to x+1,y-1: \qquad t_{xmy} = -\mathrm{i}\frac{3W_2}{2a_xa_y^2}\tau_z \otimes \sigma_z. \tag{A.38}$$

$$x,y \to x+1,y: \qquad t_x^{32} = \mathrm{i}\frac{3W_2}{a_xa_y^2}\tau_z \otimes \sigma_z. \tag{A.39}$$

For the cubic term one gets the full nearest-neighbour hopping in x-direction

$$t_x^3 = t_x^{31} + t_x^{32} = \mathrm{i}3W_2 \left(\frac{1}{a_x a_y^2} - \frac{1}{8a_x^3} \right) \tau_z \otimes \sigma_z. \tag{A.40}$$

Finally, the coupling Hamiltonian is straightforward to discretize

$$x, y: \qquad \epsilon_{x,y}^{\mathrm{c}} = 2C \left(\frac{1}{a_x^2} + \frac{1}{a_y^2} \right) \tau_x \otimes \sigma_0 \tag{A.41}$$

$$x \to x+1: \qquad t_x^{\mathrm{c}} = -\frac{C}{a_x^2} \tau_x \otimes \sigma_0 \tag{A.42}$$

$$y \to y+1: \qquad t_y^{\mathrm{c}} = -\frac{C}{a_x^2} \tau_x \otimes \sigma_0, \tag{A.43}$$

and the complete nearest-neighbour hopping terms read

$$x \to x+1: \quad t_x = -\mathrm{i}\frac{\hbar v_{\mathrm{F}}}{2a_x} \tau_z \otimes \sigma_y + \mathrm{i}3W_2 \left(\frac{1}{a_x a_y^2} - \frac{1}{8a_x^3} \right) \tau_z \otimes \sigma_z - \frac{C}{a_x^2} \tau_x \otimes \sigma_0 \tag{A.44}$$

$$y \to y+1: \quad t_y = \mathrm{i}\frac{\hbar v_{\mathrm{F}}}{2a_y} \tau_z \otimes \sigma_x - \frac{C}{a_x^2} \tau_x \otimes \sigma_0. \tag{A.45}$$

A schematic visualization of all the relevant hopping terms of the tight-binding lattice is shown in Fig. A.5 (a). Moreover, also the periodicity of the lattice is illustrated, where in the boundary condition a complex phase $\phi \in [0; 2\pi]$ is introduced. This phase is important to change the quantization condition of the discretized transverse momenta k_y, as the lattice will have a finite size. For a non-zero value of ϕ, different k_y values can be addressed in the simulations. Note that for the hopping t_{xmy} the sign of the phase ϕ needs to be reversed.

Let us now consider explicit parameters. For example, one can use the values given in Ref. [244], with $v_{\mathrm{F}} = 355$ eV nm and $W_2 = 128$ eV nm^3 for Bi_2Se_3 or $v_{\mathrm{F}} = 255$ eV nm and $W_2 = 250$ eV nm^3 for Bi_2Te_3. In Fig. A.5 (b) the spectrum of our model of the warped Dirac cone for Bi_2Te_3 is shown, as well as the corresponding quasi-1D bandstructure in Fig. A.5 (c) for $\phi = 0$. In order to check whether the Hamiltonian A.28 is appropriately describing the surface of a 3D TI with hexagonal warping, one can compute the dependence of the density of states (DOS) on the Fermi energy. Adroguer et al. [244] showed analytically that the hexagonal warping term will lead to a deviation from the linear dependence of the DOS for larger energies.

For our system we fix the lattice constant to $a = 0.5$ nm and the width to four lattice points, such that we have one subband in the energy range between E = 0 and E = 300 meV. As we want to compare to the DOS of a infinite TI slab, we have to average over ϕ. The averaging is performed over $P = 6000$ equally spaced phase values in the interval $\phi \in [0; 2\pi]$. The DOS can be computed according to

$$\mathrm{DOS(E)} = \frac{1}{2\pi} \frac{1}{2a^2} \int_0^{2\pi} \frac{d\phi}{2\pi} \langle \Psi(E,\phi) | \Psi(E,\phi) \rangle = \frac{1}{2\pi n} \sum_{i=1}^{P} \langle \Psi(E,\phi_i) | \Psi(E,\phi_i) \rangle \,. \tag{A.46}$$

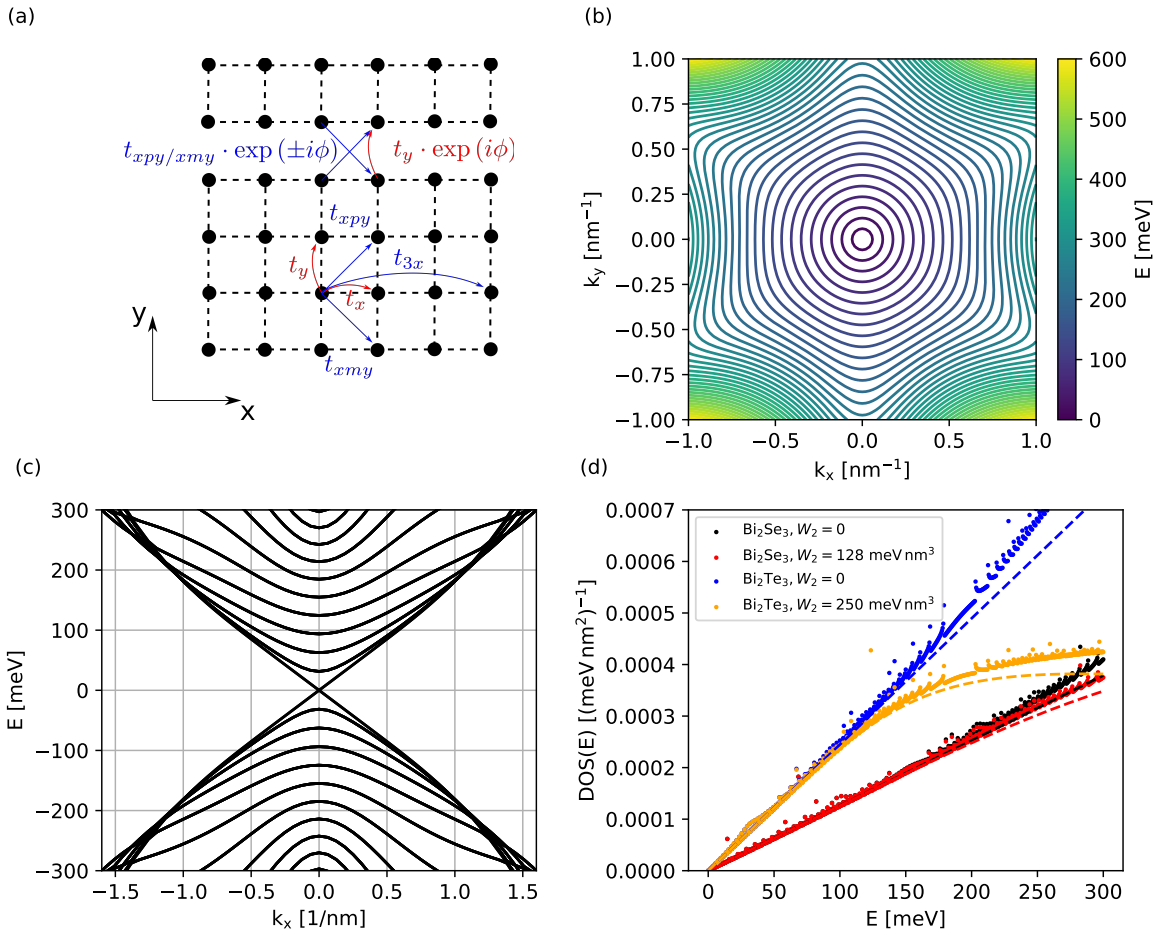

Figure A.5: (a) Schematic plot that illustrates the tight-binding implementation of the Hamiltonian given by Eq. (A.28). The blue hoppings originate purely from the hexagonal warping term. (b) and (c) show the numerically calculated conduction band of the 2D TI surface state spectrum and the quasi 1D bandstructure for a sample width of $w = 50$ nm, respectively. For the implementation the parameters were set to $v_F = 255$ meV nm and $W_2 = 250$ meV nm^3 corresponding to Bi_2Te_3. Also a coupling constant of $C = 25$ meV nm^2 was used in the simulations. (d) Numerically computed DOS(E) (dotted curves) for the cases of zero warping and the parameter values of Bi_2Se_3 and Bi_2Te_3. Also the analytical density of states are plotted in dashed lines showing good agreement with the simulations. For larger energy values the difference becomes stronger. This is expected as the convergence of the tight-binding implementation depends on the size of the lattice constant a.

The factor n in Eq. (A.46) contains a normalization factors stemming from the doubling of the orbital degrees of freedom in Eq. (A.28), the phase averaging and the area of a lattice point. It is given by $n = 2\,a^2\,P$. A straightforward check of the results can be performed by comparing to the analytically computed DOS. The case without warping is given by [244]

$$\mathrm{DOS(E)}|_{W_2=0} = \frac{E}{2\pi\hbar^2 v_\mathrm{F}^2}, \tag{A.47}$$

while the expression for the DOS in presence of warping is

$$\mathrm{DOS(E)}|_{W_2\neq 0} = \mathrm{DOS(E)}|_{W_2=0} \int_0^{2\pi} \frac{d\theta}{2\pi} \frac{1}{1 + 12b^2\tilde{k}^4(\theta)\cos^2(3\theta)}, \tag{A.48}$$

where θ is the azimuthal angle of the momentum $\boldsymbol{k} = (k_x, k_y)$ and $b = W_2 E/(2\hbar^3 v_\mathrm{F}^3)$ is a measure of the warping strength. The parameter $\tilde{k}(\theta) = k/k_\mathrm{F}$ is determined by solving

$$1 = \tilde{k}^2(\theta) + 4b^2\tilde{k}^6(\theta)\cos^2(3\theta). \tag{A.49}$$

In Fig. A.5 (d) the computed quantities are shown. Comparing, for both sets of parameters corresponding to the different materials, the analytical DOS (black and blue dashed lines) with the numerically computed DOS (dotted lines in the corresponding colors), good agreement can be observed. Only for larger energies the lines start to differ. This behavior is expected, as the convergence of tight-binding calculations for higher energies depends on the lattice constant. Still the results match quite well for the shown energy range. Next, the non-zero hexagonal warping case is treated. The numerical and analytical result are depicted as dots and dashed lines, respectively (orange and red). As for the zero hexagonal warping a good agreement is found for low energies. For higher warping the DOS behaves less linear and therefore the effect is more pronounced for Bi_2Te_3 than for Bi_2Se_3.

List of Figures

List of Tables

Bibliography

[1] J. Fuchs et al., "Crossed Andreev reflection in topological insulator nanowire T junctions", Phys. Rev. B **104**, 085415 (2021).

[2] D. Kochan et al., "Spin Relaxation in s-Wave Superconductors in the Presence of Resonant Spin-Flip Scatterers", Phys. Rev. Lett. **125**, 087001 (2020).

[3] M. Barth, J. Fuchs, and D. Kochan, "Spin relaxation, Josephson effect, and Yu-Shiba-Rusinov states in superconducting bilayer graphene", Phys. Rev. B **105**, 205409 (2022).

[4] W. Himmler et al., "Supercurrent interference in HgTe Josephson junctions", arXiv preprint arXiv:2211.06702 (2022).

[5] C. L. Kane and E. J. Mele, "Quantum Spin Hall Effect in Graphene", Phys. Rev. Lett. **95**, 226801 (2005).

[6] C. L. Kane and E. J. Mele, "Z_2 Topological Order and the Quantum Spin Hall Effect", Phys. Rev. Lett. **95**, 146802 (2005).

[7] G. Tkachov, *Topological Insulators: The Physics of Spin Helicity in Quantum Transport* (Jenny Stanford Publishing, 2015).

[8] K. v. Klitzing, G. Dorda, and M. Pepper, "New method for high-accuracy determination of the fine-structure constant based on quantized Hall resistance", Phys. Rev. Lett. **45**, 494 (1980).

[9] M. Z. Hasan and C. L. Kane, "Colloquium: Topological insulators", Rev. Mod. Phys. **82**, 3045–3067 (2010).

[10] L. Fu, C. L. Kane, and E. J. Mele, "Topological Insulators in Three Dimensions", Phys. Rev. Lett. **98**, 106803 (2007).

[11] H. Zhang et al., "Topological insulators in Bi_2Se_3, Bi_2Te_3 and Sb_2Te_3 with a single Dirac cone on the surface", Nat. Phys. **5**, 438–442 (2009).

[12] D. A. Kozlov et al., "Transport properties of a 3D topological insulator based on a strained high-mobility HgTe film.", Phys. Rev. Lett. **112 19**, 196801 (2014).

[13] *Topological Materials Database*, `https://www.topologicalquantumchemistry.com`.

[14] K. S. Novoselov et al., "Electric field effect in atomically thin carbon films", Science **306**, 666–669 (2004).

[15] K. I. Bolotin et al., "Ultrahigh electron mobility in suspended graphene", Solid State Commun. **146**, 351–355 (2008).

[16] J. Haruyama, "Graphene and Graphene Nanomesh Spintronics", Electronics **2**, 368–386 (2013).

[17] C. R. Dean et al., "Boron nitride substrates for high-quality graphene electronics", Nat. Nanotechnol. **5**, 722–726 (2010).

[18] K. Zollner and J. Fabian, "Bilayer graphene encapsulated within monolayers of WS_2 or $Cr_2Ge_2Te_6$: Tunable proximity spin-orbit or exchange coupling", Phys. Rev. B **104**, 075126 (2021).

[19] T. Naimer et al., "Twist-angle dependent proximity induced spin-orbit coupling in graphene/transition metal dichalcogenide heterostructures", Phys. Rev. B **104**, 195156 (2021).

[20] M. Gmitra and J. Fabian, "Graphene on transition-metal dichalcogenides: A platform for proximity spin-orbit physics and optospintronics", Phys. Rev. B **92**, 155403 (2015).

[21] S. Konschuh, M. Gmitra, and J. Fabian, "Tight-binding theory of the spin-orbit coupling in graphene", Phys. Rev. B **82**, 245412 (2010).

[22] M. Katsnelson, K. Novoselov, and A. Geim, "Chiral tunnelling and the Klein paradox in graphene", Nat. Phys. **2**, 620–625 (2006).

[23] J. H. Bardarson, P. W. Brouwer, and J. E. Moore, "Aharonov-Bohm Oscillations in Disordered Topological Insulator Nanowires", Phys. Rev. Lett. **105**, 156803 (2010).

[24] J. Ziegler et al., "Probing spin helical surface states in topological HgTe nanowires", Phys. Rev. B **97**, 035157 (2018).

[25] J. Ziegler, *Quantum transport in HgTe topological insulator nanostructures*, Regensburg, 2019.

[26] H. Zhao et al., "Superconducting proximity effect in a topological insulator using Fe(Te, Se)", Phys. Rev. B **97**, 224504 (2018).

[27] B. Bhattacharyya et al., "Proximity-induced supercurrent through topological insulator based nanowires for quantum computation studies", Sci. Rep. **8**, 1–12 (2018).

[28] Y. Cao et al., "Unconventional superconductivity in magic-angle graphene superlattices", Nature **556**, 43–50 (2018).

[29] M. Sato and Y. Ando, "Topological superconductors: a review", Rep. Prog. Phys. **80**, 076501 (2017).

[30] C. Nayak et al., "Non-Abelian anyons and topological quantum computation", Rev. Mod. Phys. **80**, 1083–1159 (2008).

[31] K. Flensberg, F. von Oppen, and A. Stern, "Engineered platforms for topological superconductivity and Majorana zero modes", Nat. Rev. Mat. **6**, 944–958 (2021).

[32] R. Fischer et al., "4π-periodic supercurrent tuned by an axial magnetic flux in topological insulator nanowires", Phys. Rev. Res. **4**, 013087 (2022).

[33] C.-X. Liu et al., "Model Hamiltonian for topological insulators", Phys. Rev. B **82**, 045122 (2010).

[34] C. W. Groth et al., "Kwant: a software package for quantum transport", New J. Phys. **16**, 063065 (2014).

[35] L. Susskind, "Lattice fermions", Phys. Rev. D **16**, 3031–3039 (1977).

[36] H. Nielsen and M. Ninomiya, "A no-go theorem for regularizing chiral fermions", Phys. Lett. B **105**, 219 –223 (1981).

[37] R. Stacey, "Eliminating lattice fermion doubling", Phys. Rev. D **26**, 468–472 (1982).

[38] F. Schindler et al., "Higher-order topological insulators", Sci. Adv. **4**, eaat0346 (2018).

[39] G. Deutscher, "Crossed Andreev Reflections", J. Supercond. **15**, 43–47 (2002).

[40] H. Haugen et al., "Crossed Andreev reflection versus electron transfer in three-terminal graphene devices", Phys. Rev. B **81**, 174523 (2010).

[41] R. Beiranvand, H. Hamzehpour, and M. Alidoust, "Nonlocal Andreev entanglements and triplet correlations in graphene with spin-orbit coupling", Phys. Rev. B **96**, 161403 (2017).

[42] M. Beconcini, M. Polini, and F. Taddei, "Nonlocal superconducting correlations in graphene in the quantum Hall regime", Phys. Rev. B **97**, 201403 (2018).

[43] R. J. Elliott, "Theory of the effect of spin-orbit coupling on magnetic resonance in some semiconductors", Phys. Rev. **96**, 266 (1954).

[44] Y Yafet, "g Factors and spin-lattice relaxation of conduction electrons", in *Solid state physics*, Vol. 14 (Elsevier, 1963), pp. 1–98.

[45] G. Fleury, M. Barth, and C. Gorini, "Tunneling anisotropic spin galvanic effect", arXiv preprint arXiv:2212.11698 (2022).

[46] S.-Q. SHEN, *Topological Insulators: Dirac Equation in Condensed Matter* (Springer, 2018).

[47] M. Franz and L. Molenkamp, *Topological insulators* (Elsevier, 2013).

[48] L. Fu and C. L. Kane, "Topological insulators with inversion symmetry", Phys. Rev. B **76**, 045302 (2007).

[49] J. C. Y. Teo, L. Fu, and C. L. Kane, "Surface states and topological invariants in three-dimensional topological insulators: Application to $Bi_{1-x}Sb_x$", Phys. Rev. B **78**, 045426 (2008).

[50] N. Claussen, B. A. Bernevig, and N. Regnault, "Detection of topological materials with machine learning", Phys. Rev. B **101**, 245117 (2020).

[51] T Arakane et al., "Tunable Dirac cone in the topological insulator $Bi_{2-x}Sb_xTe_{3-y}Se_y$", Nat. Commun. **3**, 1–5 (2012).

[52] Z. Ren et al., "Optimizing $Bi_{2-x}Sb_xTe_{3-y}Se_y$ solid solutions to approach the intrinsic topological insulator regime", Phys. Rev. B **84**, 165311 (2011).

[53] S. Essert, *Mesoscopic Transport in Topological Insulator Nanostructures*, 2016.

[54] J. G. Analytis et al., "Two-dimensional surface state in the quantum limit of a topological insulator", Nat. Phys. **6**, 960–964 (2010).

[55] Z. Ren et al., "Large bulk resistivity and surface quantum oscillations in the topological insulator Bi_2Te_2Se", Phys. Rev. B **82**, 241306 (2010).

[56] N. P. Butch et al., "Strong surface scattering in ultrahigh-mobility Bi_2Se_3 topological insulator crystals", Phys. Rev. B **81**, 241301 (2010).

[57] K.-M. Dantscher et al., "Cyclotron-resonance-assisted photocurrents in surface states of a three-dimensional topological insulator based on a strained high-mobility HgTe film", Phys. Rev. B **92**, 165314 (2015).

[58] X.-L. Qi and S.-C. Zhang, "The quantum spin Hall effect and topological insulators", Phys. Today **63**, 33–38 (2010).

[59] M. Kessel et al., "CdTe-HgTe core-shell nanowire growth controlled by RHEED", Phys. Rev. Mat. **1**, 023401 (2017).

[60] Y. Ando, "Topological insulator materials", J. Phys. Soc. Japan **82**, 102001 (2013).

[61] W. Zhang, "Impact of Point Defects on Electronic Properties of Topological Materials", PhD thesis (Rutgers The State University of New Jersey, School of Graduate Studies, 2019).

[62] Y. Zhang and A. Vishwanath, "Anomalous Aharonov-Bohm Conductance Oscillations from Topological Insulator Surface States", Phys. Rev. Lett. **105**, 206601 (2010).

[63] L. Brey and H. A. Fertig, "Electronic states of wires and slabs of topological insulators: Quantum Hall effects and edge transport", Phys. Rev. B **89**, 085305 (2014).

[64] R. Kozlovsky, *Magnetotransport in 3D Topological Insulator Nanowires*, 2020.

[65] F. de Juan, R. Ilan, and J. H. Bardarson, "Robust Transport Signatures of Topological Superconductivity in Topological Insulator Nanowires", Phys. Rev. Lett. **113**, 107003 (2014).

[66] R. Ilan et al., "Detecting perfect transmission in Josephson junctions on the surface of three dimensional topological insulators", New J. Phys. **16** (2013).

[67] A. G. Aronov and Y. V. Sharvin, "Magnetic flux effects in disordered conductors", Rev. Mod. Phys. **59**, 755–779 (1987).

[68] N. Tombros et al., "Electronic spin transport and spin precession in single graphene layers at room temperature", Nature **448**, 571–574 (2007).

[69] W. Han et al., "Tunneling spin injection into single layer graphene", Phys. Rev. Lett. **105**, 167202 (2010).

[70] P. Zomer et al., "Long-distance spin transport in high-mobility graphene on hexagonal boron nitride", Phys. Rev. B **86**, 161416 (2012).

[71] W. Han et al., "Graphene spintronics", Nat. Nanotechnol. **9**, 794–807 (2014).

[72] S. Roche et al., "Graphene spintronics: the European Flagship perspective", 2D Mater. **2**, 030202 (2015).

[73] A. Avsar et al., "Colloquium: Spintronics in graphene and other two-dimensional materials", Rev. Mod. Phys. **92**, 021003 (2020).

[74] A. H. Castro Neto et al., "The electronic properties of graphene", Rev. Mod. Phys. **81**, 109–162 (2009).

[75] J. W. McClure, "Band Structure of Graphite and de Haas-van Alphen Effect", Phys. Rev. **108**, 612–618 (1957).

[76] J. C. Slonczewski and P. R. Weiss, "Band Structure of Graphite", Phys. Rev. **109**, 272–279 (1958).

[77] S. Konschuh et al., "Theory of spin-orbit coupling in bilayer graphene", Phys. Rev. B **85**, 115423 (2012).

[78] E. McCann and M. Koshino, "The electronic properties of bilayer graphene", Rep. Prog. Phys. **76**, 056503 (2013).

[79] E. McCann and V. I. Fal'ko, "Landau-level degeneracy and quantum Hall effect in a graphite bilayer", Phys. Rev. Lett. **96**, 086805 (2006).

[80] H. Min et al., "Ab initio theory of gate induced gaps in graphene bilayers", Phys. Rev. B **75**, 155115 (2007).

[81] E. Icking et al., "Transport Spectroscopy of Ultraclean Tunable Band Gaps in Bilayer Graphene", Adv. Electron. Mater. **8**, 2200510 (2022).

[82] H. Sahin et al., "Graphane", WIREs Comput. Mol. Sci. **5**, 255–272 (2015).

[83] K. E. Whitener, "Review Article: Hydrogenated graphene: A user's guide", J. Vac. Sci. Technol. A **36**, 05G401 (2018).

[84] J. Bundesmann et al., "Theory of spin-orbit-induced spin relaxation in functionalized graphene", Phys. Rev. B **92**, 081403 (2015).

[85] D. Kochan, M. Gmitra, and J. Fabian, "Spin Relaxation Mechanism in Graphene: Resonant Scattering by Magnetic Impurities", Phys. Rev. Lett. **112**, 116602 (2014).

[86] M. Gmitra, D. Kochan, and J. Fabian, "Spin-Orbit Coupling in Hydrogenated Graphene", Phys. Rev. Lett. **110**, 246602 (2013).

[87] S. Irmer et al., "Spin-orbit coupling in fluorinated graphene", Phys. Rev. B **91**, 115141 (2015).

[88] K. Zollner et al., "Spin-orbit coupling in methyl functionalized graphene", Phys. Rev. B **93**, 045423 (2016).

[89] T. Frank et al., "Copper adatoms on graphene: Theory of orbital and spin-orbital effects", Phys. Rev. B **95**, 035402 (2017).

[90] D. Kochan, S. Irmer, and J. Fabian, "Model spin-orbit coupling Hamiltonians for graphene systems", Phys. Rev. B **95**, 165415 (2017).

[91] T. O. Wehling et al., "Resonant Scattering by Realistic Impurities in Graphene", Phys. Rev. Lett. **105**, 056802 (2010).

[92] R. Landauer, "Spatial variation of currents and fields due to localized scatterers in metallic conduction", IBM Journal of research and development **1**, 223–231 (1957).

[93] R. Landauer, "Electrical resistance of disordered one-dimensional lattices", Philosophical magazine **21**, 863–867 (1970).

[94] S. Datta, *Electronic transport in mesoscopic systems* (Cambridge university press, 1997).

[95] D. S. Fisher and P. A. Lee, "Relation between conductivity and transmission matrix", Phys. Rev. B **23**, 6851–6854 (1981).

[96] M. Wimmer, *Quantum transport in nanostructures: From computational concepts to spintronics in graphene and magnetic tunnel junctions*, 2009.

[97] H. K. Onnes, "Further experiments with liquid helium. C. On the change of electric resistance of pure metals at very low temperatures etc. IV. The resistance of pure mercury at helium temperatures", in *Through Measurement to Knowledge: The Selected Papers of Heike Kamerlingh Onnes 1853–1926*, edited by K. Gavroglu and Y. Goudaroulis (Springer Netherlands, Dordrecht, 1991), pp. 261–263.

[98] J. Bardeen, L. N. Cooper, and J. R. Schrieffer, "Microscopic Theory of Superconductivity", Phys. Rev. **106**, 162–164 (1957).

[99] P. De Gennes and P. Pincus, *Superconductivity Of Metals And Alloys*, Advanced Books Classics (Avalon Publishing, 1999).

[100] M. Tinkham, *Introduction to superconductivity* (Courier Corporation, 2004).

[101] J. Siegl, J. Picó-Cortés, and M. Grifoni, "Particle conserving approach to ac-dc driven interacting quantum dots with superconducting leads", Phys. Rev. B **107**, 115405 (2023).

[102] T. Klapwijk, "Proximity Effect From an Andreev Perspective", J. Supercond. **17**, 593–611 (2004).

[103] A. Gabovich, *Superconductors: New Developments* (IntechOpen, 2015).

[104] A. Zagoskin, *Quantum Theory of Many-Body Systems: Techniques and Applications*, Graduate Texts in Physics (Springer International Publishing, 2014).

[105] R. Kleiner and W. Buckel, *Superconductivity: an introduction* (John Wiley & Sons, 2016).

[106] A. F. Andreev, "Electron Spectrum of the Intermediate State of Superconductors", Sov. Phys. JETP **22**, 455 (1966).

[107] I. O. Kulik and A. N. Omel'yanchuk, "Properties of superconducting microbridges in the pure limit", Sov. J. Low Temp. Phys. (Engl. Transl.); (United States) **3** (1977).

[108] J. A. Sauls, "Andreev bound states and their signatures", Philos. Trans. Royal Soc. A **376**, 20180140 (2018).

[109] G. E. Blonder, M. Tinkham, and T. M. Klapwijk, "Transition from metallic to tunneling regimes in superconducting microconstrictions: Excess current, charge imbalance, and supercurrent conversion", Phys. Rev. B **25**, 4515–4532 (1982).

[110] F. Dolcini, "Andreev reflection", Lecture Notes for XXIII Physics Grad. Days **5**, 9 (2009).

[111] P. A. Mello and N. Kumar, *Quantum Transport in Mesoscopic Systems: Complexity and Statistical Fluctuations. A Maximum Entropy Viewpoint* (Oxford University Press, 2004).

[112] D. Beckmann, H. B. Weber, and H. v. Löhneysen, "Evidence for Crossed Andreev Reflection in Superconductor-Ferromagnet Hybrid Structures", Phys. Rev. Lett. **93**, 197003 (2004).

[113] B. D. Josephson, "Possible new effects in superconductive tunnelling", Phys. Lett. **1**, 251–253 (1962).

[114] B. D. Josephson, "The discovery of tunnelling supercurrents", Rev. Mod. Phys. **46**, 251 (1974).

[115] C. Beenakker, "Three "universal" mesoscopic Josephson effects", in *Transport phenomena in mesoscopic systems* (Springer, 1992), pp. 235–253.

[116] J. A. Sauls, "Andreev bound states and their signatures", Philos. Trans. Royal Soc. A **376**, 20180140 (2018).

[117] A. U. B. Brøyn, "Andreev bound states in Josephson junctions: unconventional pairing symmetries in weak magnetic field and strong-field formalism", MA thesis (NTNU, 2017).

[118] L. Yu, "Bound State in Superconductors with Paramagnetic Impurities", Acta. Phys. Sin. **21**, 75–91 (1965).

[119] H. Shiba, "Classical Spins in Superconductors", Prog. Theor. Phys. **40**, 435–451 (1968).

[120] A. I. Rusinov, "Superconductivity near a paramagnetic impurity", Zh. Eksp. Teor. Fiz. **9**, 146 (1968).

[121] T. O. Wehling et al., "Local impurity effects in superconducting graphene", Phys. Rev. B **78**, 035414 (2008).

[122] J. L. Lado and J. Fernández-Rossier, "Unconventional Yu-Shiba-Rusinov states in hydrogenated graphene", 2D Mater. **3**, 0 (2016).

[123] E. Cortés-del Río et al., "Observation of Yu–Shiba–Rusinov States in Superconducting Graphene", Adv. Mater. **33**, 2008113 (2021).

[124] S Nadj-Perge et al., "Proposal for realizing Majorana fermions in chains of magnetic atoms on a superconductor", Phys. Rev. B **88**, 020407 (2013).

[125] J. Li et al., "Topological superconductivity induced by ferromagnetic metal chains", Phys. Rev. B **90**, 235433 (2014).

[126] Y. Peng et al., "Strong localization of Majorana end states in chains of magnetic adatoms", Phys. Rev. Lett. **114**, 106801 (2015).

[127] W. Gerlach and O. Stern, "Der experimentelle Nachweis der Richtungsquantelung im Magnetfeld", Zeitschrift für Physik **9**, 349–352 (1922).

[128] G. E. Uhlenbeck and S. Goudsmit, "Spinning electrons and the structure of spectra", Nature **117**, 264–265 (1926).

[129] W. Heisenberg, "Zur theorie des ferromagnetismus", in *Original scientific papers wissenschaftliche originalarbeiten* (Springer, 1985), pp. 580–597.

[130] I. I. Rabi et al., "A new method of measuring nuclear magnetic moment", Phys. Rev. **53**, 318 (1938).

[131] D. Loss and D. P. DiVincenzo, "Quantum computation with quantum dots", Phys. Rev. A **57**, 120 (1998).

[132] J. Fabian et al., "Semiconductor Spintronics", Acta Phys. Slov. **57**, 565 (2007).

[133] J. Fabian and M. W. Wu, "Spin relaxation and spin dynamics in semiconductors", in *Handbook of Spin Transport and Magnetism*, edited by E. Tsymbal and I. Žutić (CRC Press, Taylor & Francis Group, 2012), pp. 303–327.

[134] I. Žutić, J. Fabian, and S. Das Sarma, "Spintronics: Fundamentals and applications", Rev. Mod. Phys. **76**, 323–410 (2004).

[135] D. Kochan, M. Gmitra, and J. Fabian, "RESONANT SCATTERING OFF MAGNETIC IMPURITIES IN GRAPHENE: MECHANISM FOR ULTRAFAST SPIN RELAXATION", in *Symmetry, spin dynamics and the properties of nanostructures, lecture notes of the 11th international school on theoretical physics*, edited by J. Barnaś, V. Dugaev, and A. Wal (World Scientific, 2014), pp. 136–162.

[136] J. W. Thomas, *Numerical partial differential equations: finite difference methods*, Vol. 22 (Springer Science & Business Media, 2013).

[137] K. M. Habib, R. N. Sajjad, and A. W. Ghosh, "Modified Dirac Hamiltonian for efficient quantum mechanical simulations of micron sized devices", Appl. Phys. Lett. **108**, 113105 (2016).

[138] Y.-F. Zhou et al., "Two-dimensional lattice model for the surface states of topological insulators", Phys. Rev. B **95**, 245137 (2017).

[139] A. Hill, "Finite-size scaling for lattice fermions in two dimensions", PhD thesis (Apr. 2013).

[140] Z. Wang et al., "Strong interface-induced spin–orbit interaction in graphene on WS2", Nat. Commun. **6**, 1–7 (2015).

[141] Z. Wang et al., "Origin and Magnitude of 'Designer' Spin-Orbit Interaction in Graphene on Semiconducting Transition Metal Dichalcogenides", Phys. Rev. X **6**, 041020 (2016).

[142] J. Amann et al., "Counterintuitive gate dependence of weak antilocalization in bilayer graphene/WSe_2 heterostructures", Phys. Rev. B **105**, 115425 (2022).

[143] T. Mayer et al., "Transport properties of band engineered p- n heterostructures of epitaxial Bi 2 Se 3/(Bi 1- x Sb x) 2 (Te 1- y Se y) 3 topological insulators", Phys. Rev. Mat. **5**, 014202 (2021).

[144] R. Peierls, "Zur Theorie des Diamagnetismus von Leitungselektronen", Zeitschrift für Physik **80**, 763–791 (1933).

[145] D. R. Hofstadter, "Energy levels and wave functions of Bloch electrons in rational and irrational magnetic fields", Phys. Rev. B **14**, 2239–2249 (1976).

[146] R. Feynman, R. Leighton, and M. Sands, *The Feynman Lectures on Physics, Vol. III: The New Millennium Edition: Quantum Mechanics*, The Feynman Lectures on Physics (Basic Books, 2011).

[147] L. Pietanesi et al., "Ferromagnetic resonance for spectroscopic investigation of topological surface states", (submitted) (2023).

[148] M. S. Jelodar and S. Datta, *ECE 495N: Fundamentals of Nanoelectronics Lecture Notes (Fall 2009)*, 2010.

[149] M. Walter, *QUANTUM TRANSPORT - Functional Nanosystems*, 2015.

[150] Y.-F. Zhou et al., "Two-Dimensional Lattice Model for the Surface States of Topological Insulators", Phys. Rev. B **95**, 10.1103/PhysRevB.95.245137 (2016).

[151] J. Zierenberg et al., "Percolation thresholds and fractal dimensions for square and cubic lattices with long-range correlated defects", Phys. Rev. E **96**, 062125 (2017).

[152] J. Dufouleur et al., "Suppression of scattering in quantum confined 2D helical Dirac systems", Phys. Rev. B **97**, 075401 (2018).

[153] C. A. Mack, "Analytic form for the power spectral density in one, two, and three dimensions", Journal of Micro/Nanolithography, MEMS, and MOEMS **10**, 1 –3 (2011).

[154] R. Kozlovsky et al., "Magnetoconductance, Quantum Hall Effect, and Coulomb Blockade in Topological Insulator Nanocones", Phys. Rev. Lett. **124**, 126804 (2020).

[155] E. I. Thorsos, "The validity of the Kirchhoff approximation for rough surface scattering using a Gaussian roughness spectrum", J. Acoust. Soc. Am. **83**, 78–92 (1988).

[156] C. A. Mack, "Generating random rough edges, surfaces, and volumes", Appl. Opt. **52**, 1472–1480 (2013).

[157] C. W. J. Beenakker, "Universal limit of critical-current fluctuations in mesoscopic Josephson junctions", Phys. Rev. Lett. **67**, 3836–3839 (1991).

[158] F. Pientka et al., "Topological Superconductivity in a Planar Josephson Junction", Phys. Rev. X **7**, 021032 (2017).

[159] B. van Heck, S. Mi, and A. R. Akhmerov, "Single fermion manipulation via superconducting phase differences in multiterminal Josephson junctions", Phys. Rev. B **90**, 155450 (2014).

[160] N. Abboud et al., "Signatures of Majorana bound states and parity effects in two-dimensional chiral p-wave Josephson junctions", Phys. Rev. B **105**, 214521 (2022).

[161] B Van Heck et al., "Coulomb-assisted braiding of Majorana fermions in a Josephson junction array", New J. Phys. **14**, 035019 (2012).

[162] S. S. Hegde et al., "A topological Josephson junction platform for creating, manipulating, and braiding Majorana bound states", Ann. Phys. **423**, 168326 (2020).

[163] P. Sriram et al., "Supercurrent interference in semiconductor nanowire Josephson junctions", Phys. Rev. B **100**, 155431 (2019).

[164] A. Furusaki and M. Tsukada, "Dc Josephson effect and Andreev reflection", Solid State Commun. **78**, 299–302 (1991).

[165] A. Furusaki, "DC Josephson effect in dirty SNS junctions: Numerical study", Phys. B: Condens. Matter **203**, 214–218 (1994).

[166] K. Zuo et al., "Supercurrent Interference in Few-Mode Nanowire Josephson Junctions", Phys. Rev. Lett. **119**, 187704 (2017).

[167] V. Ostroukh et al., "Two-dimensional Josephson vortex lattice and anomalously slow decay of the Fraunhofer oscillations in a ballistic SNS junction with a warped Fermi surface", Phys. Rev. B **94**, 094514 (2016).

[168] W. Han and R. K. Kawakami, "Spin relaxation in single-layer and bilayer graphene", Phys. Rev. Lett. **107**, 047207 (2011).

[169] T.-Y. Yang et al., "Observation of Long Spin-Relaxation Times in Bilayer Graphene at Room Temperature", Phys. Rev. Lett. **107**, 047206 (2011).

[170] S. Dushenko et al., "Gate-Tunable Spin-Charge Conversion and the Role of Spin-Orbit Interaction in Graphene", Phys. Rev. Lett. **116**, 166102 (2016).

[171] H. Steiner et al., "Structure and composition of bismuth telluride topological insulators grown by molecular beam epitaxy", J. Appl. Crystallogr. **47**, 1889–1900 (2014).

[172] T. P. Ginley, Y. Wang, and S. Law, "Topological Insulator Film Growth by Molecular Beam Epitaxy: A Review", Crystals **6**, 10 . 3390 / cryst6110154 (2016).

[173] P. G. Silvestrov, P. W. Brouwer, and E. G. Mishchenko, "Spin and charge structure of the surface states in topological insulators", Phys. Rev. B **86**, 075302 (2012).

[174] N. I. Fedotov and S. V. Zaitsev-Zotov, "Numerical analysis of surface and edge states in slabs, stripes, rods and surface steps of topological insulators", J. Condens. Matter Phys. **30**, 485301 (2018).

[175] K. Kobayashi, "Electron transmission through atomic steps of Bi_2Se_3 and Bi_2Te_3 surfaces", Phys. Rev. B **84**, 205424 (2011).

[176] M. Chen et al., "Selective trapping of hexagonally warped topological surface states in a triangular quantum corral", Sci. Adv. **5**, eaaw3988 (2019).

[177] P. Wutz, "Quantum magneto-transport in disordered bismuth-based 3D topological insulators", BA thesis (Universität Regensburg, 2020).

[178] G. Binnig and H. Rohrer, "Scanning tunneling microscopy", Surf. Sci. **126**, 236–244 (1983).

[179] G. Binnig and H. Rohrer, "Scanning tunneling microscopy—from birth to adolescence", Rev. Mod. Phys. **59**, 615 (1987).

[180] S. Amarie, T. Ganz, and F. Keilmann, "Mid-infrared near-field spectroscopy", Opt. Express **17**, 21794–21801 (2009).

[181] M. Kessel, "HgTe shells on CdTe nanowires: A low-dimensional topological insulator from crystal growth to quantum transport", PhD thesis (Universität Würzburg, 2016).

[182] D. Weiss, C. Back, and M. Kronseder, "Project A08 in CRC proposal: Topological tubes and wires and their hybrids", in *Emergent Relativistic Effects in Condensed Matter, From Fundamental Aspects to Electronic Functionality* (Universität Regensburg, 2020), pp. 155–170.

[183] S Vaitiekėnas et al., "Flux-induced topological superconductivity in full-shell nanowires", Science **367**, eaav3392 (2020).

[184] A. Setescak, "Quantum transport in topological insulators based on core-shell nanowires", BA thesis (Universität Regensburg, 2022).

[185] Y.-Y. Zhang, X.-R. Wang, and X. Xie, "Three-dimensional topological insulator in a magnetic field: chiral side surface states and quantized Hall conductance", J. Condens. Matter Phys. **24**, 015004 (2011).

[186] L.-J. Yin et al., "Landau quantization of Dirac fermions in graphene and its multilayers", Front. Phys. **12**, 1–37 (2017).

[187] L. Fritz et al., "Topological insulators in magnetic fields: Quantum Hall effect and edge channels with non-quantized theta-term", in APS March Meeting Abstracts, Vol. 2012 (2012), A32–002.

[188] M. Sitte, "Quantum Hall Effect and Surface Criticality in 3D Topological Insulators", PhD thesis (Universität zu Köln, 2012).

[189] O. Klein, "Die Reflexion von Elektronen an einem Potentialsprung nach der relativistischen Dynamik von Dirac", Zeitschrift für Physik **53**, 157–165 (1929).

[190] F. Dolcini, "Full electrical control of charge and spin conductance through interferometry of edge states in topological insulators", Phys. Rev. B **83**, 165304 (2011).

[191] J. Osca et al., "Fabry–Pérot interferometry with gate-tunable 3D topological insulator nanowires", Nanotechnology **32**, 435002 (2021).

[192] M. Fürst, "Dirac Landau levels on a pseudosphere", MA thesis (Universität Regensburg, 2022).

[193] M. Fürst, "Quantum mechanical conductivity in shaped topological insulator nanowires", BA thesis (Universität Regensburg, 2020).

[194] Y. Aharonov and D. Bohm, "Significance of electromagnetic potentials in the quantum theory", Phys. Rev. **115**, 485 (1959).

[195] H.-F. Cheung, Y. Gefen, and E. K. Riedel, "Isolated rings of mesoscopic dimensions. Quantum coherence and persistent currents", IBM J. Res. Dev. **32**, 359–371 (1988).

[196] F. Crépin and B. Trauzettel, "Flux sensitivity of quantum spin Hall rings", Phys. E: Low-Dimens. Syst. Nanostructures **75**, 379–384 (2016).

[197] M Büttiker and T. Klapwijk, "Flux sensitivity of a piecewise normal and superconducting metal loop", Phys. Rev. B **33**, 5114 (1986).

[198] Y. Tanaka, M. Sato, and N. Nagaosa, "Symmetry and Topology in Superconductors –Odd-Frequency Pairing and Edge States–", J. Phys. Soc. Japan **81**, 011013 (2012).

[199] A. R. Akhmerov, J. Nilsson, and C. W. J. Beenakker, "Electrically Detected Interferometry of Majorana Fermions in a Topological Insulator", Phys. Rev. Lett. **102**, 216404 (2009).

[200] L. Fu and C. L. Kane, "Probing Neutral Majorana Fermion Edge Modes with Charge Transport", Phys. Rev. Lett. **102**, 216403 (2009).

[201] G. Deutscher and D. Feinberg, "Coupling superconducting-ferromagnetic point contacts by Andreev reflections", Appl. Phys. Lett. **76**, 487–489 (2000).

[202] G. B. Lesovik, T. Martin, and G. Blatter, "Electronic entanglement in the vicinity of a superconductor", Eur. Phys. J. B **24**, 287–290 (2001).

[203] P. Recher, E. V. Sukhorukov, and D. Loss, "Andreev tunneling, Coulomb blockade, and resonant transport of nonlocal spin-entangled electrons", Phys. Rev. B **63**, 165314 (2001).

[204] L. Hofstetter et al., "Cooper pair splitter realized in a two-quantum-dot Y-junction", Nature **461**, 960–963 (2009).

[205] L. G. Herrmann et al., "Carbon Nanotubes as Cooper-Pair Beam Splitters", Phys. Rev. Lett. **104**, 026801 (2010).

[206] J. Schindele, A. Baumgartner, and C. Schönenberger, "Near-Unity Cooper Pair Splitting Efficiency", Phys. Rev. Lett. **109**, 157002 (2012).

[207] R. Nehra et al., "Enhancement of crossed Andreev reflection in a Kitaev ladder connected to normal metal leads", J. Condens. Matter Phys. **31**, 345304 (2019).

[208] X.-L. Qi and S.-C. Zhang, "Topological insulators and superconductors", Rev. Mod. Phys. **83**, 1057–1110 (2011).

[209] J. Fuchs, *Transport and subgap states in superconducting heterostructures of effective Dirac systems*, 2023.

[210] V. Mourik et al., "Signatures of Majorana fermions in hybrid superconductor-semiconductor nanowire devices", Science **336**, 1003–1007 (2012).

[211] A. Das et al., "Zero-bias peaks and splitting in an Al–InAs nanowire topological superconductor as a signature of Majorana fermions", Nat. Phys. **8**, 887–895 (2012).

[212] M. Deng et al., "Anomalous zero-bias conductance peak in a Nb–InSb nanowire–Nb hybrid device", Nano Lett. **12**, 6414–6419 (2012).

[213] W. Meissner and R. Ochsenfeld, "Ein neuer Effekt bei Eintritt der Supraleitfähigkeit", Naturwissenschaften **21**, 787–788 (1933).

[214] A. M. Cook, M. M. Vazifeh, and M. Franz, "Stability of Majorana fermions in proximity-coupled topological insulator nanowires", Phys. Rev. B **86**, 155431 (2012).

[215] F. de Juan, J. H. Bardarson, and R. Ilan, "Conditions for fully gapped topological superconductivity in topological insulator nanowires", SciPost Phys. **6**, 60 (2019).

[216] D. Rosenbach et al., "Quantum transport in topological surface states of selectively grown Bi2Te3 nanoribbons", Adv. Electron. Mater. **6**, 2000205 (2020).

[217] C. J. Lambert and R Raimondi, "Phase-coherent transport in hybrid superconducting nanostructures", J. Condens. Matter Phys. **10**, 901–941 (1998).

[218] Y. Chen, H.-Z. Lu, and X. C. Xie, "Forbidden Backscattering and Resistance Dip in the Quantum Limit as a Signature for Topological Insulators", Phys. Rev. Lett. **121**, 036602 (2018).

[219] A. Wolos et al., "g-factors of conduction electrons and holes in Bi_2Se_3 three-dimensional topological insulator", Phys. Rev. B **93**, 155114 (2016).

[220] R. Ilan et al., "Detecting perfect transmission in Josephson junctions on the surface of three dimensional topological insulators", New J. Phys. **16**, 053007 (2014).

[221] L. Stampfer et al., "Andreev Interference in the Surface Accumulation Layer of Half-Shell InAsSb/Al Hybrid Nanowires", Adv. Mater. **34**, 2108878 (2022).

[222] K. Gharavi et al., "Nb/InAs nanowire proximity junctions from Josephson to quantum dot regimes", Nanotechnology **28**, 085202 (2017).

[223] P Wójcik and M. Nowak, "Durability of the superconducting gap in Majorana nanowires under orbital effects of a magnetic field", Phys. Rev. B **97**, 235445 (2018).

[224] G. W. Winkler et al., "Unified numerical approach to topological semiconductor-superconductor heterostructures", Phys. Rev. B **99**, 245408 (2019).

[225] A. Weiße et al., "The kernel polynomial method", Rev. Mod. Phys. **78**, 275 (2006).

[226] L Covaci, F. Peeters, and M Berciu, "Efficient numerical approach to inhomogeneous superconductivity: the Chebyshev-Bogoliubov–de Gennes method", Phys. Rev. Lett. **105**, 167006 (2010).

[227] K. Björnson and A. M. Black-Schaffer, "Majorana fermions at odd junctions in a wire network of ferromagnetic impurities", Phys. Rev. B **94**, 100501 (2016).

[228] M. Mashkoori, K. Björnson, and A. M. Black-Schaffer, "Impurity bound states in fully gapped d-wave superconductors with subdominant order parameters", Sci. Rep. **7**, 1–10 (2017).

[229] J. W. Eaton et al., *GNU Octave version 6.1.0 manual: a high-level interactive language for numerical computations* (2020).

[230] W. Han et al., "Graphene spintronics", Nat. Nanotechnol. **9**, 794–807 (2014).

[231] W. Belzig et al., "Spin accumulation and Andreev reflection in a mesoscopic ferromagnetic wire", Phys. Rev. B **62**, 9726–9739 (2000).

[232] L. C. Hebel and C. P. Slichter, "Nuclear relaxation in superconducting aluminum", Phys. Rev. **107**, 901–902 (1957).

[233] L. C. Hebel and C. P. Slichter, "Nuclear spin relaxation in normal and superconducting aluminum", Phys. Rev. **113**, 1504–1519 (1959).

[234] L. C. Hebel, "Theory of nuclear spin relaxation in superconductors", Phys. Rev. **116**, 79–81 (1959).

[235] I.-H. Tan et al., "A self-consistent solution of Schrödinger–Poisson equations using a nonuniform mesh", J. Appl. Phys. **68**, 4071–4076 (1990).

[236] B. A. Bernevig, T. L. Hughes, and S.-C. Zhang, "Quantum spin Hall effect and topological phase transition in HgTe quantum wells", Science **314**, 1757–1761 (2006).

[237] M. König et al., "The Quantum Spin Hall Effect: Theory and Experiment", J. Phys. Soc. Japan **77**, 031007 (2008).

[238] D. G. Rothe et al., "Fingerprint of different spin–orbit terms for spin transport in HgTe quantum wells", New J. Phys. **12**, 065012 (2010).

[239] A. Zegarra, J. C. Egues, and W. Chen, "Persistent currents and spin torque caused by percolated quantum spin Hall state", Phys. Rev. B **101**, 224438 (2020).

[240] E. C. Stoner, "Collective electron ferromagnetism ii. energy and specific heat", Proceedings of the Royal Society of London. Series A. Mathematical and Physical Sciences **169**, 339–371 (1939).

[241] A. El Hamdi, "Spin-to-charge conversion at the LaAlO3/SrTiO3 interface Rashba state", PhD thesis (Université Paris-Saclay, 2021).

[242] D. Marchand and M Franz, "Lattice model for the surface states of a topological insulator with applications to magnetic and exciton instabilities", Phys. Rev. B **86**, 155146 (2012).

[243] L. Fu, "Hexagonal Warping Effects in the Surface States of the Topological Insulator Bi_2Te_3", Phys. Rev. Lett. **103**, 266801 (2009).

[244] P. Adroguer et al., "Diffusion at the surface of topological insulators", New J. Phys. **14**, 103027 (2012).

List of publications:

- D. Kochan, M. Barth, A. Costa, K. Richter, and J. Fabian, "Spin Relaxation in s-Wave Superconductors in the Presence of Resonant Spin-Flip Scatterers", Phys. Rev. Lett. **125**, 087001 (2020).
- J. Fuchs, M. Barth, C. Gorini, İ. Adagideli, and K. Richter, "Crossed Andreev reflection in topological insulator nanowire T junctions", Phys. Rev. B **104**, 085415 (2021).
- M. Barth, J. Fuchs, and D. Kochan, "Spin relaxation, Josephson effect, and Yu-Shiba-Rusinov states in superconducting bilayer graphene", Phys. Rev. B **105**, 205409 (2022).
- D. Kochan, M. Barth, A. Costa, K. Richter, and J. Fabian, "Spin relaxation and Yu-Shiba-Rusinov states in superconducting graphene", AIP Conf. Proc. **2551**, 040002 (2022).
- W. Himmler, R. Fischer, M. Barth, J. Fuchs, D.A. Kozlov, N.N. Mikhailov, S.A. Dvoretsky, C. Strunk, C. Gorini, K. Richter, and D. Weiss, "Supercurrent interference in HgTe-wire Josephson junctions", Phys. Rev. Research **5**, 043021 (2023).
- G. Fleury, M. Barth, and C. Gorini, "Tunneling anisotropic spin galvanic effect", Phys. Rev. B **108**, L081402 (2023).
- L. Pietanesi, T. Mayer, M. Marganska, M. Barth, L. Chen, J. Zou, R. Díaz-Pardo, D. Suri, A. Weindl, A. Liebig, F. Schmid, F. J. Gießibl, K. Richter, Y. Tserkovnyak, M. Kronseder, and C. H. Back, "Ferromagnetic resonance for spectroscopic investigation of topological surface states", under evaluation (2023).

Acknowledgments

I want to thank all the people who supported me while working on this thesis.

First, I want to particularly thank Prof. Dr. K. Richter for giving me the opportunity to join his group and to work on so many interesting projects. His leadership in terms of giving support when needed, but still allowing for the right amount of freedom in the progress of handling projects, allowed me to gain a lot of experience in organization and in solving occurring problems. Working in his group was always a pleasure due to his ability to generate a nice atmosphere at the chair and his friendly and fair treatment of people. With his guidance and encouragement I could grow scientifically and also personally.
Then, I also want to thank Dr. C. Gorini for all of the nice discussions on physics and the support in many of my projects. With his expertise he contributed in solving technical problems and in answering physical questions, and with his honest and bright character he always raised the motivation and contributed a lot to the pleasant working atmosphere with his funny comments and jokes. Also, I am very grateful to him for still keeping up the collaboration, despite his movement to Paris.
Moreover, I want to express my gratitude to Dr. D. Kochan for inviting me to join many of his projects. This chance allowed me to gain a big amount of scientific knowledge and tackling problems with him was also fun due to his big arsenal of jokes. Discussions with him about physics, but also about general topics in life, made working with him a valuable time at the university.
Furthermore, I would like to thank all of my colleagues for making my time at the chair so enjoyable. Working on system administrator tasks with my predecessors Dr. J. Fuchs, Dr. R. Kozlovsky, Dr. J. Rammensee, and then also with V. Junk, F. Haneder, and G. Maier was always a welcome distraction from scientific problems. I am very grateful to Dr. A. Costa, M. Fürst, Mathias Steinhuber, Fabian Haneder and Georg Maier for carefully proof reading this thesis and for giving me constructive and important feedback. Also, I want to thank the secretaries Doris Meier, Toni Siegmund, Elke Haushalter and Romy Fischer for taking care of any contract and organizational issues.

I acknowledge funding from the Sonderforschungsbereich 1277 and the Elite Network of Bavaria within the graduate school "Topological Insulators".

Finally, I am deeply grateful to my wife Theresa, Freddy and my family for supporting me throughout my studies and in the process of writing this dissertation.